# THE LATE QUATERNARY DEEP-SEA DEPOSITIONAL SYSTEM IN THE GULF OF PAPUA: LINKING SOURCE, DYNAMIC SEDIMENTATION PROCESS AND DEPOSITIONAL ARCHITECTURE

by

© Erlangga Septama

A Dissertation submitted to

the School of the Graduate Studies

in partial fulfillment for the degree of

Doctor of Philosophy

Department of Earth Sciences

Memorial University of Newfoundland

December 2015

St. John's  Newfoundland and Labrador

ABSTRACT

This study was undertaken to explore interactions among eustatic sea level change, fluvial sediment supply, oceanic processes, and seabed morphodynamics, and their controls on delivery of terrestrial sediments to the deep sea, using the Gulf of Papua (GoP), between New Guinea and Australia, as a natural laboratory. The GoP is a 500 km wide embayment that contains excellent examples of adjacent passive and active terrestrial-oceanic margins with multiple sources of terrestrial and neritic carbonate sediments. This work examines source to sink sediment delivery from river systems to the slope and deep-sea basins of the GoP, over the last ~40 ky, at millennial temporal resolution and finer. The results offer new insights into the development of sedimentary successions in deep-sea basins, and also into approaches for provenance analysis.

Mapping and integration of acoustic facies with core physical properties, sedimentary fabric, and chronostratigraphy allows placement of seafloor evolution into a well-defined temporal framework. Chronological constraints permit an assessment of changes in sediment supply and depositional environments across time and space, from marine isotope stage (MIS) 3 to MIS 1. Sand provenance provides additional insights regarding sediment sources and routing.

In summary, the study yields a narrative of sediment delivery along a ~500 km basin margin that is more complex than initially imagined. The sediment delivery to and conduit connectivity between deep-sea basins evolves over time due to the combined effects of eustasy, oceanic processes, and dynamic seabed morphology. Multiple terrestrial sediment sources along a ~500 km basin margin initially converge to form one continuous deep-sea system of channels and two major basins prior to 30 ky BP, that become bathymetrically separated by a large mass-transport

deposit. Subsequent sea-level fall approaching the late glacial maximum (LGM) initially drives re-partitioning of sediment sources to create multiple compositionally distinct depocentres, presumably due to migration and incision of individual rivers across the newly exposed coastal plain. Multiple separate deep-sea channels then regain compositional similarity near the end of the LGM, due to regional erosion into compositionally similar catchment rocks. Furthermore sand transport shuts down, except for one depocentre (MV22), fed by local volcanic, that remains active at least into the Middle Holocene.

Table of Contents

List of Tables



List of Figures

Chapter-2 the Chronostratigraphy and regional facies variation of the Pleistocene-Holocene Sediment in the deep-water Gulf of Papua



Chapter-3 Late Quaternary geomorphology, seabed evolution, and terrigenous sediment delivery to the Pandora and Moresby Troughs, Gulf of Papua

Chapter-4 Late Quaternary geomorphology, seabed evolution, and terrigenous sediment delivery to the Pandora and Moresby Troughs, Gulf of Papua

List of abbreviations and symbols

| | |
|---|---|
| AMS | = Accelerometer mass spectrometry |
| ASCII | = American Standard Code for Information Interchange |
| BEI | = Backscatter electron imaging |
| BU | = Basement uplift (Gazzi-Dickinson provenance class) |
| $^{14}C$ | = Carbon 14 |
| Cal. ka | = Calendar thousand years |
| CEN | = Centre d'Études Nordique |
| CIA | = Chemical index of alteration |
| *d* | = Euclidean distance |
| DA | = Dissected arc (Gazzi-Dickinson provenance class) |
| $\delta^{18}O$ | = Delta oxygen 18 (measure of ratio between $^{18}O$ : $^{16}O$) |
| KAnAb | = Potassium Anorthite Albite |
| KEB | = Knudsen extended binary |
| kHz | = Kilohertz |
| ky BP | = thousand years before present |
| $\gamma\rho$ | = Gamma density |
| GoP | = Gulf of Papua |
| JPC | = Jumbo piston core |
| L* | = Total lightness |
| LAS | = Log ASCII standard |

| | |
|---|---|
| LGM | = Last Glacial Maximum |
| MAR | = Mass accumulation rate |
| MBSF | = Meter below seafloor |
| MBPSL | = Meter below present sea level |
| MBSL | = Meter below sea level |
| MC | = Multi core |
| MIS | = Marine isotope stage |
| MS | = Magnetic susceptibility |
| MSCL | = Multi-sensor core logger |
| MT | = Moresby Trough |
| MTD | = Mass transported deposit |
| MUN | = Memorial University of Newfoundland |
| MV | = Melville |
| MWP-1B | = Melt water pulse 1B |
| nMDS | = Non-metric multidimensional scaling |
| NSF-MARGINS | = National Science Foundation margins programs |
| PANASH | = Paleo-climates of Northern and Southern Hemisphere |
| $^{210}Pb$ | = Radioactive isotope produced by decay of atmospheric $^{222}Rn$ |
| PT | = Pandora Trough |
| RO | = Recycled orogen (Gazzi-Dickinson provenance class) |
| RSMAS | = Rosentiel School of Marine and Atmospheric Science |
| R/V | = Research vessel |

| | |
|---|---|
| S2S | = Source to Sink |
| SAR | = Sediment accumulation rate |
| SEG-Y | = Society of Exploration Geophysics Y format |
| SEM-MLA | = Scanning electron microscopy and Mineral liberation analysis |
| SimPer | = Similarity Percentage |
| $T_{a-e}$ | = Bouma turbidite division (a-e) |
| TA | = transitional arc (Gazzi-Dickinson provenance class) |
| TC | = Transitional continental (Gazzi-Dickinson provenance class) |
| Wt% | = Weight percent |
| QFL diagram | = Quartz feldspar lithic fragment ternary diagram |
| QmKP | = Quartz monocrystalline, potassium, plagioclase |
| XRF | = X-ray fluorescence |

**Acknowledgements**

I would like to thank my research supervisor Sam Bentley, who gave me brand new experiences and insights to the world of sedimentology. Your energy and enthusiasm are contagious and made this research project an outstanding learning process.

I want to thank my academic supervisor Rick Hiscott for very helpful review and comments. My thesis also benefited significantly from discussion with my thesis committee member, André Droxler, in Department of Earth Science, Rice University, Houston.

Thanks to examiners Bradley Opdyke from the Research School of Earth Sciences, Australian National University; Christopher Fedo from Department of Earth and Planetary Sciences at the University of Tennessee, and Jeremy Hall from Department of Earth Sciences, Memorial University of Newfoundland for the insightful debate and discussion during the examination.

Special thanks to Larry Paterson and Melany McFadden of Rosenstiel School of Marine and Atmospheric Science (RSMAS) University of Miami for the discussion and assistance during the core sampling and preparation in Miami. Thanks to Rolf Aalto from Geography Department, University of Exeter to let us using the Fly-Strickland river catchment samples.

I want to thank John Hanchar, Head of Department of Earth Science MUN for facilitating the dissertation, my past committee members, Ali Aksu and George Jenner for insightful discussion about paleoclimate and geochemistry, Joe McQuaker for the financial assistance for thin section analysis. Thanks to Helen Gillespie and Trisandhi Gosine for assistance in core data preparation and analysis in Memorial University of Newfoundland (MUN), Wanda Aylward for assistance in Core Research Equipment and Instrument Training Network (CREAIT) facilities utilization. I am grateful for the help from the MUN Department of Earth Science staff, Michelle Miskell, Diane Guzzwell, Danyelle Drodge, Keir Hiscock and Kristin Hanlon for the administrative support.

Thanks for everyone who spent time with me and whose survive four harsh Canadian winters together, Peter, Lisi, Lina, Flo, Susanne, Bursin, Burcu, Dario, Kathryn, Pinar, James, Matt, Nathalie, Crystal, Liam, Rich, Jen, Dave, Megan, Alex, Anne, Eddie, Chris, Gosia, Pete, Doreen, Bahar, Kaan, Hasan and Ezgi. You’re all the best!

I want to thank my family, my wife Imel, my daughters Aurel, Aqeela and Li’l Aliya for all their love and support; I would not have been able to do this without them.

## CHAPTER 1

# The Late Quaternary deep-sea depositional system in the Gulf of Papua: linking source, dynamic sedimentation processes and depositional architecture

### 1.1. Introduction

Deep-sea basins are one of the ultimate sink for sediments derived from land and delivered to the oceans by rivers. Sediments in these basins contain important records of the processes controlling sediment supply, including tectonic, climatic, and oceanographic conditions and processes, and eustasy, and so such basins constitute important archives of earth history. In addition, deep sea basins may possess the materials and conditions required for hydrocarbon production and accumulation, and have been increasingly the focus of petroleum exploration for the last several decades (Fillon et al., 2001; Akutsu, 2007; Morley et al., 2011). For these reasons, the development of such deep-sea sedimentary successions is an important area of study.

The US-National Science Foundation MARGINS Source to Sink Program (S2S) was initiated to better understand the production, transport, and final accumulation of sediments along continental margins, particularly regarding the relative influences of tectonic, climatic, sea-level, and oceanographic processes on development of continental-margin sedimentary cover; the Gulf of Papua (GoP) and associated terrestrial fluvial sources and sedimentary basins were selected as one of the focus areas (NSF-MARGINS, 2004). GoP deep-sea basins are the ultimate sinks for sediment from the Papuan mainland and peninsula, and contain valuable history about the sedimentation rate, dispersal pattern and spatial variation (Francis et al., 2008). This modern foreland basin has formed within a continental-margin salient characterized by gradients in morphology and sediment supply, with mature rivers feeding a wide shelf margin toward the western GoP (delivering sediments to the Pandora Trough [PT]), and steep slope, small mountain rivers and narrow shelf margin to the east, adjacent to the Papuan Peninsula (delivering sediments to the Moresby Trough [MT]) (Figure 1.1.).

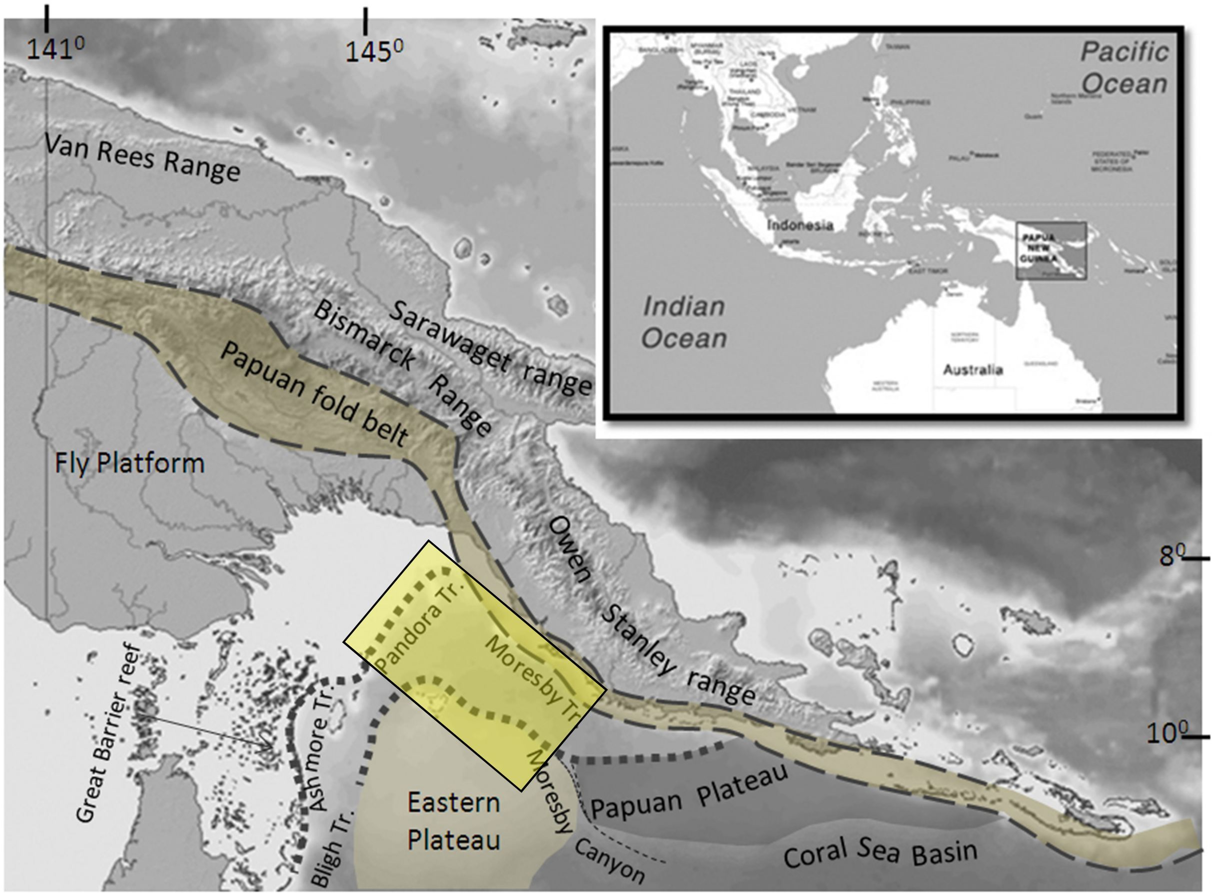


Figure 1.1. Locations of Pandora and Moresby Troughs (yellow box) in the Gulf of Papua, a foreland basin to the Papuan Orogeny, which has built the mountain ranges and fold belts to the north and east of the GoP.

This complex continental margin receives large terrigenous sediment flux from at least six medium to large rivers (the Fly/Strickland river system being the largest; 365 million tons/ year estimated for all rivers) (Milliman, 1995) and has been progressively drowned since the Last Glacial Maximum (LGM) (23-19 ky BP), with flooding of the shelf contributing to changes in sediment delivery to the deep sea (Howell et al., 2014) and sediment trapping on the shelf (Slingerland et al., 2008). The selection of the GoP as a focus area for S2S was based on certain regional characteristics considered critical to achieving program objectives, including: strong signal from large sediment yields, minimum anthropogenic effect, quantifiable closed S2S system with an active transfer into accessible deep-sea basins, potential for high resolution of stratigraphic records correlated with sea level history, and access to the entire study area (NSF-MARGINS, 2004).

Through S2S and previous study, the GoP shelf and offshore basins have been intensively investigated by multibeam bathymetry, 3.5 KHz seismic profile and core samples, and thus provide an excellent natural laboratory for analog study of the dynamic processes associated with sources, timing and depositional product (Dickens et al., 2006). This dense data set also permits us a rare opportunity to study the evolution of a regional deep-sea depositional system in higher resolution (centennial-millennial time scale, cm to m sedimentary thickness) over approximately the last 40 Kyr BP, a degree of documentation that could not be possible in many deep-sea studies.

This dissertation consists of three major chapters, framed by this introductory and one concluding chapter. Chapters II-IV are written in self-contained manuscript format, for subsequent publication as journal articles. Chapter II will investigate the Pleistocene-Holocene deep-sea sediment stratigraphy and facies variation of the Pandora and Moresby troughs. Specific objectives in Chapter II are to build a regional Late Quaternary lithofacies and stratigraphic framework for the study area by combining observations of sediment-core stratigraphy and physical properties, accelerometer mass spectrometry (AMS) C-14 data, core x-radiographs and thin sections. This framework will be used to determine depositional timing for turbidite delivery into the basin, and to evaluate regional facies variability, as influenced by glacio-eustatic, climatic and oceanographic forcing. This framework will form the basis for additional studies of seabed geomorphology and sediment provenance (Chapters III and IV). The maximum absolute age obtained for most cores is approximately 40 Ka, so the time frame for these studies encompasses marine isotope stages (MIS) 3 to 1.

Chapter III is a study of seabed morphological characterization and evolution of the Pandora and Moresby troughs over the time frame of MIS 3 to 1. The main objectives of this chapter are to document and interpret the present to near present sedimentation processes in the seafloor, and to identify acoustic and lithofacies distributions and development, including timing, delivery pathways, and depositional architecture. This chapter incorporates 3D visualization, analysis, and interpretation of seabed morphology, stratigraphy, and sediment acoustic characteristics derived from sub-bottom sonar data and sediment cores collected during the 2004 PANASH cruise of the R/V Melville (Dickens et al., 2006), and multibeam data collected and gridded during that and other cruises.

Chapter IV is a provenance analysis of turbidite sands sampled from jumbo piston cores collected from the Pandora and Moresby troughs during the PANASH cruise in 2004, incorporating morphological and stratigraphic insights from chapters II and III. This chapter addresses three questions. (1) What are the likely sources of terrestrial sediment delivered to these basins? (2) Over what time spans is sediment delivered to each basin? (3) What factors are controlling the timing and pathways of sediment delivery? This chapter will investigate the source-to-sink narrative extending back to ~40 ky BP with an assumption that neither parent rocks nor the sediment composition in the catchment have undergone significant change over that period. This study is novel because one of the first attempts to use advanced Scanning

Electron Microscopy Mineral Liberation Analysis (an advanced semi-automated image analysis approach for grain-scale compositional analysis) (Fandrich et al., 2007) coupled with similarity percentage and clustering analysis (Anderson et al., 2008) to study provenance of detrital sediments.

Chapter V reviews overall findings, strengths, and weaknesses of this dissertation, and offers suggestions for future research in both the Gulf of Papua specifically and sedimentary evolution of deep-sea basins in general.

## 1.2. References

Akutsu, T. (2007). Contribution of geological deep-water systems to reservoirs of deep-water fields, and critical points for petroleum system in deep water. Sekiyu Gijutsu Kyokaishi = Journal Of The Japanese Association Of Petroleum Technology, 72(1), 5-15.

Anderson, M.J., Gorley, R.N. & Clarke, K.R. (2008). PERMANOVA+ for PRIMER: Guide to software and statistical methods . PRIMER-E Ltd, Plymouth, UK

Fillon, R., Rosen, N., Weimer, P., Lowrie, A., Pettingill, H., Phair, R., and van Hoorn, B. (2001). Petroleum systems of deep-water basins; global and Gulf of Mexico experience. Program And Abstracts - Society Of Economic Paleontologists. Gulf Coast Section. Research Conference, 21

Fandrich, R., Gu, Y., Burrows, D., & Moeller, K. (2007). Modern SEM-based mineral liberation analysis. International Journal of Mineral Processing, 84(1), 310-320.

Francis, J.M., Daniell, J.J., Droxler, A.W., Dickens, G.R., Bentley,S.J., Peterson, L.C., Opdyke, B.N., Beaufort, L., 2008. Deep Water Geomorphology of the Mixed Siliciclastic-carbonate System, Gulf of Papua. Jour. of Geophys. Res., v. 113, p. 1-22.

Howell, A. L., Bentley, S. J., Xu, K., Ferrell Jr, R. E., Muhammad, Z., & Septama, E. (2014). Fine sediment mineralogy as a tracer of latest Quaternary sediment delivery to a dynamic continental margin: Pandora Trough, Gulf of Papua, Papua New Guinea. *Marine Geology* DOI: 10.1016/j.margeo.2014.08.003

Milliman, J.D., 1995. Sediment Discharge to the Ocean from Small Mountainous Rivers: the New Guinea Example. Geo. Mar. Let., v. 15, no. 3-4, p. 127-133.

Morley, C. K., King, R. R., Hillis, R. R., Tingay, M. M., & Backe, G. G. (2011). Deep water fold and thrust belt classification, tectonics, structure and hydrocarbon prospectivity; a review. Earth-Science Reviews, 104(1-3), 41-91. doi:10.1016/j.earscirev.2010.09.010

NSF-MARGINS 2004, National Science Foundation MARGINS Program Science Plan 2004 http://www.nsf-margins.org/publications/SciencePlans/MARGINS_SciencePlans2004.pdf accesed : 10/04/2014

Slingerland, R., Selover, R.W., Ogston, A.S., Keen, T.R., Driscoll, N.W., Milliman, J.D., 2008b. Building the Holocene Clinothem in the Gulf of Papua: an Ocean Circulation Study. Jour. of Geophys. Res., v. 113, p. 1-17.

CHAPTER 2

# Conduits, Timing and Processes of Sediment Delivery across a High-Relief Continental Margin: Continental Shelf to Basin in Late Quaternary, Gulf of Papua

## 2.1. Introduction

The Gulf of Papua (GoP) deep-sea basin is the ultimate sink for sediment from the southern margin of the Papuan mainland and peninsula, and contains a valuable historical record of the spatial and temporal variations in regional sedimentation rates and dispersal patterns. This region was selected by the US National Science Foundation MARGINS-Source-to-Sink Program (S2S) as a focus area for study of continental margin sedimentation and stratigraphy, because of the high rates of sediment transfer from land to coastal sea to marine basins, and because of relatively modest anthropogenic alteration of both terrestrial and marine portions of the sediment dispersal system; the GoP was the location of numerous S2S research cruises in 2003-2005 to study margin evolution (NSF MARGINS, 2004; Dickens et al., 2006). This modern sedimentary basin has formed within a continental-margin salient characterized by gradients in morphology and sediment supply, with mature rivers feeding a wide shelf margin in the southwest area, and steep slope, small mountain-fed rivers and narrow shelf margin in the southeast peninsular area (Figure 2.1.). Numerous studies have been published evaluating geological processes and products including local geological processes through time (e.g., Howell et al., 2014), and modern regional seabed morphology (Francis et al., 2008), but the regional geological evolution of the deepest basins remains underexplored, particularly with respect to changes in sediment flux and sources over time.

The objectives of this chapter are to build a regional Late Quaternary lithofacies and stratigraphic framework for the study area by combining observations of sediment-core stratigraphy and physical properties, accelerometer mass spectrometry (AMS) C-14 data, core x-radiographs and thin sections. Data used to evaluate the study area are derived from analysis of multi-cores and jumbo piston cores collected during the PANASH cruise of the R/V Melville cruise in 2004 (Dickens et al., 2006). In the present study, this framework will be used to determine depositional frequency and timing for turbidite delivery into the basin, and to evaluate regional lithofacies variability, as influenced by glacio-eustatic, climatic and oceanographic forcing. In Chapter 4 of this study, this framework will form the basis for additional studies of seabed geomorphology and sediment provenance. The maximum absolute age obtained for most cores is approximately 40 cal ka, so the time frame for these studies encompasses marine isotope stages (MIS) 3 to MIS 1 (ICS, 2010).

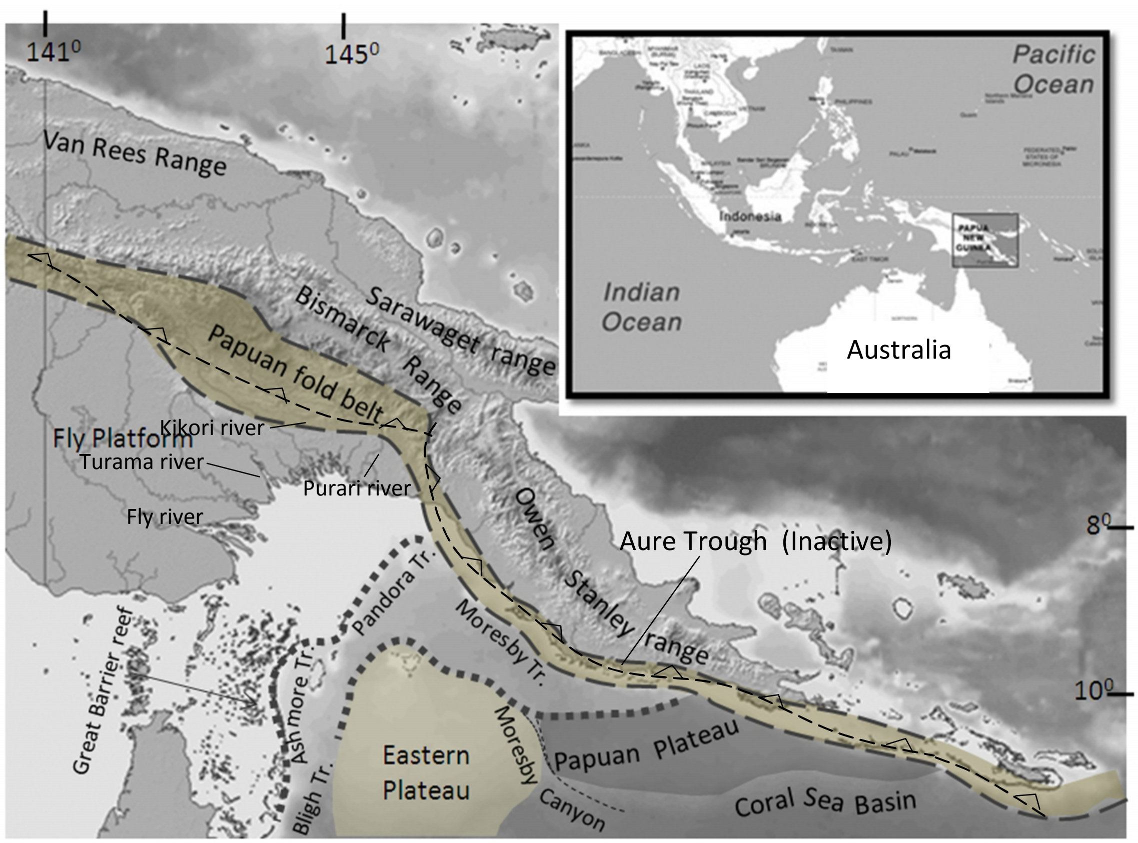


Figure 2.1. Modern physiographic and tectonic elements of the Gulf of Papua (modified after Pigram and Davies, 1987, the relic of the inactive Aure trough was re-drawn based on Cloos et al., 2005).

## 2.2. Geological background

The island of Papua is one component of a complex convergent plate boundary formed as a result of the collision between the Indo-Australian Plate and the Southwest Pacific Plate Fig. 2.1)(Pigram and Davies, 1987). The study area in the GoP is an example of an active developing foreland basin which receives intense terrigenous sediment influx from the surrounding river systems (Slingerland et al., 2008).

The Pandora and Moresby Troughs are the foredeep of the Papuan Orogen which are originally part of the inactive Aure Trough (Cloos et al., 2005), which has risen since the Late Cretaceous (ca. 65 Ma) (Figure 2.1). These foreland basins began receiving terrigenous sediment in the proximal area as early as Eocene (55.8-33.9 Ma) and reached peak depositional rates through the entire basin during the Pliocene-Holocene (< 5 Ma) when uplift in the orogenic belt intensified (Tcherepanov et al., 2008). The uplift along the collision margin has produced >4000 m relief which, combined with high precipitation rate (2-10 m/yr), produces runoff that delivers abundant sediment downstream (approximately 365 million t/yr; Milliman, 1995). The best documented influxes come from the Fly, Kikori and Purari rivers (Figure 2.1) on the Papuan mainland. Drainage from small river systems on the Papuan Peninsula has never been rigorously quantified (approximations in Milliman, 1995) but could potentially produce significant influx to the deep Moresby Trough in the eastern part of GoP (Figure 2.1.) (Howell et al., 2014).

Source rocks for deep-sea sediments mainly are found within the Papuan Orogen. This tectonic sierra is developed from the colliding New Guinea plate and the Southern Pacific subduction complex, which consists of several arcs, oceanic plateaus and micro-plates (Pigram and Davies, 1987, Pigram et al., 1989; Davies, 2012). The resulting geological formations are widely varied and include quartzo-feldspathic sediment to mafic igneous rocks (Patterson, 2006).

In this study we use the terms Papuan mainland (land north of the western part of the GoP) and Papuan Peninsula (land northeast of the eastern part of the GoP) to spatially define the sediment sources, catchment systems and basins. In general, the sediment transit time from terrestrial sources to deep-sea depocentres is relatively longer for the Papuan mainland (western GoP) (Day et al., 2008) than the Papuan Peninsula (Milliman, 1995), because of the large river systems with well-developed alluvial valleys that deliver sediment to a wide continental shelf south of the mainland region. In contrast, the Papuan peninsula (eastern GoP) is characterized by relatively small mountain-fed rivers and a narrow continental shelf (Figure 2.1).

## 2.3. Methodology

Data for this study are derived from seven jumbo piston cores (JPC) (MV22, 23, 25, 27, 29, 33 and MV54) and five additional multicores (MC) (MV19, 24, 26, 28 and MV50) collected during the 2004 R/V Melville cruise. The cores sample the shelf, shelf-break, slope, mini-basin to channel and basin floor (Figure 2.2. and Table 2.1.). Core locations were selected based on 3.5 KHz and multi-beam bathymetric data collected during the same cruise. Piston cores were logged shipboard by previous researchers (Dickens et al., 2006; Patterson, 2006; Febo et al., 2008; Muhammad et al., 2008) using a Geotek multi-sensor core logger (MSCL) for gamma-density and magnetic susceptibility. Split cores were imaged using a Geotek geoscan digital imaging system once onshore. Two multicore tubes were sampled from each deployment. One tube was extruded and sub-sampled at 1-2 cm intervals for sedimentological analyses, and second tube was extruded, sliced axially to yield a 2 cm-thick slab, and then imaged by Muhammad et al. (2008) using a portable x-radiography system.

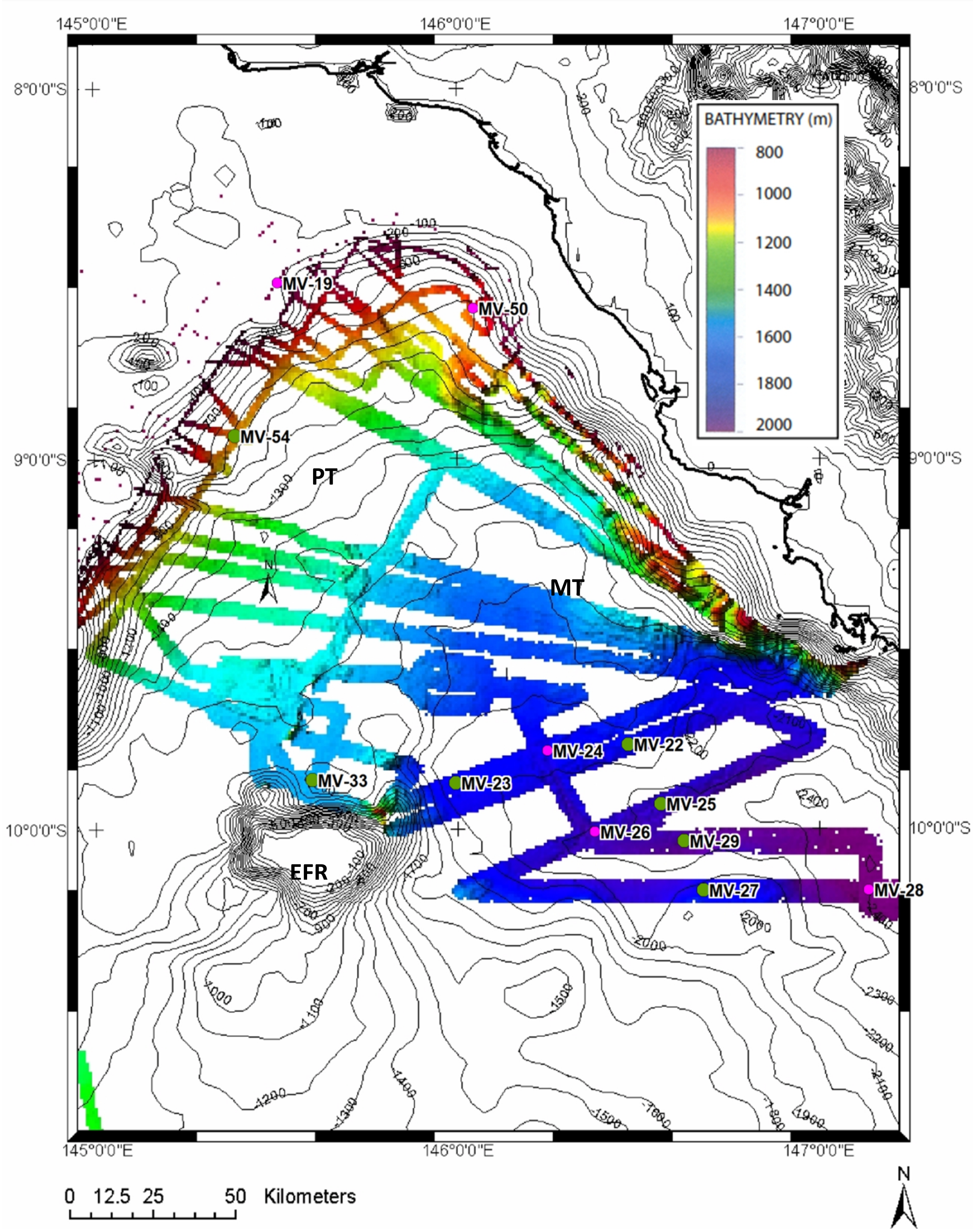


Figure 2.2. Basemap of the Gulf of Papua (NSF focus area). Bathymetry and cores were acquired during the R/V Melville cruise 2004. This study is based on 7 jumbo piston cores (JPC) and 5 multi cores (MC) ( red = multicores, green = jumbo piston cores) (EFR= Eastern Field Reef, PT=Pandora Trough, MT= Moresby Trough). Bathymetry from Daniell (2008), showing S2S swath survey tracks.

| No | Core | Type | Long | Lat | Depth (mbsl) | core Length (m) | Present day environment |
|---|---|---|---|---|---|---|---|
| 1 | MV19 | MC | 145.507 | -8.5234 | 229 | 0.5 | shelf edge to shelf break |
| 2 | MV22 | JPC | 146.471 | -9.7731 | 2058 | 12.975 | basin floor, distal part of the lobes |
| 3 | MV23 | JPC | 145.995 | -9.8762 | 2068 | 10.125 | toe of slope, part of side levee of Moresby Channel |
| 4 | MV24 | MC | 146.248 | -9.789 | 2102 | 0.5 | basin floor, Moresby Channel levee system |
| 5 | MV25 | JPC | 146.56 | -9.9333 | 2193.24 | 12.765 | basin floor, Moresby Channel levee system |
| 6 | MV26 | MC | 146.379 | -10.009 | 2232 | 0.5 | basin floor, Moresby channel, near axis |
| 7 | MV27 | JPC | 146.678 | -10.1667 | 2071 | 13.845 | sea floor rise (eastern field plateau) |
| 8 | MV28 | MC | 147.133 | -10.1667 | 2426 | 0.45 | basin floor |
| 9 | MV29 | JPC | 146.625 | -10.0333 | 2288.2 | 6.415 | basin floor, Moresby channel, near axis |
| 10 | MV33 | JPC | 145.6 | -9.867 | 1787 | 12.7 | Mini basin |
| 11 | MV50 | MC | 146.046 | -8.5993 | 795 | 0.24 | upper slope |
| 12 | MV54 | JPC | 145.389 | -8.9364 | 924.63 | 11.745 | slope |

mbsl = meter below sea level
MC = multicore
JPC = jumbo piston core

Table-2.1. Multicores and jumbo piston cores used for this study, cores are acquired during the PANASH cruise of the R/V Melville cruise in 2004.

Radiocarbon analyses are based primarily on selected species of picked planktonic foraminifera shells (*Globigerinoides ruber and Globigerinoides sacculifer*), or alternatively bulk sediment samples if foraminifera were too rare**.** Eight plug samples from hemipelagic mud layers above turbidite layers from core MV22, MV23, MV33 and MV25 were extracted in sedimentology and marine geology laboratory, Memorial University of Newfoundland, and foraminifera were hand-picked to yield 30-60 mg samples for analysis, avoiding broken or incomplete shells. Bulk samples (3.5 g) were collected from MV29 (Moresby Channel) which contained too few tests for analysis. Samples were prepared for analysis at the Centre d'Études Nordique (CEN), Université Laval, Quebec, Canada, and analysis performed at the Keck Carbon Cycle AMS Facility, University of California, Irvine, CA, USA. The reported ages were corrected to calendar years using Oxcal v.4.1 with a specific reference to the Marine09 calibration curve for marine samples and Intcal09 calibration curve for wood samples (Reimer et.al., 2013; Bronk Ramsey and Lee, 2013). A ΔR value was calculated from the average of the values at three nearby reference sites, in order to adjust the default Marine09 reservoir ages to appropriate local values. These three reference sites are in the Torres Strait (sites 1455, 1456 and 1457) and the ΔR value used is 50 yr. The reference ages from previous studies (Febo et al., 2008, Jorry et al., 2008, Patterson, 2006) were also incorporated in age models for this project, used 'as is' when a corrected calendar age was reported, or calibrated as explained above if the original C-14 age was reported (Table 2).

The total lightness data (L*) derived from Geotek Geoscan core images (calculated using the US-NIH Image-J algorithm; NIH, 2012) were used as a proxy for carbonate content, as applied successfully in other nearby cores from the same cruise (Jorry et al., 2008). L* has been

| No. | Core | Depth* (cm) | Lab | Material | C-14 Age (Year Bp) | Error (Year) | Calendar Age | | References |
|---|---|---|---|---|---|---|---|---|---|
| | | | | | | | Mean | sd | |
| 1 | MV-22 | 160 | 1 | Foraminifera | 6,895 | 20 | **7,360** | 75 | this study |
| 2 | MV-22 | 1180 | 1 | Foraminifera | 35,840 | 240 | **40,580** | 420 | this study |
| 3 | MV-23** | 232 | 2 | Wood | | | **19,455** | | Patterson, 2006 |
| 4 | MV-23 | 239 | 1 | Foraminifera | 15,570 | 45 | **18,495** | 180 | this study |
| 5 | MV-23 | 465 | 1 | Foraminifera | 26,010 | 100 | **30,405** | 190 | this study |
| 6 | MV-23 | 1000 | 1 | Foraminifera | 39,310 | 450 | **43,180** | 405 | this study |
| 7 | MV-25 | 206 | 1 | Foraminifera | 10,200 | 25 | **11,140** | 105 | this study |
| 8 | MV-25 | 1134 | 1 | Foraminifera | 43,700 | 1300 | **46,955** | 1275 | this study |
| 9 | MV-29*** | 589 | 1 | Foraminifera | >51,200 | | **>50,000** | | this study |
| 10 | MV-33**** | 154 | 3 | Foraminifera | 10,625 | | **11,805** | 190 | Jory et al., 2008 |
| 11 | MV-33**** | 333 | 3 | Foraminifera | 11,325 | | **12,765** | 100 | Jory et al., 2008 |
| 12 | MV-33 | 1215 | 1 | Bulk Sediment | 19,560 | 70 | **22,815** | 255 | this study |
| 13 | MV-54***** | 190 | 3 | Wood | 13,320 | 25 | **16,385** | 260 | Febo et al., 2008 (raw) |
| 14 | MV-54***** | 475 | 3 | Wood | 14,160 | 35 | **17,230** | 155 | Febo et al., 2008 (raw) |
| 15 | MV-54***** | 830 | 3 | Wood | 14,175 | 40 | **17,250** | 160 | Febo et al., 2008 (raw) |
| 16 | MV-54***** | 994 | 2 | Wood | 14,810 | 80 | **18,100** | 235 | Febo et al., 2008 (raw) |

The delta R local from Torres Strait (site 1455, 1456, 1457)
The calendar age calculation is using Marine09 curve for marine samples and Intcal09 curve for wood samples
Laboratory code: (1) University California Irvine via CEN Universite Laval, (2) National Ocean Sciences AMS (NOSAMS), (3) University of California at Irvine
* Below sea floor
** Only calendar age was reported
***Age is exceeded the limit of C-14 dating
****Errors are not reported by author
*****Raw data from Febo et al., 2008, the raw data is corrected using intcal09 curve in this study

Table-2.2. Radiocarbon calendar ages from core samples, including data generated for this study, and for studies cited in the table.

correlated with peak calcium from XRF scans to compensate for the influence on L* of other light minerals; such as, kaolinite, fluorite, or light-colored silicates (e.g., Jorry et al., 2008).

Relative elemental abundances were determined using an Avaatech X-ray fluorescence core scanner for core MV-22, 23, 25 and 27 at the University of Miami Rosentiel School of Marine and Atmospheric Science (RSMAS). Cores were scanned at 1 cm intervals, with elemental data from Al to Bi recorded as counts per measurement (McFadden personal communication, 2010). At that time, graphic logs of JPC stratigraphy were also prepared from visual observations.

Piston cores and multicores were imaged X-radiographically using a portable Thales Flashscan 35 flat panel imaging detector illuminated with a Medison-Acoma x-ray generator PX15-HF. Multicores were imaged while on ship (by NSF Margin team during R/V Melville cruise, 2004). Split half-round piston cores were imaged at RSMAS in 2010. For half cores, an aluminum compensator plate was used to provide uniform exposure of the semi-cylindrical core (Principato, 2004; Freifeld et al., 2006) (by Erlangga Septama during visit to RSMAS, 2010).

Samples from select multicores and piston cores were processed to create petrographic thin sections, modified after the method of Kuehl el al. (1988). The 3x5 cm sub-samples were extracted with metal spatulas from selected multi-core slabs and u-channel samples of piston cores, following study of core X-radiographs. Samples were flash-frozen in liquid nitrogen, freeze-dried and impregnated with low viscosity LR-white resin under partial vacuum condition (600-750 torr). The impregnated sediment sample was thin sectioned using standard lapidary equipment to approximately 70 micron thickness for study.

In addition to the above analyses, oxygen isotope analysis from MV-27 (McFadden 2010, personal communication) is also incorporated as a reference. The age model for this core is based on correlation to the chronostratigraphy of standard global oxygen isotopic curves, interpolated to give tie points at multiples of 10 cal ka in the hemipelagic component of the MV-27 succession (Figure. 2.3.).

## 2.4. Results

Core locations, lengths, water depths, and present-day environments are indicated in Table 2.1.

### Jumbo Piston Core Sediments

Core sediments are generally composed of mud, silt, and medium to fine sand. Major composition is quartzo-feldspathic, with lesser amounts of amphibole, muscovite, and lithic fragments. Smaller quantities of woody fragments, calcareous mud, and mollusk fragments are also present.

Core MV-54 (11.745 m long) was acquired from the middle NW slope of Pandora Trough (924 m below sea level) (Figure. 2.2.). The sediment is composed primarily of dark gray faintly laminated mud to apparently homogeneous greenish muddy sediment with few thin beds of fine grained sand, with more discrete thin layers (< 5 cm, composed of quartz and volcanic lithic fragments) of sandy sediment in the upper 4 m of core. Gamma density of muds in the upper 3 m of the core is 1.38-1.46 g/cm$^3$, and 1.58-1.6 g/ cm$^3$ for muddy sediment deeper in the core. Sand layer density is 1.75-1.89 g/ cm$^3$ with a skewed bell-shaped curve character (sharp based sand layer with a rapid rise in density at the base and gradual drop off at the top). The general gamma-

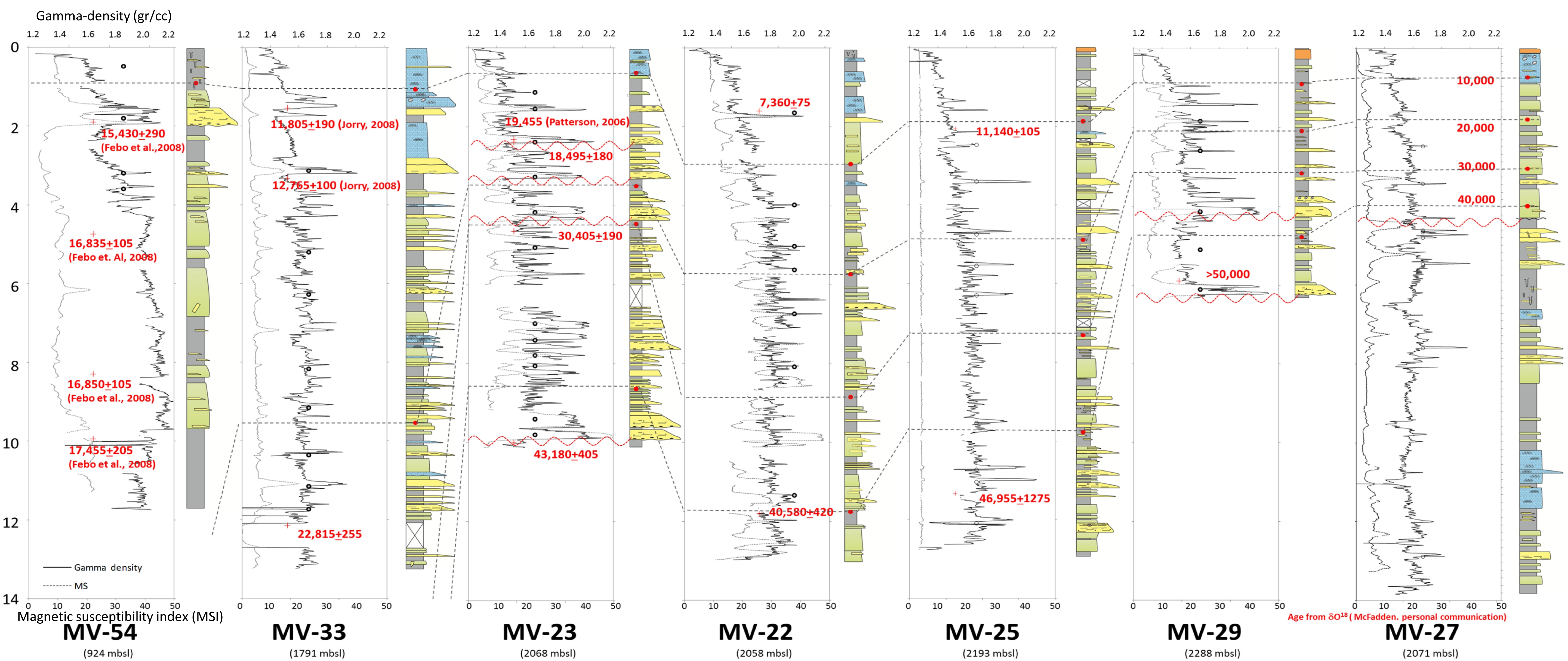

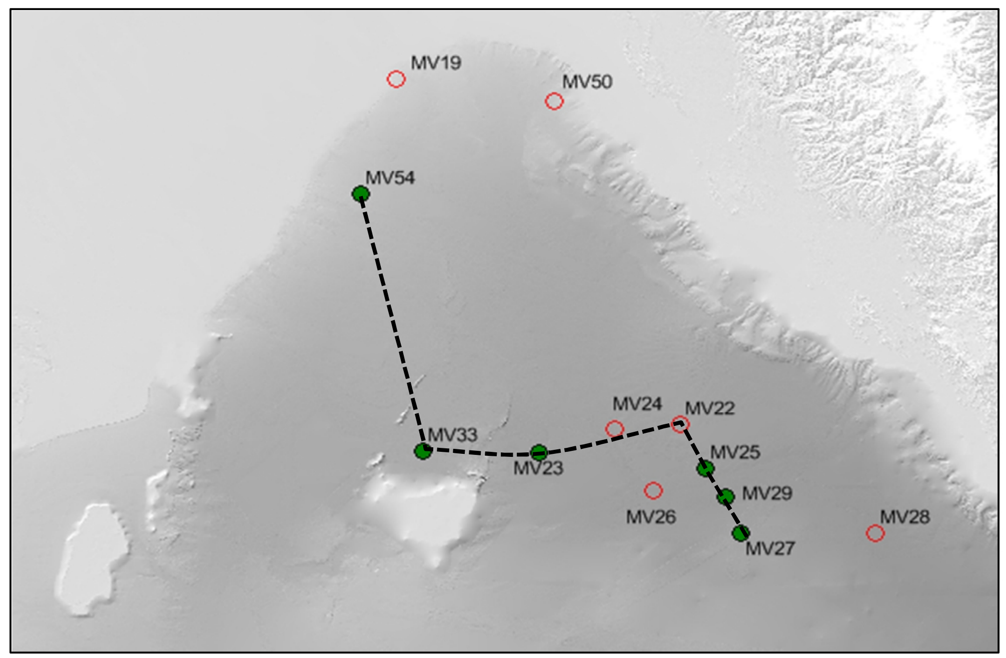


Figure 2.3. Chronostratigraphic correlation across the Gulf of Papua, from slope through mini-basin, toe of slope and Moresby channel. The time-lines are interpolated every 10 cal Ka based on sediment accumulation rates in the hemipelagic component of the sedimentary succession. Erosional bases to sand beds were interpreted based on log and core observations (vertical scale for core depth from seafloor in meter, horizontal scale :Magnetic susceptibility (MS) in $*10^{-5}$SI below and Gamma Density in $gr.cm^{-3}$ above).

density log character is serrated in the upper part, and gradually changes into blocky character downward (Figure 2.3.).

In core MV-33 (total length 12.7 m) from a mini-basin in the northern toe of slope of Eastern Fields Reef, 1787 m below sea level (Figure 2.2), the uppermost 1.5 m of the core is composed of calcareous pelagic mud interlayered with trains of coarse-sand-size bioclasts that display reworked textures. The lower portion of the core contains 35 siliciclastic sand layers 15-50 cm thick interlayered with mud. These sand layers are fine- to medium-grained, dominated by quartz and dark volcanic lithic fragments, and less abundant woody debris. These siliciclastic sands are interbedded with calcareous pelagic sandy mud, in which the disseminated coarse grains are mostly skeletal fragments and large foraminifera. The gamma density log shows a highly serrated character with mud density of 1.4-1.45 g/cc in the interval 0-2.5 m, gradually increasing to 1.5 g/cc deeper in core. Sand density is 1.75-1.98 g/cc (mostly 1.75 in calcareous layers) in the upper 2.5 m of core, and around 1.78 g/cc below 2.5 m.

Core MV-23 (10.12 m long), from the toe of slope in Pandora Trough (2068 m below sea level) (Figure 2.2.), contains 23 sand beds interbedded with mud. The gamma density log has a serrated curve with sharp basal contacts (evident in both the log curve and thin sections). Density logs of the sandy layers mostly reflect fining upward with a few blocky patterns in the bottom part of the core (10 m). The log shows a mud density of 1.38-1.4 $g/cm^3$ and sand density of 1.86-1.98 $g/cm^3$, both tending to increase downward. This core is incomplete because of sand loss from the bottom part of the core. This core also contains a gap or missing samples in the interval from 6.9-6.5 m.

Core MV-22 (12.97 m length, 2058 m below sea level) acquired from the lower eastern slope of Moresby Trough; (Figure 2.2.) is mostly mud with sand layers 2.5-10 cm thick (Figure

2.3.). Some sand layers are lenticular, and major minerals in all layers include amphibole, biotite and muscovite. Mud density increases gradually downward in this core, from soft mud in the upper 25 cm of the core with density near 1.26 g/cc, to 1.38-1.42 g/cc in the interval 25-281 cm (near 10 cal  ka; Figure 2.3.), to near 1.57 g/cc below 281 cm. Sand layer density is 1.7-1.78 g/cc.

Core MV-25 (12.77 m long), and core MV-29 (6.42 m long) were collected on the eastern edge of the Moresby Trough thalweg (2193 m and 2288 m below sea level respectively) (Figure. 3). Core MV-25 contains 12 units of thinly interbedded mud, silt, and fine sand, interlayered with thicker muddy beds. The gamma density curve is highly serrated with individual layers being bell shaped, with mud density of 1.38 g/cm$^3$ (0-246 cm), 1.43 g/cm$^3$ (246-469 cm), and 1.57-1.59 g/cm$^3$ (bellow 469 cm). Sand layer density is 1.78-1.9 g/cm$^3$.

Core MV-29 down-channel from MV-25 contains interlayered sand and mud in layers that thicken downward. The core is relatively short, and only recovered 5.99 m probably due to sand loss in the bottom part. Mud density varies from 1.38 g/cm$^3$ above 85 cm depth; to near 1.42 g/cm$^3$ below 85 cm). Basal contacts of sandy layers over mud are sharp on the gamma density curve.

Core MV-27 (13.845 m long, 2071 m below sea level) is the core that is farthest down Moresby Channel, near the thalweg (Figure 2.2). This core contains ten layers of mostly fine sand (5-10 cm thick), interlayered with mud. The sand is fine grained and mainly composed of dark lithic fragments and quartz, and displays a fining upward succession in the upper 4 m.

Multicore Sediments

Multicores MV-19, -24, -26, -28 and -50 were evaluated for this study (Figure 2.2), and are <50 cm in length. Core MC MV-24 (2102 mbsl) shows a vertical succession of sand with divisions consistent with typical $T_c$-$T_e$ units in the Bouma sequence (Bouma, 1962) that are partially cross cut by large (2-3 cm diameter) horizontal burrows.

MV-26 (water depth 2232m) consists of a hemipelagic mud layer with mottled appearance, overlying a layer of coarse and poorly sorted lithic wacke incompletely sampled near 45 cm depth (70% mixed metamorphic, mafic-igneous, and sedimentary fragments, with grain size of 0.3-2.5 mm, in carbonate-mud/foraminifera mud matrix).

MV-28 was retrieved from 2426 mbsl, and appears to have almost fully penetrated the surficial hemipelagic mud drape. It reveals a sediment accumulation rate (SAR) of 0.1 cm/yr and mass accumulation rate (MAR) of 0.05 g/($cm^2$yr) (Muhammad et al., 2008). The mud drape overlies basal muddy layers with several interbeds of thinly cross-stratified fine sand (1-2 cm).

Multi core MV-19, acquired from the shelf break in the corner between Pandora and Moresby Troughs at a water depth of 229 mbsl (Figure 2.2.), consists of mottled silty mud layers interbedded with homogeneous fine- to medium-grained sand. Multi core MV-50 from the upper slope (795 mbsl) shows finer grained materials (silt to mud) with no distinct layering. Both MV-19 and MV-50 show abundant vertical and horizontal burrows with dimensions of 1.5 - 4 cm in length and 0.25 - 0.3 cm in diameter.

Radiocarbon Geochronology and Sedimentation Rates

Calendar ages of $^{14}C$ analyses from this study and other samples dated from these cores (Patterson, 2006; Febo et al., 2008; Jorry et al., 2008) range from 7.36 cal ka to older than 40 cal ka, encompassing Marine Isotope stage (MIS) 3 to 1 (Figures 2.3 and 2.4, Table 2.2). The open slope cores MV-54 and MV-33 from a mini-basin adjacent to the Pandora trough show the highest $^{14}C$ sediment accumulation rates (SAR) among all piston cores in this study. Most of MV-54 (1.90-9.94 m below sea floor [mbsf]) was deposited between 16.38 and 18 cal ka, with SAR of 203-271 cm/ka for upper and lower intervals, and a middle interval of much higher SAR (Table 2.2., Figure 2.3b). For MV-33, the sediment from 1.54-1.215 mbsf was deposited from 11.8 to 12.76 ka, with SAR of 87.8 cm/ka (bottom) to 186 cm/ka (top).

Core MV-23, from the western slope of Moresby Trough, has four $^{14}C$ dates: 19.455 cal ka at 2.32 mbsf (wood), 18.495 cal ka at 2.39 mbsf (forams), 30.405 cal ka at 4.65 mbsf (forams) and 43.180 cal ka at 10 mbsf (forams). Focusing on ages from forams (ignoring the age reversal created by the woody debris), these ages yield a SAR of 19-42 cm/ka, with highest rates during MIS-3.

Core MV-22 from the lower reaches of Moresby Trough has two dated intervals: 7.360 cal ka (MIS-1) at 1.60 mbsf, and 40.580 cal ka (MIS-3) at 11.80 mbsf, yielding SAR of 30.7 cm/ka, including the youngest age for this data set (middle MIS-1).

SAR for cores in deeper southeastern Moresby Trough and deeper Moresby Channel are generally lower. Cores MV-25 and MV-29 were acquired from the side levee of Moresby Channel (Figure 2.2). MV-25, at water depth of 2193 m, displays SAR of 25.9 cm/ka from 10.2 to 47 cal ka, spanning from MIS-3 to early MIS-1. SAR for core MV-29 over $^{14}C$ timescales is not known, due to the $^{14}C$ age of >51.2 cal ka at 5.89 mbsf. Analysis of $\delta^{18}O$ stratigaphy (McFadden, 2010, personal communication) from core MV-27 in Eastern Field Plateau showsthat this particular area is probably experiencing the slowest SAR of all cores in this study, 0.8 cm/ka from MIS-6 to MIS-1 (Figures 2.3 and 2.4).

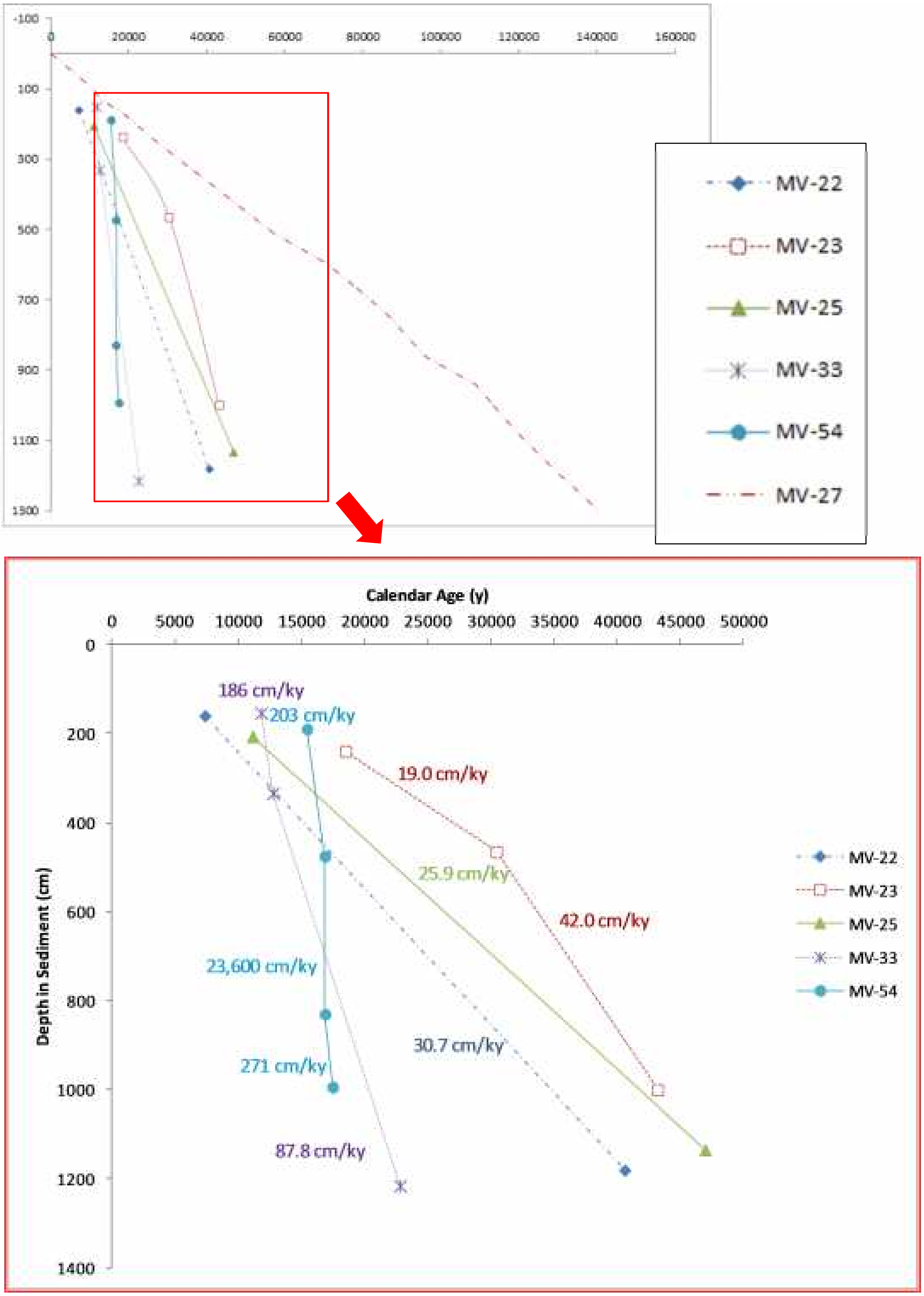


Figure 2.4. Age-depth plots. Accumulation rates are calculated directly from calibrated C-14 age to C-14 age. Core MV-27 curve is derived from d18O data (McFadden, personal communication, 2010) Each core top is assumed to have an age of 0 cal yr BP, but could be older if the sediment-water interface was not recovered in piston cores.

Results of thin section and X-radiograph analysis are incorporated into general core lithology described above, and facies descriptions presented below. Specific examples discussed below are provided in Figures 2.5. and 2.9. In jumbo piston cores, thin-section study displays different textures which help distinguish pelagic mud from hemipelagic mud from what are interpreted as muddy turbidites. Non-laminated pelagic/hemipelagic mud appears to have higher porosity than normally graded mud in turbidites. The higher porosity results in more extensive ice-freezing artifacts (Figure 2.5a). Also, pelagic mud is non-laminated and highly burrowed whereas the turbidite mud shows distinct gradation (Figure 2.5b). Abundant fecal pellets occur in the pelagic/hemipelagic mud in contrast with turbidite mud. Pellets are generally elliptical with long axes of 100-200 μm, and with apparent random distribution (Figure.2.5c). Graded mud is intensively burrowed only in the upper part of each occurrence, giving a mottled texture in x-radiographs. Bioturbation is sometimes intensified in sand layers or underlying mud. Most burrows evident in pelagic/hemipelagic mud are similar to the ichnogenus *Phycosiphon sp*., and seem to be associated with the fecal pellets (Figure 2.5d.), but are rarely found associated with turbidite mud.

Multicore MV-24 (2102 mbsl) shows a vertical succession of muddy turbidites with typical $T_c$-$T_e$ divisions that are partially cross cut by large horizontal burrows similar to echinoderm burrows (e.g. Bromley, 1996) (Figure 2.6.). Modern $^{210}$Pb activities and sedimentation rates in this core (0.14 cm/yr.; Muhammad et al., 2008) suggest a moderate to low depositional rate.

MV-26 (water depth 2232m) displays preferential grain orientation of large fragments (Figure 2.7.), consistent with reworking beneath a transiting sediment gravity flow.

MV-28 (45 cm in length, not shown) retrieved from 2426 mbsl, shows mud-dominated sequences with thin cross stratification, in fine sand layers, that is interpreted as the $T_c$ division of the Bouma (1962) sequence. The Recent $^{210}Pb$ SAR of 0.1 cm/yr. and MAR of 0.05 g/cm$^2$.yr (Muhammad et al., 2008) suggest very slow modern sedimentation at this locale.

**2.5. Lithofacies**

Six lithofacies are distinguished on the basis of the observed depositional elements, sedimentary structures, micro-fabrics, texture and the presence of bioturbation either from direct core observation or core x-radiographs. The major depositional elements found in cores include: (1) well laminated sedimentary units of alternating thin sand (dark grey), silt and mud (light grey), (2) thick graded sand (3) thin sand laminae infill in thick mud sometimes as lenses, pockets or showing pinch out termination in one direction, (4) non-laminated/homogeneous calcareous pelagic mud (light grey) and light colored medium to thick calcarenite with abundant bioclasts (5) hemipelagic mud and (6) blocky and deformed slumped sediment. The detailed descriptions of the lithofacies are as follows (Fig. 2.8., Table 3).

Lithofacies-1, this facies is characterized by varve-like interlaminated mud, silt and thin fine-grained sand, with layers well defined in cores and x-radiographs. This lithofacies shows a distinct fining-upward pattern with density curves having a typical thin bell shaped character in sandy units, with overall serrated/ saw tooth curve characters [e.g. interval 2-3 mbsf in MV-22 and all light green colored in Fig. 2.3]. The typical sequence begins with dark gray-greenish thin mud (2-3 cm), underlain by silt and then dark-blackish sand (1-2 cm) with the frequency and the thickness of the sand laminae decreasing upward towards the seabed. This succession is usually overlain by a hemipelagic mud drape shows a transition upward from the heterogeneous lithofacies 1 into faintly laminated mud into more uniform mud.

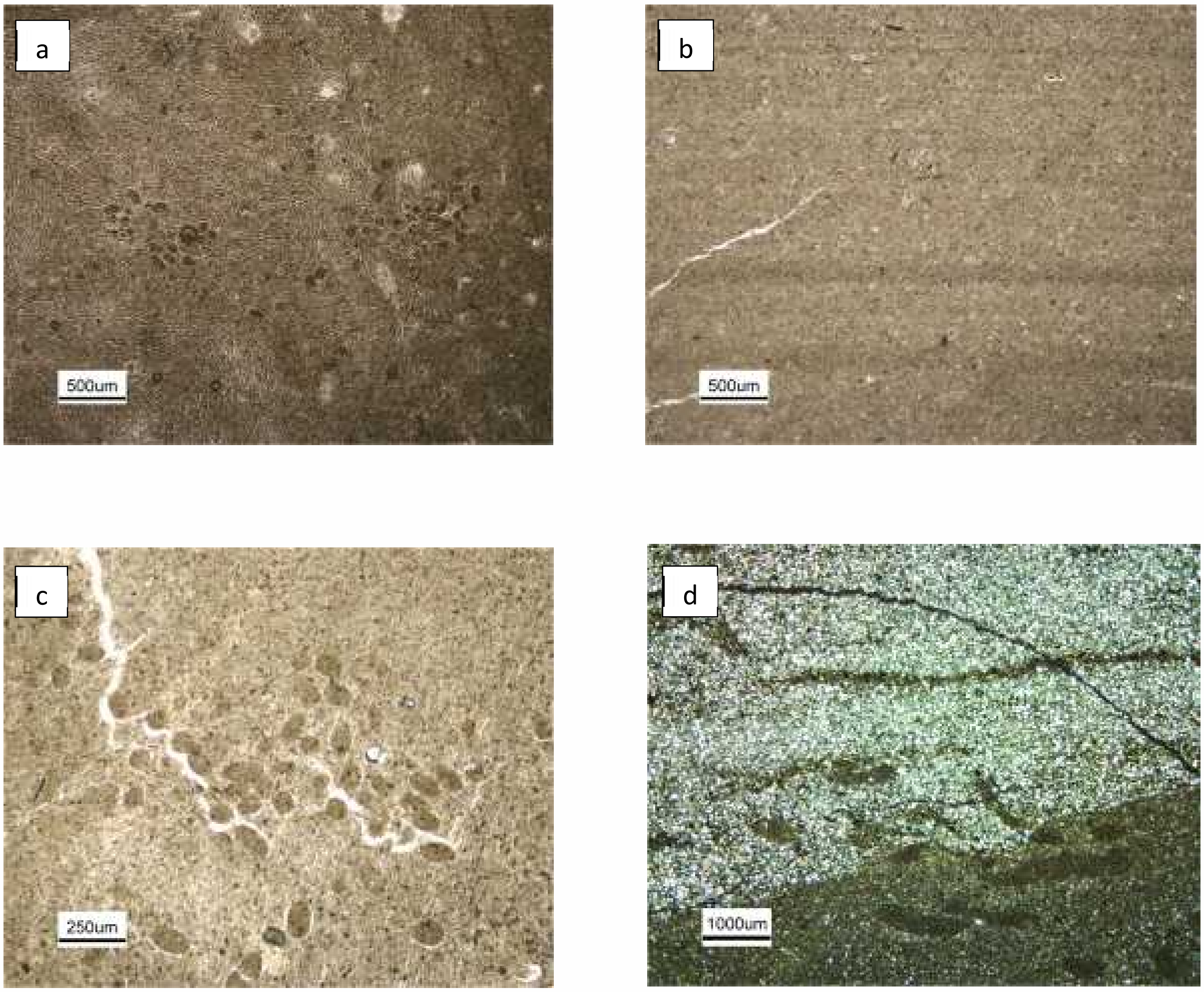


Figure 2.5. (**a**) the granular texture of background sediments in this image is actually an artifact from freezing formed during the bulk sediment sample immersion into liquid nitrogen. This artifact can be used to differentiate between homegeneous pelagic/hemipelagic mud (lithofacies 5) and turbidite mud (lithofacies 1). (**b**) Distinctive size gradation is observed in the turbidite mud (Bouma division Td) (lithofacies 1). (**c**) Fecal pellets are common in hemipelagic mud (lithofacies 5) but rarely found in normally graded beds. (**d**) Sharp contact between graded beds and underlying silt and mud (lithofacies 2). The contact zone shows a prominent burrow interpreted as a *Phycosyphon* trace.

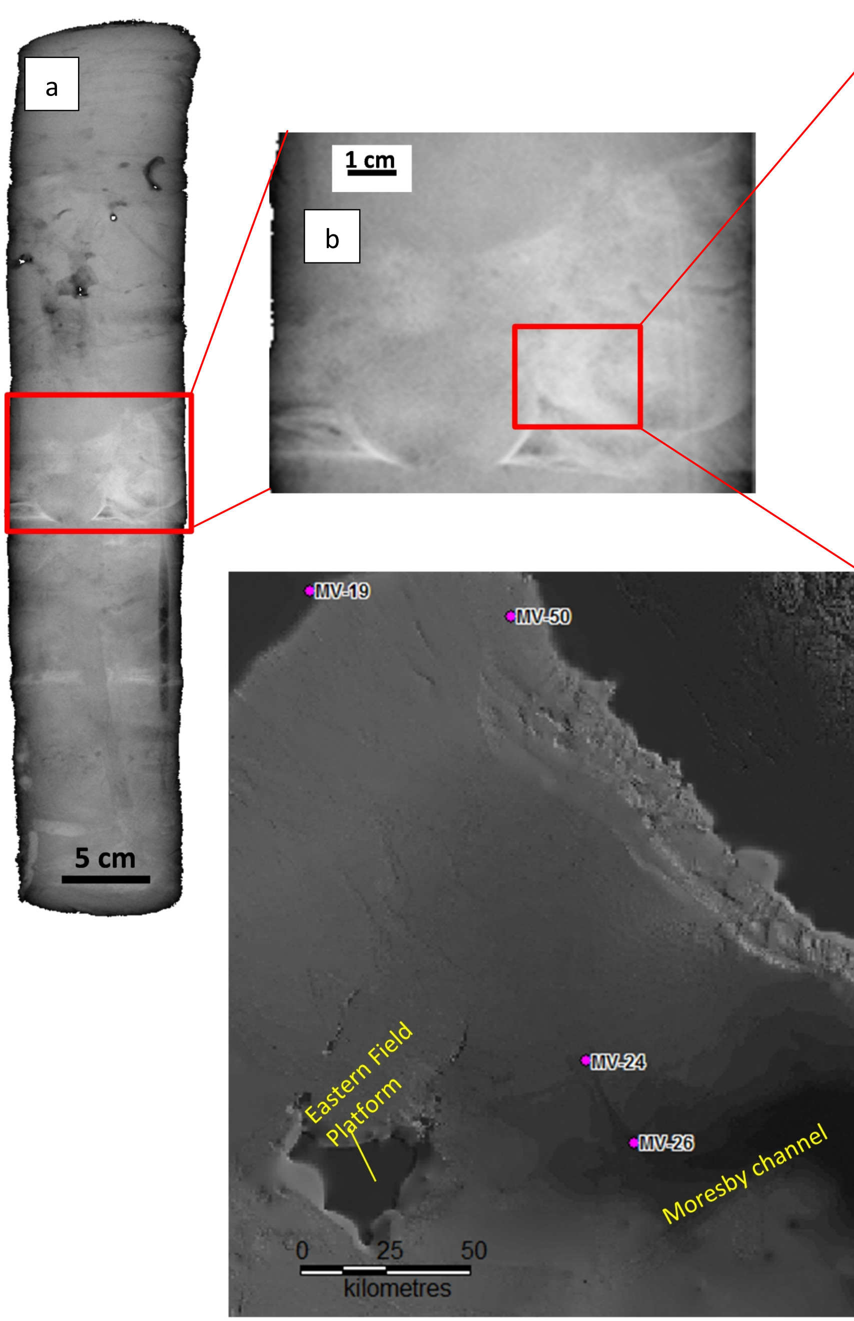

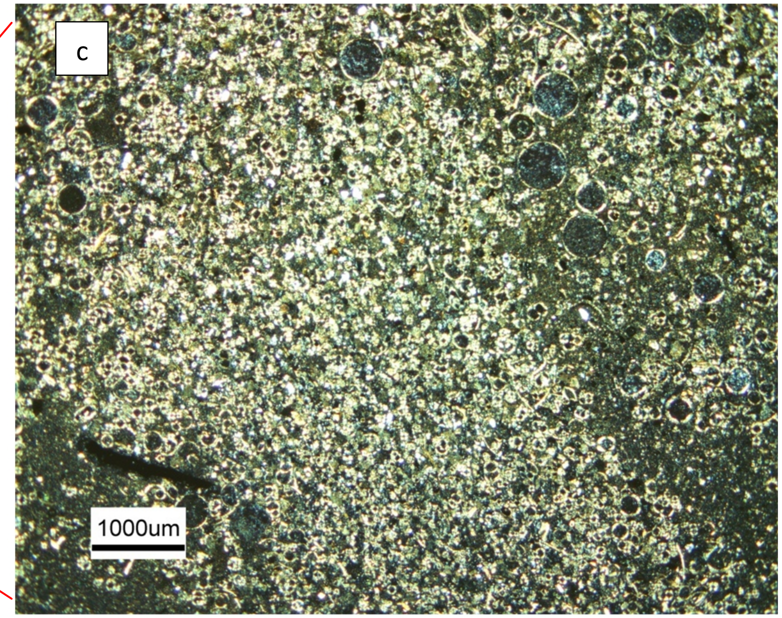


Figure 2.6. Multicore MV-24 was acquired from water depth 2102 mbsl. **(a)** the core x-radiograph shows complex burrows initiated where terrigenous materials (sand layers of Lithofacies 2 or 3) provide a fresh food supply for deep sea organisms. The vertical burrow is *Skolithos* and the concentric shape (enlargement of x-radiograph) in **(b)** and cross polarized light (xpl) of thin section in **(c)** is likely a surface trail created by echinoderm species. The stratigraphic arrangement of the burrows reflects adaptation of organisms to the periodic turbidite depositional cycle. The red rectangle is showing the location of the enlargement and thin section.

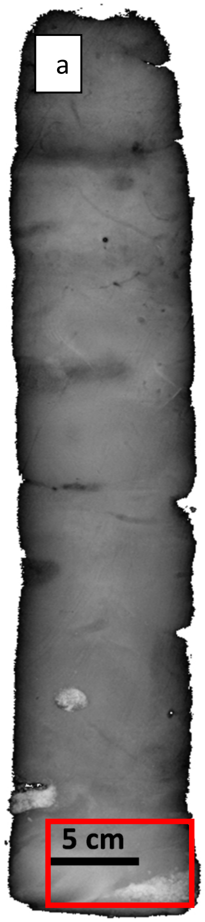


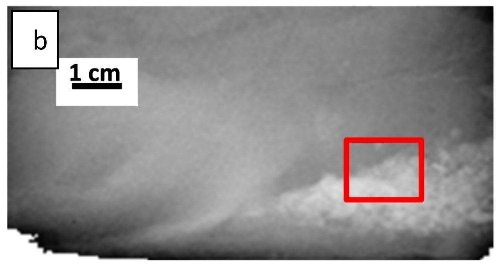


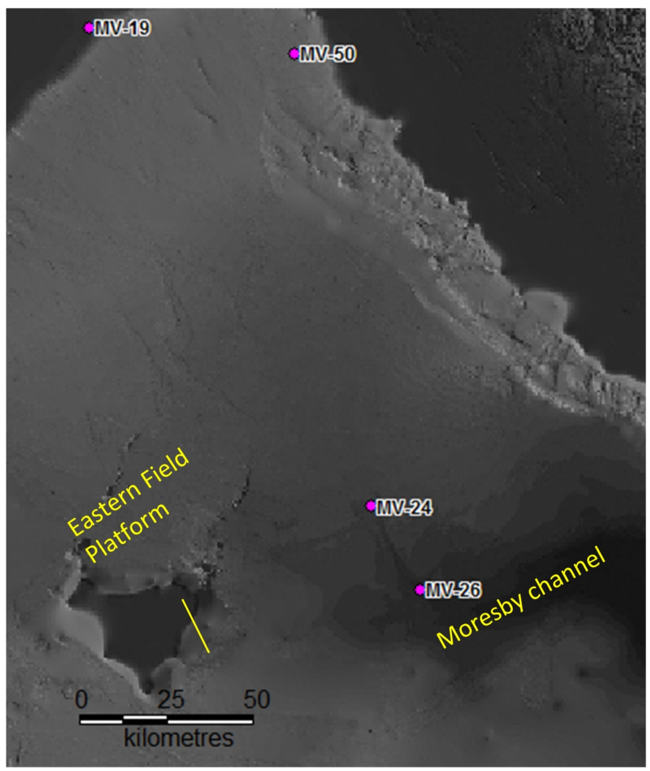


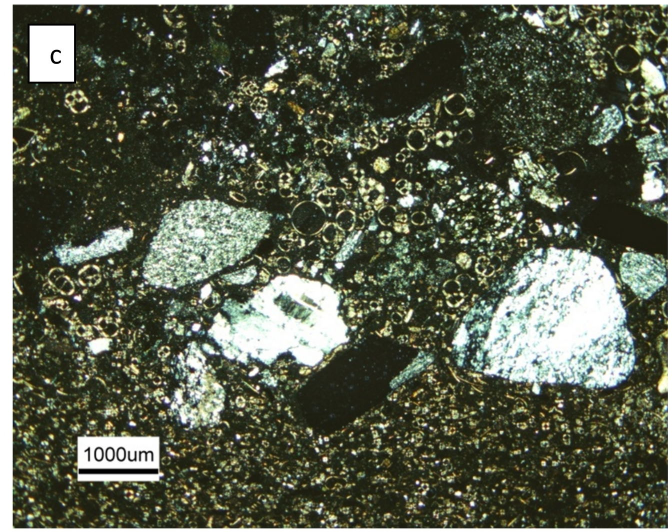


Figure 2.7. **(a)** multicore MV-26 acquired from water depth 2232 mbsl. The base of the core x-radiograph (lithofacies 2) shows lag deposit which is probably formed beneath a turbidity current. The grains show a preferential orientation that is likely the paleoflow direction (red square is showing te location of the enlargement) **(b)** is the enlargement of the x-radiograph and **(c)** is the cross polarization light (xpl) of the thin section. (The red rectangle is showing the position of the enlargement and thin section).

Lithofacies-2, sheet-like sandy layer: dark grey to blackish colored layers of varied thickness (3->50 cm)(Figs. 2.8 and 2.9). This lithofacies displays upward fining of each depositional unit, typically with saw-tooth or bell shaped gamma-density curve character (Fig. 2.9), and sharp lower contacts that appear erosional in thin section (Fig. 2.5d). There are lag deposits of coarse grained sand sometimes found near the contact between a sand bed and the underlying mud (e.g., MV-23, Fig. 2.8). From the visual appearance, three sub-facies are distinguished. Sub-facies-2a consists of normally graded muddy beds, consistent with the Bouma sequence $T_{d-e}$ (Fig. 2.7). Thin silty mud lenses are sometimes present and are embedded in the mud layer of this sub-facies (Figs 2.6 and 2.7). Sub-facies-2b consists of thinly bedded normally graded layers dominated by fine to medium sand, sometimes displaying Bouma sequence $T_{b-c-d}$ but mostly only $T_b$ or $T_{b-c}$ divisions (Fig. 2.5b, thin section; Fig. 2.8 [MV-23], and Fig. 2.9). This sub-facies shows distinct layering, rich in biogenic materials including foraminifera and wood fragments that may be aligned. Sub-facies-2c consists of medium to thick (15-50 cm) beds of medium- to fine-grained sand, characterized by Bouma sequence $T_{a-b}$ (MV-23, Fig. 2.9). The bottom part is typically normally graded, sometimes massive, with an upward transition into laminated sand and silt. Beds of sub-facies-2c show sharp erosional contacts with occasional basal lag deposits.

Lithofacies-3, thin sand layer/lenses/pinch-out-infill in thick hemipelagic mud. The sand is fine grained, dark grey to blackish colored, showing distinct lamination of typical Bouma division $T_b$. The gamma density curve shows a stack of thin bell-shaped curves, one for each depositional unit (e.g. successions of thin sand layers in all cores; Fig. 2.3). Depending upon the resolution, very thin bell-shaped segments may appear as needle-like spikes intercalated inside lithofacies 2 or 5. Direct core observation and x-radiographs show that the sand layers either have bidirectional terminations (giving lenses), or may pinch out or inter finger with surrounding mud (MV-22, Fig. 2.8).

Lithofacies-4, calcareous mud and sand: comprised of light grey to cream colored mud, primarily biogenic, highly calcareous and dominated by fecal pellets, traces of shell, and foraminiferal tests. The sediment is highly burrowed, with the primary vertical burrow being *Skolithos* whereas shorter patchy burrows are interpreted as *Phycosiphon* (MV-33, Fig. 2.8). The log character from gamma-density curves is slightly serrated with an overall low density (e.g. intervals : 0-1.7 mbsf Of MV-33, and mostly upper part of MV-23, MV-25 and MV-27 (Fig. 2.3)). This facies is mostly present in the upper part of cores where observed and is distributed widely but most prominently in proximity to the drowned Miocene carbonates (Jorry et al., 2008) such as in cores MV-33 and MV-23 (Figs. 2.2 and 2.3). In core MV-33, lithofacies-4 occurs as a series of layers which are intercalated with hemipelagic mud and calcareous sand. This lithofacies is distinguished easily from its color during visual direct core observation and also from XRF calcium data and L* measurements (MV-33, Fig. 2.10).

Lithofacies-5, hemipelagic mud: comprised of subtly laminated dark gray mud with moderate to intense bioturbation. The gamma-density log is characterized by a lightly serrated curve of generally low density (e.g. most of the dark green colored units in Fig. 2.3). This lithofacies is widely distributed across the study area (Fig 2.8).

Lithofacies-6**,** slump or debrite deposits, showing either distinct deformed stratification, folded strata with an irregular surface boundary, or being massive without any distinct layering. In some cases this lithofacies is composed of soft mud that might have been deformed during piston core recovery. The gamma-density curve shows a tabular and blocky log character or coarsening upward pattern. This lithofacies only found exclusively in MV-27 (interval 8.5 mbsf).

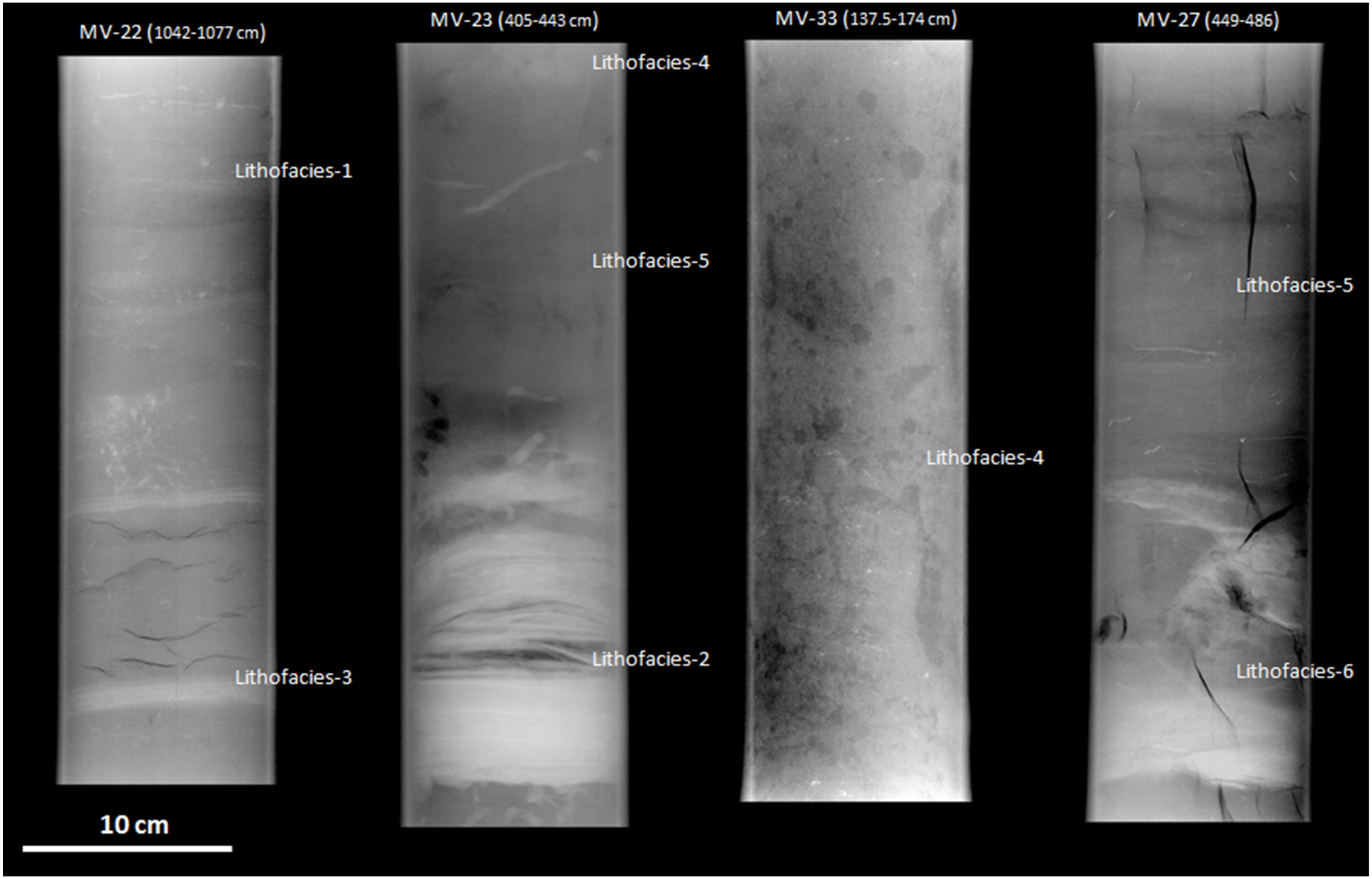


Figure 2.8. X-radiographs of various lithofacies observed in the jumbo piston cores (see text for the details).

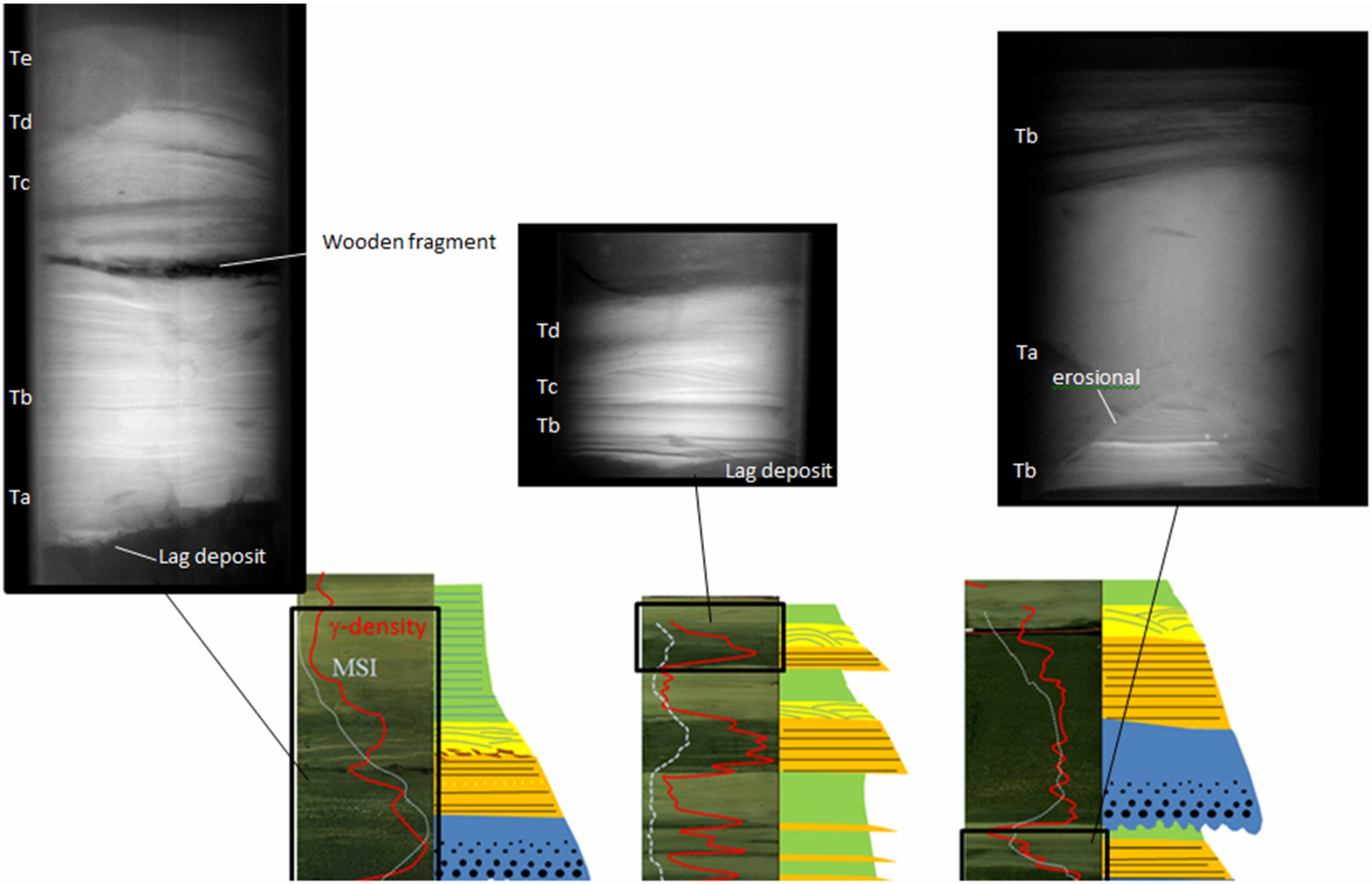


Figure 2.9. The turbidite facies observed in Pandora Trough toe-of-slope (MV23) (lithofacies 2) showing the variation from complete Bouma sequence to beds without lower Bouma divisions or without upper Bouma divisions. The black square on the core shows the position of the core x-radiograph. Schematic profiles of density (red) and magnetic suscptibility (gray) are superimposed on core images, next to graphic logs.

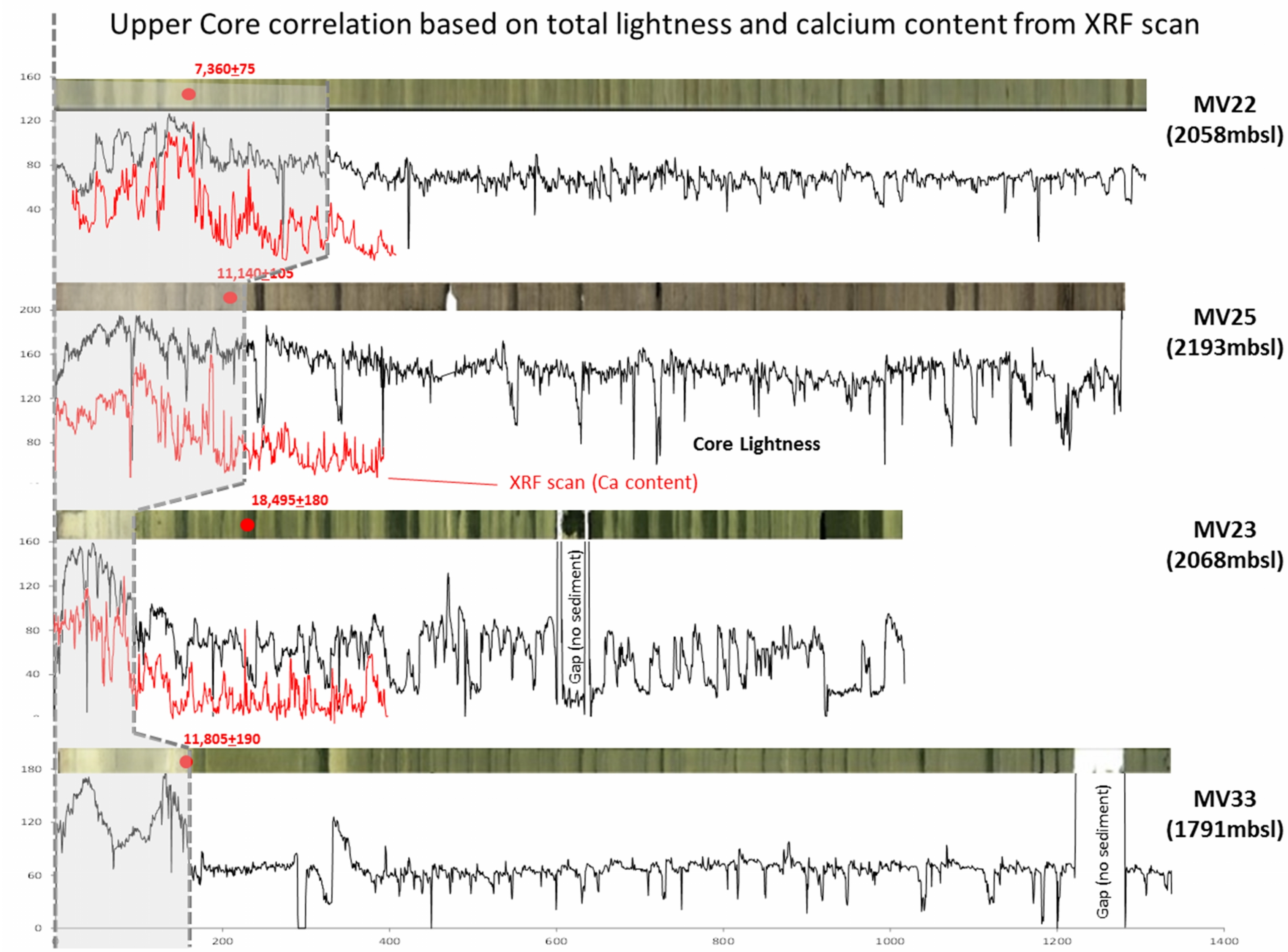


Figure 2.10. Correlation based on total lightness (L*, black profile) and calcium content from XRF scans (red profile) help define the upper part of the core (pre-MWP-1B).

## 2.6 Interpretation and Discussion

### 2.6.1 Piston Core SARs and Lateral Correlation

Bathymetric data and core observations encompass five major depositional environments in two major depositional troughs (Pandora and Moresby Troughs) namely slope (MV-54), toe of slope lobe (MV-22, MV-23), mini-basin (MV-33), channel-levee system (MV-25, MV-29 and MV-23) and stable deep sea plateau (MV-27) (Figures 2.1. and 2.2). Figures 2.11a and 2.11b illustrate spatial and temporal variations in SAR. Figure 2.11b was prepared by temporally interpolating $^{14}C$ SAR in 10 ka increments indicated on Figure 2.3, incorporating $\delta^{18}O$ stratigraphy of McFadden [2010, personal communication]), including MIS boundary ages [ICS, 2010], and assuming that the top of each core represents an age of 0 cal ka. This assumption is probably incorrect, owing to likely loss of surficial sediment during core penetration; if this is the case, this uppermost SAR estimate is a minimum value. With these caveats, the correlation across the five major environments shows temporal and spatial patterns in the SARs across the GoP over the last glacial cycle (Figures. 2.3., 2.11a and 2.11b).

There also exist differences between SARs from $^{14}C$ ages (e.g. Figure 2.4) and MIS correlations (Figure 2.11). For MV-54, the highest $^{14}C$ SAR value is 23,600 cm/Kyr as compared to >57 cm/Kyr in MIS calculation. The rapid $^{14}C$ SAR may be due to slump deposition. As well, averaging over long timescales will generally result in lower SAR than when averaged over shorter timescales (Sadler, 1981). As well, the correlation for MV-54 is tenuous, owing to the age of the core bottom likely being younger than the MIS 2-1 boundary.

Slope core MV-54 and Pandora trough mini-basin core MV-33 are the closest to the Papuan mainland river systems, and show the highest SARs in this study, and both span the general time frame of mid MIS-2 (14-29 cal ka) to early MIS-1 (0-14 cal ka). Core MV-54 is primarily homogeneous marine mud (lithofacies-5 and -6) whereas core MV-33 contains numerous sand layers, including calcareous units (lithofacies-2, -3, and -4). The lack of sand in core MV-54 suggests that this core is located away from the major slope channel whereas core MV-33 more likely is fed by an active channel. This suggests that the mature river systems of the Papuan mainland most likely acted as the major deep-sea feeder during MIS-2, and sediment

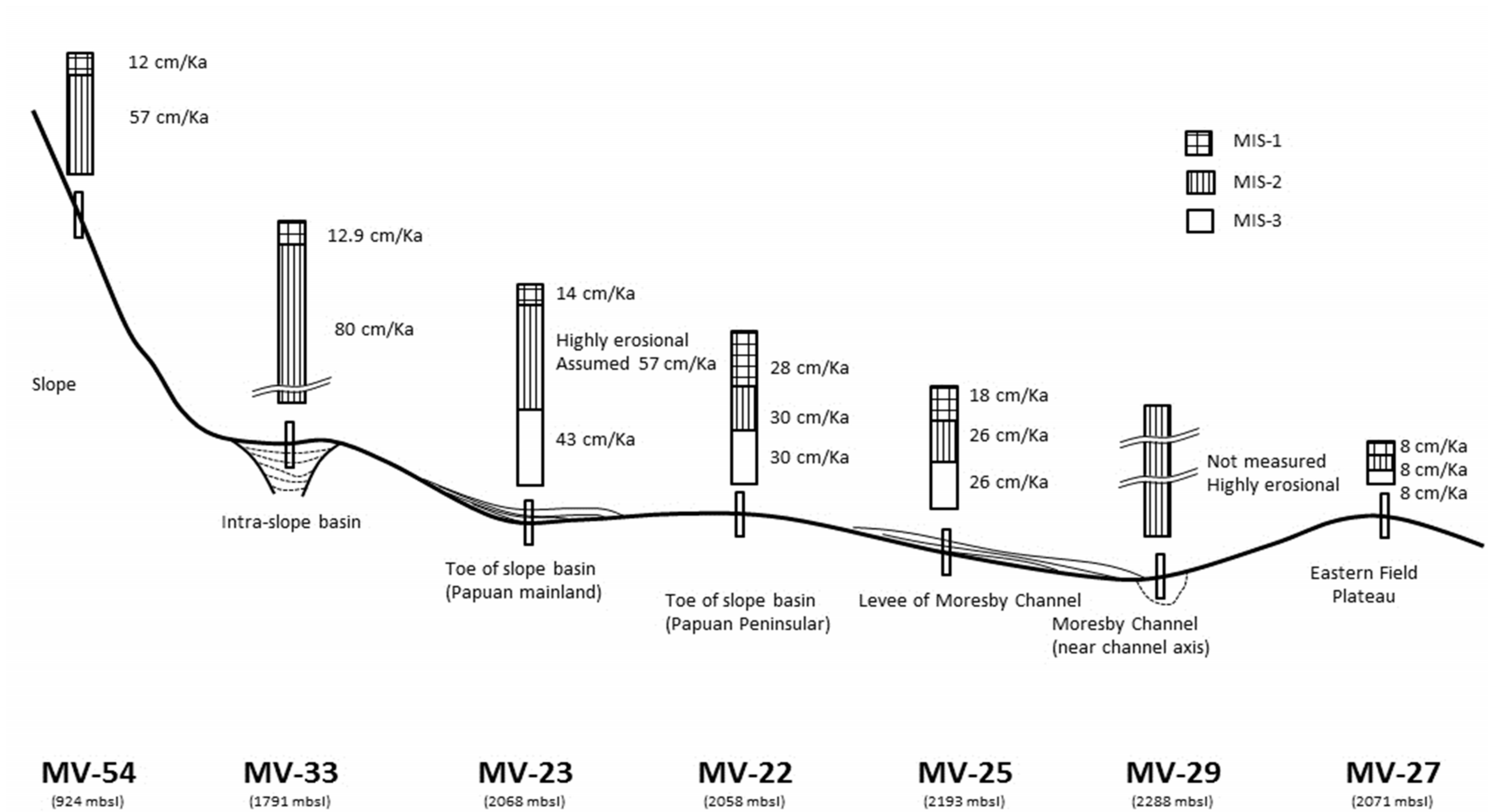


Figure 2.11.(a) Variation in net sediment deposition across the Gulf of Papua, from shelf margin to the deep water area. The thickness shown for MIS-1 through MIS-3 is proportional to the interpreted sediment accumulation rate (SAR). The basin where MV-33 was taken is based on the Fugro seismic data (unpublished).

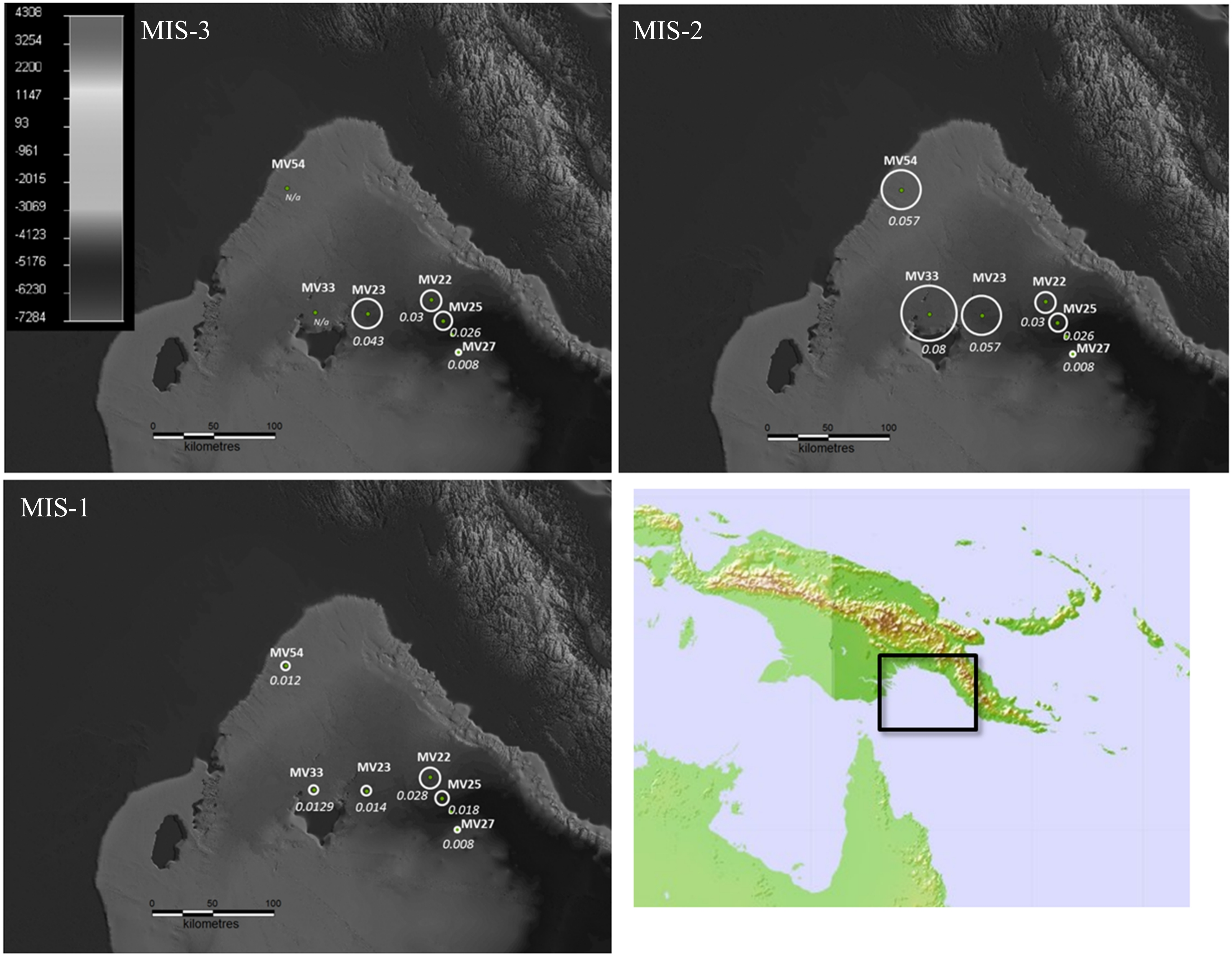


Figure 2.11.(b) Bubble map of the SAR for each marine isotope stage (MIS) (cm/yr). The bubble radius is proportional to the SAR (cm/yr).

supply in this region was largely cut off as sea level rose above the shelf edge, consistent with observations over smaller regions of Jorry et al (2008) and Febo et al. (2008).

### 2.6.2 Interpretation of the lithofacies

<u>Lithofacies-1</u>: this lithofacies is characterized by a distinguished interlamination of mud (mud is graded in thin section (Fig 2.5b)), silt and thin fine grained sand, fairly bioturbated and low in carbonate content, the core location (MV-22) is associated with wave-like depositional features (Francis et al., 2008; Chapter 3 of this study) thus the facies is interpreted as reworked sediment associated with bottom currents and only found in Moresby Trough and also channel area such as in Moresby Channel or Pandora toe of slope(Fig. 2.8).

<u>Lithofacies-2</u>: this lithofacies is divided into 3 sub-facies, sub-facies 2a : occurs as a layer that is intensely burrowed by a horizontal trace maker (e.g. MV-24), suggesting that the trace-maker might have been attracted to organic matter within this muddy unit (Fig. 2.6). These traits suggest deposition via a combination of a low density, low energy turbidity current and subsequent hemipelagic deposition. Sub-facies-2b consists of thinly bedded normally graded layers dominated by fine to medium sand, sometimes displaying Bouma sequence $T_{b\text{-}c\text{-}d}$ but mostly only $T_b$ or $T_{b\text{-}c}$ divisions (Fig-5b, thin section; Fig-8 [MV-23], and Fig. 9). The aligned biogenic materials (including foraminifera and wood fragments) suggest a mixing of reworked shelf materials and fluvial deposits via channel pathway deposited in distal fan. Sub-facies-2c consists of medium to thick (15-50 cm) beds of medium- to fine-grained sand, characterized by Bouma sequence $T_{a\text{-}b}$ (MV-23, Fig. 9). Sometimes this sub-facies is only present as a $T_b$ layer, suggesting deposition from upper plane bed condition, and/or erosion by subsequent flows.

Lithofacies-3: direct core observation and x-radiographs show that the sand layers either have bidirectional terminations (producing lenses), or may pinch out or interfinger with surrounding mud (MV-22, Fig. 8). This lithofacies is interpreted to represent distal sedimentation from relatively high energy sediment-gravity flows where the sand supply is limited.

Lithofacies-4: Textural observations on the sandy layers suggest that these beds could be differentiated on the basis of depositional mechanism, either as bed load (coarse grained, predominately with bioclasts) carried along by a tractive current, or as the deposit of suspension and gravitational settling as interpreted for the 'calci-turbidites" of Jorry et al. (2008). This lithofacies is restricted chronostratigraphically, being associated with the timing of Melt Water Pulse 1B (Jorry et al., 2008) (Fig. 2.10).

Lithofacies-5: Visually, this lithofacies cannot be conclusively identified either as a hemipelagic mud, or the muddy portion of a turbidite (Bouma Turbidite sequence $T_e$). Previous study (Brunner and Ledbetter, 1987; Stanley and Maldonado, 1981) distinguished such units by their grading in mean silt particle size, coarseness in mean silt particle size and particle size frequency distribution in the silt fraction.

Lithofacies-6: This lithofacies is found in cores retrieved from steeper regions of the slope (MV-27, Fig. 8), or associated with the levee-channel system (lithofacies-2 and -5). Slump is interpreted to develop when the levee gradient exceeds critical values for failure. Associated with this unit sometimes is a fine- to very fine-grained sand injectite, providing evidence for penecontemporaneous sedimentary processes developed as a result of the overburden pressure during the shallow burial (MV27, Fig. 8).

### 2.6.3. Sediment delivery down the Moresby Trough and Channel

SARs in eastern Moresby Trough and the deeper basin in Moresby Channel are lower and correspond to longer time spans than for MV-54 and MV-33 (at least ca. 7-45 cal ka, from youngest to oldest dates). Only MV-23 has sufficient $^{14}C$ dates to resolve changes in SAR over time, and its data suggest declining SAR from regressive to transgressive phases of MIS-2 (Figure. 2.4). However, the relatively young date (7.4 cal ka) near the top of core MV-22 (1.6 mbsf) suggests that some sediment is still reaching Moresby Trough in the Holocene, supported by measureable $^{210}Pb$ SAR (0.14 cm/y) near this location (multi-core MV-24), reported by Muhammad et al. (2008) and discussed above.

Core MV-23 in the toe-of-slope of Pandora Trough is composed primarily of lithofacies-2, -4 and -5. It contains a succession of 23 turbidites showing Bouma (1962) divisions $T_{a-b}$ in the lower part (>7.5 mbsf), $T_b$ or $T_{b-c}$ in the middle interval (between 7.5 – 3 mbsf) and nearly complete Bouma sequences of $T_{b-e}$ in the upper core interval (< 3 mbsf) (Figure 2.9). This setting is interpreted to be the product of a channel system in the lower part of the core which evolved over time to an off-channel axis mud-dominated depositional levee setting. The lack of upper Bouma divisions in the base of the core is typical of proximal channel-fill deposits accumulated near a channel axis (Middleton and Hampton, 1973; Lowe, 1982; Yuansheng et al., 2008), whereas $T_b$ or $T_{b-c}$ sequences are characteristic of high energy flow of proximal levee overbank complexes, indicated by climbing ripples produced as flow velocity decreases.

The finer and lower energy deposits comprising the upper part of core MV-23 are consistent with deposition in a more distal overbank environment (Middleton and Hampton, 1973; Lowe, 1982; Yuansheng et al., 2008). Figure 2.9 (left panel) shows the last/uppermost turbidite sequence found in core MV-23, a typical Bouma sequence $T_{b-e}$ with wood fragments deposited in the boundary between $T_b$ and $T_c$. These fragments are the best evidence of the deposit originating from reworked coastal/fluvial materials. A dated wood fragment (19.455 cal ka) from this depth (2.32 mbsf, Table 2.2, from Patterson, 2006) and the calendar age of forams dated from 6 cm deeper in the core is 18,495 cal ka (Table 2.2) are consistent with the age of the late stages of the LGM sea-level lowstand (ca. 20 cal ka). The slightly older calendar age of the wood relative to the forams suggests that the transit time for such woody debris from fluvial sources to the basin floor (> 150 km; Figure 2.2.) would have been on the order of 1000 years at that time.

Cores MV-25 and MV-29 show evidence of sand-load turbidity currents entering the deep-sea basin via the large Moresby channel system. Both cores are located in the off-axis region of the large channel-levee system (Francis et al., 2008; Chapters 3 and 4 of this study). Core MV-25 shows interlaminated mud, silt and fine-grained sand (Figure 2.3) deposited over a 40 ka period, and is interpreted to have been deposited in a side levee environment outside the major channel axis (by 0.6-1 km), based on present-day bathymetry and morphology. The thin turbidite layers in MV-25 are consistent with $T_b$ units, suggesting energetic bed-load deposition possibly through a large flow-stripping system. The core MV-29 shows incomplete recovery (5.99 m length), and is more sand dominated. The $^{14}C$ age acquired for hemipelagic mud in the core bottom is >51.2 cal ka, essentially at the upper limit for $^{14}C$ dating, although the overlying sandy deposits could be younger (possibly eroded into old mud), and consistent with the depositional ages of nearby cores MV-23 and MV-25.

The chronology (Figs. 2.3 and 2.4) suggests that this depositional system in the lower Moresby Trough and Moresby Channel was active long before the LGM and reached the peak of deposition near LGM time. These observations from MV-23 are valuable evidence for the regional lateral variation of the deposit, documenting the activation and de-activation of the large Moresby Channel system as controlled in part by sea level fluctuations.

Overall, the highest SARs appear to characterize MIS-2 for each basin based on the cores studied herein. No data exist for the Pandora Trough during MIS-3, but core measurements for the Pandora Trough during MIS-1 demonstrate negligible sediment delivery after Melt Water Pulse 1b (Jorry et al., 2008). The Moresby Trough received modest sediment supply from MIS-3 through to MIS-1 and likely to the present, at least as far down-channel as the locations of MV-22 and MV-24, based on $^{14}C$ data presented here, and Modern $^{210}Pb$ geochronology of Muhammad et al. (2008).

### 2.6.4. Later Patterns near the Eastern Shelf-Slope Break

At the same time that sediment supply to the location of MV-54 waned (~14-15 cal ka), sediment supply to the outer shelf and upper slope to the east appears to have increased, based on the analyses of Howell et al. (2014) on cores MV-41, -46, and -49 (near the transition from Pandora Trough to Moresby Trough, where the shelf-edge veers southward and the shelf narrows). These combined observations suggest that sediment supply to the western Pandora Trough may have been cut off by rising sea level ca. 14-15 cal ka, but sediment supply to the deep eastern Pandora and northern Moresby troughs was re-routed and locally increased by changing sediment delivery patterns during the period of transgression.

### 2.6.5. Controls on Deep Water Sediment Delivery

Previous studies have determined that deep water sedimentation commonly reached its peak in many regions worldwide near the LGM (23-19 cal ka), and de-glacial periods mostly have been considered non-depositional in deep water (e.g. Muhammad et al., 2008, Bentley et al. 2015). However there is an exception in the Moresby Trough where the evidence from the age model gathered from core MV-22 shows that the turbidite depositional cycle continued until 7.4 cal ka. This age, if correlated with oxygen isotopes excursion curves (Waelbroeck et al., 2002), corresponds to a sea level rise by more than 90 m since the LGM (the outer edge of shelf would have been drowned at 60-100 mbsl). Two possible factors that might account for this late turbidity-current activity are: (1) The shelf-slope setting, where the shelf in the Papuan Peninsula is relatively narrow (30-40 km) and steep, enabling the river mouth easier access to the shelf edge, with a higher gradient to facilitate movement of hyperpycnal flows from the river mouth across the seafloor to the shelf edge (if they were to occur) (Puig et al., 2003), and (2) lack of shelf trapping mechanisms combined with the occurrence of long-shore drift currents which could entrain and deliver sediment from far distant sources, as advocated elsewhere (Normark, 1978, Flood et al, 1991, Posamentier and Kolla, 2003, and Covault et al, 2007; Covault et al., 2011, Howell et al., 2014).

In the GoP area, hydrodynamic processes that developed as the continental shelf was flooded may have helped deliver terrigenous materials to the numerous canyon heads along the Papuan Peninsula shelf margin, and from there into deep water in the Moresby Trough. Previous studies have shown that winds, ocean currents, and waves create clockwise coastal circulation patterns and sediment transport, moving material from the central GoP shelf to the southeast (Wolanski et al., 1995; Keen et al, 2006; Selover et al., 2006; Slingerland et al., 2008). Such processes appear to have been active on the upper slope of the eastern GoP during the latest Pleistocene and earliest Holocene (Howell et al., 2014). Such processes should also be capable of providing sediment to deep basins farther east, along the Papuan Peninsula margin, and onward to the seabed near MV-22 during the Holocene (Figure 2.12). Possible evidence for this is visible in the greater frequency of sandy beds in core MV22 below depth of ~5 m bsf (Fig. 2.3), which could be the result of gravity driven flows (hyperpycnal or turbidity currents or a combination of the two) that are probably more effective at delivering coarse fluvial sediments to the slope than are hypopycnal flows of suspended sediment. This cross shelf flux would have likely been enhanced by potential contributions of hyperpycnal discharge from nearby small mountainous rivers; such flows have not been documented from these rivers, but their size, likely sediment yield, and catchment geometry makes them good candidates for such flows (Milliman, 1995). However, because of the distance separating most cores from the shelf edge and river mouths, and the lack of detailed knowledge for all of these catchments through time, the role of hyperpycnal flows remains speculative.

**2.6.6. Spatial integration of sediment accumulation through time**

By using SARS for each environmental combined by the predicted affected depositional area (e.g. shelf plain and shelf edge (MV-54): 19,230 sq km, minibasin (MV-33): 1,646 sq km, toe of slope (MV-23): 2,748 sq km, Moresby channel and basin floor (MV-22, MV-25and MV-29): 3,352 sq km and sea rise in Eastern Field plateau (MV-27): 2,355 sq km) sediment accumulation rate for for each MIS can be estimated, reported in $m^3$/y (values in parentheses are mass accumulation in millions of t/y, assuming average sediment bulk density of 1.5 g/$cm^3$ as indicated in Fig. 2.3). In MIS-3 the total accumulation is 2.3 million $m^3$/yr (3.45); in MIS-2 including the LGM the total sediment budget is 145 million $m^3$/yr (219); and in MIS-1 the total sediment budget is 3.8 million $m^3$/yr (5.7) (Table 2.4). Comparison of these accumulation rates with Milliman's (1995) estimated discharge from northern GoP rivers of 365 million t/yr suggests that the locus of major sediment accumulation is strongly modulated by sea level change, even though more detailed analysis does suggest continued local sediment delivery to the deep sea during highstand conditions (e.g., MV-22, Figs. 2.4, 2.12).

### 2.7. Conclusions

Six lithofacies across the deep water Gulf of Papua (GoP) are identified based on core visual and textural observation. Chronological constraints permit an assessment of changes in sediment supply and depositional environments across time and space, from MIS 3 to MIS 1. The sediment delivery to the deep water GoP is dominated by two mechanisms, gravity-driven flows down slopes and into deep sea basin primarily during lowstands in western portions of the study area, and hemipelagic sediment accumulation during transgression and highstand. Although the sediment flux appears to be overall dominated by sediment gravity flows, hemipelagic sediment delivery is widespread during periods of sea level highstand. In eastern portions of the study area, off-shelf sediment delivery continued into the Holocene in sufficient local volumes to produce turbidity currents. This late, localized sediment delivery appears to have been facilitated by oceanographic processes that allowed seaward sediment transport after flooding of the shelf.

In summary, deep water sedimentation during the late Pleistocene and Holocene in the Gulf of Papua is characterized by mostly fine sediment delivery, controlled by a combination of fluvial discharge, local morphology and oceanographic processes. This modern analog differs in its complexity from traditional highstand-lowstand sediment-delivery paradigms, in Moresby Trough, sediment delivery continued through late Holocene transgression, creating a coalescing high-stand fan system.

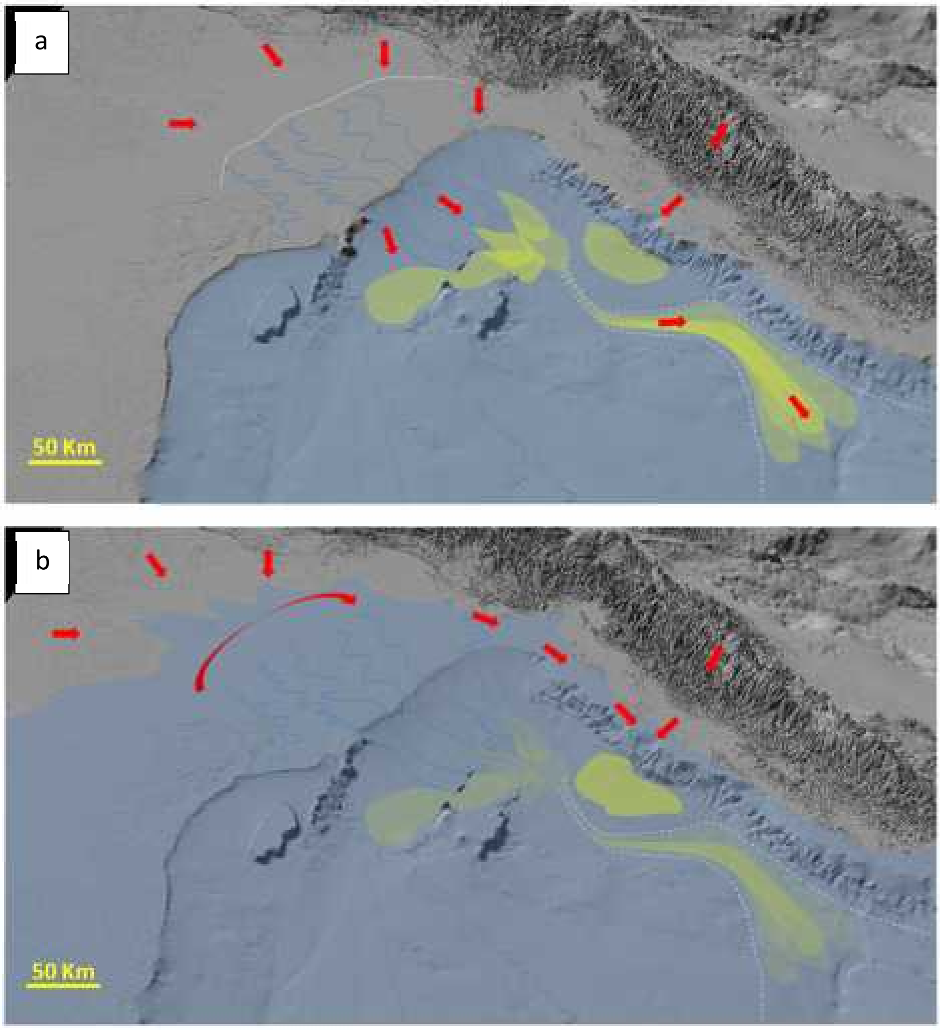


Figure 2.12. Hypothetical depositional model. **(a)** The channel system was initiated at the lowstand of sea level. **(b)** During the MIS-1 highstand of sea level, the sedimentation in the western part of GoP (Pandora Trough system) probably ceased; however, deposition in the eastern part of the GoP (Moresby Trough system)  still continues although with a slower depositional rate.

| Lithofacies Division | General Core description | log character | x-radiograph | Petrographic | Core example |
|---|---|---|---|---|---|
| Lithofacies-1 | Mud dominated, dark greenish thin mud underlain by silt and dark-blackish sand | serrated, fining upward | varve interlaminated between light (higher density) and dark (lower density) sediment | dark mud, no distinct variation, | MV-22, MV-54 |
| Lithofacies-2 | Dark grey to blackish colored layers of varied thickness, fining upward Sheet-shape sand geometry, thin silty mud lenses | typically saw-tooth or bell shaped with thick sand layer in the bottom part | Laminated sediment, intensely burrowed | sharp contact, appear erosional, grain orientation | MV-23, MC-24 |
| Lithofacies-3 | Sand dominated, thin sand lenses intercalated in thick mud. The sand is fine grained | thin bell shaped sometimes spike | distinct lamination of thin sand, fairly burrowed, bidirectional termination of sand | lenses of sand with distint termination | MV-22 |
| Lithofacies-4 | calcareous mud and sand, light grey to cream colored mud, biogenic dominated with fecal pellet, traces of shell and foraminiferal test | serated and low density | light colored thick sand, intensively burrowed | sand are bioclast with skeletal fragment | MV-33, MV-23 |
| Lithofacies-5 | slightly laminated dark grey mud with moderate to intense bioturbation | lightly serated | dark low density sediment, with some thin sand lamination | thinly laminated mud | MV-27 |
| Lithofacies-6 | semi-mottled apearance, varying distinct deformation, or massive without any distinct layering | tabular and blocky log with coarsening upward pattern | mostly shows irregular sand shape | n/a | MV-27 |

Table 2.3.

| No | Environmental | affected area | Jumbo Piston Cores | | | | | | | SARS (cm/yr) | | | Sediment Budget ( thousand m3) | | |
|---|---|---|---|---|---|---|---|---|---|---|---|---|---|---|---|
| | | (sq km) | MV-22 | MV-23 | MV-25 | MV-27 | MV-29 | MV-33 | MV-54 | MIS-3 | MIS-2 | MIS-1 | MIS-3 | MIS-2 | MIS-1 |
| 1 | Moresby Channel and Basin Floor | 3,352 | X | | X | | X | | | 0.028 | 0.028 | 0.023 | 938.56 | 938.56 | 770.96 |
| 2 | Pandora Trough toe of slope | 2,748 | | X | | | | | | 0.043 | 0.057 | 0.014 | 1,181.64 | 1,566.36 | 384.72 |
| 3 | Pandora shelf break and slope | 19,230 | | | | | | | X | n/a | 0.057 | 0.012 | n/a | 10,961.10 | 2,307.60 |
| 4 | Minibasin | 1,646 | | | | | | X | | n/a | 0.08 | 0.0129 | n/a | 131,680.00 | 212.33 |
| 5 | Sea rise in Eastern Field Plateau | 2,335 | | | | X | | | | 0.008 | 0.008 | 0.008 | 186.80 | 186.80 | 186.80 |
| | | | | | | | | | | | **Total** | | 2,307.00 | 145,332.82 | 3,862.41 |

Table-2.4.

## 2.8. References

Bentley, S.J., Blum, M.D., Maloney, J., Pond, L.G., and Paulsell, R.L., 2015, The Mississippi River Source to Sink System: Perspectives on Tectonic, Climatic, and Anthropogenic Influences, Miocene to Anthropocene. In revision, Earth Science Reviews.

Bentley, S.J., and Nittrouer, C.A., 2003, Emplacement, modification, and preservation of event strata on a flood-dominated continental shelf: Eel Shelf, northern California. Continental Shelf Research 23: 1465-1493.

Bouma, A.H., 1962. Sedimentology of some Flysch deposits: A graphic approach to facies interpretation. Elsevier. 168 p.

Bromley, R.G., 1996. Trace fossils. Biology, taphonomy and applications (Second edition). Chapman & Hall (London): 361 pp.

Bronk Ramsey, C., and Lee, S., 2013. Recent and Planned Developments of the Program OxCal. Radiocarbon, 55(2-3), 720-730.

Brunner, C.A., Ledbetter, M.T., 1987. Sedimentological and micropaleontological detection of turbidite muds in hemipelagic sequences: an example from the late Pleistocene levee of Monterey Fan, Central California Continental Margin, Marine Micropaleontology, V. 12, 223-239

Cloos, M., Sapiie, B., Quarles Van Ufford, A., Welland, R.J., Warren, P.Q., and McMahon, T.P., 2005, Collisional delamination in New Guinea: The geotectonics of subducting slab breakoff, Geological Society of America special paper 400 doi: 10.1130/2005.2400

Covault, J.A., et al., 2007. Highstand fans of the California Borderland: The overlooked deep-water depositional system: Geology, 35, 783-786.

Covault, J.A., et al., 2011. Terrestrial source to deep-sea sink sediment budgets at high and low sea levels: Insights from tectonically active Southern California, Geology, 619-622, doi:10.1130/G31801.1

Davies, H.L., 2012, The Geology of the New Guinea – the Cordilleran Margin of the Australian Continent, Episodes vol.35 no.1, p. 1-16

Day, G., et al., 2008. The depositional web on the floodplain of the Fly River, Papua New Guinea. Journal of Geophysical Research: Earth Surface, 113: 2156-2202, http://dx.doi.org/10.1029/2006JF000622

Dickens, G. R., Droxler, A. W., Bentley, S. J., Peterson, L. C., Opdyke, B. N., Beaufort, L., & Zarikian, C. A. (2006). Sediment accumulation on the shelf edges, adjacent slopes, and basin floors of the Gulf of Papua. Margins Newsletter, 16, 1-5.

Febo, L.A., et al., 2008. Late Pleistocene and Holocene sedimentation, organic carbon delivery, and paleoclimatic inferences on the continental slope of the northern Pandora Trough, Gulf of Papua, J. Geophys. Res., doi:10.1029/2006JF000677

Flood, R.D., et al., 1991. Seismic facies and late Quaternary growth of Amazon submarine fan. In: Weimer, P., and Link, M.H. (Eds.), Seismic facies and sedimentary processes of modern and ancient submarine fans: New York (Springer-Verlag), 415-433.

Francis, J.M., Daniell, J.J., Droxler, A.W., Dickens, G.R., Bentley, S.J., Peterson, L.C., Opdyke, B.N., Beaufort, L., 2008. Deep water geomorphology of the mixed siliciclastic-carbonate system, Gulf of Papua J. Geophys. Res., doi:10.1029/2007JF000851

Freifeld, B.M., et al., 2006. On-Site Geologic Core Analysis Using a Portable X-ray Computed Tomographic System, From: Rothwell, R.G., 2006, New Techniques in Sediment Core Analysis. Geological Society, London, Special Publications, 267, 165–178. 0305-8719/06/, The Geological Society of London.

Howell, AL., Bentley, S.J., Xu, K, Ferrell, R.E., Muhammad, Z, and Septama, E, 2014, A clay mineral provenance study of the Northern Pandora Trough Continental Margin, Papua New Guinea. Marine Geology DOI: 10.1016/j.margeo.2014.08.003.

ICS (International Commission on Stratigraphy), 2010. Global chronostratigraphical correlation table for the last 2.7 million years. Online at http://www.stratigraphy.org/upload/QuaternaryChart1.JPG, accessed 4/24/2014.

Jorry, S.J., et al., 2008. Bundled turbidite deposition in the central Pandora Trough (Gulf of Papua) since Last Glacial Maximum: Linking sediment nature and accumulation to sea level fluctuations a millennial timescale, J. Geophys. Res., doi:10.1029/2006JF000649

Keen, T.R., et al., 2006. Potential transport pathways of terrigenous material in the Gulf of Papua, Geophys. Res. Lett., 33, L04608, doi:10.1029/2005GL025416

Kuehl, S.A., et al., 1988. Microfabric study of fine-grained sediments: observations from the Amazon subaqueous delta. J. Sed. Petrol. 58, 12–23

Lowe, D.R., 1982. "Sediment gravity flows: II. Depositional models with special reference to the deposits of high-density turbidity currents". *Journal of Sedimentology* (Society of Economic Paleontologists and Mineralogists): 52, 279–297.

Middleton, G.V. and Hampton, M.A., 1973. "Sediment gravity flows: mechanics of flow and deposition". *Turbidites and deep-water sedimentation* (Pacific Section of the Society of Economic Paleontologists and Mineralogists, Short Course Lecture Notes): p. 1–38.

Milliman, J. D., 1995, Sediment discharge to the ocean from small mountainous rivers: The New Guinea example, Geo Mar. Lett., 15(3– 4), 127–133.

Muhammad, Z., et al., 2008. Excess 210Pb inventories and fluxes along the continental slope and basin of the Gulf of Papua, J. Geophys. Res., doi:10.1029/2006JF000676

Normark, W.R., 1978 "Fan valleys, channels, and depositional lobes on modern submarine fans: Characters for recognition of sandy turbidite environments", American Association of Petroleum Geologists Bulletin, 62 (6), p. 912-931.

NSF MARGINS Office, 2004. NSF MARGINS Program Science Plans, pp. 170, Lamont-Doherty Earth Obs., Columbia Univ., Ithaca, N. Y.

NSF Margins Office, 2009, S2S Nuggets and 2009 Review Documents. [http://www.nsf-margins.org/S2S/S2S.html](http://www.nsf-margins.org/S2S/S2S.html), accessed 11/18/2014.

Patterson, L.J., 2006. Petrological and geochemical investigations of deep sea turbidite sands in the Pandora and Moresby Troughs: Source to sink Papua New Guinea focus area, M. S. thesis, Louisiana State University.

Pigram C.J., and Davies, H.L., 1987. Terranes and the accretion history of the New Guinea Orogen: Bureau of Mineral Resources Journal of Australian Geology and Geophysics , 10, 193-212

Pigram, C.J., et al., 1989. Tectonic controls on carbonate platform evolution in southern Papua New Guinea: Passive margin to foreland basin, Geology, 17, 199– 202.

Posamentier, H.W., and V. Kolla, 2003. Seismic geomorphology and stratigraphy of depositional elements in deep-water settings: Journal of Sedimentary Research, 73, 367–388.

Principato, S.M., 2004. X-radiographs of sediment cores, a guide to analyzing diamicton in: Francus, P. (ed), Image analysis, sediments and paleo-environments, Kluwer Academic Publishers, Dordrecht, The Netherlands, 165-185.

Puig, P., Ogston, A. S., Mullenbach, B. L., Nittrouer, C. A., & Sternberg, R. W, 2003. Shelf-to-canyon sediment-transport processes on the Eel continental margin (northern California). *Marine Geology*, *193*(1), 129-149.

Reimer, P. J., Bard, E., Bayliss, A., Beck, J. W., Blackwell, P. G., Ramsey, C. B., & van der Plicht, J., 2013. IntCal13 and Marine13 Radiocarbon Age Calibration Curves 0–50,000 Years cal BP. Radiocarbon, 55(4), 1869-1887..

Slingerland, R., et al., 2008. Building the Holocene Clinothem in the Gulf of Papua: an Ocean Circulation Study. Jour. of Geophys. Res., 113, 1-17.

Stanley, D.J., and Maldonado, A., 1981. Depositional models for fine-grained sediment in the western Hellenic Trench, Eastern Mediterranean, Sedimentology 28, 273-290

Tcherepanov, E.N., et al., 2008. Neogene evolution of the mixed carbonate-siliciclastic system in the Gulf of Papua, Papua New Guinea, J. Geophys. Res., 113, F01S21, doi:10.1029/2006JF000684

Waelbroeck, C., Labeyrie, L., Michel, E., Duplessy, J.C., McManus, J.F., Lambeck, K., Balbon, E. and Labracherie, M., 2002, Sea-level and deep water temperature changes derived from benthic foraminifera isotopic records: Quaternary Science Reviews, v. 21, p. 295–305, doi:10.1016/S0277-3791(01)00101-9.

Wolanski, E., et al., 1995. Water circulation in the Gulf of Papua, Cont. Shelf Res., 15, 185–212.

Yuansheng, D.U., et al., 2008. First record of the contouries from lower Devonian Lip-trap Formation in Southeast Australia, Sci China Ser-D earth sci July 2008 vol.51 no.7 939-946

## CHAPTER 3

# Late Quaternary Geomorphology, Seabed Evolution, and Terrigenous Sediment Delivery to the Pandora and Moresby Troughs, Gulf of Papua

### 3.1. Introduction

The study of seabed morphology can provide valuable insights regarding formative sedimentary processes. Because deep-sea sedimentary processes range greatly in terms of temporal and spatial scales over which they operate, morphological analysis to infer formative process may be more elucidating than attempts to directly study the relevant processes. This study presents the 3D visualization, analysis and interpretation of seabed morphology, stratigraphy, and sediment acoustic characteristics derived from sub-bottom sonar data and sediment cores collected during the 2004 PANASH cruise of the R/V Melville in the Gulf of Papua (GoP) (Dickens et al., 2006), and multibeam data collected and gridded during that and other cruises (Figure 3.1a) (Daniell, 2008). The GoP, with associated large river systems and deep ocean basins was selected as a focus area for the US-NSF MARGINS Source to Sink (S2S) Program (NSF MARGINS, 2004), owing to the large terrigenous sediment flux, the presence of active sedimentary processes in fluvial, shelf, and deep-sea settings, and the relatively closed nature of the system over millennial timescales, through its connection to the Coral Sea abyssal plain.

This continental margin receives large terrigenous sediment flux (331 million tonnes/ year) (Milliman, 1995) from rivers that have low anthropogenic and deforestation impacts in the upstream area. The shelf and slope exhibit morphological gradients from the wide gentle shelf-slope setting in the Pandora Trough to the narrow-steep shelf-slope setting in the Moresby Trough, which have all been progressively drowned since the Last Glacial Maximum (LGM)

(23-19 cal ka). The shelf-slope depositional complex built extremely rapidly during the Neogene, and contains hydrocarbon systems that are presently being exploited (Tcherepanov et al., 2008). This area has been intensively sampled and investigated with multibeam bathymetric data collection, 3.5 kHz seismic profiling, and core collection, and thus provides an excellent "natural laboratory" for analog study of the dynamic processes associated with sediment delivery and deposition. This rich data archive (Dickens et al., 2006) allows a rare opportunity to study the evolution of a regional deepwater depositional system at fine temporal and spatial resolution (centennial-millennial time scale, centimeter to meter sedimentary thickness) over approximately the last 40 cal ka (Chapter 2 of this study), a degree of documentation that is not possible in many deepwater studies. The main objectives of this study are to study seabed and shallow subsurface morphology, stratigraphy, and sediments, so as to infer active sedimentary processes over space and time. These observations will allow identification of primary pathways, timing, and mode of sediment delivery across the study area, over the past ~40 ky.

This study will first assess the descriptive morphology of the two major contrasting depocentres in the GoP (Pandora and Moresby troughs), with their associated canyons, channels and slopes, by integrating a published bathymetric grid (Daniel, 2008) with 3.5 kHz seismic data to generate a general acoustic facies classification and distribution map. Core data (Chapter 2 of this study) will then be used to relate lithofacies to acoustic facies, and elucidate detailed depositional processes at work in the area. Previous study has concentrated on linking seafloor geomorphology with broad inferred patterns of sediment delivery and accumulation (Francis et al, 2008). The present will build on the work of Francis et al. (2008) by use of a much more extensive chronostratigraphic framework (Chapter 2 of this study), and much more detailed

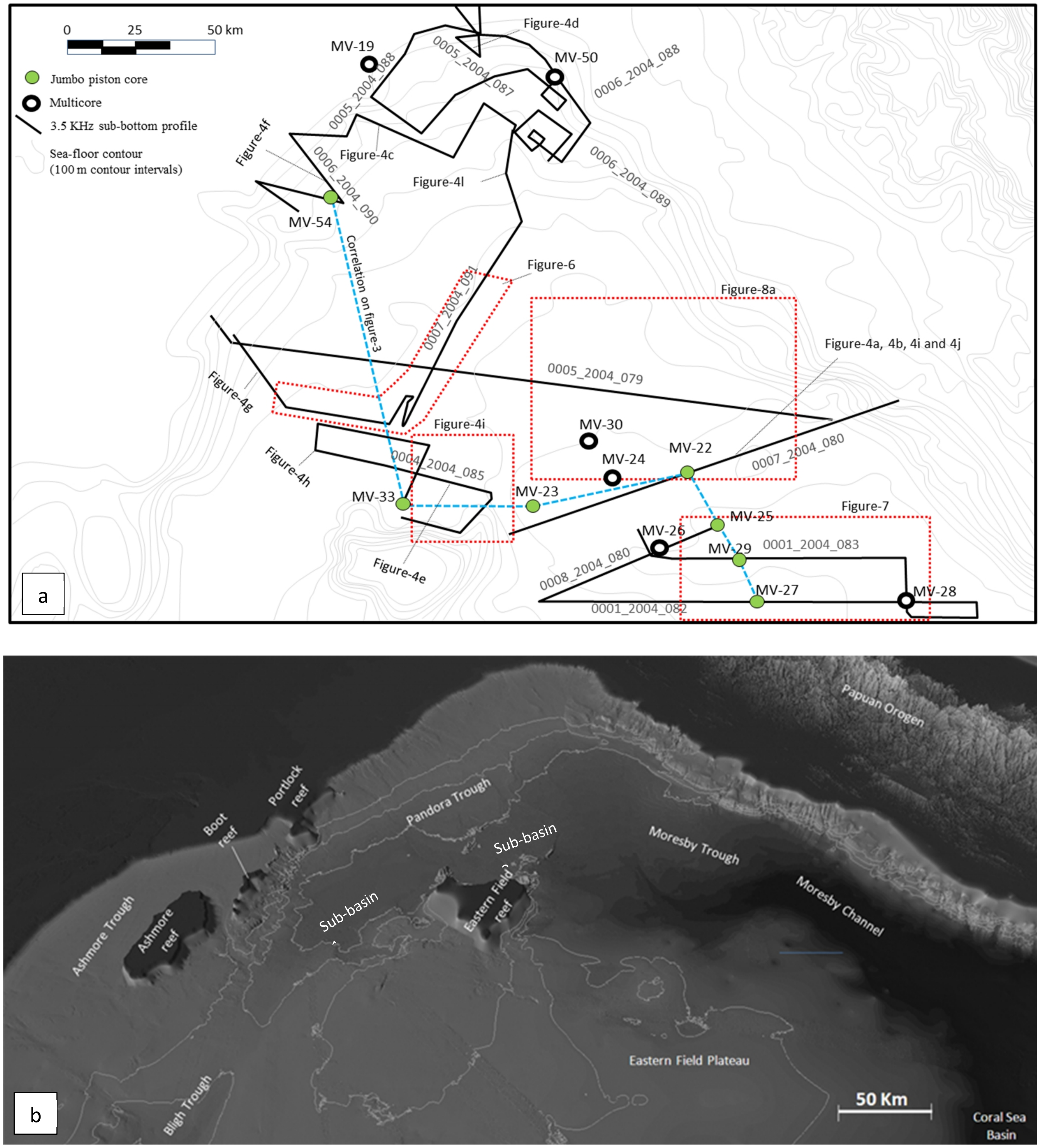


**Figure 3.1 (a)** Base map of the study area. The topographic map is created using bathymetric data compiled by Daniell (2008) and is overlayed with various data available for the study (jumbo piston cores and multi cores; multi-beam bathymetric data, sub-bottom profile data). Annotations shows figures used in this thesis. **(b)** 3D perspective view showing major morphological depocentres in the Gulf of Papua (notes the two subdivisions of Pandora Trough and Moresby Fan).

Regionally there are five morphological basins in the modern Gulf of Papua and adjacent northern Coral Sea (Figure 3.1b and 3.1d) (Francis et al., 2008; Daniell, 2008):

(1) The Bligh Trough forms the southwestern boundary of the study area, and is the eastern border of the Great Barrier Reef and the southwestern terminus of the Pandora Trough and southern terminus of the Ashmore Trough. It is oriented North-South with water depth ranging from 1500 - 2300 meters.

(2) The Coral Sea Basin is a wide abyssal plain covering an area of 100,000 $km^2$, with water depth ranging between 2500 to more than 4500 m. It is the most distal and deepest area of the Gulf of Papua and is interpreted as the ultimate depositional sink, connected to the Papuan mainland and peninsula by Moresby Channel.

(3) The Ashmore Trough to the west is the smallest basin and depocentre (2,009 $km^2$) and has water depth ranging of 500 – 900 m. This depocentre is surrounded by elongated semi-drowned carbonate platforms (Tcherepanov et al., 2008) that grew on the top of the northeast-southwest oriented structural ridges (Ashmore Reef to the east, Boot Reef and Portlock Reef to the north-northwest, and the Great Barrier Reef to the west).

(4) The Pandora Trough is the largest basin and depocentre in the northern GoP, covering 17,350 $km^2$, located parallel to the toe of the slope of the Gulf of Papua's continental shelf margin. It is elongated through south-southwest – north-northeast, with water depth of 1500 - 2000 m, with an extensive continental shelf adjacent to the basin.

(5) The Moresby Trough is elongated north-northwest – south-southeast direction and covers an area of 6,300 $km^2$ parallel with the adjacent Papuan Peninsula, with water depth of 2000-2500 m. It has an open northwestern boundary with the Pandora Trough (roughly along the 2000 m isobath), and feeds into Moresby Channel to the south, which connects this basin with the Coral

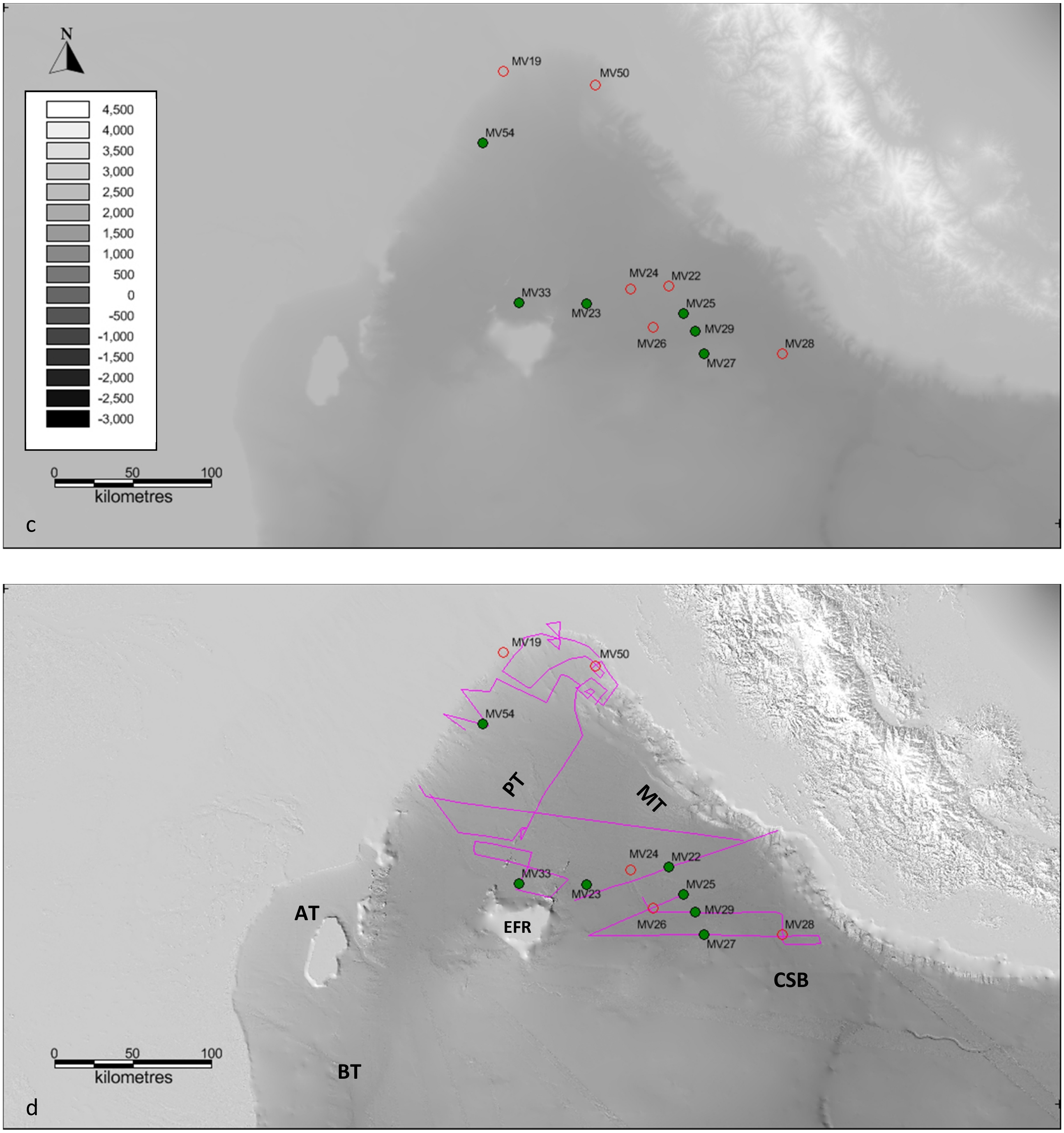


**Figure 3.1 (c)** Bathymetric map of the area (Daniell, 2008) in gray-scale shows regional extent of the Gulf of Papua and five morphological basin in the area, Bligh Trough (BT), Coral Sea Basin (CSB), Ashmore Trough (AT), Pandora Trough (PT), Moresby Trough (MT) and Eastern Field reef (EFR); this thesis is only focused in Pandora Trough and Moresby Trough **(d)** Sun-shaded bathymetric map (sun direction is toward NE) overlayed with sub-bottom track-line (purple line), jumbo piston cores (green filled circle) and multi-cores (red empty circle).

Sea Basin. This trough is fenced by adjacent mature canyons, which are 2.5 – 8 km wide and 300 - 700 m deep with steep slopes (up to 10.5° or 185 m/km).

This study will focus on seafloor morphology and sedimentary processes in two of these basins: the Pandora and Moresby troughs, extending from shelf break to the basin floor, in order to evaluate the most prominent pathways for sediment delivery from the northern GoP shelf edge to the deeper Coral Sea to the south.

**3.2. Geologic Setting**

The Pandora and Moresby Troughs are tectonic elements of the Papuan basin, and have existed as active depocentres since early Cenozoic time. The Papuan basin was originally part of Northern Australian margin which evolved from a passive margin with complex rifting episodes from early Mesozoic (Pigram and Pangabean, 1984) to the Paleocene (Weissel and Watts, 1979, Pigram and Symonds, 1991), forming an epicontinental sea with active foreland basin in Middle Oligocene (Pigram et al., 1989). Anti-clockwise rotation of New Guinea against the Northern Australian Queensland Plateau caused spreading that has been active since late Eocene and ceased before late Oligocene (Gardner, 1970), creating the Coral Sea abyssal plain to the south and the Pandora and Moresby troughs to the north, which are separated by plateaus (Eastern Plateau, Papuan Plateau and Queensland Plateau) (Figures 3.1a and b.).

Continued northward movement of the northern edge of the Australian craton caused a collision between the New Guinea plate with the Southern Pacific subduction complex, which consists of several arcs, oceanic plateaus and micro-plates (Pigram and Davies, 1987, Pigram et al., 1989). That collision marked a temporal transition from passive margin to the active foreland margin in Middle Oligocene. This movement was also responsible for the development of the Papuan fold belt and foreland basin immediately to the south of the collision range (Figure 3.2).

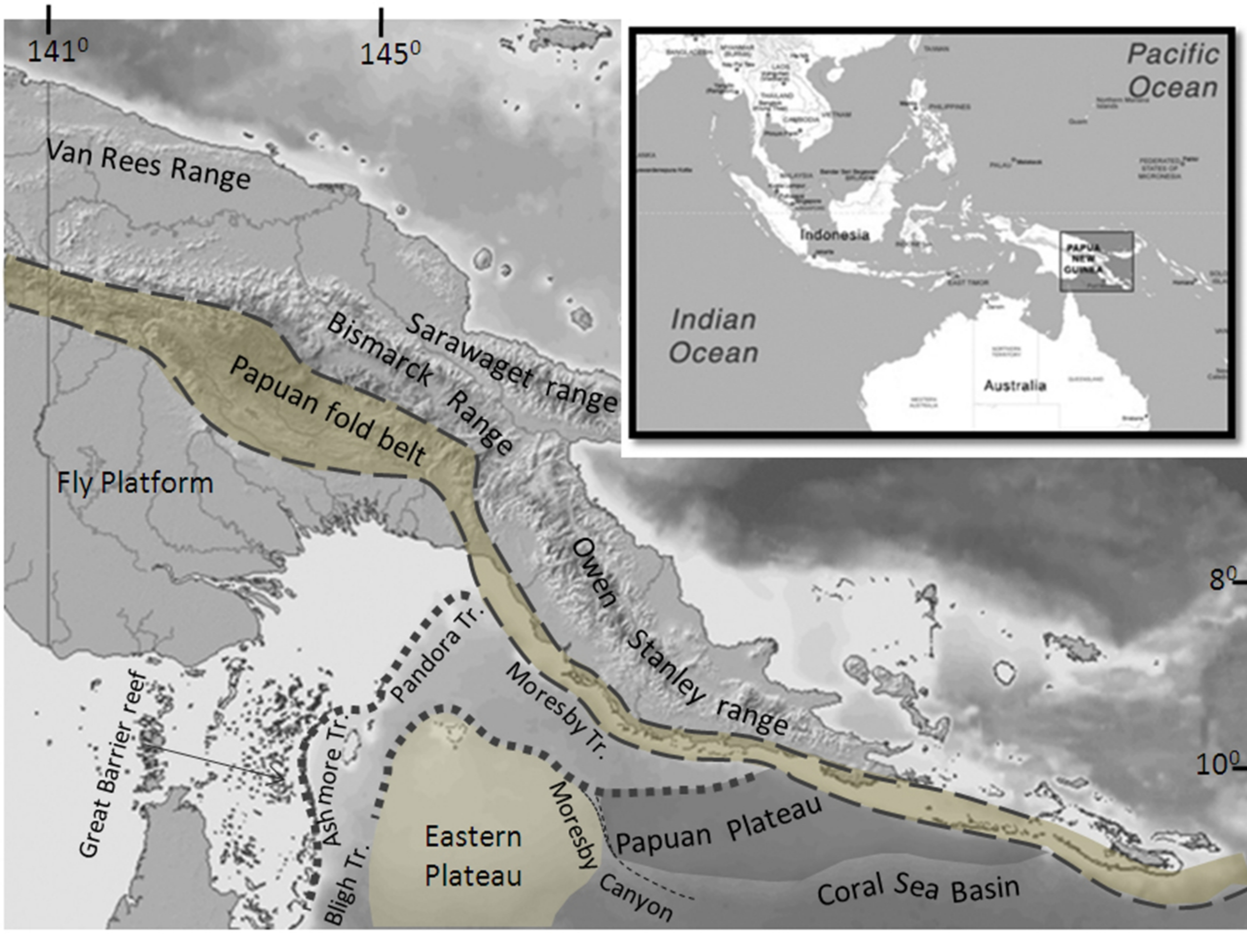


**Figure 3.2** Physiographic and tectonic elements of the Gulf of Papua and Papua New Guinea (modified after Pigram and Davies, 1987).

The trough remained sediment-starved from late Oligocene to late Miocene. Lack of the terrigenous siliciclastic input enabled the development of carbonate platforms on the south-southwest of the area. In Late Miocene rapid siliciclastic deposition fed the foredeep, which overflowed and inundated the carbonate growth in the northeastern margin (Tcherepanov et al., 2008). During Pliocene time, carbonate development in this locale ceased and shifted southward beyond the reach of the siliciclastic sources, where reefs continue to grow (e.g., the Great Barrier Reef, and barrier reefs along the GoP coast of the Papuan Peninsula) (Pigram, et al., 1989).

### 3.3 Methodology

High frequency (3.5 kHz) seismic profiles and 12-30 kHz multibeam data were obtained during the R/V Melville cruises in the Gulf of Papua in 2004 (Francis et al., 2008). These data were used to help develop a new regional bathymetric grid (Daniell, 2008) of 3.6 arc-second cell size (approximately 110 meters grid), incorporating data from other sources. For the present study, the Daniell (2008) grid was exported using Fledermaus-Avgrid into ASCII files, then imported as a horizon into Schlumberger Petrel for the primary visualization surface. The 3.5 kHz seismic lines in Knudsen extended binary (KEB) were firstly segmented according to their depth window in SounderSuite - Post Survey, and exported as SEG-Y data. The SEG-Y data were then imported to Petrel as 8 byte seismic data. The jumbo piston core data were logged shipboard by scientific team during the cruise using a Geotek Multi-sensor core logger (MSCL). The log data are modified into Log ASCII Standard (LAS) and imported into Petrel, to tie them into corresponding seismic data. The 2060 km of 3.5 kHz sub-bottom profile acquired during 2004 R/V Melville cruise provide a high resolution seismic image to a maximum depth of about 100 m, which is sufficient to observe and correlate echo boundaries with most of the jumbo piston core data markers.

The acoustic facies interpretation is made based on seismic characterization, relief roughness of the seafloor surface, characteristic reflective strength, penetration, sub-bottom reflector and internal reflector characteristics, linked with characteristics of nearby jumbo piston cores or multi-cores, where available. The classification scheme is adapted from several previous classification schemes (e.g. Damuth and Hayes, 1977, Jacobi and Hayes, 1992, Chough et al., 1997, Gee et al., 1999, Cronin et al, 2005), and is selectively tailored to reflect much detail of available character specific to the Gulf of Papua seafloor. Each assigned class was digitized in segments with starting and ending nodes readable in MapInfo or Arc-Info format.

Chronostratigraphy is mainly based on age models from radiocarbon analysis of Chapter 2 of this study, augmented by radiocarbon dates from previous studies (Febo et al., 2008; Jorry et al., 2008; Patterson, 2006) (Figure 3.3).

## 3.4. Results

### 3.4.1. Depositional Boundaries from Visualization

Pandora Trough: visually, this basin has indistinct geometry with open boundaries to southeast and southwest. Therefore, in order to delineate this trough, boundaries were derived from the interpolation of regional features and manifested relief from structural ridges and the interpretation from the 3.5 kHz sub-bottom profile. Based on these features, this trough can be separated into two parts that appear to relate to sediment delivery and depositional architecture (Figures 3.1a, b, c and d.).

Pandora Trough sub-basin-1 (2,470 km$^2$) is southernmost and is a closed/confined basin with a channel system fed from shelf break to the centre of the basin (Figure 3.1b). The average gradient based along shelf-to-basin transects is 7.5° - 5° (131 m/km – 87 m/km) on the upper slope, 2° - 1.5° (34.9m/km-26m/km) on the middle slope and 0.5° (8.7 m/km) at the toe of slope. Lower gradients are associated with the mini-basin occurrence; however gradients measured as high as 21° (383 m/km) are evident from the canyon steep walls.

Pandora Trough sub basin-2 (14,880 Km$^2$) (Figure 3.1b) lies adjacent to the Pandora shelf with three distinct morphologies: (a) steep gullies and structural ridges in the southern part, (b) rough surfaces with highly irregular topography in the north-northwest part of the sub basin and (c) a relatively smooth and undisturbed seafloor in between (a) and (b).

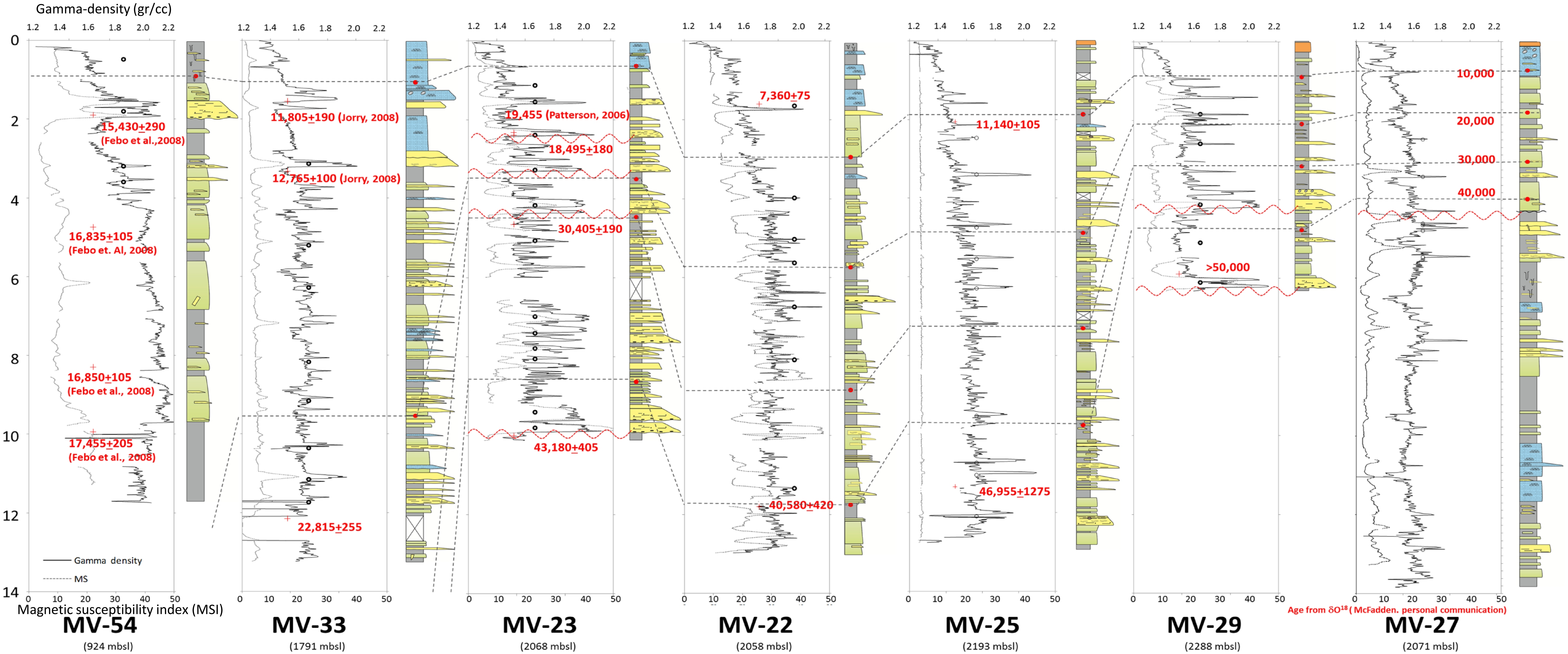

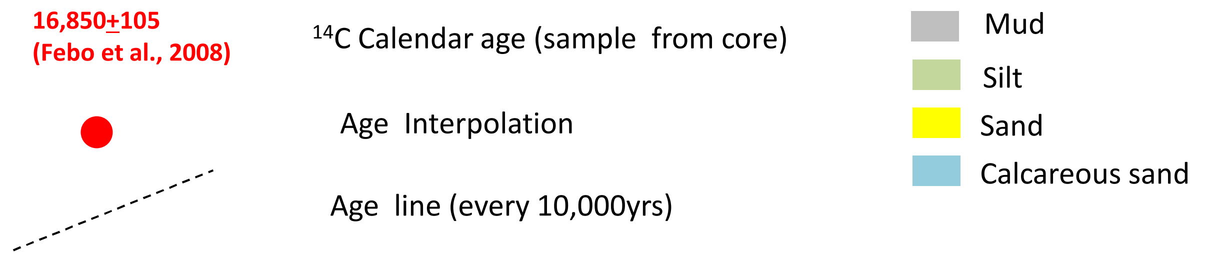

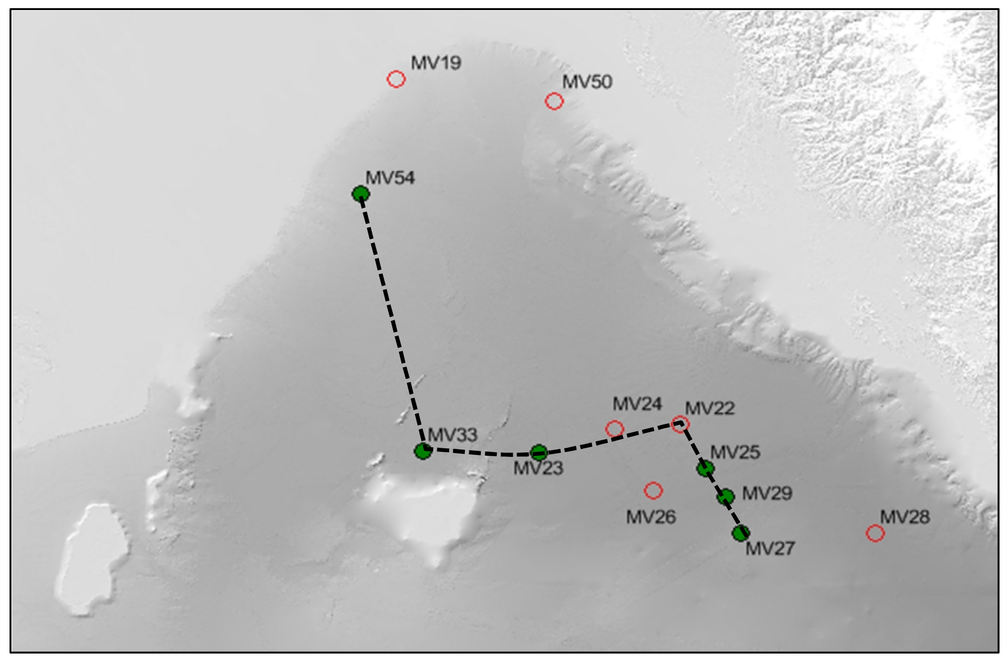


Figure 3.3. Chronostratigraphic correlation across the Gulf of Papua, from slope through mini-basin, toe of slope and Moresby channel, described in chapter 2 of this study. The time-lines are interpolated every 10 cal Ka based on sediment accumulation rates in the hemipelagic component of the sedimentary succession. Erosional bases to sand beds were interpreted based on log and core observations. The correlation on the upper part of the core (e.g. 10 Ka) also considering the peak of Ca from XRF scan data of cores MV-22, MV-25, MV-23 and MV-33

The structural ridge in (a) is oriented southwest-northeast with steep slopes of 19 - 35° (344 – 700 m/km), with heights of 200 - 700 m above the seafloor. The dated dredge sample (MV-36) suggests that this ridge is a drowned Miocene carbonate with an age of approximately 20 Ma (Francis et al, 2008, Tcherepanov et al., 2008).

Moresby Trough: in contrast with the Pandora Trough, the shelf and slope adjacent to the Moresby Trough is narrow and steep with a U-shaped mature canyon and an average topographic height (from the canyon base to the top of channel ridge) of 600 m and width of 3000 m. Morphology the toe of slope includes a distinct fan feature, which is aligned in a parallel direction with the ridge. Moresby Trough can be divided into two areas: the upper part, which connects with the Pandora Trough, and the lower part, which merges abruptly with the seafloor in 2000 meters deep and receives terrigenous sediment from the Papuan Peninsula (see also Figures 3.1a, b, c and d).

### 3.4.2 Acoustic Facies Classification

The acoustic facies classification consists of three major facies groups: non-stratified echo-characters, stratified echo-characters and echo-characters with rough or undulating relief. Stratification in sediment was assessed from sub-bottom reflectors whereas the depositional and erosional relief was determined from hyperbolae's shapes and vertices on the seafloor surface (Table 1 and 2). For clarity and continuity, interpretation of sedimentary environment follows each facies description in Table 2 and figure 3.4a to 3.4l.

| Group | Facies Class | Description | Example | Core | Interpretation |
|---|---|---|---|---|---|
| 1 | | **Non Stratified, gentle - moderate steep relief** | | | |
| | 1a | Strong flat non prolonged seafloor echo with low penetration (15-40 meter) |  | MV-24<br>MV-26<br>MV-28<br>MV-29 | hard surface probably thinner sheet shapes debris flow overlayed by Thick muddy hemipelagic layer |
| | 1b | Strong flat highly prolonged seafloor echo deep penetration (100 meter or more) |  | n/a | alternating turbidite/ debris with thick hemipelagic layer, mature seafloor with no/ low rate depositional |
| | 1c | Strong irregular highly prolonged seafloor echo deep penetration (100 meter or more) |  | n/a | rough surface, fine grained mass transport deposits or thick debris flow layer |
| 2 | | **Stratified gentle - moderate steep relief** | | | |
| | 2a | Strong flat seafloor echo with weak- transparent sub-bottom reflector, medium to deep penetration (40-more than 100 meter) |  | MV-19<br>MV-41<br>MV-46 | hard surface overlied by muddy turbidite or muddy hemipelagic layer |
| | 2b | Strong continous seafloor echo, with continous sub-bottom reflector, with stratigraphic event termination | 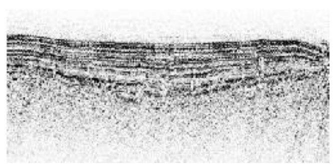 | MV-23<br>MV-27<br>MV-33<br>MV-66 | sheet shape turbidte layer, confined, distal part of fan or channel fill deposit |
| 3 | | **Highly Undulating relief** | | | |
| | 3a | weak to strong single seafloor echo with overlaping hyperbolae, weak to semi prolonged, no sub-bottom reflector, low penetration | 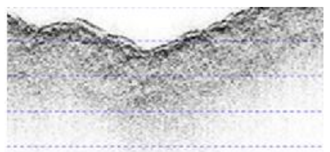 | MV-54 | slump (?) or muddy channel levee system or MTC |
| | 3b | Strong seafloor echo, irregular surface, highly prolonged, with close space intensely overlaping hyperbolae | 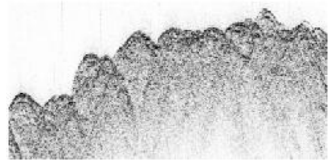 | n/a | conical shape might resemble coherence block from mass transport deposits. |
| | 3c | Strong seafloor echo, continous paralel sub-bottom reflector, with overlaping broad hyperbolae | 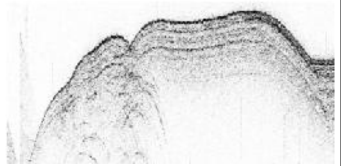 | MV-36<br>(dredge) | carbonate platform or structural ridge |
| | 3d | Strong seafloor echo continous paralel sub-bottom reflector, slightly overlaping or no overlaping. | 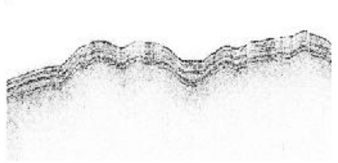 | MV-22 | sheet shape turbidite in fan or channel levee |
| | 3e | Transparent lens/convex shapes, with strong or weak echo on the base | 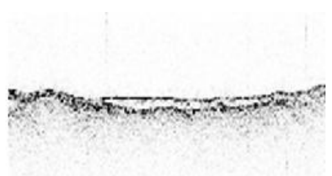 | n/a | mud drape over small basin or muddy channelized deposits or muddy debris/ slump |

Table 1 Facies Clasification in Gulf of Papua

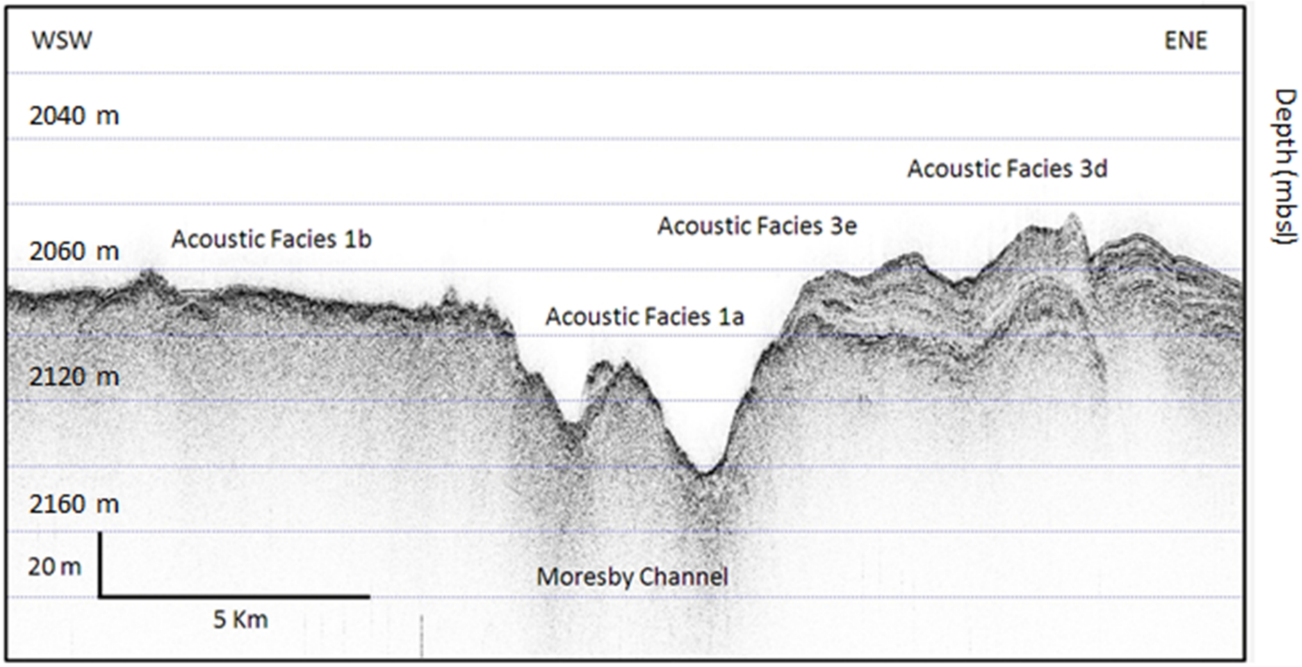


**Figure 3.4 (a)** 3.5 kHz section 0007_2004_080 shows seafloor on Moresby channel with a medium sound penetration without parallel sub-bottom reflector, interpreted as acoustic facies 1a. Facies 1a change gradually into acoustic facies 3e, where the steep gully wall is prone to slumping and facies 3d toward ENE, showing layering with 0.5 – 2 m bed thickness. In contrast, toward WSW the facies changes into acoustic facies 1b. The channel seafloor was interpreted as a high impedance surface (probably silt or coarser grained materials) with strong bottom current, influenced by erosional processes.

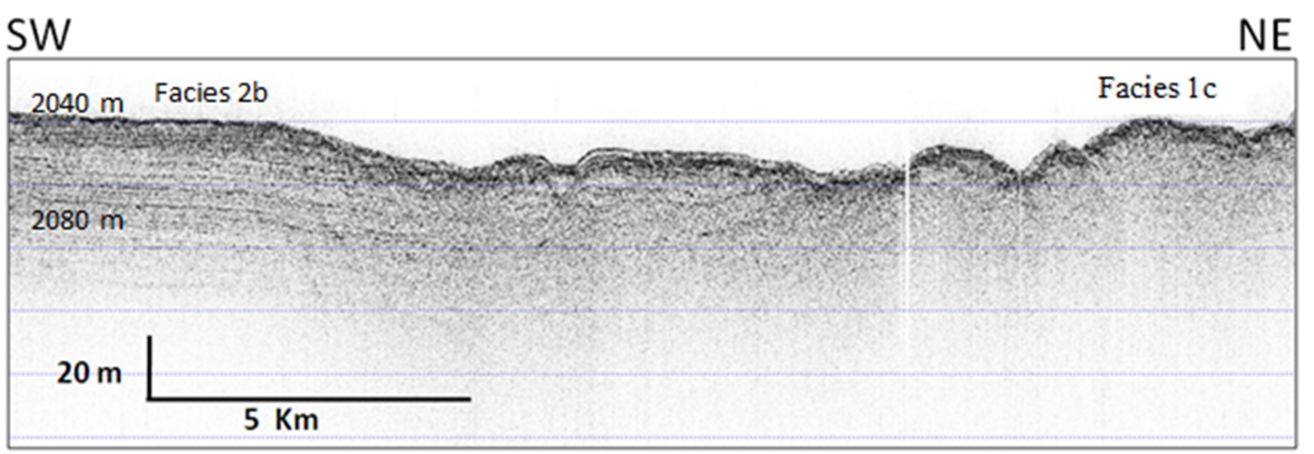


**(b)** 3.5 kHz section 0007_2004_080 is showing acoustic facies 1c which changes laterally into acoustic facies 2b toward SW. Facies 1c is interpreted as seafloor with strong bottom current and dominated by erosional processes. Acoustic facies 2b was interpreted as fan shaped deposits, which are located downslope from the mouth of a mature canyon adjacent to the Papuan Peninsula.

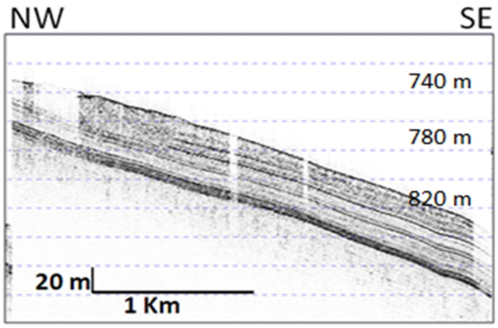

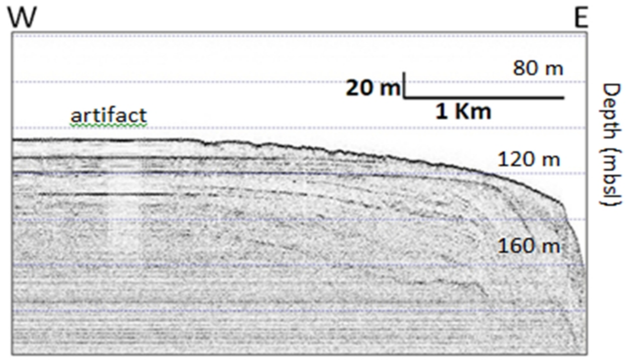


**(c)** 3.5 kHz profile 0005_2004_079 **(left)** and 0005_2004_087 **(d, right)** shows a typical characteristic of the facies 2a, with a strong flat seafloor echo and a weak-transparent sub bottom reflector. The shelf margin-upper slope break deposits (section 0005_2004_079, left) show a strong reflector approximately 30 m below the seafloor, which is interpreted as a hard surface as a result of erosional processes, likely develop when sub-aerially exposed during sea level fall. The shelf plain deposit (section 0005_2004_087, right) shows a distinct layering of what is probably fine sand or silt that are deposited in the shelf edge delta (The straight lines to the left are artifacts produced by the ship while holding station).

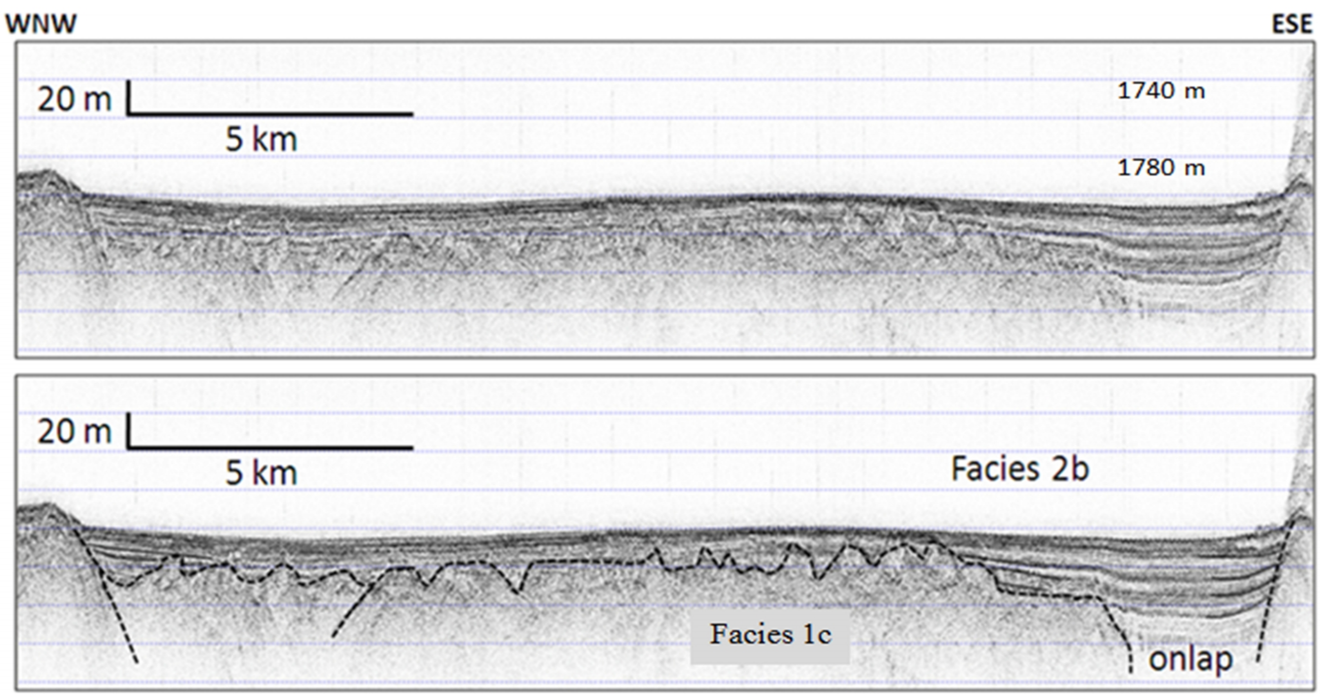


**(e)** 3.5 kHz profile 0004_2004_085 showing an acoustic facies 2b draped over acoustic facies 1c, the facies showing a distinct layering of 1 - 5 m layers, facies 2b thickness controlled by relief on the buried facies 1c surface (> 75 m in the thickest place). To the ESE and WNW the layer terminates by onlap termination.

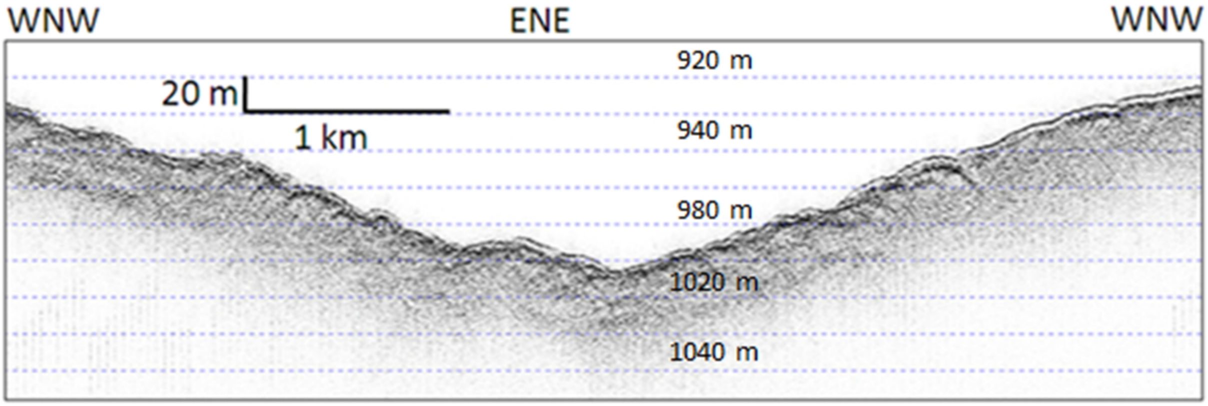


**(f)** 3.5 kHz profile 0006_2004_090 shows acoustic facies 3a in the upper slope of the Pandora Trough. The facies shows slightly overlapping small hyperbolae 2 - 10 m high and 20 - 40 m wide. This facies is interpreted as a small channel levee system on the slope. The v shape is due to the track-line trajectories.

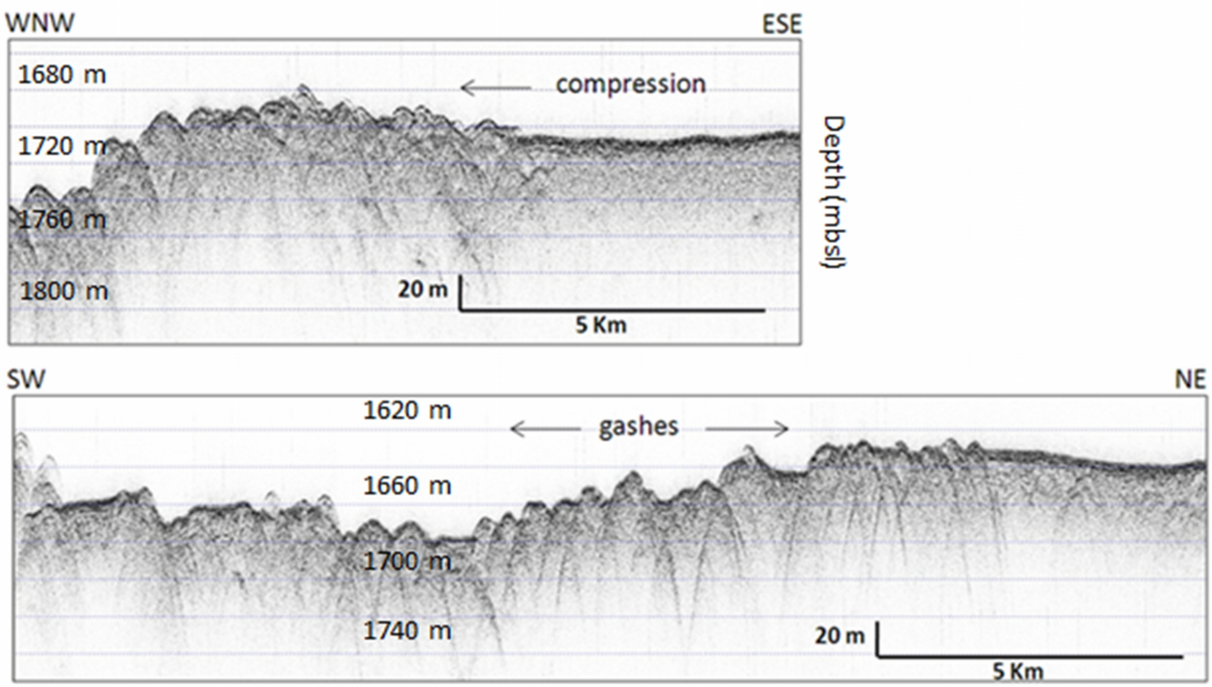


**(g)** 10. 3.5 kHz profile 0007_2004_091 (above) and 0004_2004_085 (below) **(h)** shows the typical character of acoustic facies 3b, which has an irregular surface and a highly prolonged echo with closed space overlapping hyperbolae. The dip direction on lineaments provides a clue to whether it is compressional **(g)** or extensional **(h)**.

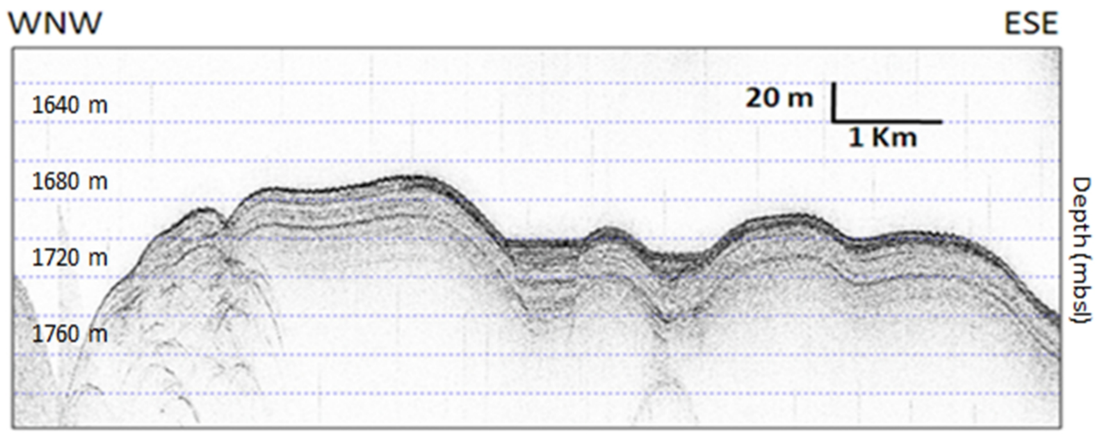


**(i)** 3.5 kHz profile 0004_2004_085 showing character of acoustic facies 3c with continuous parallel sub-bottom reflector with broad hyperbolae, interpreted as the remnant of the structural ridge. Between the mini-basins, a package of sediment is evident that resembles acoustic facies 2b

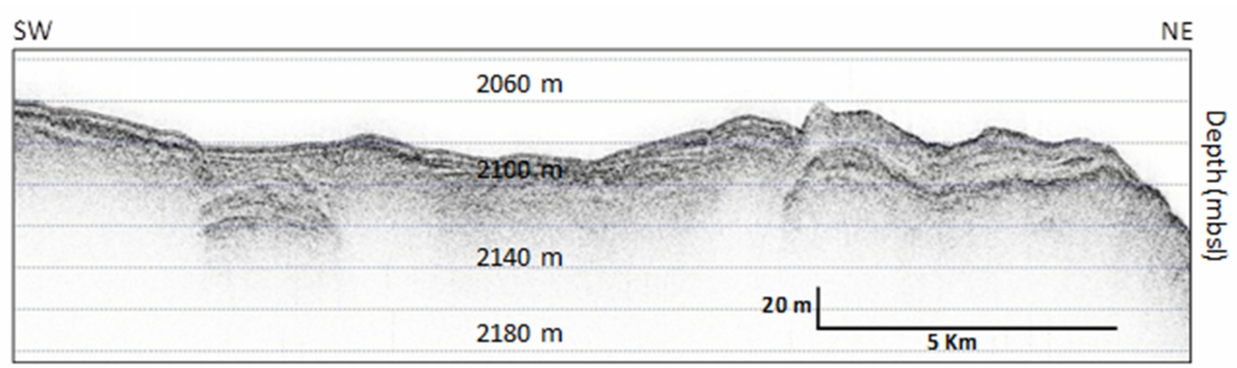


**(j)** 3.5 kHz section 0007_2004_080 shows strong seafloor echo with semi-continuous sub bottom reflector.

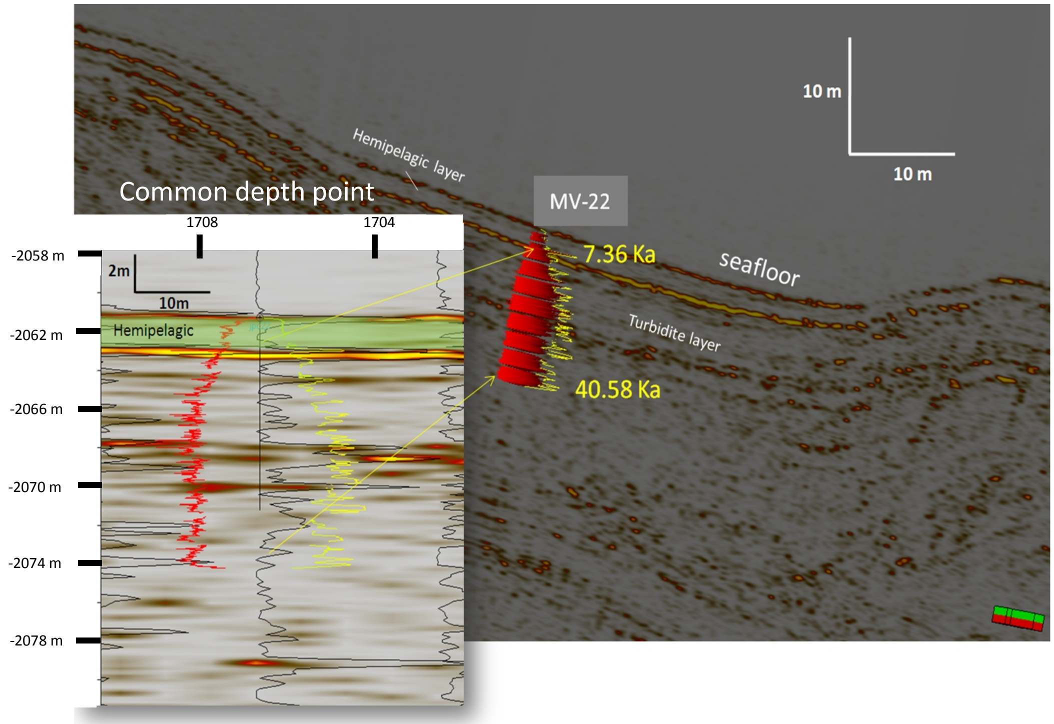


**(k)** The seismic-core tie between section 0007_2004_080 with core MV-22 density log, interpreted stratigraphy, and calibrated ages, showing good correlation between the density contrast creates by sand layering with the seismic reflectors (red curve = gamma-density, yellow curve = magnetic susceptibility index, black curve = seismic wiggle plot of 3.5 KHz sub-bottom profile).

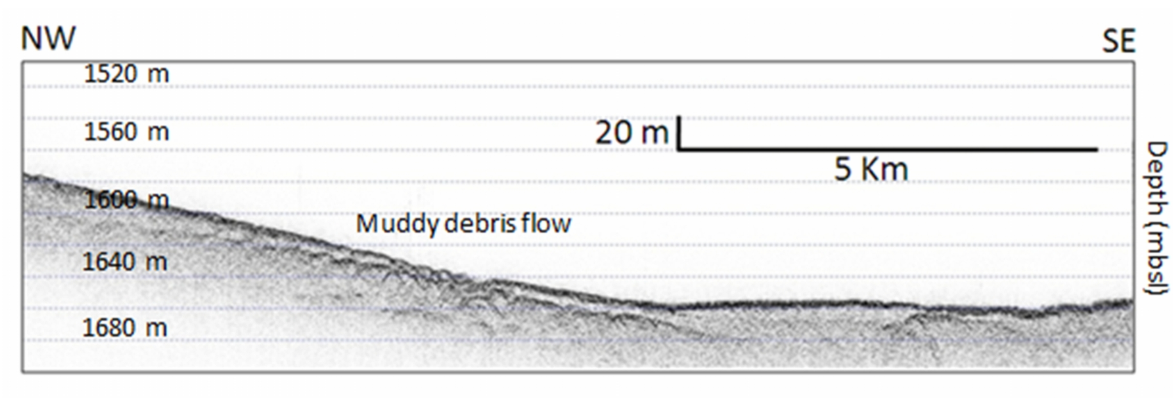


**(l)** 3.5 kHz section 0007_2004_091 showing the transparent lens shape in facies 3e is interpreted as slump deposit. The irregular surface with small hyperbolae toward NNE (upslope) is correlated with acoustic facies 3a, suggesting the process originated as one single large mass transported deposit with head detached and slumping downslope. The weak reflector in the base of the slump suggests the lack of density contrast between the slump body and the basin floor.

| No. | Facies code and accoustic description | Sediment characters in core | Interpretation |
|---|---|---|---|
| 1 | **Facies 1a** shows a non-stratified seafloor with very shallow sound penetration (<30 m) and medium to low prolonged echo (section 0007_2004_080, Figure 4a.). This characteristic was found only on the deeper basin floor or channel floor in the middle part of the study area in the Moresby Trough. | This acoustic facies was sampled by multicores MV24, 26, 28 and jumbo piston cores MV29. Multicore MV24 shows a vertical succession of hemipelagic mud and cross lamination fine grained sand that are partially crosscut by distinct horizontal and vertical burrows. MV26 (2232 mbsl) consists of a hemipelagic mud layer with mottled appearance overlying a layer of coarse and poorly sorted muddy lithic sand with oriented grains (This thesis, chapter 2). MV28 (45 cm in length) retrieved from 2426 mbsl, possibly only penetrates the surficial hemipelagic mud drape. It contains muddy beds with cross-stratified sand lamina. Core MV29 (6.41 m long, 2288 mbsl) contains a layer of hemipelagic mud overlying a series of 9 fine grained sand layers, 1.5-20 cm thickness, with the sand showing a tendency to thicken downward. | The sharp non prolonged sub-bottom echo exhibits no sound absorption and the surface acts as an acoustic isolator, thus, the affected area could be interpreted as prevailing coarse grained and high impedance lithology such as sand or silty sand (e.g. Pratson and Laine, 1989, Chough et al., 1997, Cronin et al., 2005). These observations are consistent with a hard, reflective seafloor covered with thick mud drapes. This accoustic facies is interpreted as channel floor in figure 3.5 |
| 2 | **Facies 1b** is non-stratified to semi-stratified seafloor with semi prolonged This facies has been observed particularly in the proximal and middle section of the Moresby Channel suggesting the deposition of coarse grained materials from gravity-induced flows followed by periods of hemipelagic accumulation from suspension to the present day. seafloor echo and a medium to deep sound penetration (60->100 meters), which is decreasing downward. This echo facies has been observed in axial and marginal regions of Moresby Channel mostly associated with convergent relief such as gentle bulges or saddle topography (Figure 4a.). | Not penetrated by core | Multibeam bathymetric data shows that this facies is mostly located in convergent relief such as gentle bulges or saddle topography where the bottom current processes creates more optimal erosional than the depositional processes.<br>The echo character suggests flat ground with medium to coarse grained materials overlain by thin muddy or fine grained deposits with presumably low to moderate depositional rates. The semi-stratified features suggest two possibilities: either (1) the extensive presence of sandy or silty turbidite layers (more sand abundance than in facies 1a) or (2) the bottom current has totally swept the recent seafloor mud and exposed an older and coarser layer to the seafloor surface. (Figure 4a. which shows this facies associated with facies 1a, 3d and 3e).<br>This facies is interpreted as levee deposit in figure 3.5. |
| 3 | **Facies 1c** shows a very prolonged bottom echo with no sub-bottom reflector, and an irregular seafloor surface. This character has a medium to deep sound penetration (40 - >100 m) and is found mostly within water depth of 1350 - 1780 m on the middle slope with an average slope gradient of 0.52°. The small hyperbolae observed are generally less than 20 m wide, but some exceed 50 m wide (Figure 4b.). | Not penetrated by core | This facies is interpreted to cover a total area of 780 $km^2$ most of which is included in the Pandora slope system (Figure 1b.). The small hyperbolae feature could be interpreted as small sutures within chaotic mass transport deposits (MTDs), implied by the rugged topography and relief. Section 0007_2004_080 (Figure 4b., see also Figure 4e.) shows that this facies is covered by sheet-like turbidite deposits (facies 2b) of the back levée depositional system in Moresby Channel. This facies interpreted as fine grained mass transport or debris flow or the buried MTD's surface (Fig 3.5.) |
| 4 | **Facies 2a** shows a distinct seafloor echo with a strong sub-bottom echo overlain by an acoustically transparent layer. It shows several weak to semi-continuous sub-bottom reflectors with a thickness of 2-5 m. The total transparent layer thickness is 40 m. This facies occurs mostly on the shelf edge of the northwest slope of the Pandora Trough and is more sparsely distributed on the Papuan Peninsula shelf edge (Figure 4c and 4d.). | Core MV-41, located in the shelf edge (92 mbsl) is consolidated mud, with little or no lamination, and intensive burrowing in the first 30 cm from the surface. Multi core MV19 (only penetrated 50 cm from seafloor) acquired from shelf break in the corner between Pandora-Moresby Troughs, with water depth of 229 mbsl, shows mottled silty mud layers mixed with fine to medium sand and no evident layering. Multi core MV-50 (only penetrated 50 cm below seafloor) from the upper slope (795 mbsl) shows finer sediments (silt to mud) with no distinct layering. Both MV19 and MV50 are intensely bioturbated (chapter 2 of this thesis). | The strong and very prolonged sub-bottom echo is interpreted as impedance-contrast boundary (possibly an erosional surface, coarse grained lag deposits or non-depositional horizon) overlying younger unconsolidated sediment. This suggests that in the past, this area has undergone a major erosional or weathering event: either subaqueous turbidity flows or debris flows, or subaerial exposure (this facies appears in some locations at water depths roughly coincident with sea level of the LGM in the region; Howell et al., 2014). This facies appears to cover the area of active sedimentation in the upper slope of the Pandora Trough (5,825 $km^2$). The echo-character of this facies gradually changes downslope to a more transparent surface layer with the virtual disappearance of the sub-bottom reflectors: this suggests more mud-dominated materials downslope. This facies is interpreted as shelfal deposit in Figure 3.5. |
| 5 | **Facies 2b** shows either flat or convex seafloor surface, with a strong continuous seafloor echo and a continuous sub-bottom reflector, which can be traced for tens of kilometers. It is also shows as patchy flat surface deposit with the distinct stratigraphic termination (e.g. onlap or downlap) which borders facies 3c (Figure 4e.). Sound penetration commonly exceeds 100 m. This facies is found in the transitional area between the Pandora and Moresby Troughs (near 2000 m depth), and in the toe of the Eastern Field Carbonate Platform (between the slope in Pandora and carbonate platform). | This unit is penetrated by cores MV-23, 25, 27, 33 and 66, all of which contain successions of turbidites, dominantly sandy with interbedded muds (Jorry et al., 2008; chapter 2 this thesis). | This unit is interpreted as continuous sheet-like turbidite deposits alternating with hemipelagic mud layers (Fig 3.5.). The echo-character, which was ground verified with core data, shows a disagreement with the previous references (e.g. Damuth and Hayes, 1977 and Chough et al., 1997), which associate this echo-character with mud dominated layered deposit intercalated with very thin sand layers. However, our ground truth indicates that sandy layers >40 cm thick are also common. |
| 6 | **Facies 3a** shows a moderate to strong single seafloor echo with a weak to medium prolonged sub bottom echo with overlapped hyperbolae (30 - 55 m wide). This unit lacks stratification and has sound penetration of 10 – 20 m. This unit is found mostly near moderate to steep walls or gullies (e.g. at coordinates 146.726E, 9.629S within Moresby Fan and at coordinates 146.249E, 10.030S in proximal area of Moresby canyon) (Figure 4f.). | | This unit is interpreted as high-impedance relatively undisturbed seabed. Several local small hyperbolae with v shape vertex below or above the average seafloor also exist in the area and can be interpreted as either channelized slope or developed levee in the slope system (Figure. 4f). In facies map (Fig 3.5.) this facies is interpreted as undisturbed seafloor (grey color). |
| 7 | **Facies 3b** is the most prominent facies of the Pandora slope. It shows a strong seafloor echo with a highly irregular surface, with non-stratified and highly prolonged sub bottom echo with closed space and intensely overlapping hyperbolae (17-25 m wide) (Figure. 4g and 4h). No cores are available to verify the lithology and sedimentary structure of this facies. | | The conical shape in the seafloor is 15-35 m high and resembles: an individual coherent block embedding in a MTD, or open crevasses. The chaotic internal echo characters reflect internal heterogeneities (Figure 4g. and 4h.). In plan-view, seabed bathymetry allows discrimination among these three types of features: parallel crescentic shape pointing downslope resemble pressure ridges (Figure. 4g.); parallel crescentic shapes pointing upslope could represent rotational blocks or just a random line such as in extensional gashes (Figure 4h.). The extensional gashes were dominant in the upper and middle slope where the slope is higher than $1.12^0$, whereas imbrications are prominent in the toe of the slope or the basin floor where the gradient is low/flat, or where the flow is blocked by the remnant of carbonate platform (see further discussion and Figure 8b.). This facies is interpreted as mass transported deposit (MTD) in figure-3.5. |
| 8 | **Facies 3c** shows a strong seafloor echo; continuous parallel sub-bottom reflector and broad overlapping hyperbolae (ranging between 300 - 800 m wide) (Figure 4i.). No cores are available to verify the lithology and sedimentary structure of this facies. | | This unit is found in the Pandora Trough and is observed as lineaments with a major orientation of SSW – NNE in the South western part of the Pandora Trough and SSE – NNW in the North eastern part of the Pandora Trough (Figure 1b. and Figure 4i.). The rugged relief with height of 50 - 150 m and strong echo reflectors suggests an erosional landscape with a hard seafloor surface. This leads us to an interpretation for this facies as outcropped structural ridges. The dredge sample acquired from the Eastern Field Platform (MV-36) confirmed this facies as the drowned Miocene carbonate platform (Tcherepanov et al., 2008), see Fig 3.5. |
| 9 | **Facies 3d** shows a strong seafloor echo, a continuous parallel sub-bottom reflector and slightly overlapping hyperbolae. This unit is found exclusively in the Moresby Trough near toe of the slope of the Papuan Peninsula. The sub-bottom reflectors are parallel and follow the undulatory pattern of the seafloor surface. The strike-parallel seismic section (0007_2004_080) shows narrow non uniform peak hyperbolae (35 - 60 m wide) and approximately 3 - 11 m high from the baseline (Figure 4j). | This acoustic facies is penetrated by core MV-22, which contains hemipelagic mud at the seabed, apparently related to the first break in the seismic data (Figure 4k.). Below hemipelagic mud, a muddy turbidite succession of nine sand layers (5-10 cm thick) is intercalated with very thin sand lenses. The core contains 4.2 % sand overall. | The narrow non-uniform peaked hyperbolae could be interpreted either as sediment wave features or ridge created by bottom current or gravity driven flow, respectively. The multibeam bathymetric data shows contour-parallel lineaments inside the large fan shaped features (see the details in further discussion). Thes features persist laterally tens of kilometers and geometrically resemble a large fan system. The system covers an area of 4,672 $km^2$ of area and volume of 50.5 $km^3$ by trapezoidal volume calculation, assuming a sediment thickness of 200 m (e.g. base of fan in -2085 mbsl from seismic profile 0007_2004_080) in the upper fan or proximal area, and 25 meters in the lower fan or in the distal area. This facies is interpreted as sediment wave in Fig. 3.5. |
| 10 | **Facies 3e** shows a transparent lens with convex up sediment geometry, an irregular base, a strong to moderate echo with shallow (less than 30 m) sound penetration (section 0007_2004_091, Figure 4l.). The lens shows downlap termination in the lower part of slope paired with the headwall scarp features in the upper slope. No cores are available to verify the lithology and sedimentary structure of this facies. | JPC MV54 (924 mbsl) in the Pandora Trough slope and MV-49 located in Moresby Trough slope (862 mbsl) contains muddy layers interbedded with three thin medium – fine grained sand layers on the upper part which are interpreted as thin sheet-flow deposits (overall core contains 4.7 % sand). | This unit is often found in a stacking arrangement (e.g. at coordinates 145.867E, 8.648S) and deposited in confined regions (e.g. at coordinates 145.899E, 8.841S and 145.716E, 8.743S). In the plan view the head-scarp is mostly associated with scalloped features (Francis et al., 2008) and occur in the shelf edge with water depth of 270 -1300 m. This acoustic facies unit was interpreted as a slump deposit with a distinct headwall scarp (Figure 4l.). This facies is interpreted as muddy slump produced from shelf deposit (Fig 3.5.). |

Table 3.2 Summary of acoustic facies description, sediment characters in core and interpretation

### 3.4.3 Seafloor Facies Distribution

The interpreted facies are plotted on the corresponding sub-bottom track-line, placed into geo-referenced spreadsheet entries, and extrapolated to create a map of the generalized facies distribution on the seafloor (Figure 3.5). The map shows that some of the facies distributions are strongly associated with specific ranges of water depth. Acoustic facies 2a occurs from the shelf-edge to 150-450 mbsl, and acoustic facies 1a and 1b occur in water depth >2000 m. Local relief is also associated with facies distribution; the slope of the Pandora Trough is characterized by acoustic facies 3b and 1c (interpreted as a series of mass transport deposits (MTDs), the latter considered to be the older and finer grained MTDs) then grades into facies 3e where the seafloor slope gradients become gentler. In the carbonate platform toe of slope, the flat seafloor surface is characterized by acoustic facies 2b which appears to conform to the Pandora depocentre of ponded turbidites.

Although some facies are associated with particular seabed sediment type and grain size (e.g. facies 1a and 1b) that might be directly controlled by depositional processes, the lithology of the seafloor is not always strongly correlated with a particular facies class. The Moresby Trough slope is characterized by acoustic facies 3d with the Northwest-Southeast orientation interpreted as the remnant of structural ridge. The remnants of high relief features with the same characteristics are also found in the seafloor adjacent to the Pandora Trough slope which is confirmed from the dredge core sample as the drowned Miocene carbonate with Southwest-Northeast orientation (Tcherepanov et al., 2008).

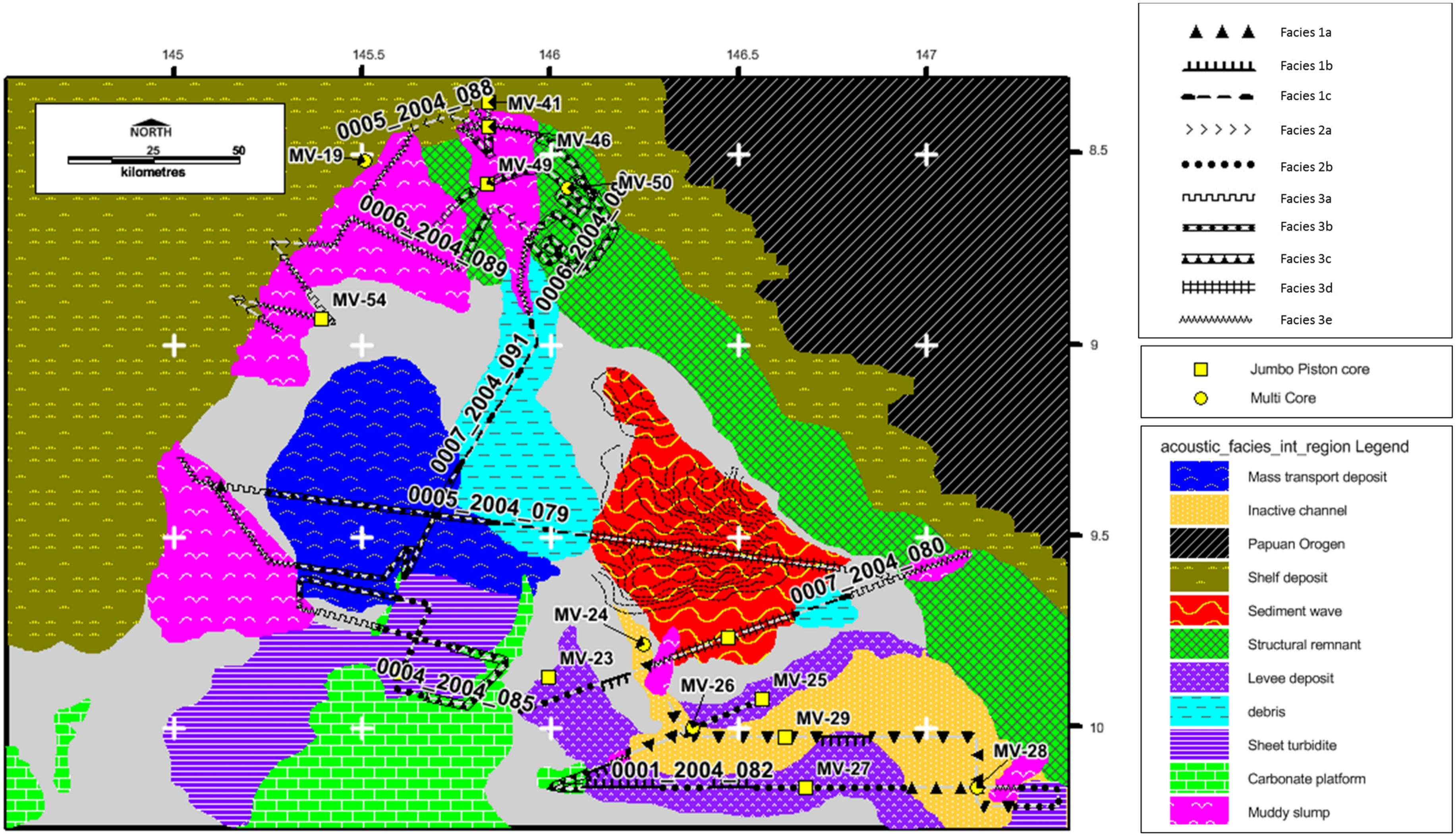


**Figure 3.5** Generalized facies map extrapolated from the 3.5 kHz sub-bottom profile character integrated with multibeam bathymetric and core data. Seismic lines and core locations are more clearly visible in Fig. 3.1. Facies numbers and descriptions are indicated in Table 2.

### 3.5. Discussion

### 3.5.1 Depositional Elements

Based on integrated acoustic facies mapping and core analysis, we can extend our understanding of seabed processes and products into the subsurface. There are five large seabed morphological elements we consider to be the most striking depositional features in the study area: mass transport deposits (MTDs) in the (1) Pandora Trough slope and (2) Moresby Channel, (3) sheet-like turbidites in the Northern Pandora Trough toe of slope, (4) sediment wave-like features in the Moresby Trough toe of slope, and (5) ponded turbidites in the Pandora basin/depocentre. The ponded turbidites have been evaluated in detail by Jorry et al. (2008), so we will focus on features 1-4.

### 3.5.2. Multi-flow MTDs in the Pandora Trough

The seafloor of the northwestern Pandora Trough is dominated by rough and uneven topography which is interpreted to be composed of MTDs of remarkable size. The MTD complex is 76 km wide in the widest part, with possible maximum thickness of 150 m from sub-bottom profiles (Figure 3.6 and 3.7). The multibeam bathymetric and 3.5 kHz sub-bottom data show that the MTD covers an area of ~5,006 km$^2$. A profile through the mass transport complex reveals an internal character showing a mixture of chaotic, irregular, and variable amplitudes from transparent to coherent sets of reflections (Figure 3.6). The MTD surface shows distinct multi orientation lineament features which vary in a range of: N 64$^0$ W in the western part into N 18$^0$ E and N 33$^0$ E on the eastern edges.

The interpretation of the suture orientation indicates that the mass transport complex was compartmentalized and formed by a series of events. There is evidence that there are several flow units comprising one mass transport complex. The lack of evidence of headwall scarp,

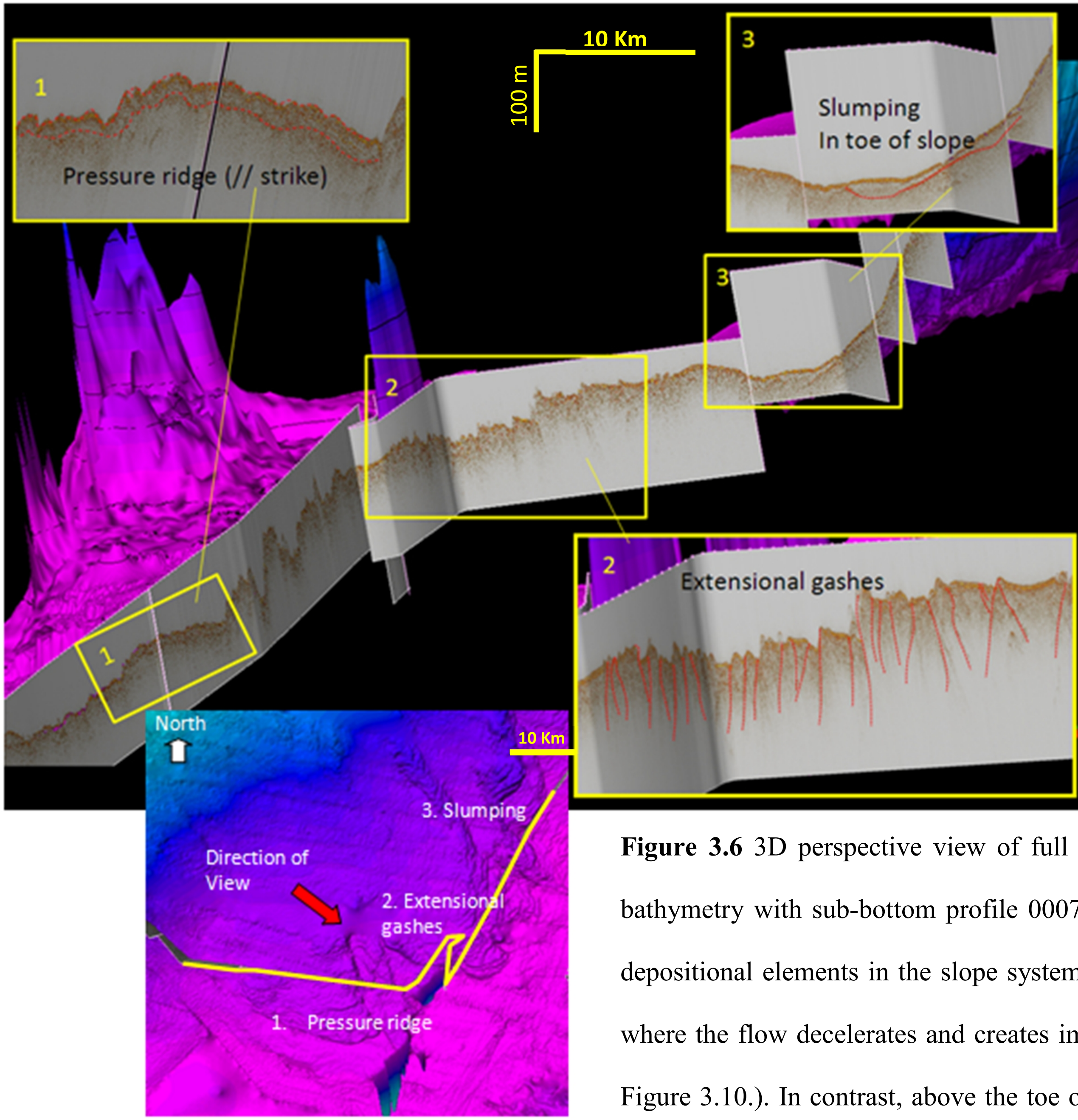


**Figure 3.6** 3D perspective view of full extent of the Pandora Trough slope, integrating bathymetry with sub-bottom profile 0007_2004_ 091 looking southwest, showing typical depositional elements in the slope system. A pressure ridge occurs in the toe of the slope where the flow decelerates and creates imbrication (shown parallel in this figure, see also Figure 3.10.). In contrast, above the toe of the slope the flow velocity accelerates creating an extensional gash pattern in middle part.

slump scars and run-out track also mean that Francis et al.'s (2008) hypothesis that the MTDs initiated from the scalloped morphology on the shelf edge can be dismissed; rather, we suggest that the MTDs flowed as a transient series, starting from surficial slumping in the upper slope, becoming perched on mid slope. Overburden that accumulated in the mid-slope added to the shear stress, which after reaching a critical point; triggered the slope failure consisting of muddy flows and rotational blocks. Assuming that the major flow direction was perpendicular to major axis of the pressure ridge, the slide is interpreted to flow from northwest to southeast direction with a total run-out distance of 17 - 30 km. During the event, a portion of the flow (759 $km^2$ area) detached and flowed southwestward. There is also evidence of flow acceleration by extensional gash or crease structure on the slope with major orientation $N10^0E$. The downslope run-out decelerated at the toe of the slope, creating an extensive pressure ridge with major orientation of $N70^0W$. Other smaller MTDs are also evident but their relationship to this larger event is not known.

### 3.5.3 Moresby Channel MTDs

In the corner between the Pandora Shelf and the Papuan Peninsula shelf, a large lens-shaped transparent unit is also observed and is interpreted as a large muddy debris flow with north-south flow direction (Figure. 3.4l.). Although the geometry is not clearly defined in bathymetric data, the maximum width of this deposit is inferred to span 12 km in the upper slope, tapering 7.5 km in the lower part, constrained on both sides by structural ridges. The total run-out of this deposit could reach more than 60 km. In contrast with irregular seabed of the Pandora slope MTD (Figures. 3.1b, 3.1d, 3.4g, 3.4h and 3.5) to the southwest, this MTD possess a smooth surface with an average thickness of 15 m. The sub-bottom profile 0007_2004_080

(Figure 3.4b, Figure. 3.4e and Figure 3.1a. for location) shows that this unit is overlain by the Moresby Channel levée deposit. This levee is dated >40 cal ka (core MV-22 in Fig. 3.3 and Chapter 2 of this study) and ceased rapid accumulation soon after 18 cal ka (core MV-23 in Fig. 3.3 and Chapter 2 of this study). Age of the superjacent levee deposits indicate that the debris flow was deposited >40 cal ka (Figs. 3.1b and 3.3).

### 3.5.4. Turbidites at the Toe of Slope in Pandora Trough

Sheet-like deposits are evident in 3.5 kHz sub-bottom profile 0007_2004_080 (Figure 3.1a). The centre of the depositional package is 20 – 30 m thick and 10 – 15 m thick at the edges. The internal character of the deposit shows a divergent character with several layers, each layer having a thickness of less than 1 m particularly in the upper part (verified by core data), but the sub-bottom profile shows the possibility that the layer not penetrated by core is thickening downward with thicknesses ranging from 1 - 5 m. The sub-bottom profile also shows that the deposit is 30 km long. For comparison, stratigraphy of core MV-23 (2068 mbsl) was projected 6 km to seismic section 0007_2004_080 (Fig. 3.1a). This core shows turbidite layering with layer thickness of 10-50 cm. The seismic section shows a wedge shape character with downlap event termination to the northeast, which might be correlated with massive sand layers (20-50 cm) with $T_a$-$T_c$ turbidite sequence character, near the core bottom (9.64-9.165 mbsf). This unit could be interpreted as the remnant of the older fan wedge originated from upslope deposited before MTD event. The geometry of the fan is inconclusive; however 2D profiles and bathymetry suggest flow to the southeast. Above this massive sand unit were deposited a series of thin to medium sheet shape turbidite sands (5-20 cm) with $T_b$-$T_e$ turbidite sequence, interlaminated with hemipelagic mud.

The last turbidite sequence found in the core MV-23 was a typical Bouma sequence $T_b$-$T_e$ with the wood fragments deposited in the boundary between $T_b$ and $T_c$, indicative of deposition from deceleration of the waning flow.

The turbidite sequence variation in core MV-23 is interpreted as the effect of the lateral facies change in the depositional system, as the levee slope moderated ongoing deposition, becoming gentler upward. The core age model presented in Chapter 2 of this study shows that this turbidite succession was deposited between MIS-3 (57-29 cal ka) and MIS-2 (29-14 cal ka). The oldest turbidite in the core dated from foraminifera is 43.180 $\pm$ 0.45 cal ka (10 mbsf) and the youngest turbidite date is 18.495 $\pm$ 0.18 cal ka (2.39 mbsf). These results show that sediment delivery through Moresby channel decreased then became dormant after that period due to the combination of the MTD blockage and shelf flooding.

### 3.5.5. General sediment delivery in Pandora Trough

Observations in the Pandora Trough slope show no indication of an active channel fan system in the modern seafloor, and $^{210}$Pb analysis also shows slow sedimentation accumulation rates (SAR) (Muhammad et al., 2008). Collectively, results show that the present seafloor is no longer receiving substantial terrigenous sediment supply.

Age models for cores MV23, MV33 and MV54 (Chapter 2 of this study) (Figures. 3.1a and 3.3) illustrate evolving sediment supply and accumulation over space and time. In core MV-23, the last/ youngest turbidite was deposited near 18.495 cal ka. Slightly closer to the GoP shelf, where the down-slope pathway is not blocked, in MV-33, the youngest turbidite dates to 11.83 cal ka (Jorry et al., 2008). On the middle GoP/Pandora Trough slope in MV 54, the youngest turbidite is younger than 15.850 cal ka (Febo et al., 2008). Therefore there is a time lag between direct shelf – slope sediment transfer in the Pandora Trough mini-basin (MV-33 core location) and the northern Pandora trough (MV-23 core location). It is also clear that the persistence of turbidite sedimentation in upslope portions of the basin in the northern Pandora Trough shows that delivery to lower portions of the basin must have been blocked after the MTD event.

The last turbidite deposited in MV-23 is immediately superjacent to the uppermost $^{14}C$ dates in this core (19.5-18.5 cal ka), and constrains the youngest age of the large MTD event in the Pandora slope to the LGM or just afterward, which is the time frame for the last substantial terrigenous sediment supply to this basin. During MIS-3, sea level dropped 60-80 m below present sea level, reaching 100-120 mbsl at the LGM (23-19 cal ka), in MIS-2. During that period, the shelf was exposed and was possibly incised by fluvial systems that extended to near the shelf edge. This enabled nearly direct delivery of terrigenous sediment to the adjacent canyon head, thus feeding the deepwater basin through the channel system. However the sea level fall combined with rapid sedimentation loading also helped trigger the mass transport event in the Pandora Trough (e.g. Lee et al., 2002). This MTD creates rugged seafloor likely responsible for blocking further downslope sediment delivery in the Northern Pandora Trough (i.e., near MV-23) (Figure 3.7).

To the west and southwest, sediment-delivery pathways from the shelf to basin remained active longer, to near the start of Holocene time. The end of substantial and direct shelf – slope – basin floor sediment delivery to the MV-33 location is approximately the age of the youngest turbidite in this core, which is ca. 12 cal ka (Jorry et al., 2008). Within this period the upper slope area (e.g. core MV-54 and farther east; Febo et al., 2008; Howell et al., 2014) also received sediment from the shelf (Figure 3.7).

### 3.5.6. Moresby Channel

This is a large axial channel system flowing in an almost east-west direction, then deflected northwest-southeast down-gradient. This channel is possibly a down-gradient continuation from the channel systems in the Pandora Trough, which is interpreted to be partially buried underneath the MTD on the North Pandora slope. Before MTD emplacement, this channel network possibly delivered gravity-driven sediment flows from the Papuan mainland into the Pandora Trough, the Moresby Trough, and also further down-flow into the Coral Sea basin.

This channel system flows down as far as 287 km into the lower reach of the Moresby Trough and transitions to the Coral Sea Basin, where relief decreases. There are two jumbo piston cores (JPC) penetrating this channel floor (MV-25 and 29); they generally consist of thin muddy turbidite layers (Figure 3.8) suggesting fine grained sediment delivery by turbiditic current in the past. Core MV-25 is in the flank of the channel and interpreted to be a levee facies.

The age model for MV-29 (Figure 3.3)(Chapter 2 of this study) suggests very slow sediment accumulation, and/or bypass. Although we do not have an exact date of the youngest turbidite deposited in this core, age and stratigraphy from up-gradient levee core MV-23 and very low $^{210}$Pb sediment accumulation rates from multi-core MV28 (Muhammad et al., 2008), suggest that this submarine channel was no longer active after the LGM (23-19 cal ka) and the hemipelagic accumulation may be reduced by bottom currents (Figure 3.7).

The sediment character from core shows that the turbidite could reach as far as 30 Km from active channel axis (e.g. perpendicular distance between Moresby channel axis with MV-23) and could reach as high as 230 metres (vertical offset between MV-25 and MV-29).

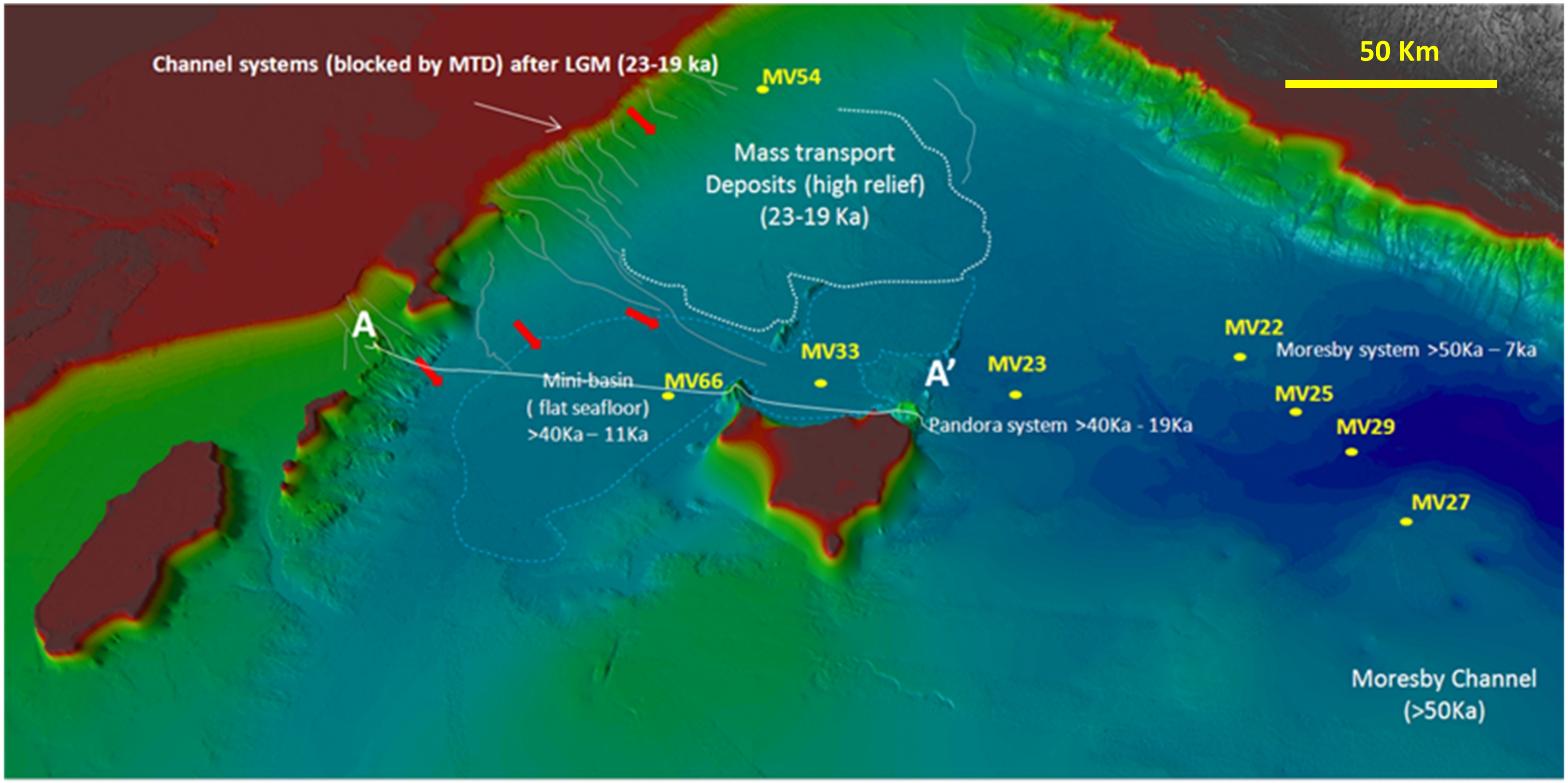


Seismic courtesy of Fugro and Total EP (Fugro)

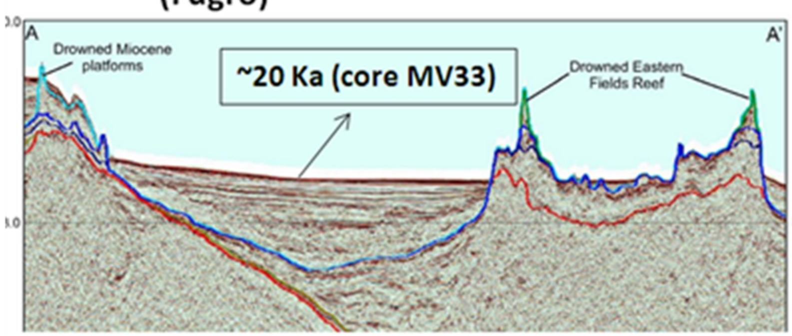


**Figure 3.7** 3D perspective view toward N-NE shows the relationships between Pandora mini-basins and North Pandora Trough, where the MTD blocked the sediment transport via slope channel (unpublished seismic data from Andre Droxler, Rice University, courtesy of Fugro).

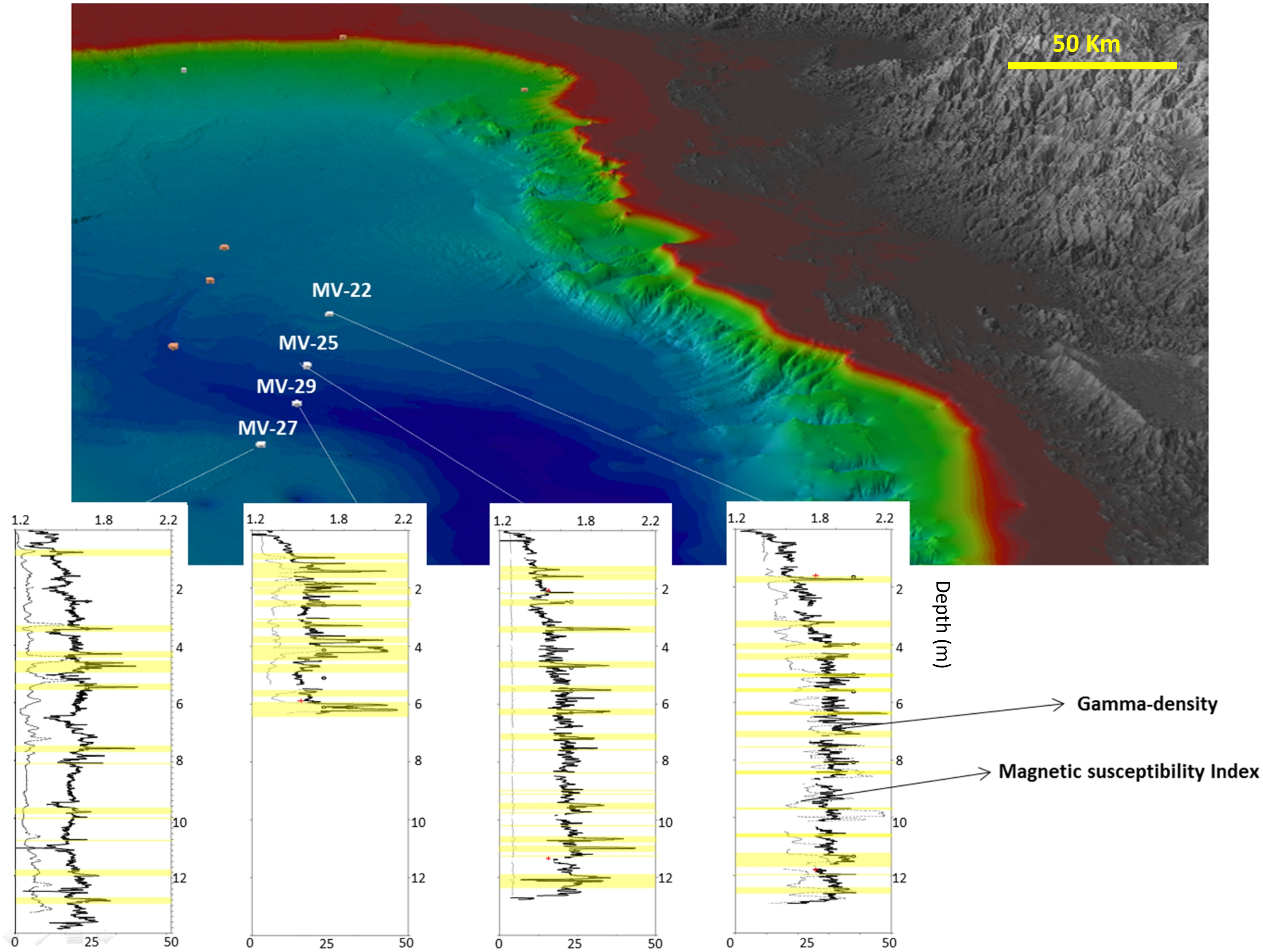


**Figure 3.8** 3D perspective view of Moresby Channel from south-southeast, showing gamma density logs (upper axis, grr/cc) and magnetic susceptibility index (MSI) (lower axis, MI) of cores MV-27, MV-29, MV-25 and MV-22 (Chapter 2 of this study). Sandy turbidites are highlighted in yellow on core logs. Although core MV-27 is located 200 m high above and >20 kilometers away from the channel floor, turbidite sands of likely Moresby Channel origin are found in the core. The age model from core MV-27 shows the sedimentation began as early as 160 Ka. The main channel seafloor is characterized by acoustic facies 1a and 1b; core MV-29 shows a turbidite sequence draped by hemipelagic mud, suggesting cessation of turbidity currents after the LGM (23-19 Ka).

### 3.5.7. Large Sediment Waves: Moresby Fan

We use the name "Moresby Fan" for the mound-shaped deposit spread laterally along the toe of slope of Papuan Peninsula (Figures 3.1b, 3.9a, and 3.9b). This fan is located adjacent to the upper section of the Moresby channel. The fan covers 2,685 $km^2$. A series of wave-like sediment features are evident on the surface of the fan, with crest orientations from north northwest – south southeast on the upper part, turning east-west in the distal area. The total inclination from toe of slope to seafloor is 0.8° (13.4m/ Km) over a distance up to 42 km, with wave crests generally perpendicular to the fan length (Figures.3. 9a).

Internal wave-like cross-strata are shown in seismic sections 0004_080 and 0004_079 (Figure. 3.9a) both acoustic facies 3d. Wave dimensions generally increase from proximal to near the distal extent, and then diminish rapidly. Proximal height and length are 10-15 m and 500 - 700 m respectively, increasing to 35 - 60 m height and wavelength of 1.2 – 2.6 km distally. Sub-bottom profile data show a consistent pattern of stoss and lee slope on sediment waves, with an average stoss side angle of 6 - 6.8° degree and lee side angle of 1 - 1.8° degree. Although we have no data regarding physical transport processes, the seismic section (Figure 3.9a.) clearly shows an aggradation pattern suggesting upslope migration of the sediment waves. In general these waves occur on seafloor slopes higher than 0.5 - 0.6° (8.7-10.4 m/Km) (Figure 3.9a.).

The core stratigraphy mostly shows a series of thin fine grained sand-silt and mud layer (5 - 10cm) with Tb-Td sequence, and thin silty-sandy lenses (0.5 – 1 cm) interbedded on hemipelagic mud (this thesis chapter 2) (Figure 3.3.). The gamma-density profile shows a saw-tooth character with serrated features produced by alternating coarse and fine layers (Figure 3.3). These observations suggest that this core is within the distal region of the large submarine fan.

Interpreted 3.5 kHz sub-bottom profiles establish some of the regional stratigraphic units (Figures 3.4k. and 3.8). In Figure 3.9a, the purple indicates the youngest unit, dated to 7.36 cal ka (Figure 3.3), at the top of the youngest turbidite sand in the core. The oldest date in MV-22 is 40.58 cal ka which corresponds to the green horizon (Figure 3.4k and 3.a). This evidence suggests that the process of sediment wave construction probably started at or before MIS-3.

The 3D geomorphology (Figure. 3.9b) also shows a local tectonic control on the sedimentation processes. Large mounded features are evident at the mouth of the canyon feeding the fan. Relief suggests that the sedimentation pathway via the canyon was periodically plugged and avulsed anti-clockwise by syn-depositional right-lateral faulting. This fault uplifts the seafloor as high as 165 meters. If we presume the sedimentation is started at MIS-3 (ca. 57 cal ka); the tectonic uplift rate averaged to ~ 0.3 cm/y.

Francis et al. (2008) suggested that this feature is a confined fan-shaped MTD which is transported via a major canyon. Section 0007_2004_080 illustrates the geometrical properties of this sediment wave and includes the evidence from core data (MV-22) which has never been incorporated before. We have identified internal geometries that are too regular to favor an interpretation of MTD emplacement, at least for the uppermost 30-40 m of sediment. We also observed that the sediment transfer and deposition of this fan is strongly confined and controlled by the large canyon system (2.5-8 Km width and 300-700 m deep).

Many previous studies define sediment waves in the deep-sea environment as linked to cross-flow over levee in the adjacent of the active channel system (e.g. turbidite induced sediment wave) (Damuth, 1979, Normark, 1980; Carter et al., 1990; Savoye et al., 1993; Nakajima et al., 1998; Migeon et al., 2000; Wynn et al., 2000; Normark et al., 2002; Migeon et al., 2004) or bottom current related sediment wave migration (Lee, et al., 2002; Masson et al., 2002, Oiwane et al., 2015). Compared to both type of sediment wave characteristics based on references, the features in the Moresby Fan is unique, and probably are formed due to the combination of both processes. These are observation from our study area:

1. The turbiditic induced sediment wave is generally formed in the side levee of the channel systems, whereas in this area no such levee system is identified. The large Moresby Canyon system is not in the close proximity with this feature. It is likely that the sediment wave is formed in the terminal fan.
2. The wave geometry in turbiditic induced sediment wave usually has shown an overall basin-ward decrease in wave dimensions (Wynn and Stow, 2002). This is observed in the present study, suggesting the up-slope migration of the sediment wave.

Two possible explanations for the creation of this unusual sediment wave feature are likely:

(1) The feature is a series of large bedforms produced by turbidity currents. The flow creates a deformation front when the velocity suddenly decreases upon arrival in the seafloor, and due to the repeated flow deposition via the channel, those deposits become amalgamated as a stacked complex (e.g. Bouma and Treadwell, 1975, Normark, 1980, Carter et al., 1990, Jacobi and Hayes, 1992 and Migeon et al., 2000).

(2) The feature has inherited morphology which is dominated by pre-existing undulating topography that results from older (MIS-3 or earlier) MTD emplacement on the basin floor. The morphology of the pressure ridge at the leading edge of the MTD created undulatory surfaces that promoted the deposition and ponding of the turbidite sediments. Large scalloped features (16.8 km in diameter) on the shelf edge at 22.5 km up-slope from the Moresby fan have been observed and could be presumed to be the sources of the failure body.

Unlike deeper core locations along the channel axis in Moresby Trough to the southeast (MV-25, 27, and 29), the MV-22 age model and stratigraphy shows turbidite deposition on Moresby Fan continued until 7.4 cal ka., well after most of the shelf was flooded, and when sea level had approached present elevation (Waelbroeck et al., 2002). Two possible factors could favor this scenario: (1) The shelf- slope setting, where the shelf of the Papuan Peninsula is relatively narrow (30-40 km) and steep, creating a short and steep cross-shelf path for sediment delivery to canyon heads from fluvial sources (as documented on the modern California Shelf, by Puig et al., 2003); and (2) shelf current systems along or oblique to shelf isobaths that are more effective than trapping mechanisms, allowing along-shelf to slope transport over substantial distances (Normark, 1978; Flood et al, 1991; Posamentier and Kolla, 2003; Covault et al, 2007, Covault et al., 2011). In our case, terrigenous materials from the Papuan mainland could flow into canyon head and then deeper depocentres in the Moresby Trough. Similar oblique shelf-to-slope transport and slope accumulation was documented by Howell et al. (2014), at the shelf-edge apex and upper slope location of cores MV-41, MV-46 and MV-49, respectively (Figure 3.5), that is likely driven by oceanic processes on the shelf. This highstand off-shelf transport appears to be highly localized, however, because cores analyzed from other locations on the adjacent middle to upper slope (MV-54 southwest of MV-46 and MV-49, and MV-51; between the location of MV-46 and MV-22) document sediment-starved conditions for the late Holocene (Febo et al., 2008) (Figure 3.5). The Moresby Fan appears to be effective at capturing most of the sediment delivered from upslope locations, however, no substantial Holocene sediment accumulation is observed at downslope locations near cores MV-25 and MV-29.

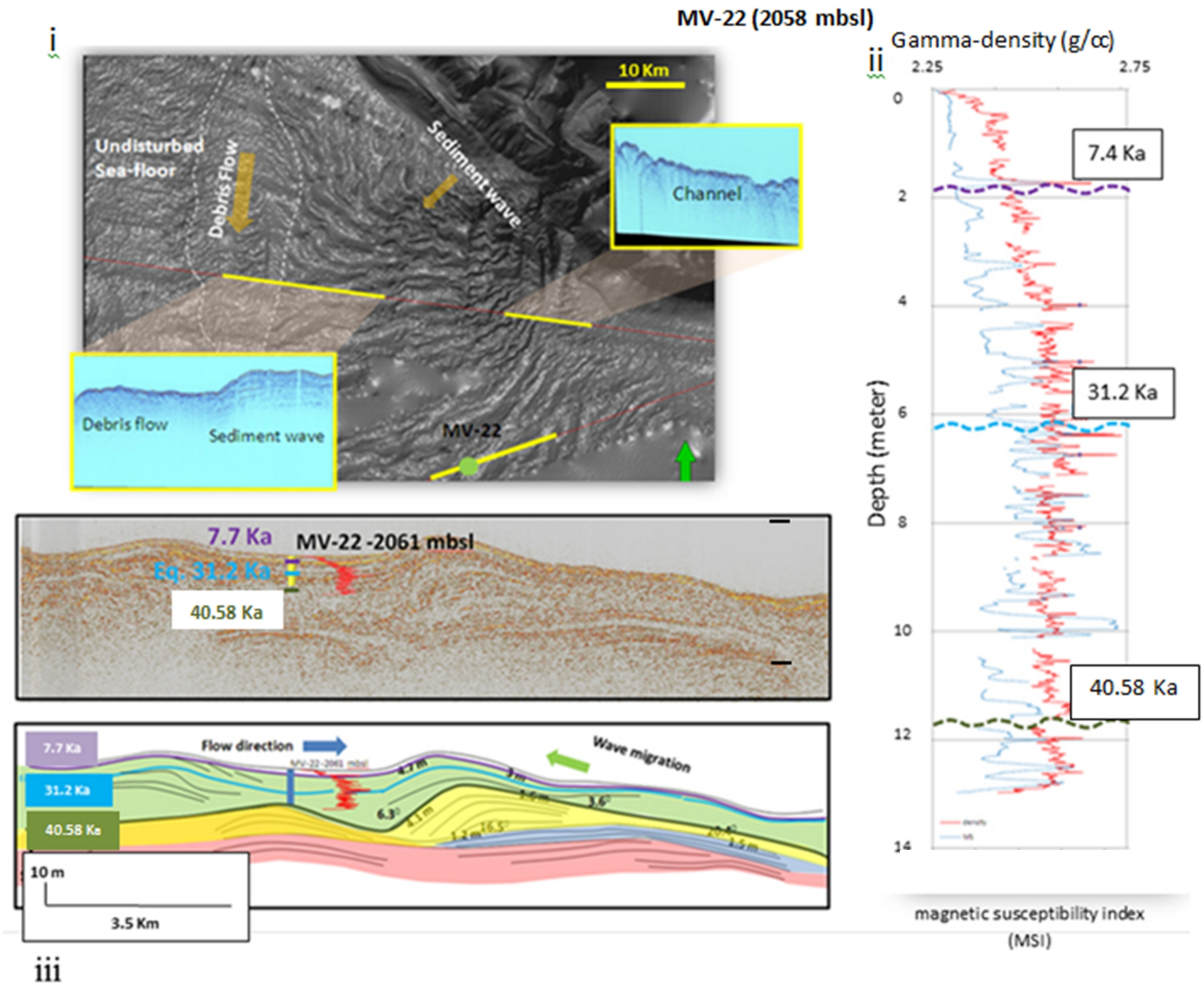


**Figure 3.9 (a)** (i) vertically exaggerated (1:10) seafloor bathymetry showing differences among undisturbed seafloor, debris flow, and sediment waves in Moresby Trough; the arrow shows interpreted flow direction toward southwest; (ii) Core MV-22 (log of density: top axis, g/cc, red profile; log of magnetic susceptibility: bottom axis, blue profile, SI units), located in the outer part of the Moresby Fan, has oldest turbidites dated to near 35.84 cal ka (late MIS-3) and youngest turbidite dated to 7.4 cal ka (Chapter 2, this study); (iii) sub-bottom profile 0007_2004_080 (above) and interpretation (below) showing a character of the sediment wave interpreted to be formed in multiple phases during MIS-3-MIS-2, with superimposed core location, depth, and schematic density log (red).

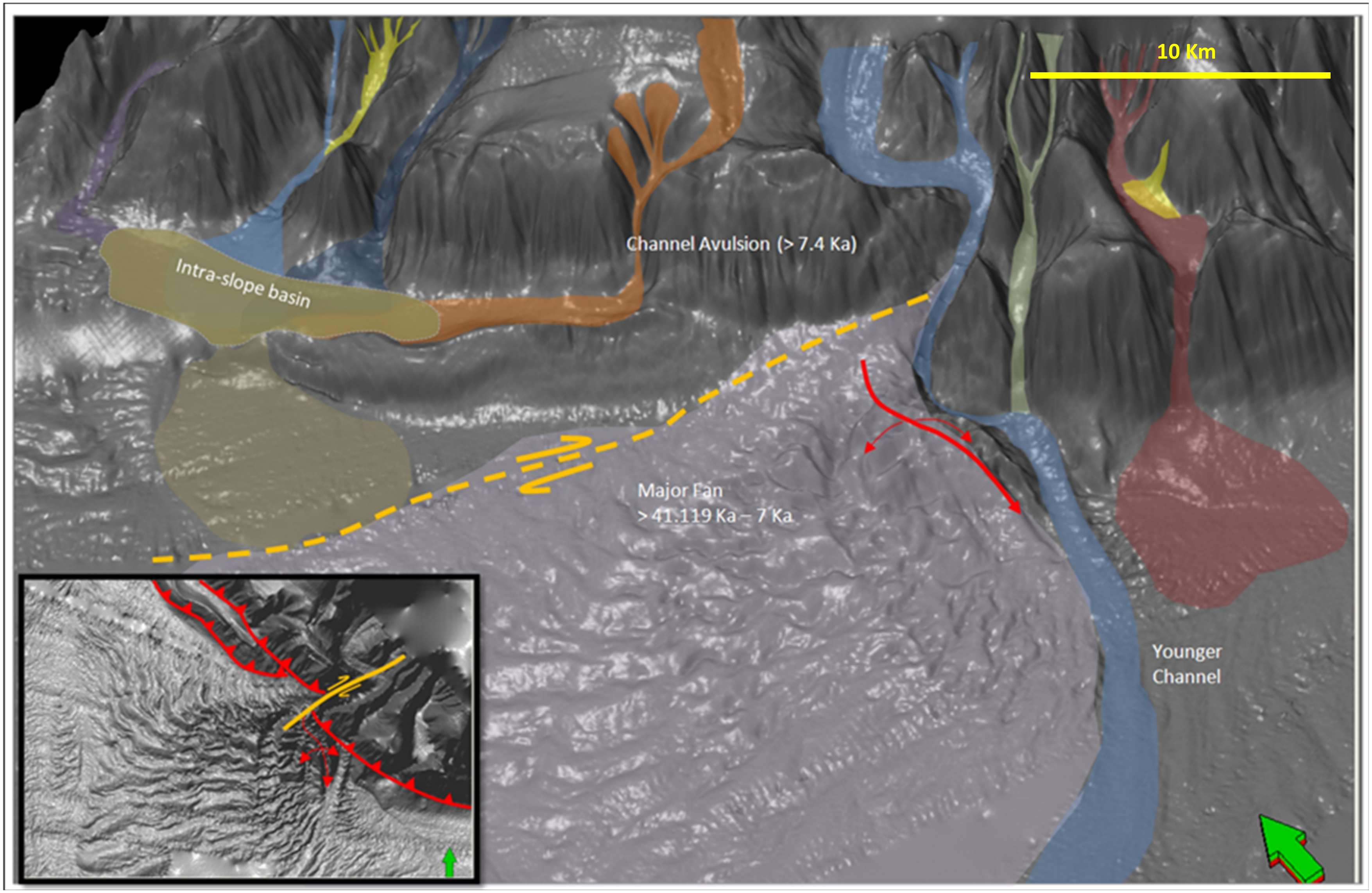


**Figure 3.9 (b)** 3D view of Moresby Trough looking toward East-Northeast the Moresby Fan complex (vertical exaggeration of 5x); the major was constructed during MIS-3 (near 41.119 cal ka) and continued to build until MIS-1 (7.4 cal ka). The fan then became dormant due to eastward channel avulsion caused by right lateral fault which scraped floor material as high as 165 m, creating a deflection and depositional of younger channel afterward.

### 3.6. Conclusion

In this chapter, acoustic properties of sub-bottom profiles and geological properties of sediment cores have been used to define acoustic facies that in turn characterize large-scale depositional elements of the Pandora and Moresby troughs. However, there are many uncertainties associated with interpretation due to the limitations of the data such as: limit of core depth of penetration, the sparse space of the sub-bottom profile with the possibility of interpretation pitfalls from seismic resolution, projection, and side-sweep effect from the neighbouring high relief features.

Distribution and cross-cutting relations of facies have been placed in a chronostratigraphic framework using the previously determined $^{14}C$ age models of Chapter 2 in this study, demonstrating that, within the temporal limits of the age models, the peak depositional period in Pandora Trough occurred during MIS-2. At that time, a large deep-sea channel network apparently linked the Pandora and Moresby troughs, allowing long-distance transport of terrigenous sediments by large turbidity currents from the Papuan mainland, through Moresby Trough and Channel, to the Coral Sea basin. The turbidite cloud reached at least 30 km laterally (evidence from levee core MV-23) and 200 m vertically (overbank deposits in MV25, MV27 and MV29).

Near the LGM, shelf-edge failure led to emplacement of MTDs on the floor of the Pandora Trough, blocking intermediate reaches of this channel network, ending flow of large turbidity currents from the Pandora Trough to the Moresby trough. Intermittent turbidity currents continued to feed minibasins upslope of the MTD complex (MV-33) until early MIS-1 (earliest Holocene).

Along the shelf edge of the Papuan Peninsula, substantial sediment delivery by turbidity currents continued until at least 7.4 cal ka (MV-22) and possibly the present, contributing to the formation of large sediment waves of Moresby Fan. However, this Holocene turbidite sedimentation does not extend much farther into the Moresby Trough, based on negligible Holocene sediment accumulation deeper in the basin.

This study, combined with the observations of Febo et al. (2008), Jorry et al. (2008), and Howell et al. (2014), has shown that sediment delivery from fluvial sources to deep basins in the GoP is controlled by a complex interplay of changing sea level, evolving basin bathymetry (influenced by depositional and tectonic processes), and oceanic transport of sediment from shelf to slope. These conditions have created highly localized conduits for shelf to slope sediment delivery that respond both to global forcing (eustatic sea level) as well as local conditions (shelf gradient, mass wasting, currents, and source proximity), resulting in a complex network of deep-sea depositional morphologies active from the LGM to later Holocene time.

## 3.7. References


Bouma, A.H. and Treadwell. T.K., 1975, Deep-sea dune like features: Marine Geology, v.19,p.M53-M59

Carter, L., Carter, R.M., Nelson, C.S., Fulthorpe, C.S., And Neil, H.L., 1990, Evolution of Pliocene to recent abyssal sediment waves on Bounty Channel levees, New Zealand: Marine Geology, v. 95, p. 97–109.

Chough, S.K., Hwang, I.G., 1997, The Duksung fan delta, SE Korea, growth of delta lobes on a Gilbert-type top-set in response to relative sea-level rise. J. Sediment. Res. 67, 725-739

Covault, J.A., et al., 2007. Highstand fans of the California Borderland: The overlooked deep-water depositional system: Geology, 35, 783-786.

Covault, J.A., et al., 2011. Terrestrial source to deep-sea sink sediment budgets at high and low sea levels: Insights from tectonically active Southern California, Geology, 619-622, doi:10.1130/G31801.1

Cronin, B.T., Akhmetzhanov, A.M., Mazzini, A., Akhmanov, G., Ivanov, M., Kenyon, N.H., and TTR-10 Shipboard scientist, 2005, Morphology, evolution and fill: Implication for sand and mud distribution in filling deep-water canyons and slope channel complexes: Sedimentary Geology, v.179, p. 71-97

Damuth, J.E. and Hayes, D.E., 1977, Echo character of the East Brazillian continental margin and its relationship to sedimentary processes. Marine Geology, v. 24, p. 73-95

Damuth, J.E., 1979, Migrating sediment waves created by turbidity currents in the northern South China Basin: Geology, v. 7, p. 520–523.

Daniell, J. J., 2008, Development of a bathymetric grid for the Gulf of Papua and adjacent areas: A note describing its development, J. Geophys. Res., 11 3, F01S15, doi:10.1029/2006JF000673.

Dickens, A.F., 2006, Solid state C-13 NMR analysis of size and density fractions of marine sediments; insight into organic carbon sources and preservation mechanism. Geochim. Cosmochim, Acta 70: 666-686

Febo, L. A., S. J. Bentley, J. H. Wrenn, A. W. Droxler, G. R. Dickens, L. C. Peterson, and B. N. Opdyke, 2008, Late Pleistocene and Holocene sedimentation, organic carbon delivery, and paleoclimatic inferences on the continental slope of the northern Pandora Trough, Gulf of Papua, J. Geophys. Res., doi:10.1029/2006JF000677

Flood, R. D., Manley, P. L., Kowsmann, R. O., Appi, C. J., & Pirmez, C. (1991). Seismic facies and late Quaternary growth of Amazon submarine fan. In Seismic facies and sedimentary processes of submarine fans and turbidite systems (pp. 415-433). Springer New York.

Francis, J. M., Daniell, J.J., Droxler, A.W., Dickens, G.R., Bentley, S.J., Peterson, L.C., Opdyke, B.N., and L. Beaufort., 2008, "Deep water geomorphology of the mixed siliciclastic-carbonate system, Gulf of Papua," *Journal of Geophysical Research (Earth Surface)*, v.113.

Gee, M.J.R, Masson, D.G., Watts, A.B., Allen, P.A., 1999. The Saharan debris flow: an insight into the mechanics of long run-out submarine debris flows. Sedimentology 46, 317-335.

Gardner, J.S.,1970, Geomorphic significance of avalanches in the Lake Louise area, Alberta, Canada, Arctic and Alpine Research, 2, No. 2: 135-144.

Howell, AL., Bentley, S.J., Xu, K, Ferrell, R.E., Muhammad, Z, and Septama, E, 2014, A clay mineral provenance study of the Northern Pandora Trough Continental Margin, Papua New Guinea. Submitted July 2013, Marine Geology.

Jacobi, R.D. and Hayes, D.E, 1992, Northwest African Continental rise: effects of near bottom processes inferred from high resolution seismic data. In Poag CW, de Graciansky PC (eds) Geologic evolution of Atlantic continental rises. Van Nostrad Reinhold, pp 293-325.

Jorry, S.J., Droxler, A.W., Mallorino, G., Dickens, G.R., Bentley, S.J., Peterson, L.C., and B.N. Opdyke, 2008, "Bundled turbidite deposition in the central Pandora Trough (Gulf of Papua) since Last Glacial Maximum: Linking sediment nature and accumulation to sea-level fluctuations at millennial time scales," *Journal of Geophysical Research (Earth Surface)*, v.113, doi:10.1029/2006JF000649

Lee, H.J., Syvitsky, P.M., Parker, G., Orange, D., Locat, J., Hutton, E.W.H., Imran, J., 2002, Distinguishing sediment waves from slope failure deposits: field examples, including the Humboldt Slide, and modelling results Marine Geology 192, 79-104.

Masson, D.G., Howe, J.A., Stoker, M.S., 2002, Bottom current sediment waves, sediment drifts and contourites in the northern Rockall Trough, Marine geology 192, 215-237

Migeon, S. Savoye, B., and Faugeres, J.C., 2000, Quaternary development of migrating sediment waves in the Var deep-sea fan: distribution, growth pattern and implication for levee evolution: Sedimentary Geology, v. 133, p. 265–293.

Migeon, S., Savoye, B., Babonneau, N., Lucy Spy Andersson, F., 2004, Processes of sediment wave construction along the present zaire deep-sea meandering channel: role of meanders and flow stripping

Milliman, J. D. 1995, Sediment discharge to the ocean from small mountainous rivers: The New Guinea example, Geo Mar. Lett., 15(3– 4), 127–133.

Muhammad, Z., S. J. Bentley, L. A. Febo, A. W. Droxler, G. R. Dickens, L. C. Peterson, and B. N. Opdyke, 2008, Excess 210Pb inventories and fluxes along the continental slope and basin of the Gulf of Papua, J. Geophys. Res., doi:10.1029/2006JF000676

Nakajima, T., Satoh, M., And Okamura, Y., 1998, Channel–levee complexes, terminal deep sea fan and sediment wave associated with the Toyama Deep-Sea Channel system in the Japan Sea: Marine Geology, v. 149, p. 25–41.

Normark, W. R. (1978). Fan valleys, channels, and depositional lobes on modern submarine fans: characters for recognition of sandy turbidite environments. AAPG Bulletin, 62(6), 912-931.

Normark, W.R , 1980, Modern and ancient submarine fans: reply, American Association of Petroleum Geology Bulletin, 64, 1108-1112

Normark, W.R., Piper, D.J.W., Posamentier, H., Pirmez, C., AND Migeon, S., 2002, Variabilityin form and growth of sediment waves on turbidite channel levees: Marine Geology, v. 192,p. 23–58.

NSF-MARGINS, 2004, National Science Foundation MARGINS Program Science Plan 2004. , pp. 170, Lamont-Doherty Earth Obs., Columbia Univ., Ithaca, N. Y. http://www.nsf-margins.org/Publications/SciencePlans/MARGINS_SciencePlans2004.pdf, accessed 10/04,2014.

Oiwane, H., Ikehara, M., Suganuma, Y., Miura, H., Nakamura, Y., Sato, T., Nogi, Y., Yamane, M., Yokoyama,Y., 2015, Sediment waves on the Conrad Rise, Southern Indian Ocean, implications for the migration history of the Antartic circumpolar current, Marine Geology 348, 27-36

Patterson, L. J., 2006, Petrological and geochemical investigations of deep sea turbidite sands in the Pandora and Moresby Troughs: Source to sink Papua New Guinea focus area, M. S. thesis, Louisiana State University.

Pigram C. J., and Pangabean H., 1984, Rifting of the Northern margin of the Australian continent and the origin of some micro-continents in Eastern Indonesia, Tectonophysics, 107, 331-353.

Pigram C. J., and Symonds, 1991, A review of the timing of msjor tectonic events in the New Guinea orogen; Journal of the South East Asian Earth Science, v.6 p307-318, doi: 10.1016/0743-9547(91)90076-A.

Pigram C. J., and Davies, H. L., 1987, Terranes and the accretion history of the New Guinea Orogen: Bureau of Mineral Resources Journal of Australian Geology and Geophysics , v.10 p193-212

Pigram, C. J., P. J. Davies, D. A. Feary, and P. A. Symonds, 1989, Tectonic controls on carbonate platform evolution in southern Papua New Guinea: Passive margin to foreland basin, Geology, 17, 199– 202.

Posamentier, H.W., and V. Kolla, 2003. Seismic geomorphology and stratigraphy of depositional elements in deep-water settings: Journal of Sedimentary Research, 73, 367–388.

Puig, P., Ogston, A. S., Mullenbach, B. L., Nittrouer, C. A., & Sternberg, R. W., 2003. Shelf-to-canyon sediment-transport processes on the Eel continental margin (northern California). Marine Geology, 193(1), 129-149.

Savoye, B., Piper, D.J.W., AND Droz, L., 1993, Plio-Pleistocene evolution of the Var deep-sea fan off the French Riviera: Marine and Petroleum Geology, v. 10, p. 550–571.

Tcherepanov, E. N., A. W. Droxler, P. Lapointe, G. R. Dickens, S. J. Bentley, L. Beaufort, L. C. Peterson, J. Daniell, and B. N. Opdyke, 2008, Neogene evolution of the mixed carbonate-siliciclastic system in the Gulf of Papua, Papua New Guinea, J. Geophys. Res., 113, F01S21, doi:10.1029/2006JF000684

Waelbroeck, C., Labeyrie, L., Michel, E., Duplessy, J.C., McManus, J.F., Lambeck, K., Balbon, E., and Labracherie, M., 2002, Sea-level and deep water temperature changes derived from benthic foraminifera isotopic records: Quaternary Science Reviews, v. 21, p. 295–305, doi:10.1016/S0277-3791(01)00101-9.

Weissel, J.K. and A.B. Watts, 1979, Tectonic evolution of the Coral Sea Basin, J. Geophys. Res., 84, 4572-4582,.

Wynn, R.B., Masson, D.G., Stow, D.A.V., AND Weaver, P.P.E., 2000, Turbidity current sediment waves on the submarine slopes of the western Canary Island: Marine Geology, v.163, p. 185–198.

Wynn, R.B. and Stow, D.A.V., 2002, Classification and characterisation of deep-water sediment waves. Marine Geology Special Issue, v.192, 7-22.

## CHAPTER 4

# Source-to-sink sediment delivery in the Gulf of Papua from SEM-MLA-aided provenance analysis of deep-sea turbidite sands

### 4.1. Introduction

Deep-sea sedimentary basins contain important records of terrestrial climatic and tectonic processes and conditions, encoded in the composition and distribution of sediments delivered from uplands to such oceanic basins. In addition to their valuable archives of earth history (e.g., Kiyokawa and Yokoyama, 2009) such deep-water basins are also the locations of increasingly complex petroleum exploration activities (Petzet, 2007). These basins generally represent the ultimate sink for terrigenous sediments, prior to entering the next phase of the rock cycle, via tectonic subduction and recycling (e.g. Underwood and Fergusson, 2005). Understanding how these deep-sea sedimentary systems develop due to combined effects of tectonics, climate, and eustasy is thus important both from the perspective of earth history, and from the applied perspective of petroleum-system evolution. Deep-sea basins and fans commonly accumulate sediment from multiple terrestrial sources (Shapiro et al., 2007), owing to the development of convergent deep-sea channel networks that transport gravity-driven sedimentary flows across continental margins. For this reason, spatial and temporal influences on sediment supply can be complex, and numerous techniques for the determination of sediment provenance have been applied over decades. This study will evaluate the effectiveness of a relatively new approach for provenance analysis – scanning-electron microscopy mineral-liberation analysis (SEM-MLA) (Fandrich et al., 2007) of deep-sea turbidite sands to the Pleistocene-Early Holocene development of two deep-sea sedimentary basins in the Gulf of Papua (GoP), northern Coral Sea, south of Papua New Guinea (Fig. 4.1).

The US-NSF Margins Source to Sink Program (S2S) was initiated to better understand the production, transport, and final accumulation of sediments along continental margins, particularly regarding the relative influences of tectonic, climatic, sea-level, and oceanographic processes on development of continental-margin sedimentary cover (NSF Margins, 2004); the GoP and associated terrestrial fluvial sources and sedimentary basins were selected as one of the S2S program focus areas. To date, numerous GoP studies have explored coastal and shelf processes and stratal accumulations (e.g., NSF MARGINS, 2009), but studies of deep-sea processes and products over timescales up to millennia have been mostly restricted to a small number of cores collected in proximal basins and upper slope settings (Jorry et al., 2008, Febo et al., 2008, Carson et al., 2008; Howell et al., 2014) along with one preliminary study of basinal morphology (Francis et al., 2008). At the present time, the sources and timing of sediment delivery to much of the deep-sea region of the GoP remain largely unexplored, and so the primary questions of the S2S program remain at least partially unanswered. In this study, we will explore the timing, sources, and connectivity of sediment delivery to the two largest deep-sea basins in the GoP: the Pandora and Moresby troughs (Fig. 4.1) (PT and MT, respectively) (Francis et al., 2008), through provenance analysis of turbidite sands found in cores collected during the PANASH cruise of the R/V Melville in 2004 (Dickens et al., 2006), spanning approximately the last 40-50 thousand years (ky).

A source-to-sink system is defined as a series of sediment depocentres or reservoirs connected by delivery conduits, and commonly separated by geomorphic boundaries; in this study, major depocentres include the continental shelf, slope, and marginal basins, connected by canyons and channels, and separated by the shelf-slope break and toe of slope (NSF Margins, 2009). The present study will focus on coarse fluvial sediment delivery from river mouths in the Papuan mainland and Peninsula to deep basins through the late Pleistocene and Holocene epochs. Elemental, mineralogical, and statistical analyses will be used to identify patterns and trends, which will be placed in a chronostratigraphic and morphological context using our previous studies of cores and geoacoustic data sets (Chapters 2 and 3 of this study). There are two key questions we attempt to answer by this study: (1) what are primary terrestrial sediment sources to the deep sea in our study area (2) and how do the sources and conduits interact and evolve over space and time? This study is novel because it is one of the first efforts to use SEM-MLA for detrital provenance analysis.

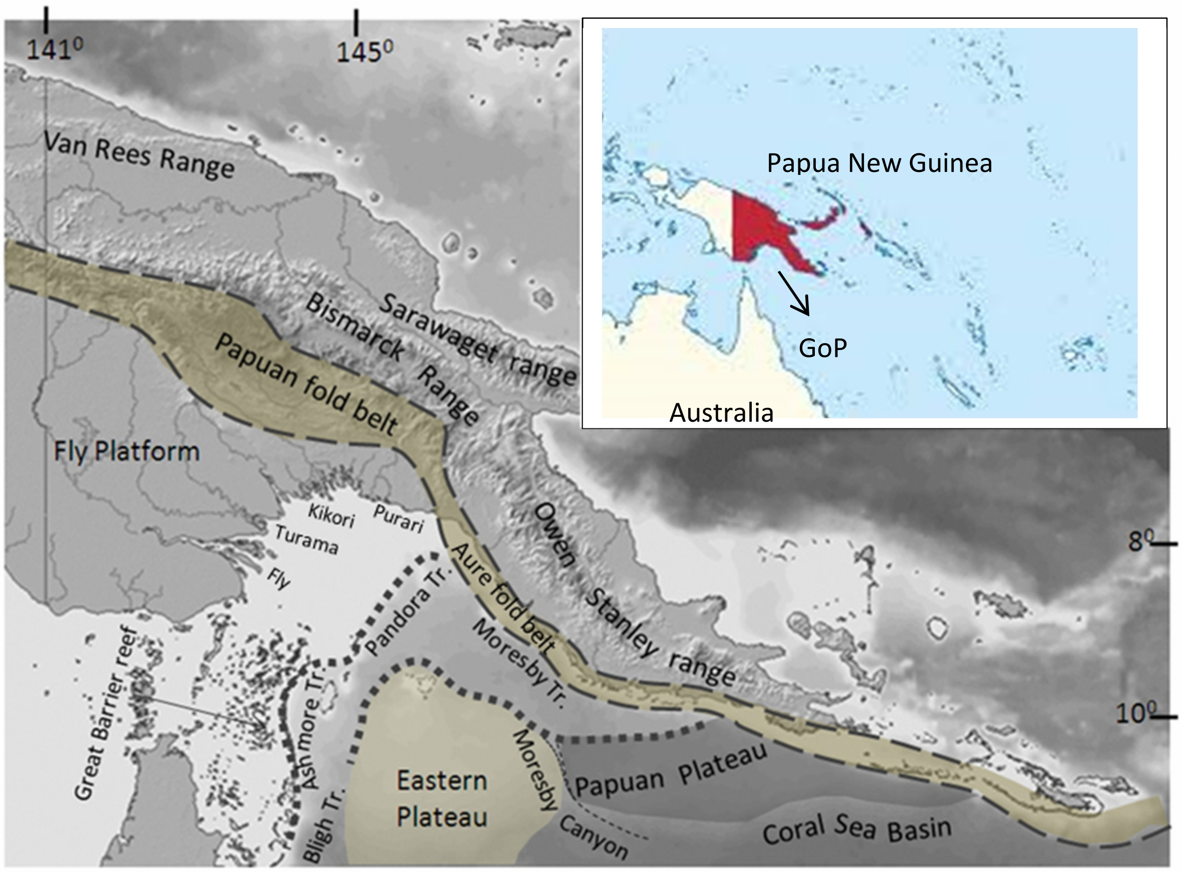


**Figure 4.1**. The physiographic and tectonic elements of the Gulf of Papua (Modified after Pigram and Davies, 1987).

### 4.2. General geology and source to sink overview in Gulf of Papua

The island of Papua is one component of a complex convergent plate boundary formed as a result of the collision between the Indo-Australian Plate and the Southwest Pacific plate. The GoP is an active foreland basin that receives abundant terrigenous sediment influx from the surrounding river systems (Slingerland et al., 2008).

The Pandora and Moresby Troughs are the foredeep of the Papuan Orogen that has built since the Late Cretaceous (ca. 65 Ma) (Fig. 4.1). These foreland basins began receiving terrigenous sediment in the proximal area as early as Eocene (55.8-33.9 Ma) and reached peak depositional rates through the entire basin during the Pliocene-Holocene (< 5 Ma) when uplift in the orogenic belt intensified (Tcherepanov et al., 2008). The uplift along the collision margin has produced >4000 meters relief, which, combined with high precipitation rate (2-10 m/yr), produces runoff that disperses abundant sediment downstream (approximately 365 million tonnes/year; Milliman, 1995). The best documented influxes come from Fly, Kikori and Purari rivers in Papuan mainland. Drainage from small river systems on the Papuan Peninsula has never been rigorously quantified (approximations in Milliman, 1995) but could potentially produce significant influx to the deep Moresby Trough in the eastern part of GOP (Fig. 4.1) (Howell et al., 2014). During early stages of the S2S program, these eastern rivers draining the Papuan Peninsula were under appreciated with respect to the potential for voluminous sediment supply, and the Fly-Strickland, Purari, and Kikori Rivers were thought to be dominant sediment sources. However, the more recent shelf-edge clay-mineral provenance study of Howell et al. (2014) demonstrated that these eastern rivers have been important sediment sources during latest Pleistocene to middle Holocene time.

Source rocks for deep-sea sediments in this study mainly originate from the Papuan Orogen. This tectonic sierra developed from the colliding New Guinea plate and the Southern Pacific subduction complex, which consists of several arcs, oceanic plateaus and micro-plates (Pigram and Davies, 1987, Pigram et al., 1989). The resulting geological formations are highly varied and range from quartzo-feldspathic and carbonate marine sedimentary rocks to extensive ultramafic complexes (Davies, 2012).

In this study we use the terms Papuan Mainland (land north of the western part of the GoP) and Papuan Peninsula (land northeast of the eastern part of the GoP) to spatially define the sediment sources, catchment systems and basins. In general, the sediment transit time from terrestrial sources to deep-sea depocentres is relatively longer for the Papuan mainland (western GOP) (Day et al., 2008) than the Papuan Peninsula (Milliman, 1995), because of the large river systems with well-developed alluvial valleys that deliver sediment to a wide continental shelf south of the mainland region. In contrast, the Papuan Peninsula (eastern GoP) is characterized by relatively small mountain-fed rivers and narrow continental shelf (Fig. 4.1).

Geological mapping of Steinshouer et al. (1999; primarily classified by age and to a lesser extent gross lithology) and the synthesis of Davies (2012; descriptive text that can be used to elucidate the Steinshouer map, but not on a 1:1 basis) document geological variability of river catchments from the Papuan mainland to the Papuan Peninsula (Fig. 4.2). Davies (2012) describes the upland geology of the Fly, Ramu, and Turama river catchments (feeding sediment to the western shelf of the study area) as a mixture of Neogene marine shelf and reworked terrestrial sediments with minor volcanics of andesitic to basaltic composition. Farther east, bedrock geology of the Kikori and Purari catchments are characterized by more extensive andesitic to basaltic volcanics, and blocks of meta-sediments, green-schist, gneissic granites, and

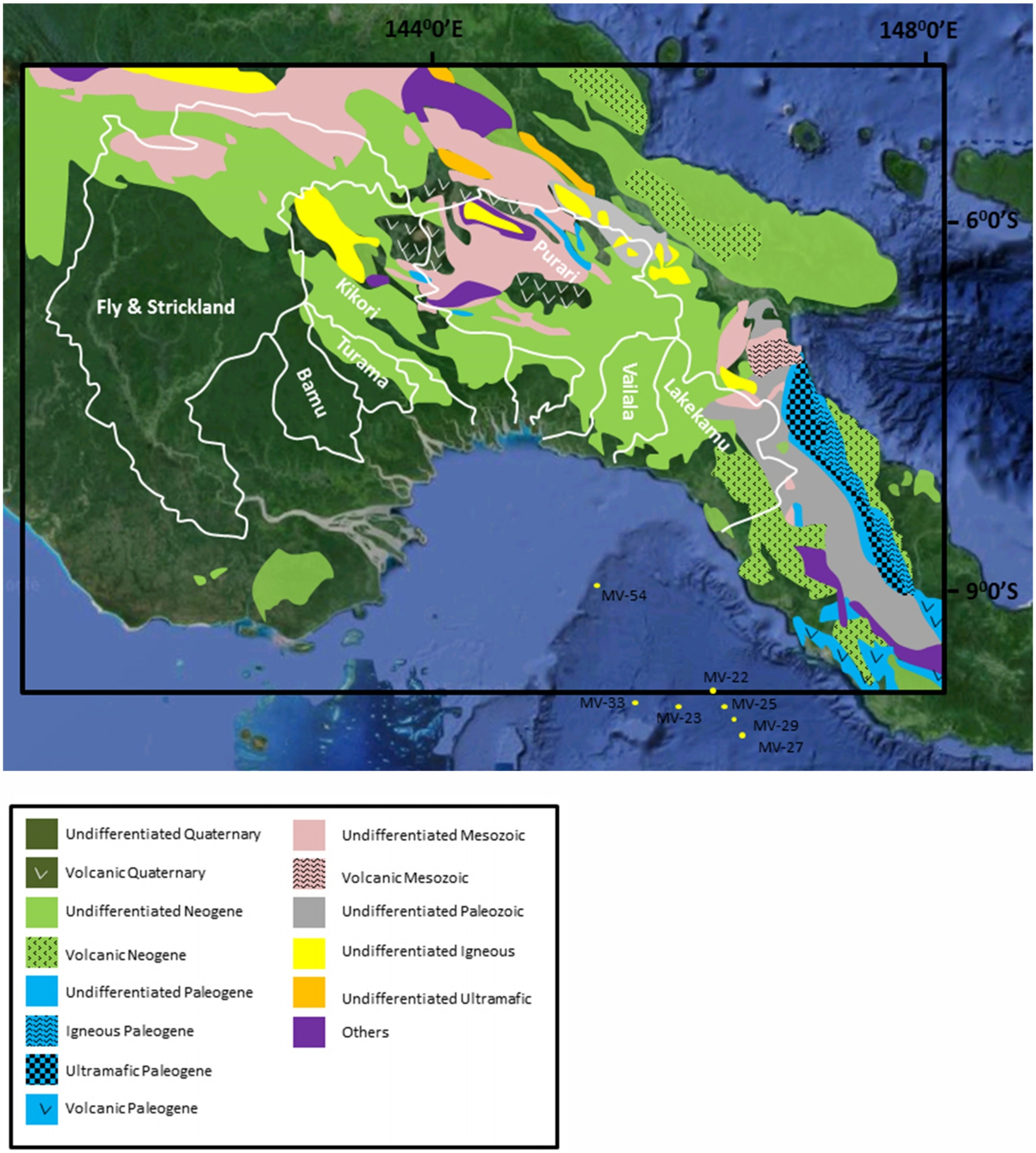


**Figure 4.2**. Geological map of Papuan Mainland and Papuan Peninsular (Modified after Steinshouer et al., 1999, Howell et al., 2014), the background earth surface and bathymetry are captured from Google Earth©). White line illustrated the river system catchment area (After Howell et al., 2014).

granitoids (Davies, 2012). The Lakekamu and Vailala river catchments (feeding sediment to the easternmost shelf of this study area) include the Papuan and Aure Fold Belt and Owen Stanley Range; Fig. 4.1), are composed of folded felsic metamorphic rocks, accretionary prisms intruded by gabbro, metabasites, and a large ultramafic belt within an extensive ophiolite complex (Davies, 2012). These formations extend southeastwards towards the coastline most proximal to the location of core MV-22. These formations impart a unique mafic-ultramafic mineral signal to the deep sea basin, including pumice and volcanic debris (Patterson, 2006), ultramafic grains and lithic fragments, and low-grade products of oceanic metamorphism (e.g., actinolite and epidote) (Garzanti et al. 2000, Bloomer et al. 2005 and Garzanti et al. 2007). Thus, from west to east, catchment geology generally increases in both volcanic (andesitic to basaltic) and mafic/ultramafic content (although no one data source documents this trend completely and unambiguously).

## 4.3. Methodology

### 4.3.1. Sample Collection and Preparation

Cores and geoacoustic data were collected during the R/V Melville PANASH cruise in March-April 2004 (Pandora and Ashmore troughs) (Fig. 4.1; Dickens et al., 2006). Core locations were selected following geoacoustic surveys, in order to document specific morphological elements of the basins. The geoacoustic dataset includes SEABEAM 2000 12 kHz multi-beam and Knudsen Engineering 3.5 kHz sub-bottom data collected aboard the R/V Melville that contributed to the bathymetric grid of Daniell (2008) which is the basis for bathymetry in Figures 4.1 and 4.3.

Jumbo piston cores were collected from the R/V Melville in 2004 (Fig. 4.1 and Table 4.1) and logged onboard by scientific team using a Geotek Multi-Sensor Core Logger (MSCL) for whole-core gamma density (GD) and magnetic susceptibility (MS). A total of 53 samples were collected from PANASH jumbo piston cores (Fig. 4.3 and Table 4.1), and three samples were obtained from Fly and Strickland river point bars for comparison. The marine samples were acquired from seven jumbo piston cores that sampled major geomorphic elements in the PT and MT: Pandora slope, Pandora toe of slope and mini-basin (MV-54, 23 and 33), Moresby Channel (MV-25 and 29), and eastern and western flanks of Moresby Trough (MV-22 and MV-27 respectively) (Dickens et al., 2006; Francis et al., 2008; chapters 2 and 3 of this study). Fluvial samples from downstream point bars on the Fly and Strickland rivers, and upstream on the Strickland near the Ok Tedi Mine were provided by R. Aalto, collected in 2010 (Aalto, personal communication, 2011).

The marine samples were selected and extracted from relatively thick sandy layers identified in core images, magnetic susceptibility, and gamma-density data from a Geotek Multi Sensor Core Logger (described in Chapter 2 of this study). Morphologic and seismic characterization of core locations are derived from Chapter 3 of this study (Figs. 4.1 and 4.3), and age models used for chronostratigraphic control as well as lithostratigraphic core descriptions are from Chapter 2 of this study (Fig. 4.4).

Samples were wet sieved to retain the sand-sized fraction (0.0625-2 mm), then treated to remove organic carbon and biogenic carbonate (in practice total carbonate) with hydrogen peroxide and hydrochloric acid. Air-dried samples were then grain-mounted using epoxy resin under vacuum and polished using diamond suspension under 30 – 15 – 5 – 1 - 0.1 μm polisher (Septama, Micro-analysis facilities laboratory, Inco Centre Memorial University of

Newfoundland). Mounts to be used for SEM-MLA were carbon sputtered to augment conductivity (Buckwalter-Davis et al., 2012). In order to review petrographic properties and allow comparison of SEM-MLA methods to traditional provenance techniques

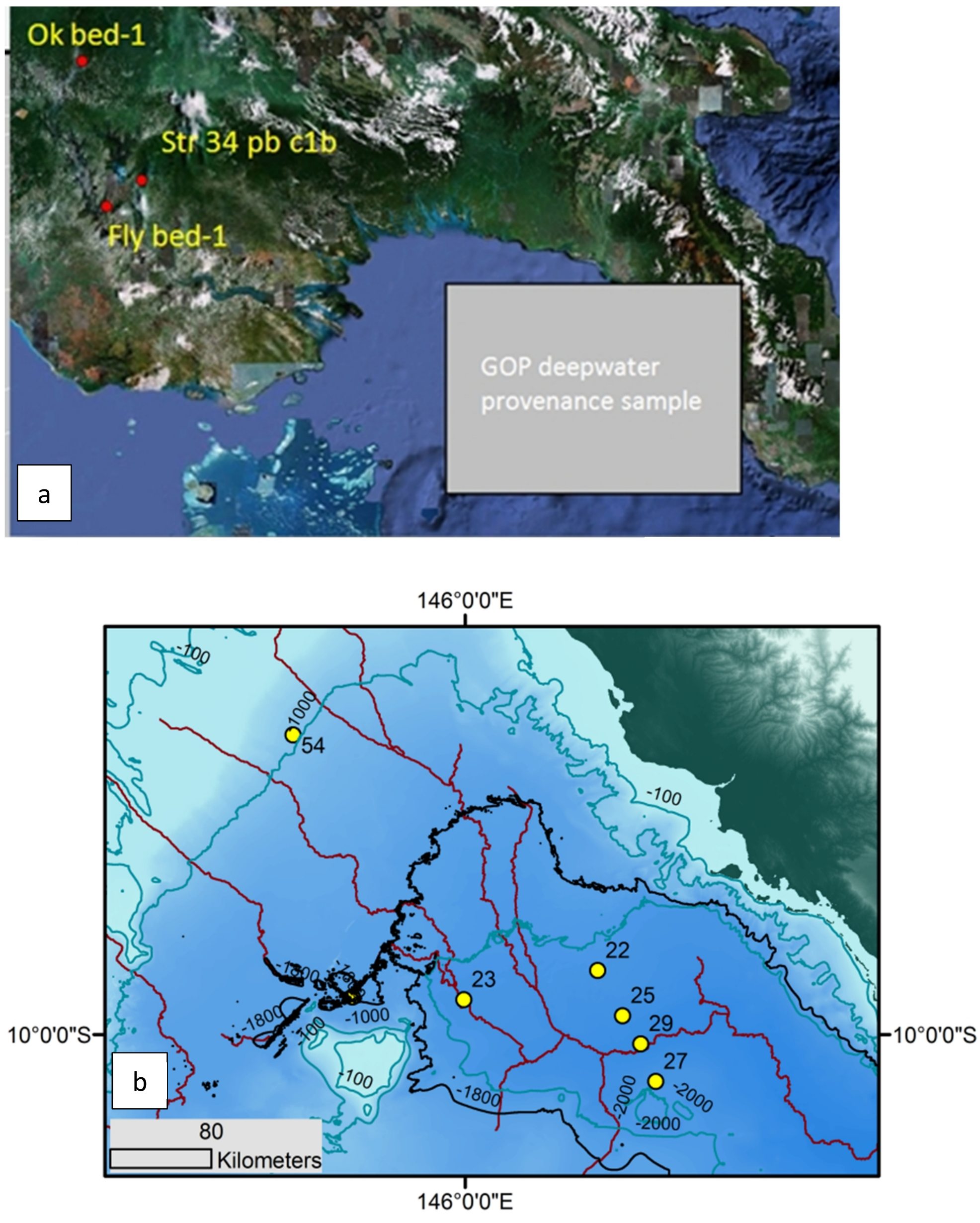


**Figure 4.3**(a) The base-map of the study area, samples are acquired from 7 Jumbo piston cores and stream samples in Fly and Strickland river system (b) inset of cores location in deep sea Gulf of Papua (GoP). Isobaths are labeled in meters below sea level, and the burgundy lines identify deep-sea channel thalwegs extracted from a DEM based on slope by Patterson (2006).

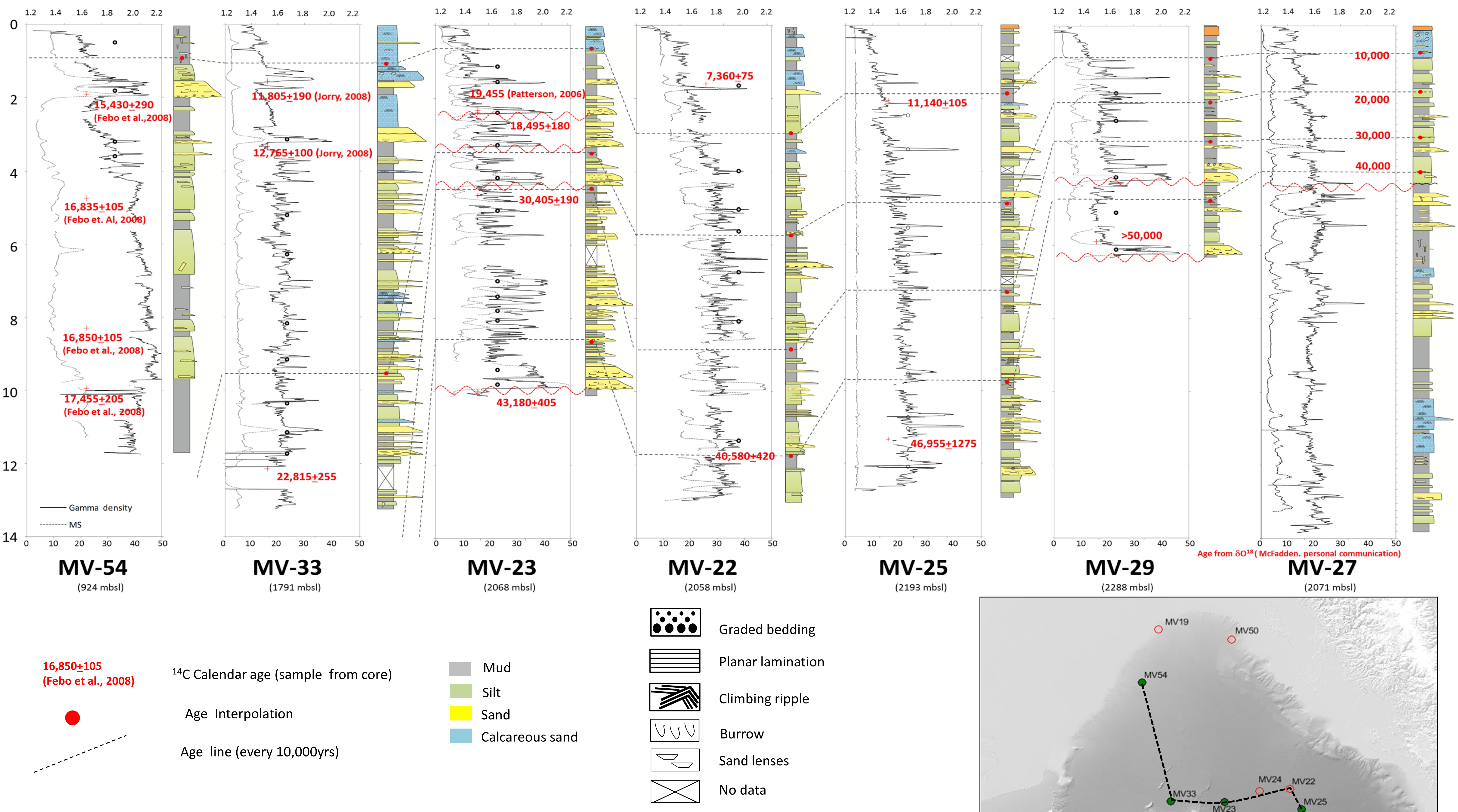


Figure 4.4 Chronostratigraphic correlation across the Gulf of Papua, from slope through mini-basin, toe of slope and Moresby channel, described in chapter 2 of this study. The time-lines are interpolated every 10 cal Ka based on sediment accumulation rates in the hemipelagic component of the sedimentary succession. Erosional bases to sand beds were interpreted based on log and core observations. The correlation on the upper part of the core (e.g. 10 Ka) also considering the peak of Ca from XRF scan data of cores MV-22, MV-25, MV-23 and MV-33

(e.g., Dickinson and Suczek, 1979), five samples (70 μm thin sections) were also prepared for manual point counting.

SEM-MLA was performed with FEI Quanta 400 scanning electron microscope (Septama, Micro-analysis facilities laboratory, Inco Centre Memorial University of Newfoundland). SEM collects backscatter electrons rather than light waves from the minerals surface, enabling grain magnification up to 50,000 times. The results then are quantified by mineral liberation analysis (MLA). The MLA technique first relies on *backscattered electron imaging* (BEI), as a measure of average atomic number, for discriminating grain boundaries, and then offers a variety of x-ray options for classifying the grains as recognized minerals based on their density in the spectral library (Buckwalter-Davis et al., 2012).

#### 4.3.2. Detrital modal analysis

**Manual QFL ternary diagram.** Point counts to prepare Gazzi-Dickinson ternary diagrams (Dickinson, et al., 1983) were performed on five slides for 300 grains per slide; samples were taken from three cores from different depositional settings: MV-22 (MT), MV-23 (PT) and MV-25 (Moresby Channel). Only framework grains (non-matrix) were counted and recalculated based on three major compositions: quartz (Q), feldspar (F) and lithic fragment (L). This method reduces the dependencies of grain size and alteration and allows accurate determination of original detrital mode and provenance (Ingersoll et al., 1984, Marsaglia and Ingersoll, 1992).

**Semi-automated SEM-MLA**. SEM MLA is an automated scanning, image-processing, and elemental analysis that relies upon pre-set rules for recognition of grain size, shape, and composition (Fandrich et al., 2007). In this procedure, “particles” are defined as individual clasts, whether composed of one or multiple minerals. “Grains” are defined as portions of particles composed of one mineral phase, whether mono- or poly-crystalline (Fandrich et al., 2007). We defined lithic fragments as any assemblage of minerals where neither quartz (Q) nor feldspar (F) formed more than 80 % of particle, and three or more minerals with weight percent< 20% were aggregated as a single particle with an enclosing ellipse major axis (grain size) of 0.0625-2 mm. We calibrated the detection process using reflected spectra from lithic fragments of known composition. Based on these criteria and calibration of instrument detection methods, SEM-MLA has a limited ability to automatically distinguish among lithic fragments by rock type (e.g. volcanic, sedimentary or metamorphic rocks).

Our study is one of the first attempts to perform Gazzi-Dickinson provenance study using automated SEM-MLA; therefore, to verify our approach we used both traditional and SEM-MLA methods to compare results: (1) manual point counts (2) SEM-MLA grain-based counts, (3) SEM-MLA particle-based counts, and (4) SEM-MLA area-based counts. Grain based point counts: the grain-based point counts were done on 30-50,000 grains >3.9 µm in size from the mineral composition database. Particle-based point counts: this method was performed on 30-50,000 particles >62.5 µm (fine sand size) with a minimum percentage (%) of a particular mineral were >80% and >60% of a particle. If neither quartz (Q) nor feldspar (S) formed >80% of a particle and there were more than three minerals present then the particle was classified as lithic (L). The total (L) classification also included the pumice class and clay minerals. Area based counts: this method used the mineral map from SEM-MLA instead of grains or particles, with area based on total pixel number for each mineral (Appendix-2). Other than the manual point counts specified above, all provenance data discussed hereafter were derived from SEM-MLA.

**Detrital Feldspar:** The analysis of detrital feldspar can be used to define the origin of plagioclase minerals in sand, as feldspar minerals make-up one of the major frameworks in almost all siliciclastic sediment (in average of 25 – 45 % in this particular study area). Previous study has described variation in detrital plagioclase composition that can be used to characterize source rocks (e.g., Trevena and Nash, 1981; Weltje and Eynatten, 2004). Sediment sourced from metamorphic terranes generally is depleted of K-feldspar because potassium in general is depleted at the temperature of metamorphism. In contrast, K-feldspar will increase with significant depletion of plagioclase Ca (hence anorthite composition) in volcanic rocks; plutonic rock tend to plot in between or overlap with metamorphic and volcanic rocks (Trevena and Nash, 1979).

The other potential variation in detrital feldspar is the enrichment of the Na Plagioclase during diagenesis and low-grade metamorphism. Albitization can occur both in K-feldspar and plagioclase feldspar although the latter requires deeper burial (Morad et al., 1990, Gonzales Acebrón et al, 2010). Albitization is commonly associated with the recycled orogen type provenance as a secondary product from the burial diagenesis of the sediment or meta-sediment rock fragments. This phenomenon can be observed if the morphology of the parental feldspar or plagioclase is intact (Gonzales Acebrón et al, 2010). The visual observation by using backscatter electron image verified by density spectra is performed during the SEM-MLA analysis, and can be used to discriminate between detrital albite and diagenetic albite (see further discussion in interpretation and discussion section).

### 4.3.3. Chemical Index of Alteration

The chemical index of alteration (CIA) (Nesbitt and Young, 1982) is calculated from sand samples as a weathering index to identify change caused by chemical weathering of grains. This proxy represents a measure of the amount of clay made during hydrolysis of feldspar (Price and Velbel, 2003, Nesbitt and Young, 1982). The formula represents the ratio of the predominant but immobile $Al_2O_3$ to the mobile cation $Na^+$, $K^+$ and $Ca^+$ represented as major oxides (Nesbitt and Young, 1982, Bahlburg and Dobrzinski, 2011).

$$CIA = \frac{Al_2O_3}{Al_2O_3+Na_2O+K_2O+CaO} * 100 \qquad \text{Eq. 1}$$

Whole rock major oxides from samples are converted from elemental assay by adding the weight contributed by the appropriate number of oxygen atoms in the particular oxide (e.g. 10 wt% Al is equivalent to 18% wt% $Al_2O_3$). The weakness of this methodology is the elemental assay is derived from the mineralogical formulas calculated in MLA (total minerals sample in the database), thus the abundance and CIA results are approximations because the full chemical analysis of the samples was not determined. Data are presented in a ternary diagram and down-core plot. This methodology can also show spatial and temporal weathering trends.

#### 4.3.4. Multivariate Statistical Approach

Multivariate statistical analysis is performed to detect the trends within the data and explore correlations between datasets. We utilize Similarity Percentage (SimPer) (Anderson et al., 2008) to filter the important minerals that contribute to similarity/dissimilarity. This method provides discrimination between sample clusters and shows the contribution percentage of minerals to dissimilarity.

Non-metric Multidimensional Scaling (nMDS) is an ordination technique that transforms data into an n-dimensional domain, using mineral abundance as Cartesian coordinate, and rank similarities of the resultant distances that are projected into a 3-dimensional and 2-dimensional domain (Clarke & Warwick 2001). This method can discriminate samples into more detailed clusters based on their mineralogy (hence more detailed grouping or petro-facies class than modal detrital analysis). To measure the degree of dissimilarity from each sample in this study we determine Euclidean distance (*d*), then create a dendrogram relating clusters by the separating distance *d*:

$$d(p,q) = \sqrt{\sum_{i=1}^{n}(q_i - p_i)^2} \qquad \text{Eq. 2}$$

where $p$ ($p1, p2, p3, \ldots. pn$) and $q$ ($q1, q2, q3, \ldots. qn$) are two sample points within Euclidean n-dimensional domain (Anderson et al., 2008).

## 4.4. Results

### 4.4.1. QFL Modal analysis

Manual thin section point counts: results show that most samples from manual point counts display less lithological variability on a QFL diagram than do SEM-MLA results (Fig. 4.5a) and most point count results for our samples classify into the Recycled Orogen field (Fig. 4.5b).

SEM-MLA Grain-based: This method produces most lithic-rich results (Fig. 4.5a). This is possible because in some cases the classification includes coarser matrix as the lithic fragment thus enriches the quantity of the total undifferentiated lithics (31-49 %) over the other framework grains. In general the grain-based method represents a classification based on the smallest individual mineral constituent whether it is sand- or silt- sized. Tight clustering is evident using this method, not unlike manual point counts.

Particle based point count: both of the approaches (thresholds of >60 and >80 wt. %) plot apparently close together without any evident shifting (Fig. 4.5a). This is confirmed by the similar composition for each method in the weight percent minerals (Table 4.1). Results distribute data across the following fields: transitional arc, dissected arc, recycled orogen and transitional continental. These results based on automated classification show lower lithic percentages compared to the manual point counts.

Area based counts: results using this approach encompass the fields of transitional arc, dissected arc and recycled orogen. The results compare well with particle-based point counts; however there is a possibility that results are skewed toward minerals with coarser grain size as they tend to be volumetrically larger (Fig. 4.5a).

Overall, particle-based point counts appear to encompass the largest number of fields (Fig. 4.5b). Figure 4.6b shows that in general most samples are moderate to low in lithic fragments (0-30%) except samples from Pandora mini-basin (MV33) and two samples from MT (MV22). All samples from MT are moderate to high in feldspar (30-80%). Terrestrial samples from Fly and Strickland rivers are low in feldspar (9-12 %) but high in lithics (34-43%) and quartz (47-53%). The sample from Ok Tedi, in contrast, shows low lithic content (7.34 %) but high feldspar (50.36%) and quartz (42.29%). This sample is just downstream from an open cut copper mine into monzonite, monzodiorite and syenite (Aalto, 2011, personal communication). The samples from PT (MV54 and MV23) plot mostly with samples from Moresby Channel (MV25 and MV29) the west of MT (MV27). Samples from MV33 show distinct separation from other Pandora Trough samples (Fig. 4.5b)

### 4.4.2 Detrital feldspar analysis

The QmKP (Quartz monocrystalline, potassium feldspar and Plagioclase feldspar) ternary plot was used to explore compositional variation between potassium feldspar and plagioclase feldspar (Fig. 4.6a and b). SEM-MLA could not distinguish the monocrystalline quartz (Qm) over the polycrystalline quartz (Qp) directly. The discrimination was done by particle observation (>80% of a particle is Quartz), if the impurities present (e.g. sericite) as a grain in that particle (1-20%),

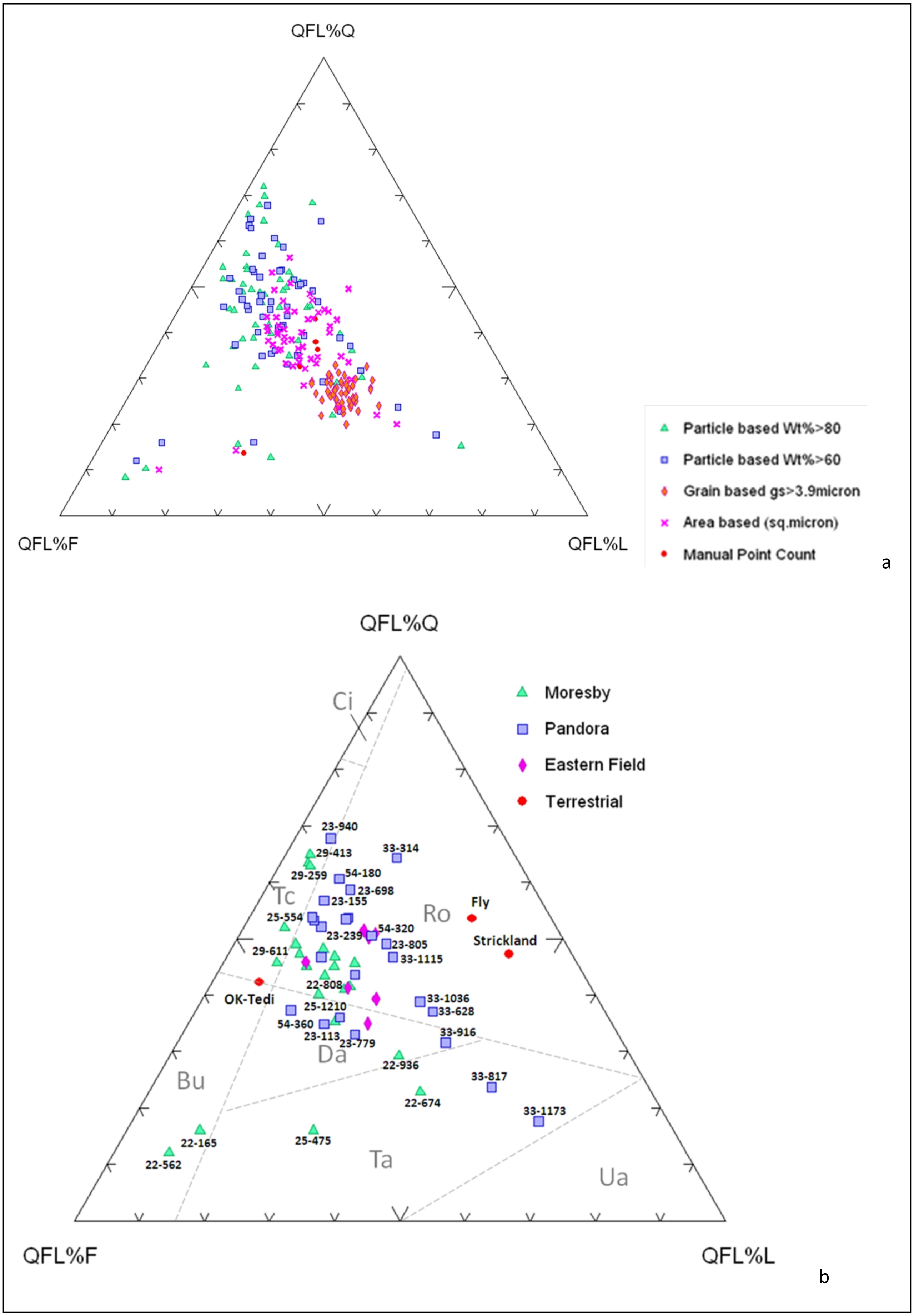
QFL%Q
QFL%F
QFL%L
Particle based Wt%>80
Particle based Wt%>60
Grain based gs>3.9micron
Area based (sq.micron)
Manual Point Count
a
QFL%Q
Ci
Tc
Ro
Da
Bu
Ta
Ua
Moresby
Pandora
Eastern Field
Terrestrial
23-940
33-314
29-413
29-259
54-180
23-698
23-155
Fly
25-554
23-239
54-320
Strickland
23-805
33-1115
29-611
22-808
OK-Tedi
33-1036
33-628
25-1210
54-360
23-113
23-779
33-916
22-936
33-817
22-674
33-1173
22-165
22-562
25-475
QFL%F
QFL%L
b

**Figure 4.5**. (previous page) Ternary diagrams of QFL detrital modal analysis (a) a comparison between manual point count of the thin section, particle based point count, grain based and area based (see text for details) (b) the particle based point count as the selected technique for QFL modal analysis. Axis increments are each 10%.

then the particle will classify as Qp. Samples from the PT mini-basin (MV33-817 and 1173), PT slope sample MV54-49, and the Ok Tedi terrestrial sample are elevated in K-feldspar, as is Moresby Fan sample MV 22-675 and Moresby Channel sample MV25-1104. The following samples are high in plagioclase feldspar: MV33-817 and 1173 (Pandora Trough), MV54-49 (middle slope of Pandora Trough), two samples from Moresby fan (MV22-165 and MV22-562) and one sample from Moresby Channel (MV25-475).

The KAnAb (potassium feldspar, anorthite and albite) ternary plot was used to distinguish the composition variation in feldspar and to detect the presence of authigenic feldspar. The plot shows that samples MV54-49, 33-314, 33-817 and 33-817 from the PT slope and mini-basin are slightly elevated in K-feldspar whereas samples MV22-502, 22-808, 22-936, 25-245, 29-413 and 29-510 from MT show elevated in Na-plagioclase (albite). The terrestrial sample from OK-Tedi is high in K-Feldspar (53 %) (Fig.4. 6b).

### 4.4.3 Chemical index of alteration (CIA)

Figure 4.7a is a ternary plot of CIA variables (Eq. 1) and shows a gradient in $Al_2O_3$:$CaO$+$Na_2O$ composition from Moresby Trough (high in $CaO$+$Na_2O$) Pandora Trough (higher in $Al_2O_3$), especially samples from slope (MV54) and Pandora mini-basin (MV-33). Samples from MV33 and MV54 show higher $Al_2O_3$ (hence CIA) values than most samples from Moresby Trough (Fig. 4.7a and Table 4.2).

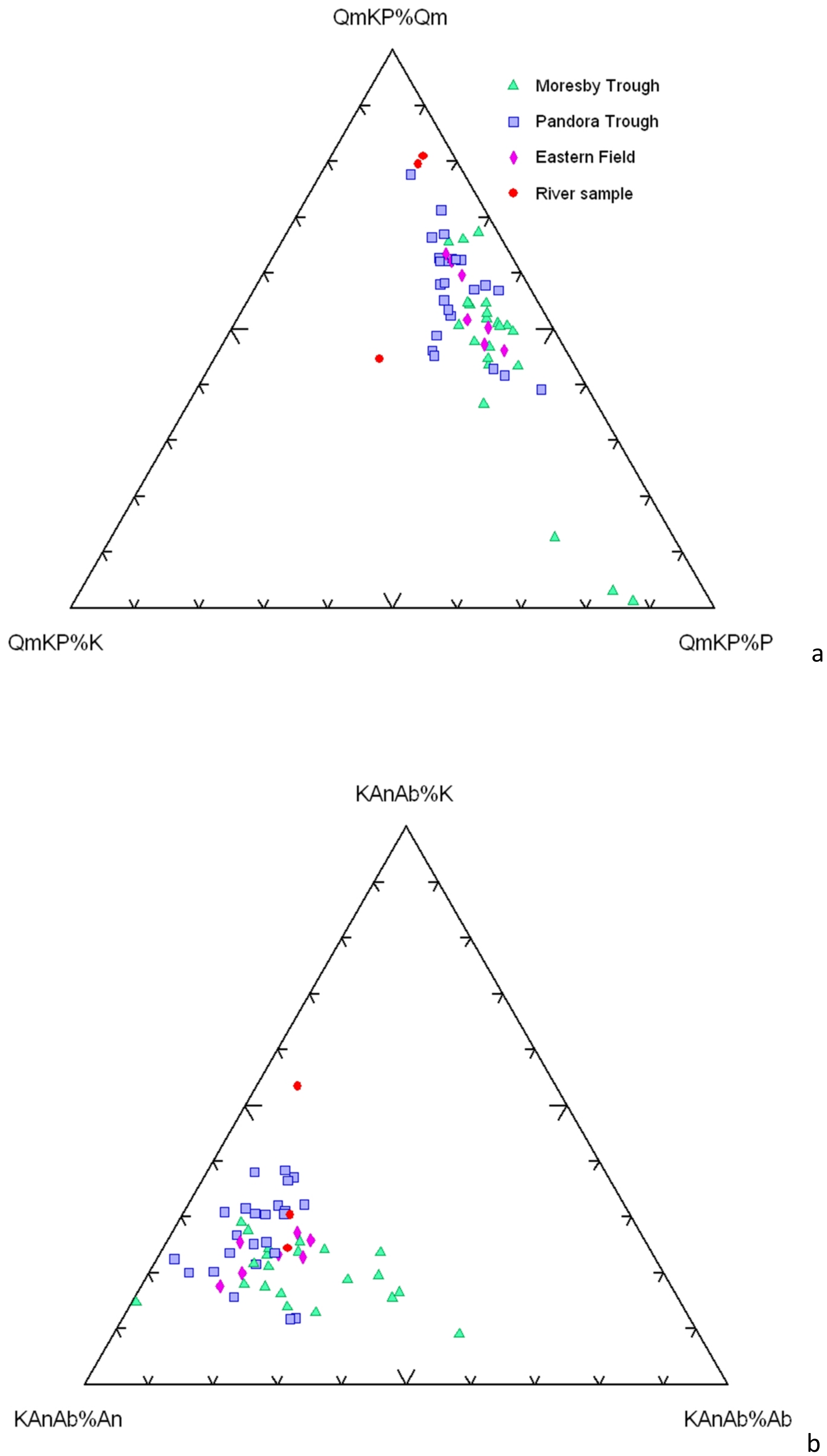


**Figure 4.6**. The detrital feldspar analysis ternary diagram (a) QmKP (b) KAnAb plot. Axis increments are 10% each.

The samples from Moresby channel (MV25, and MV29, MV27) overlap with samples from Pandora toe of slope (MV23) in having $Al_2O_3 < 75\%$. Samples MV33-1173 and MV33-314 are relatively low in $Al_2O_3$ but elevated in $K_2O$. Terrestrial samples from both Fly and Strickland Rivers show high $Al_2O_3$. Two samples from MT (MV22-165 and 562) shows $Al_2O_3$ <60% (Fig. 4.7a). Table 4.2 shows that core samples from MT are generally lower overall in CIA compared to core samples from PT, but in-core variability is comparable.

Profiles of CIA in cores MV22, MV23 and MV-25 (Fig. 4.7b) show an apparently correlated minimum in CIA around approximately near the LGM, during mid to late MIS2, followed by a CIA increase during deglacial time. Core MV29 has no constrained age model, but also shows a CIA minimum at the same depth range in seabed. (Fig.4.7b). In contrast, a CIA minimum occurs in MV27 prior to MIS2.

| ***Composition*** | ***MV22-156*** | | | ***MV23-805*** | | | ***MV25-554*** | | |
|---|---|---|---|---|---|---|---|---|---|
| | Grain % | Particle % | Area % | Grain % | Particle % | Area % | Grain % | Particle % | Area % |
| **Lithic fragment** | 22.70 | 5.47 | 10.26 | 28.57 | 32.42 | 40.49 | 28.25 | 23.50 | 24.80 |
| **Amphibole** | 5.95 | 7.23 | 16.20 | 1.84 | 1.75 | 1.06 | 2.72 | 2.94 | 4.99 |
| **Quartz (mono)** | 0.60 | 0.70 | 0.78 | 8.77 | 8.39 | 27.11 | 11.82 | 12.62 | 26.19 |
| **Quartz (poly)** | 21.78 | 26.61 | 8.77 | 19.15 | 18.17 | 5.00 | 14.82 | 15.73 | 5.40 |
| **Chloritoid** | 0.25 | 0.3 | 0.18 | 0.45 | 0.42 | 0.36 | 0.15 | 0.17 | 0.04 |
| **Epidote** | 0.32 | 0.38 | 0.11 | 0.45 | 0.41 | 0.20 | 1.64 | 1.76 | 1.64 |
| **Anorthite** | 7.25 | 8.74 | 33.54 | 7.82 | 7.42 | 7.71 | 11.34 | 12.18 | 15.25 |
| **Albite** | 0.03 | 0.03 | 0.01 | 4.48 | 4.19 | 3.57 | 5.57 | 5.89 | 5.18 |
| **Muscovite** | 0.10 | 0.12 | 0.11 | 8.02 | 7.99 | 3.41 | 4.13 | 4.40 | 2.31 |
| **Orthoclase** | 0.49 | 0.57 | 0.29 | 2.17 | 2.06 | 2.97 | 3.60 | 3.85 | 2.97 |
| **Pumice** | 22.58 | 28.03 | 6.12 | 13.62 | 12.94 | 5.33 | 11.28 | 11.98 | 4.86 |
| **Perthite** | 17.94 | 21.81 | 6.93 | 4.65 | 4.39 | 0.91 | 4.68 | 4.98 | 2.33 |

**Table-4.1** Comparison of composition percentages for SEM-MLA grain, particle (80%), and area counts in selected samples, for mineral compositions that describe greatest dissimilarities among sample clusters.

| Core and geographic region | CIA mean ± 1 std deviation |
|---|---|
| MV22 (MT) | 67.0±7.2, n=8 |
| MV25 (MT) | 69.5±1.8, n=9 |
| MV27 (MT western flank) | 71.5±2.4, n=7 |
| MV29 (MT) | 64.2±2.8, n=5 |
| **All MT** | **68.1±3.6** |
| MV23 (PT) | 71.2±3.0, n=12 |
| MV33 (PT floor) | 73.0±4.7, n=8 |
| MV54 (PT middle slope) | 71.8±3.4, n=4 |
| **ALL PT** | **72.0±3.7** |

**Table-4.2** Summary CIA results for all cores

| Grain Composition | Clusters from SimPer Analysis, with number of samples (n) per cluster | | | | | | | | | | | |
|---|---|---|---|---|---|---|---|---|---|---|---|---|
| | **1, n=2** | **2, n=2** | **3, n=2** | **4, n=5** | **5, n=1** | **6, n=5** | **7, n=9** | **8, n=11** | **9, n=1** | **10, n=1** | **11, n=1** | **12, n=10** |
| **Lithic fragment** | 5.96 ± 0.91 | 28.40 ± 0.94 | 31.39 ± 1.30 | 34.47 ± 1.94 | 22.87 | 20.40 ± 1.54 | 29.39± 1.19 | 26.46 ± 1.20 | 28.64 | 25.28 | 26.01 | 26.56 ± 1.41 |
| **Amphibole** | 7.69 ± 0.93 | 2.38 ± 0.43 | 3.26 ± 0.95 | 2.09 ± 0.43 | 2.86 | 5.35 ± 1.22 | 2.15 ± 0.64 | 3.75 ± 0.92 | 3.97 | 5.40 | 3.37 | 5.52 ± 0.70 |
| **Quartz (mono)** | 0.93 ± 0.35 | 5.13 ± 0.39 | 9.00 ± 1.86 | 11.22 ± 1.67 | 12.28 | 6.66 ± 1.01 | 8.02 ± 1.37 | 7.12 ± 1.28 | 12.24 | 8.13 | 9.09 | 7.83 ± 0.63 |
| **Quartz (poly)** | 24.41 ± 2.06 | 13.96 ± 1.24 | 14.45 ± 0.88 | 10.99 ± 1.99 | 15.30 | 14.99 ± 1.25 | 16.39 ± 1.08 | 14.88 ± 1.38 | 12.25 | 9.33 | 11.59 | 11.98 ± 1.31 |
| **Chloritoid** | 0.21 ± 0.11 | 0.37 ± 0.23 | 1.13 ± 0.44 | 0.69 ± 0.15 | 0.16 | 1.93 ± 0.75 | 0.59 ± 0.17 | 0.98 ± 0.47 | 2.30 | 2.96 | 0.81 | 2.22 ± 0.51 |
| **Epidote** | 0.33 ± 0.06 | 0.31 ± 0.02 | 0.44 ± 0.21 | 0.87 ± 0.38 | 1.71 | 2.37 ± 0.56 | 0.58 ± 0.30 | 1.91 ± 0.50 | 0.83 | 3.37 | 2.51 | 2.24 ± 0.69 |
| **Anorthite** | 8.15 ± 0.49 | 7.75 ± 0.27 | 6.16 ± 2.46 | 8.08 ± 0.87 | 11.85 | 9.64 ± 1.10 | 8.18 ± 0.58 | 10.16 ± 0.92 | 8.83 | 10.44 | 12.18 | 10.23 ± 0.86 |
| **Albite** | 0.11 ± 0.10 | 3.82 ± 0.23 | 3.67 ± 0.03 | 4.86 ± 0.47 | 5.73 | 4.95 ± 1.34 | 4.66 ± 0.32 | 5.11 ± 0.61 | 4.44 | 7.16 | 7.18 | 5.38 ± 0.54 |
| **Muscovite** | 0.17 ± 0.08 | 7.18 ± 2.71 | 11.14 ± 2.09 | 7.38 ± 1.23 | 4.29 | 8.74 ± 1.50 | 7.31 ± 1.01 | 6.90 ± 0.93 | 9.96 | 11.05 | 7.77 | 8.54 ± 0.79 |
| **Orthoclase** | 0.52 ± 0.05 | 2.93 ± 0.43 | 2.27 ± 0.36 | 2.30 ± 0.24 | 3.75 | 2.22 ± 0.59 | 2.89 ± 0.39 | 2.51 ± 0.58 | 3.35 | 1.15 | 2.08 | 2.38 ± 0.57 |
| **Pumice** | 25.34 ± 2.71 | 5.20 ± 3.61 | 2.36 ± 0.15 | 4.96 ± 1.79 | 4.85 | 4.88 ± 1.73 | 3.36 ± 0.59 | 5.53 ± 1.93 | 1.53 | 3.01 | 4.05 | 3.40 ± 0.91 |
| **Perthite** | 23.19 ± 2.80 | 17.40 ± 1.73 | 9.34 ± 0.67 | 8.26 ± 0.90 | 11.66 | 9.32 ± 2.58 | 12.19 ± 1.69 | 10.81 ± 1.42 | 7.16 | 5.21 | 9.30 | 7.51 ± 1.23 |

**Table 4.3** Average and standard deviation of compositions in clusters identified by SimPer cluster analysis of SEM-MLA data

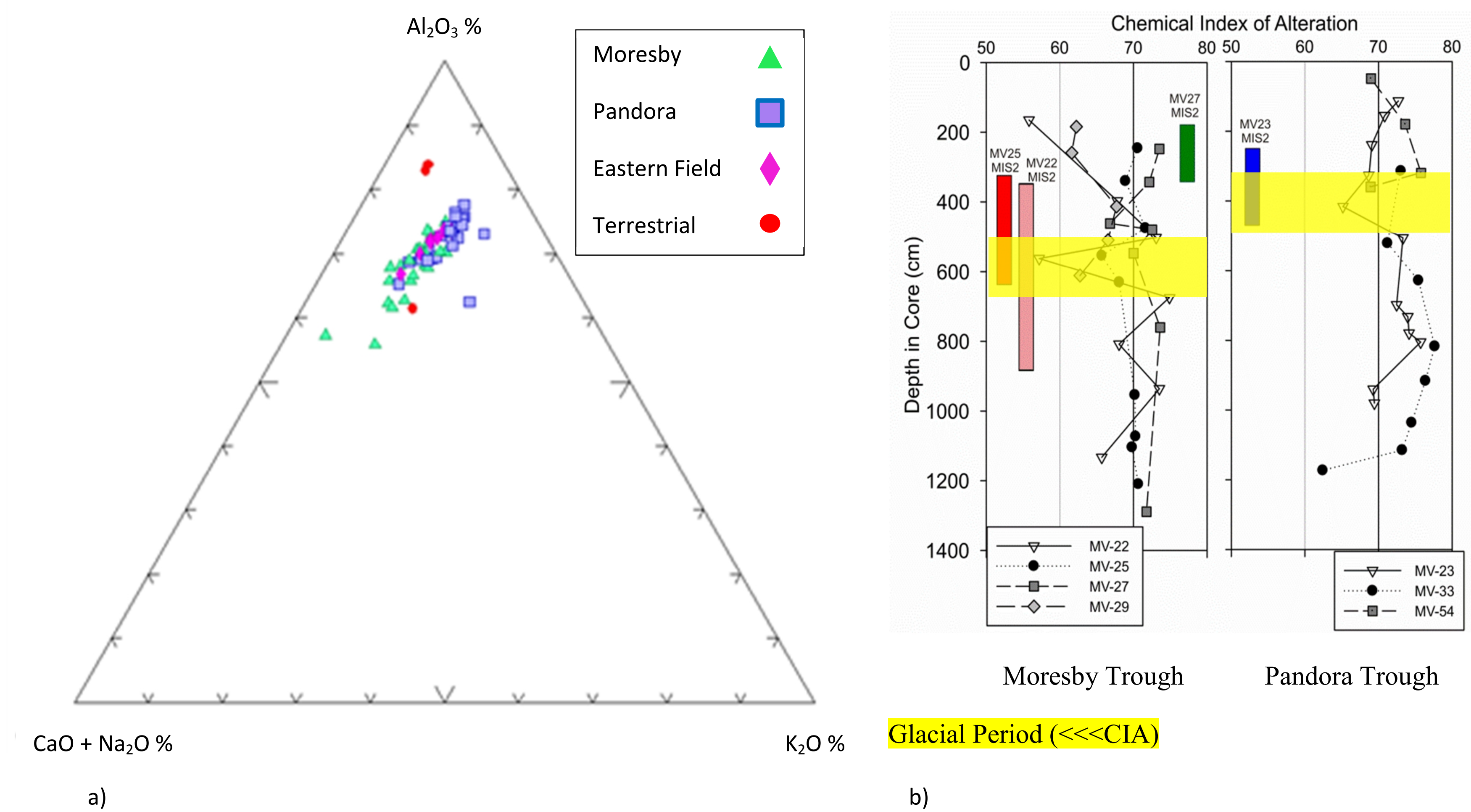


**Figure 4.7.** The Chemical Index of Alteration analysis of the samples (a) ternary diagram (increments 10% each) and (b) down-hole CIA variation in seven jumbo piston cores.

### 4.4.4 Multivariate Statistics

SimPer analysis shows that there are 12 particle compositions that account for most dissimilarity in grain populations: monocrystalline quartz, polycrystalline quartz, perthite, chloritoid, amphibole, pumice, undifferentiated lithic fragments, albite, orthoclase, muscovite, anorthite and epidote (Table 4.3). SimPer analysis allows the content of these minerals to represent the cluster coordinates within a 12D domain. In Figure 4.8a, results are rotated and projected into a 2D space at the orientation that provides the greatest separation of results. Samples from Pandora Trough (MV23, 33 and 54) generally fall on the right and left sides of the plot, while Moresby Trough (MV-22, 25, 27 and 29) fall in an irregular field extending from top to bottom in the centre of the plot (Fig. 4.8a). The relatively great Euclidean distances separating multiple samples from one core (e.g., all samples from MV-23) demonstrate that there are both compositional variations between locations, and also within individual cores. Sample MV22-165 and MV22-562 are outliers with $d$=38 (Fig. 4.8b). The correlation matrix and modal mineralogy data (Table 4.3) show that the major variables contributing to the differences for these outliers from other clusters are the abundance of the pumice, polycrystalline quartz and amphibole. These samples therefore are not included in subsequent cluster analysis. Figure 4.8c is a dendrogram plot separating results into 12 clusters, each separated by a Euclidean distance of $d$<12 (Eq. 2).

How well the algorithm calculated the ordinate distance match to original dissimilarities is measured by a stress factor (stress = standardized residual sum of squares) (Chen and Chen, 2000, Anderson et al., 2008). After removal of outliers, the Kruskal fit scheme shows an acceptable/good stress value of 0.11 in 2D projection (K2) and excellent with stress value of 0.05 in 3D projection (K3) (Kruskal, 1964) (Fig. 4.8b).

To explore provenance patterns in time and space, Figure 4.8d shows provenance samples color-coded according to clusters in Figure 4.8c, then correlated stratigraphically where possible. Results show that before 20 ky BP (thick dashed black line in Fig. 4.8d), Pandora Trough was characterized by clusters 2, 4, and 7, whereas at that time Moresby Trough was characterized mostly by cluster 8 in all four Moresby Trough cores, with local contributions from clusters 4, 5, 6 and 7 . Variables that contribute to the dissimilarity are (% contribution): undifferentiated lithic fragments (25.02 %), pumice (16.43%), perthite (12.82%), anorthite (10.13%), polycrystalline quartz (9.85%) and monocrystalline quartz (7.33%). The Pandora Trough system is richer in: lithic fragments, perthite and quartz (both monocrystalline and polycrystalline) and Moresby Trough more abundant in pumice, anorthite and amphibole. There are lateral variations between location of MV29 (cluster 6) and the surrounding Moresby channel system (cluster 8) with major contributions to dissimilarity from undifferentiated lithic fragments (37.47%), perthite (13.57%), muscovite (12.82%), pumice (8.5%) and amphibole (8.46%). In comparison with surrounding cores, MV29 is depleted in lithics, perthite and pumice.

After 20 ky BP, Moresby Trough sediments shift from primarily cluster 8 to laterally correlated cluster 12. This shift is indicated by upward variation in perthite (26.26%), quartz polycrystalline (19.05%), pumice (14.9%), muscovite (9.45%) and amphibole (8.59%). Quartz and pumice decrease upward, and muscovite and amphibole increase upward.

In Pandora Trough, both MV54 and MV33 contain younger sediments from cluster 3 which consists of >75% combined lithics, polycrystalline quartz, muscovite, perthite, and monocrystalline quartz (Table 4.3). These sediments overlie cluster 7 that is found deeper in MV-23 (probably deposited before 30 Kyr and ceased afterward) but continuously deposited in MV-33. Cluster 3 is depleted in anorthite, with respect to cluster 7.

Sediments within similar age ranges from MV33 (ponded turbidites: Jorry et al., 2008) and toe of slope deposits (MV23), show contrasting composition, with MV-33 sediments from cluster 2 and 7 after 22,815 ky BP (the oldest age from MV-33), and MV-23 sediments from clusters 4 and 8 ( ~19- 30.4 ky BP). The major minerals contributing to dissimilarity are: perthite (47.53 %), quartz (19.34 %) and lithic fragments (17.18 %). The PT mini basin (MV-33) is depleted in undifferentiated lithic fragments and quartz but elevated in perthite. After 20 ky BP, sediment composition in MV33 shifts to cluster 3 but in MV-23 shifts to cluster 12, with cluster 12 depleted in lithics and elevated in amphibole, anorthite, and epidote compared to cluster 3. The lateral variation between MV-33 (clusters 2 and 7) and the rest of the Moresby channel system (clusters 6, 8, 10, and 11) is found in perthite (elevated in MV-33), polycrystalline quartz (elevated in MV-33), amphibole (depleted in MV-33), lithic fragment (elevated in MV-33) and anorthite (depleted in MV-33).

Western Moresby Channel (MV27) composition is similar to Moresby Trough before 40 ky BP (cluster 5), and shifts to clusters 4 and 7 after 40 ky BP, more similar to Pandora Trough (e.g. MV-23 core location) composition.

### 4.5. Interpretation and discussion

The timing and sources of terrestrial /fluvial sediment delivery to the deep GoP basins are presented using three distinct quantitative approaches for provenance analysis, all using data derived from SEM-MLA analysis described above. The Gazzi-Dickinson approach provides a well-documented approach to turbidite sand provenance analysis, across three dimensions that allows for comparison with many prior studies using this approach. CIA analysis will provide insights regarding the intensity of weathering before and during sediment delivery. Multivariate

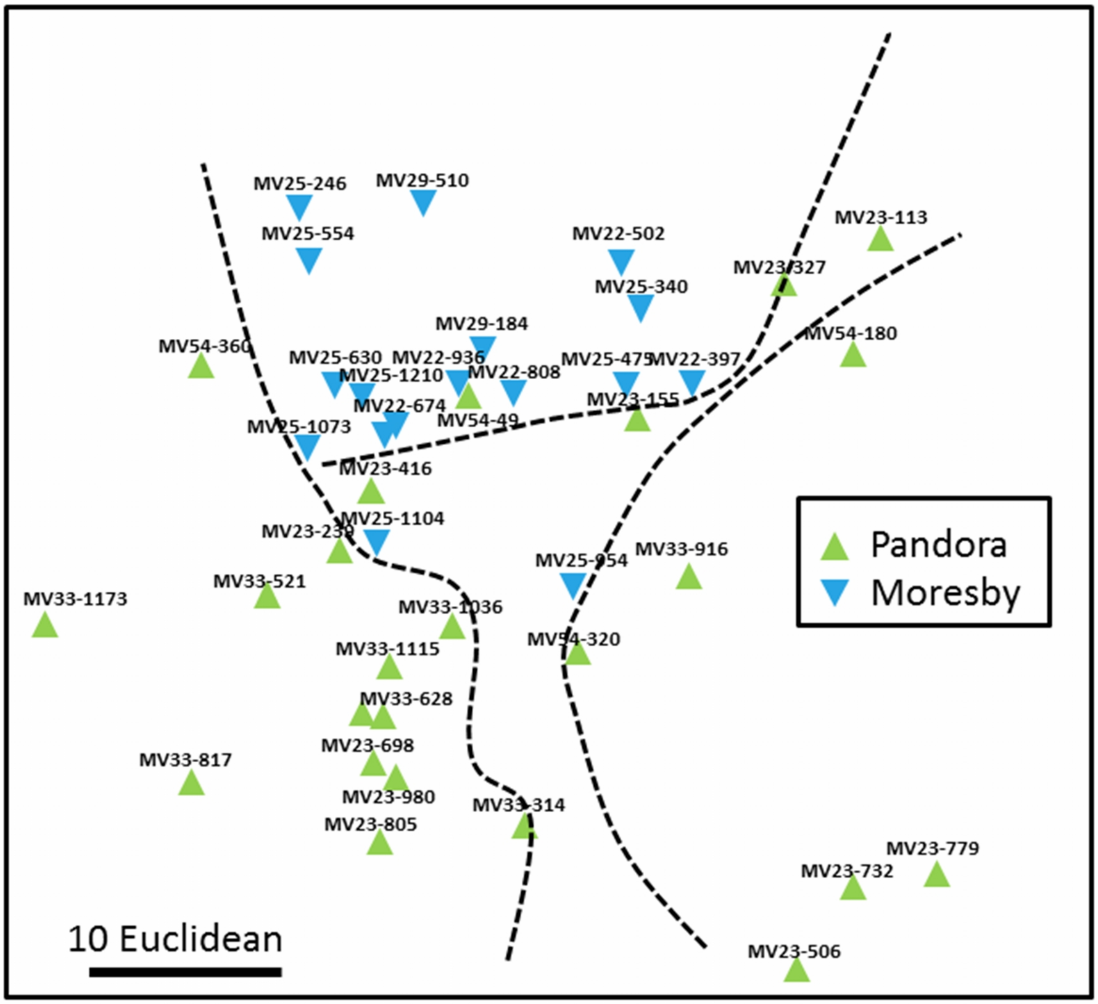


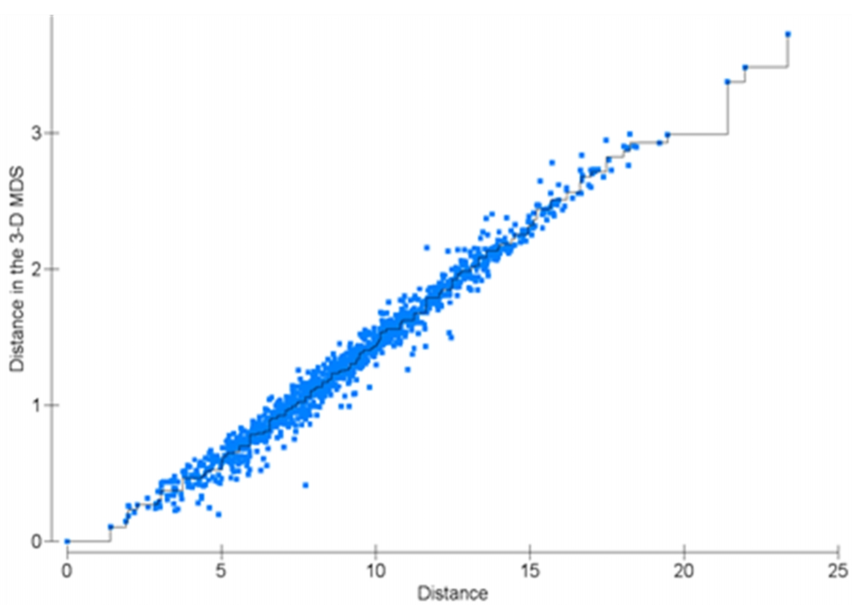


**Figure 4.8**. The non-metric dimensional scaling analysis (nMDS) (a) the test projection of 12D data shows a distinct geographical separation (b) *Kruskal* fit scheme in 3D

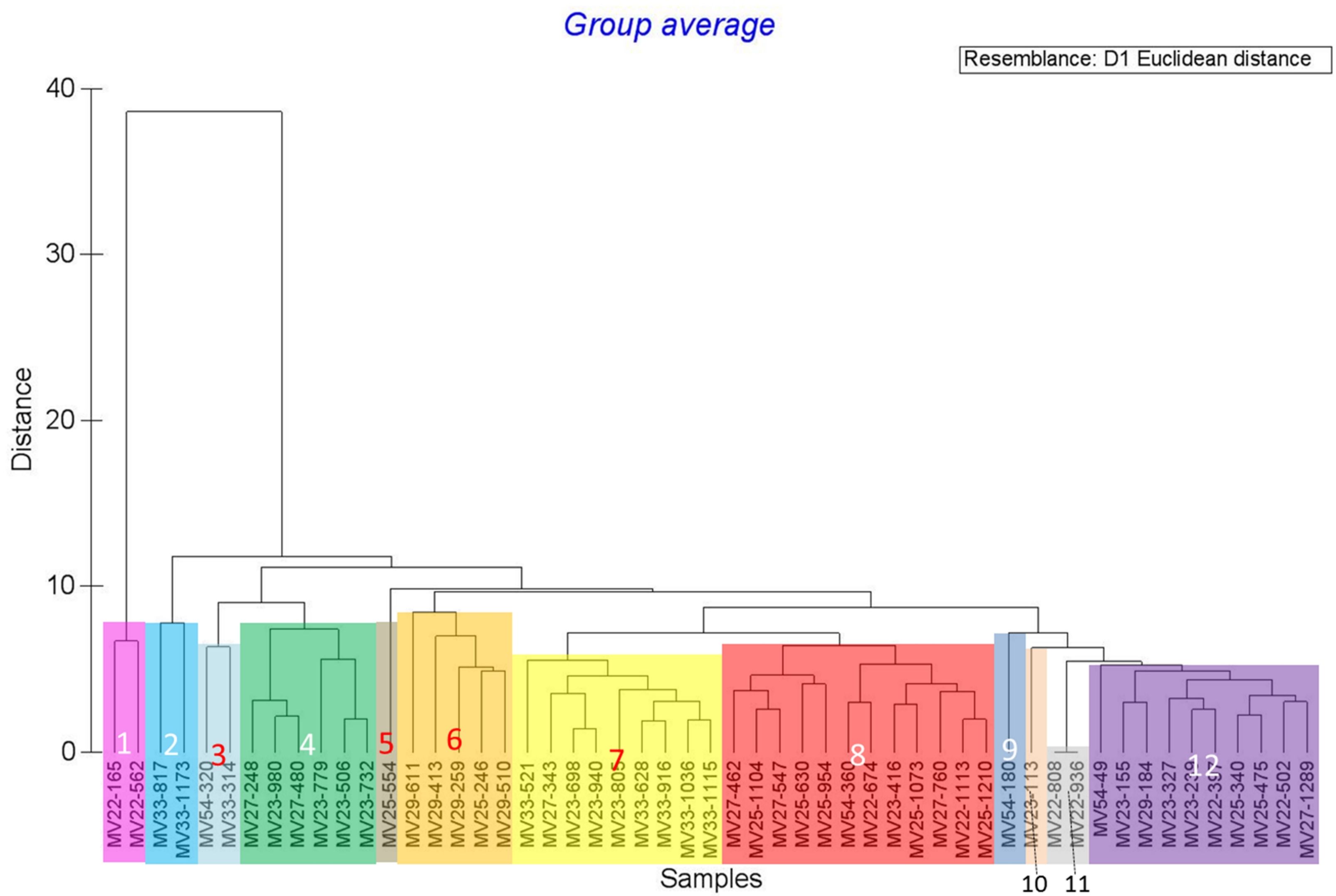


**Figure 4.8**(c) The dendogram that discriminate the data spread into 12 population

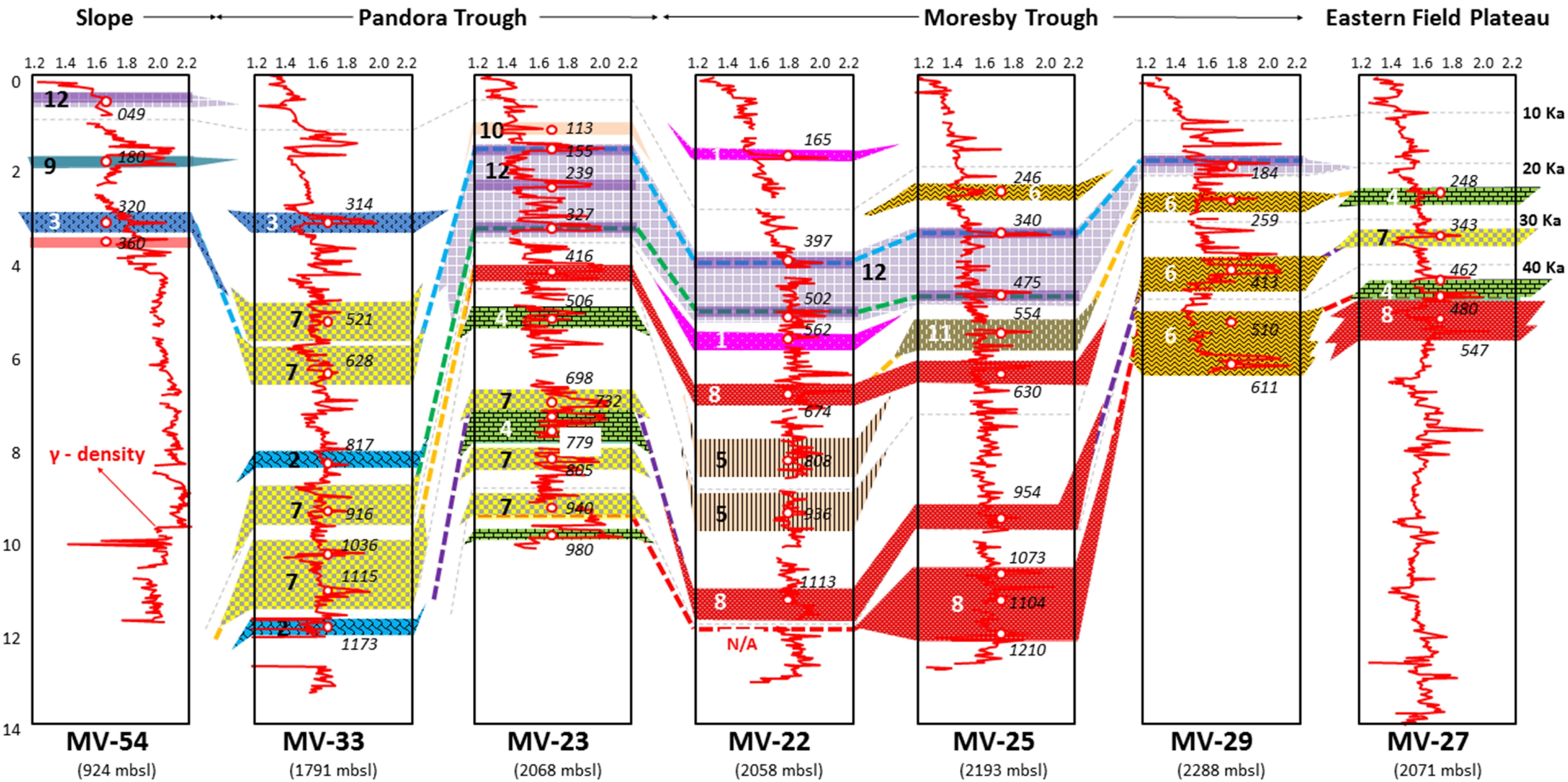


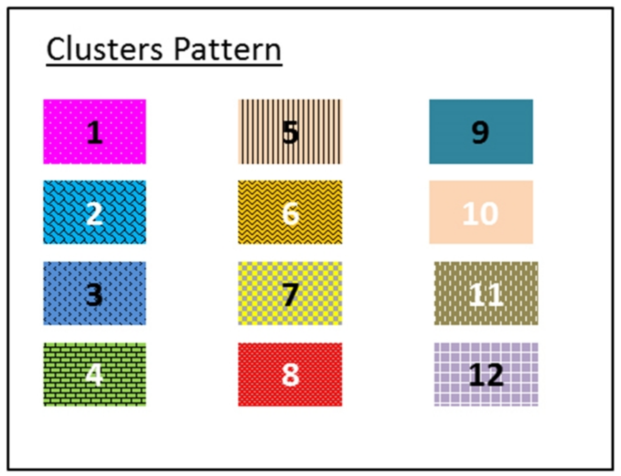


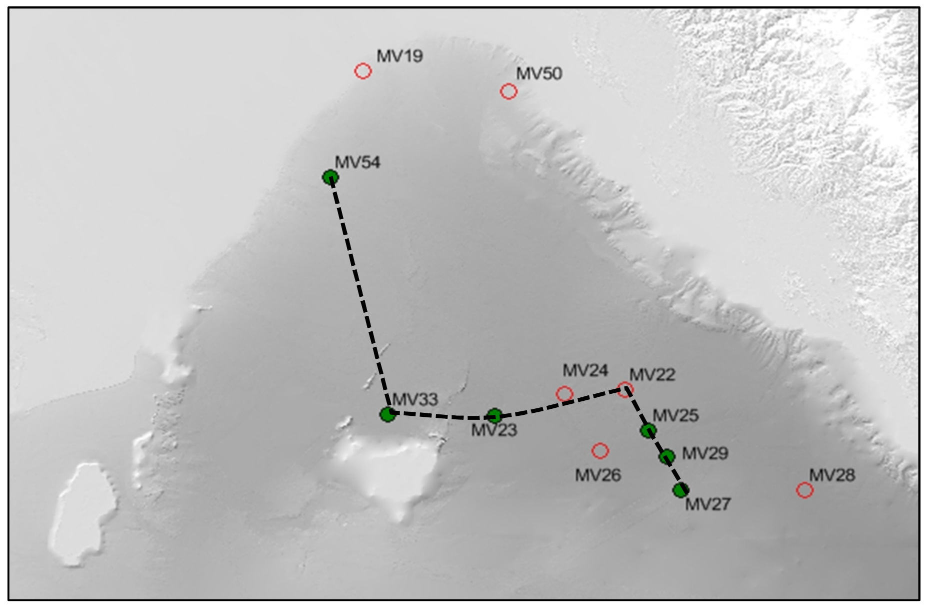


Figure 4.8d The correlation of the clustering results to see the possible stratigraphic relationships between core. Large number labels (white font) identify cluster number, and small italic label identify sample code (sample code correspond to sample depth [cm] in core.

statistical approaches will provide a richer perspective on sediment compositional variability that is limited only by the characteristics of grain populations (i.e., clusters in Table 3) rather than three prescribed ternary axes.

**4.5.1 Gazzi-Dickinson ternary diagram**

Turbidite sand provenance in Gulf of Papua was initially reported as contrast variation between the mature quartzofeldspathic sand derived from Papuan Mainland and immature glass rich volcaniclastic sand with rhyolitic composition (75-77% wt. SiO2 and 4.9 – 7.6 wt.% of Na2O + K2O from the Papuan Peninsula (Patterson, 2006). However, Patterson (2006) collected data from only cores MV-22 and MV-66 with three samples from each core. Our results build on this, and show more compositional variation and wider trends compositional trends, ranging from recycled orogen (RO) and magmatic arc provenances such as transitional and dissected arc (TA and DA) in Pandora Trough to continental block provenances such as Basement Uplift (BU) and transitional continental (TC) in Moresby Trough (Fig. 4.5b). These variations likely reflect variability in sources terranes and sedimentary transport and routing. Based on the ternary diagram we divided the provenance in the GOP into:

<u>Recycled orogen</u>: these sediments originated from collisional uplift of the Papuan orogen. This constitutes a background pattern in the entire study area and is at times a major assemblage in both Pandora and Moresby Troughs. The composition range is 40-75 % quartz, 10-55 % lithic fragments and 20-48 % feldspathic minerals. Although not quantified specifically, we note that the detritus eroded from these source rocks is rich in sedimentary to metasedimentary lithic fragments (Fig. 4.9b). There are compositional variations among sediments originating from the Papuan Peninsula and Papuan mainland mostly in volcanic and mafic composition, particularly

due to ultramafic and metamorphic rocks from the ophiolite belt of the Papuan Peninsula, not found in the Papuan Mainland (Fig. 4.2).

High Feldspar: the composition of these samples reflects the provenance derived from source terranes within continental plates rich in potassium feldspar to plagioclase feldspar (continental block provenance). There are two provenance classes within this group found in the study area, basement uplift (BU) and transitional continental (TC), which might not have originated from continental block provenance. One possible explanation is that some of the samples are high in feldspar content and mature minerals such as zircon because of volcanogenic sources (samples MV22-165 and MV22-562) (Fig. 4.9A), and some contain high proportion of eroded felsic intrusives (all samples from MV-29) (Fig. 4.9b). In this case, the ternary diagram fails to discriminate provenance effectively, as all samples plot into the continental block field.

High Albite: there are two albitization patterns common in sand, either diagenetic, e.g. where the partial albitization following the fractures zone or other weak zones such as grains contact, twinning zone; or zoning, evident as radial zoned albitized appearance where anorthite resides in the middle or grain core as it is has a higher melting point (Ramseyer et al., 1992, Gonzales Acebrón et al, 2010). One sample from Moresby Channel (MV25-475) shows partial albitization in K-feldspar which is probably diagenetic in origin (Fig. 4.10).

Magmatic arc: this is defined as provenance derived from volcanogenic arc, either directly as volcaniclastic debris (un-dissected arc) or derived as a by-product of denudation processes of the volcanic highland and the underlying intrusives (dissected arc) (Dickinson and Suczek, 1979). This provenance shows substantial pumice/amorphous mineral percentage (6-15 %); igneous lithic fragments are common (Fig. 4.9c). This provenance class was found in both of the trough systems. PT is more dominated by dissected arc, with where the elevated potassium feldspar came mostly from roofing of the plutonic/hypabyssal rocks such as pegmatite, whereas samples from Moresby Trough are more dominated by transitional arc lithologies, with sources such as Neogene and tertiary volcanic rocks abundant in Papuan Peninsula (Fig. 4.2).

### 4.5.2 Chemical index of alteration (CIA)

The CIA ternary diagram (Fig. 4.7a) and summary Table 4.2 shows that most samples from the Pandora Trough system and the Fly/Strickland rivers are highly weathered (high in $Al2O_3$). This is consistent with both the observed geology (abundant recycled shelf and terrestrial sediments and uncommon recent volcanics), as well as the long-distance transport through extensive alluvial valleys of the large rivers feeding the western GoP, and most proximal to the central and eastern Pandora Trough. Samples from Moresby Trough show lower CIA, consistent with delivery from proximal sources (including the Papuan Peninsula) that include abundant young volcanic and intrusive rocks (Fig. 4.9c). Transit times from sediment source to sink would be shorter here than farther west, due to short and steep rivers with less alluvial valley storage than the Fly/Strickland, for example (Brunskill, 2004).

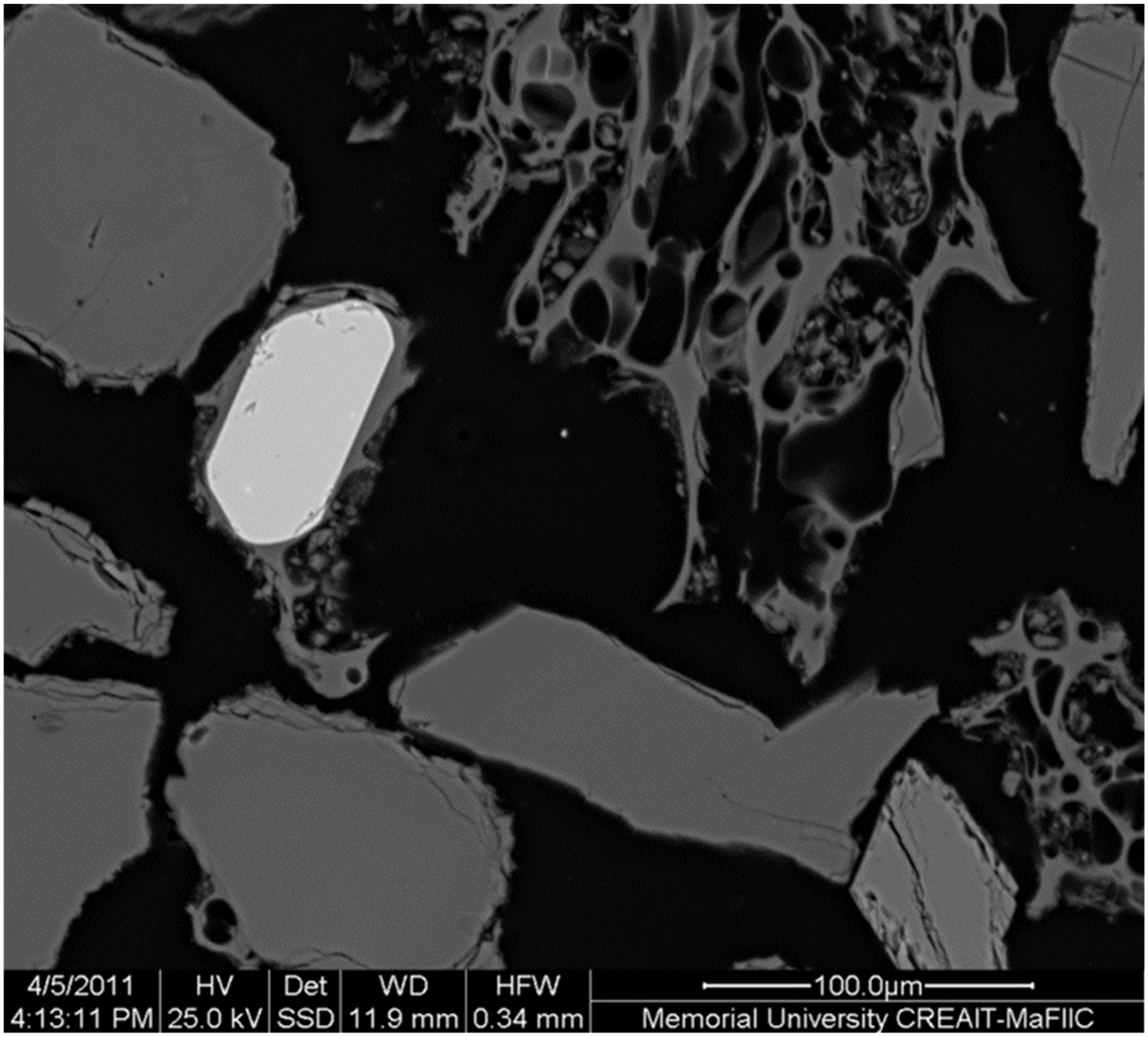


**Figure 4.9**. (a) Backscatter image of sample MV-22-562 (core MV-22 interval 562 cm) shows a zircon mineral that associated with fresh pumice

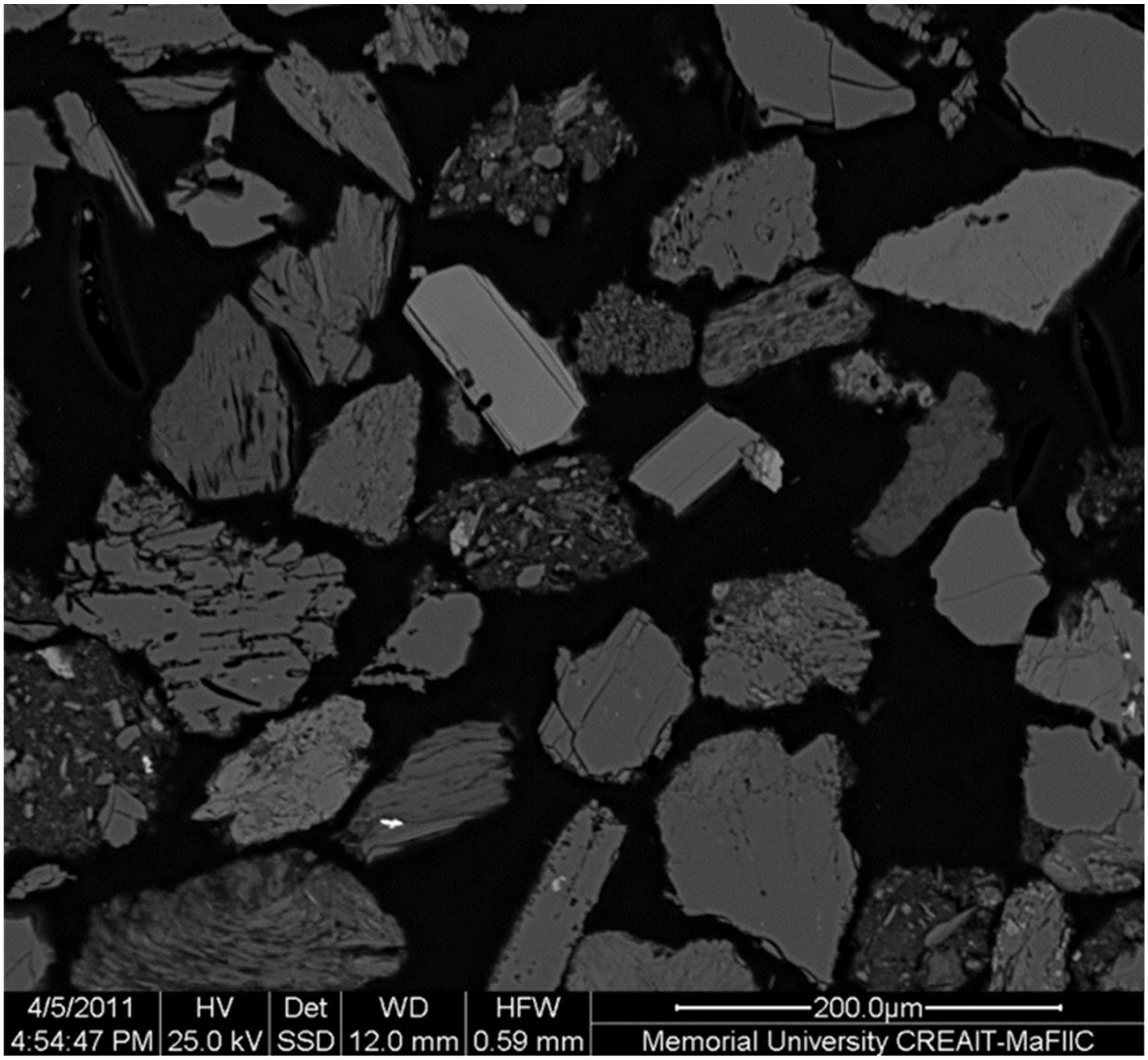


**Figure 4.9**. (b) sample MV-29-611 shows abundance of eroded intrusive fragments together with sedimentary and metasedimentary lithic fragments.

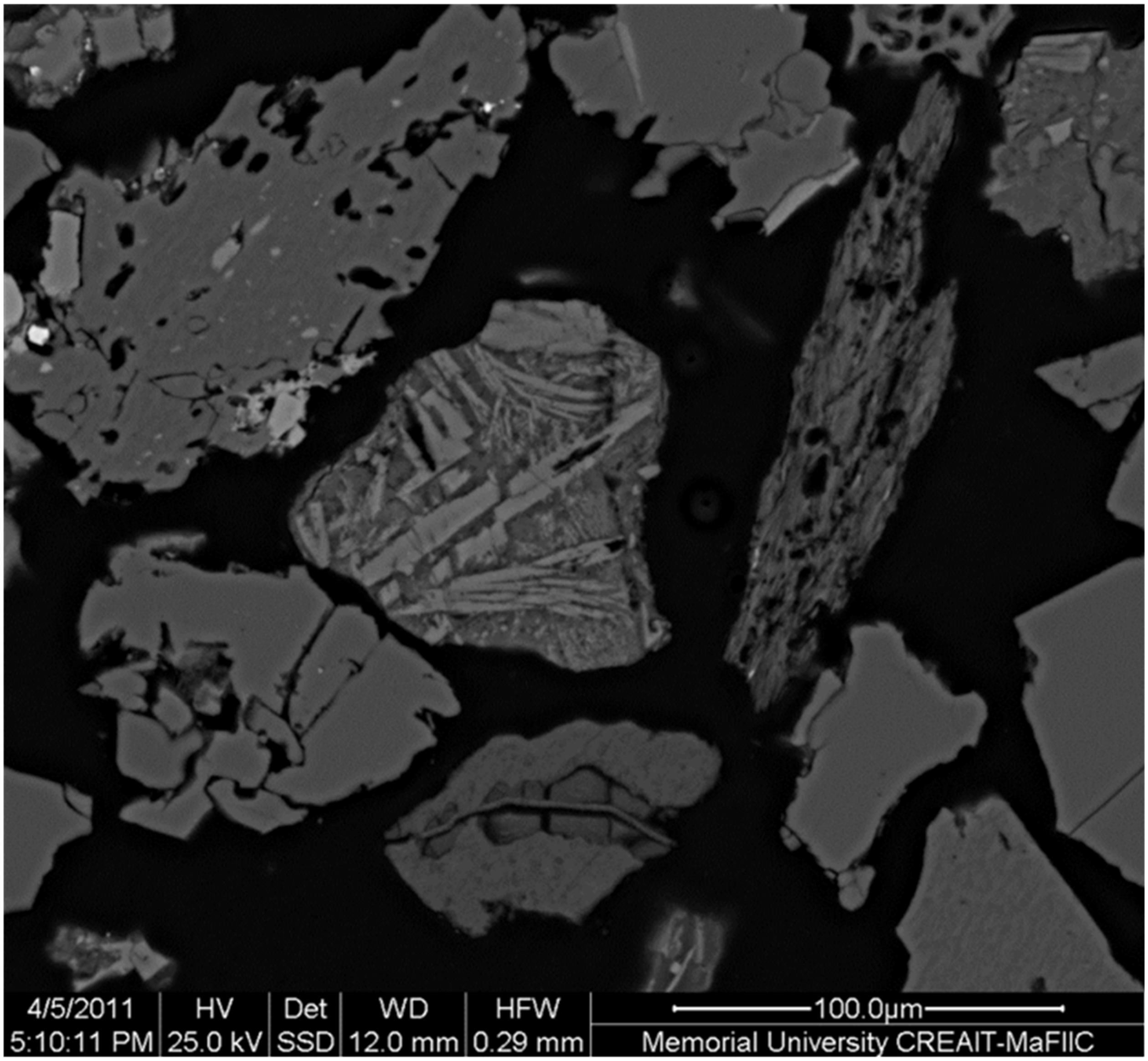


**Figure-4.9** (c) Sample MV25-1073 shows eroded mafic extrusive fragment and pumice materials

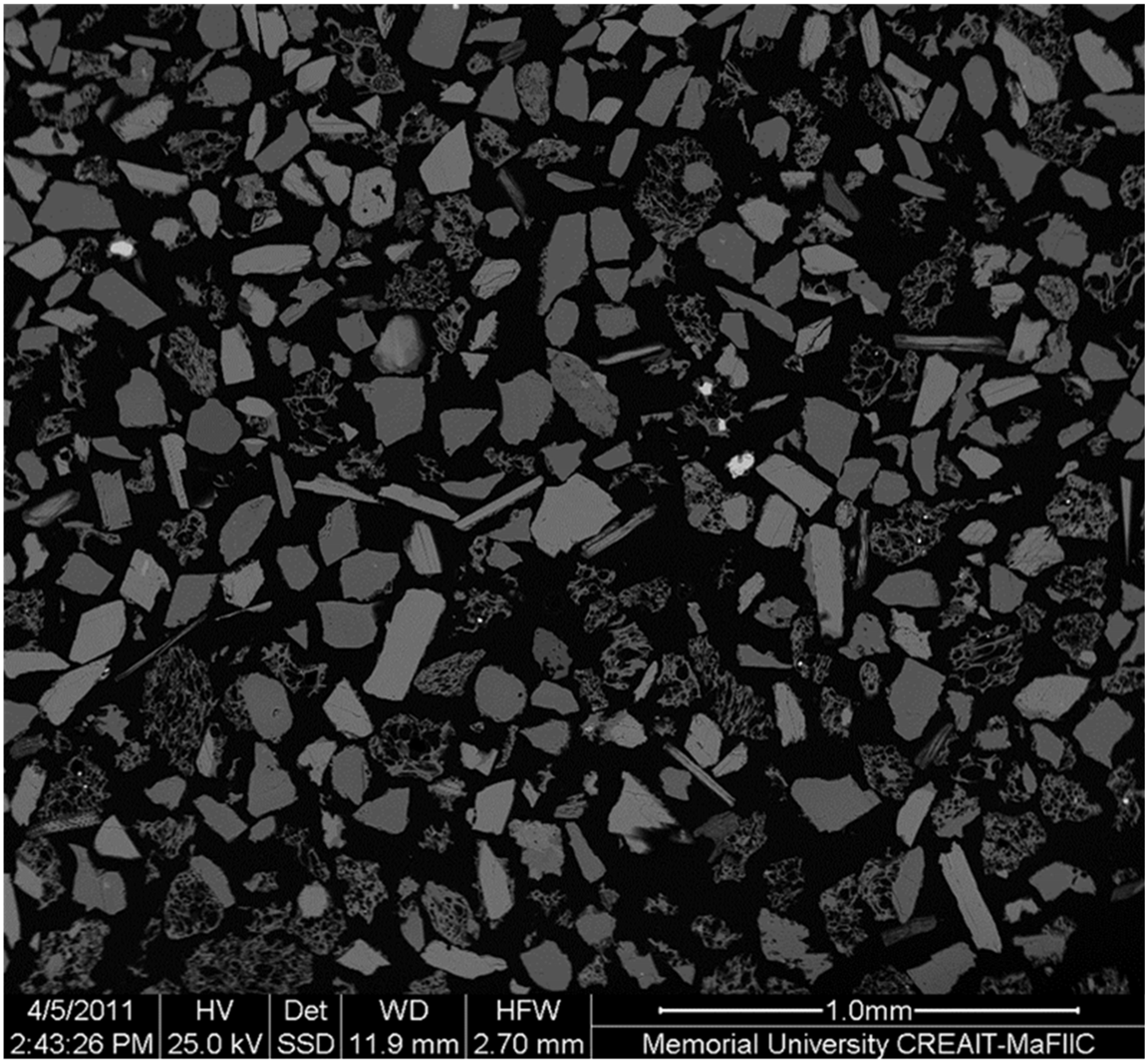


**Figure-4.9** (d) Sample MV-33 -1173 which is abundance in pumice

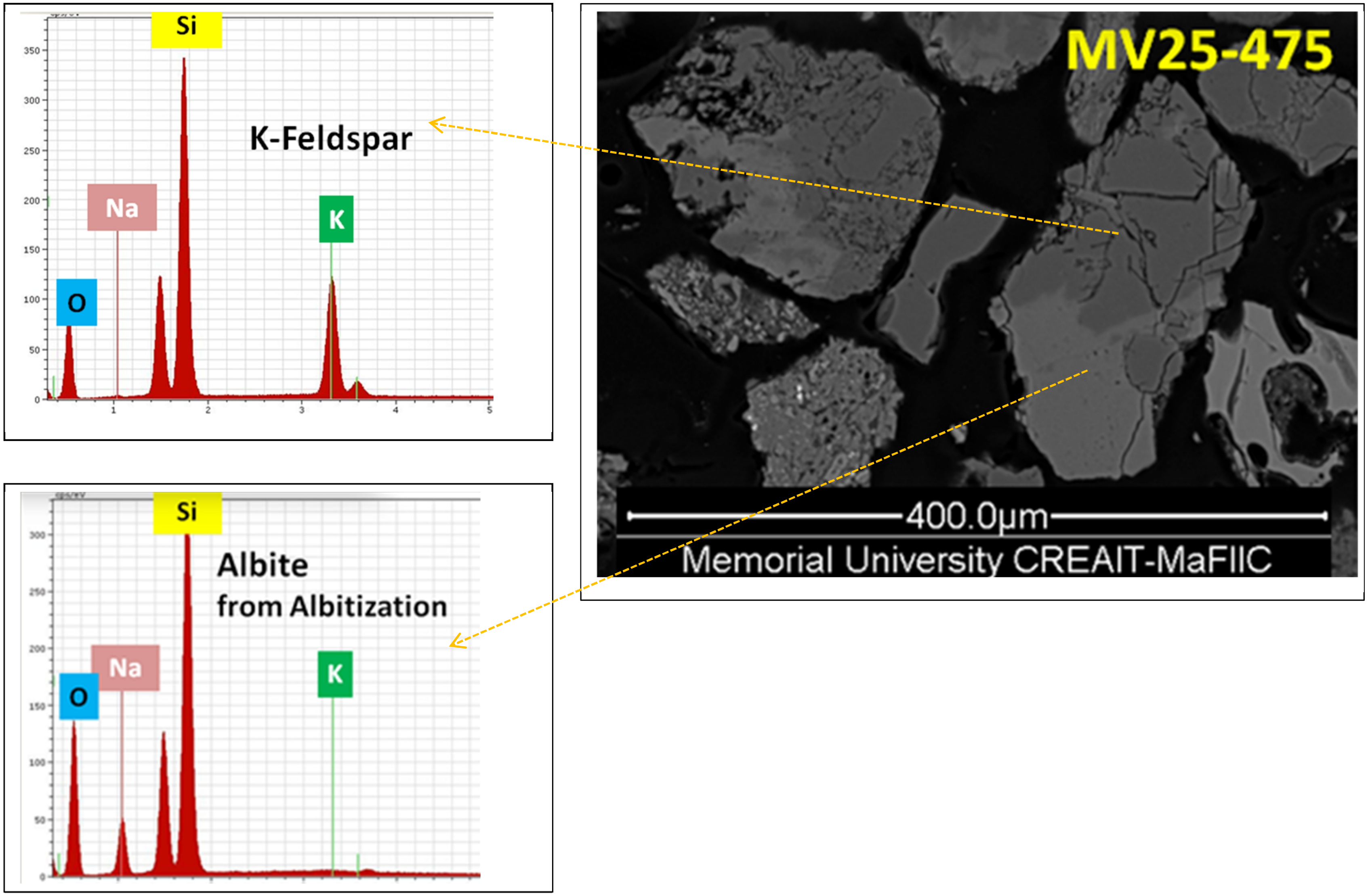


**Figure 4.10**. Backscatter image of sample MV25-475 shows partial Albitization (see text for details).

High $K_2O$ characterizes two samples from the PT basin floor, MV33-1173 and MV33-314 (Fig. 4.7a). This might be explained by volcanic activity providing fresh volcanic sources. The backscatter image of MV33-1173 (Fig. 4.9d) also shows that this sample contains abundant pumice. Similarly, Moresby Fan samples MV22-165 and MV22-562 are relatively low in $Al_2O_3$ also low in CIA (Fig. 4.8a). Each of these cases could be explained by sediment sourcing from fresh volcanic formations during their respective time frames.

These results suggest a reduction in the degree of chemical weathering experienced by formations providing sediment to the lower PT and MT, which could be explained by cooler conditions and less intense chemical weathering rates around the LGM (Fig. 4.7b; Nesbitt and Young, 1982).

**4.5.3 Non metric multidimensional scaling analysis (nMDS)**

Samples MV22-165 and MV22-562 were statistically classified as outliers (and excluded from cluster analysis) due to their unique composition (cluster 1, Table 4.3) which is consistent with volcanogenic origin. Seabed delivery could have been relatively direct, via atmospheric fallout, or via seabed-sediment transport of lightly reworked material.

Stratigraphic correlation of clusters (Fig. 4.8d) shows that before 20 ky BP, PT and MT received sediment from different sources (PT, primarily clusters 2, 4, and 7; MT, primarily clusters 3, 6, and 8). Major compositional differences are that the PT system before 20 ky BP is richer in lithic fragments, perthite and quartz (polycrystalline and monocrystalline) whereas Moresby Trough system is richer in anorthite, amphibole and pumice. These results suggest that Pandora Trough turbidite sands are sources from felsic plutonic, sedimentary, and meta-sedimentary source rocks of the Papuan orogeny (Davies, 2012, and Fig. 4.2), which is mostly drained by relatively large rivers (Fig. 4.1). In contrast, Moresby Trough turbidite sands originated from strata including younger volcanic and ultramafic rocks of the Papuan Peninsula (Fig. 4.2) delivered via smaller, steeper rivers with more rapid transport and shorter residence time in alluvial deposits. Provenance of MV27, on the western flank of MT, has a similar characteristic with the MT provenance before 40 Kyr. BP (cluster 8), then switches to provenance more consistent with PT cores (clusters 4 and 7, high in quartz, feldspar and lithic fragments) after that period.

After 20 ky BP, sediment composition becomes similar across the PT upper slope (MV-54), PT toe of slope (MV-23) and the entire Moresby Trough system except MV 27, with increased quartz and feldspar grains of cluster 12 (Fig. 4.8d, Table 4.3). Comparison of cluster 9 mineral compositions with terrestrial sample composition (Figs. 4.6a and 4.6b) and regional geology (Fig. 4.2) suggests that this channel levee system was receiving mixed sources both from the Papuan mainland and Papuan Peninsula. This linked depositional system extended from Pandora Trough toe of slope MV23 (also just upslope from Moresby Channel) into Moresby Trough (MV25 and MV22). Samples from this system post 20 ky BP are high in perthite, polycrystalline quartz similar to the Pandora Trough provenance but also high in mafic minerals such as amphibole and anorthite, more consistent with MT and the Papuan Peninsula, suggesting major sediment sources from the northern GoP and Papuan mainland were mixing with Neogene volcanics from the Papuan Peninsula.

Most samples from MV29 (interpreted in Chapter 2 of this study to be near the channel thalweg) show more mature composition depleted in lithic fragments and perthite, and elevated in mafic components such as amphibole (cluster 6, Fig. 4.9b and Table 4.3) compared to other localities in Moresby Channel, suggesting a localized source from the Papuan Peninsula not widely represented in other cores.

### 4.5.4 Synthesis

Figure 4.11 conceptually illustrates sediment sources and delivery to the PT and MT over five time spans encompassed by one or more core age models, supplemented with a Pleistocene-Holocene sea level curve (Lisiecki and Raymo, 2005) highlighting the time interval of interest (oldest to youngest): Early MIS3 (>40 ky BP; sea level 50-70 meters below present sea level (mbpsl); Fig. 4.11a,), late MIS3 (30-40 ky BP; sea level 60-80 mbpsl; Fig. 4.11b); early MIS2 (20-30 ky BP; sea level 70-120 mbpsl; Fig. 4.11c); mid MIS2 (17-20 ky BP; sea level 100-120 mbpsl; Fig. 4.11d); and late MIS2/early MIS1(<17 ky BP; sea level 100-50 mbpsl; Figs. 4.11e and 4.11f). Ages of marine isotope stages are from Lisiecki and Raymo (2005).

Early MIS3 (>40 ky BP)

During early MIS 3 (Fig. 4.11a), sea level was ~50-70 m lower than present, and there were two major sediment sources to the MT and PT documented by cores with sediments of this age (MV23, 25, and 27), likely the Papuan mainland and Papuan Peninsula to the east, based on proximity and lithology (Figs. 4.1 and 4.2). Sediments along the western flank of Moresby Trough were likely sourced from the central to eastern Papuan Mainland including felsic and recycled sedimentary provenances (MV23 basal samples, clusters 4 and 7) (Davies, 2012)(Fig. 4.2). Eastern MT and Moresby Channel likely received sediments from the Papuan Peninsula and easternmost mainland via rivers entering the eastern GoP (MV25 and MV27 basal samples, cluster 8), including relatively abundant volcanics and ultramafics (Davies, 2012) (Fig. 4.2).

Late MIS3 (33-40 ky BP)

During late MIS3 (Fig. 4.11b), sea level was falling through ~70-80 mbpsl, which may have induced incision and erosion in near-coastal portions of many river systems, and enhanced sediment transport across the narrowing continental shelf (Covault et al., 2007, Covault et al., 2011). MT continued to receive sediments consistent with Papuan Peninsula rock types (MV22 and 25; clusters 8 and 10, Table 4.3) (Davies, 2012) (Fig. 4.2). Chronostratigraphy for MV27 is constrained by $\delta^{18}O$ stratigraphy (McFadden, unpublished, cited in chapter-2 of this thesis), 2015), and with the cluster stratigraphy in Figure 4.8d suggests that sediments of cluster 4 were being transported down the eastern PT (MV23) and western MT (MV27) during this time interval (Fig. 4.3b), suggesting a shared source for sediment in these two cores during at least part of this time span.

Figure 4.3b illustrates modern bathymetry in the study area, along with submarine channel thalwegs determined from slope analysis of the modern bathymetric data set used for Figure 4.3b (Daniell, 2008, processed as described in Patterson, 2006, and Francis et al., 2008). It is unlikely that terrigenous sand could have been delivered to MV27 from locations directly upslope at that time, because MV27 is located on the deep flank of a mid-ocean plateau (Eastern Fields Plateau), with no obvious sources of terrigenous sand. Although modern bathymetry has almost certainly changed from the local bathymetry of 30-40 ky BP, the presence of a modern thalweg connecting locations of MV23 and MV-29 (immediately downslope of MV27) does suggest the possibility that comparable delivery conduits might have existed during late MIS3. Core chronostratigraphy documents 3-10 m of local seabed aggradation at these core locations over the past 30-40 ky. The present water depths at MV23 and 27 are comparable (2068 and 2071 m respectively), but present difference in depth between MV23 and the thalweg at MV 29 (water depth 2288 m) is

~220m over a distance of ~200 km (slope of ~11 m/km), within the range of gradients required for sustained turbidity current transport (Wright et al., 2001).

Collectively, these observations suggest that sediments sourced from geologically distinct locations and carried by sediment-gravity flows (northwest of MV 54 and 33, and northeast of 54 and 23; Figs. 4.2 and 4.3b) could be delivered to one location from multiple submarine channels that presently converge between MV23 and MV29. Based on modern channel elevations and core locations in Figure 4.3b, sand that accumulated near MV27 ca. 20 ky BP to >40 ky BP (chapter-2 and 3 of this thesis) would have required turbidity currents suspending sand >200m above the thalweg elevation downslope of MV27. Core MV29 is constrained chronostratigraphically by only one basal dead radiocarbon measurement and tenuous litho-correlation (Chapter 2 of this study), and contains sediments of different composition from surrounding cores (cluster 6), potentially from a unique local source not previously identified, or at a different time (if our lateral chronostratigraphic correlations are incorrect). Considering the flow energy likely required for elevating sand suspensions >200m above the bed, non-deposition or seabed erosion (exposing older sediments) is one plausible explanation for the provenance contrast between MV29 and surrounding cores in sediments >2m in the seabed. One possible explanation for differing lithologies in sediments of the same age in MV27 compared to MV22 and 25 is that only turbidity currents along the MV23-MV29 route were energetic enough to deposit sands 200 m upslope from the thalweg (i.e., at MV27), whereas turbidity currents arriving from more eastern thalwegs did not suspend sand to the same elevations. This mixing of sediments from multiple sources at this time is supported by the comparable CIA values for sediments of this age in these cores, shown in Figure 4.7a (CIA values of 65-75 immediately preceding MIS2 in each core).

Early MIS2 (20-30 ky BP)

During early MIS2 (30-20 Kyr BP), (Fig 4.11c) sea level dropped through 70-120 mbpsl, sub-aerially exposing continental shelves adjacent to the PT and MT. Our age models cannot resolve elevated sediment supply at this time, but core lithology (Chapter 2 of this study)documents abundant sandy turbidites in core sediments of this age from the PT (MV23 and 33) and MT (MV 22 and 25) (Fig. 4.4). Sand compositions indicated by cluster analysis (Figs. 4.8 and 9b) suggest multiple local sources. Single occurrences of individual clusters include clusters 1 and 11 in MV22, and cluster 5 in MV25. Cluster 8 is shared by MT cores MV22 and 25, as well as MV23 which is >200 km up-channel, along a channel axis very distant from that feeding MV22. The MV27 location, 200 m above the thalweg on the western edge of MT, continued to receive sand from turbidity currents with the same composition as the previous time span (clusters 4 and 7) which differs from the composition of sands that accumulated both closer to the main thalweg, and along up-channel location MV23 (Figs. 4.3b for location and Fig. 4. 8d).

During this time span, the occurrence of cluster 4 at MV27 is unique, and is the last sand body deposited at this location, to the present. Cluster 4 compared to cluster 8 is enriched in monocrystalline quartz and lithic fragments, and depleted in epidote, amphibole, polycrystalline quartz, and chloritoid, and is generally consistent with the more sedimentary/felsic provenance of western catchments feeding sediment to our study area. Contrasting sediments were accumulating both up-channel and down-slope, suggesting that contrasting delivery mechanisms may have been transporting sands to the locations of MV27, compared to MV23 (PT) and MV 22 and 25 (MT), such as direct or indirect volcanic delivery, versus fluvial supply of reworked terrestrial sediments. It is also possible that our age models for this time period are inaccurate, resulting in faulty chronostratigraphic correlations. Regardless, this time span appears to have been characterized by diverse sediment sources and compositions, which is generally consistent with many regional rivers crossing the exposed shelf, delivering local sediment directly to the most proximal basins, a condition consistent with the lowest sea level of the LGM that occurred near the end of this time span.

<u>Mid MIS2 (17-20 ky BP)</u>

Mid MIS2 (20-17) Kyr BP (Fig 4.11d), sea level 100-120 mbpsl, coincides with the Last Glacial maximum (23-19 Kyr BP from Oxygen isotope curve, 20-18 Kyr BP from CIA curve in this study). The sea level is in the lowest position recorded, and shelf area is sub-aerially exposed. During this time, sand is no longer being deposited at MV27, and the locations of MV23, 22, 25, and 29 (based on potentially inaccurate chronostratigraphic correlation) are all accumulating sediments of cluster 12 composition. Compared to cluster 8 composition (which characterized many cores during the previous time span; Fig. 4.8d), cluster 12 is enriched in chloritoid and amphibole, and depleted in pumice and perthite (Table 4.3), suggesting possible increase in the relative proportion of sediment delivery from the more mafic/ultramafic Papuan Peninsula, compared to the more felsic/sedimentary Papuan Mainland (Fig. 4.2; Davies 2012), or alternatively, expanded exposure and erosion of such mafic/ultramafic materials in proximal catchments.

This similarity of sediments deposited in the up-channel regions of MV23 and 22 to the thalweg-proximal locations of MV25 and 29 contrasts with the compartmentalized composition of sediments deposited during the previous time interval. This relative uniformity could be due to either the effects of very large turbidity currents that transport uniform material across large areas, or because similar sediment types are being produced in multiple catchments. Cessation of sand accumulation at MV27 at this time suggests that the latter explanation could be more plausible. This uniformity does not encompass sediments accumulating in PT at this time (MV33, clusters 2 and 8). The lack of continuity between MV33 and MV23 is possibly attributable to blockage of sediment-gravity flows by a large mass-transport deposited between PT and MT, that likely occurred near the LGM, according to morphological and chronostratigraphic analysis (Chapter 2 of this study).

Late MIS2/early MIS1(<17 ky BP)

During late MIS2/early MIS1(<17 ky BP sea level 110-0 mbpsl) (Fig 4.11e and f), sediment delivery to deep GoP basins decreased greatly, particularly following the Younger Dryas stadial (Jorry et al., 2008), although local delivery of mostly muddy sediment continues to the present at modest rates (Muhammad et al., 2008; Howell et al., 2014). Sandy sediment delivery to the location of MV54 appears to begin abruptly ca. 16 ky BP (Febo et al., 2008) then cease abruptly as well ca. 15-14 ky BP, near the time of a major deglacial melt-water pulse (Melt-water Pulse 1A) (Liu et al., 2004; Kubo and Syvitski, 2006; Febo et al., 2008) (Fig. 4.4). During this time, sandy MV54 sediments were composed of (old to young) of clusters 8, 3, 9, and 12, a general increase over time of mafic/ultramafic and low-grade metamorphic products (Table 4.3, Fig. 4.8d). These relatively rapid changes in sediment composition at MV54 are consistent with changes in organic content and magnetic properties identified in the same core by Febo et al. (2008), and are coincident with the flooding of the outer shelf at that time (based on the regional sea level curve of Howell et al. [2014]); this suggests that these changes are associated with sediment dispersal processes that shift rapidly as the shelf and associated incised river channels are flooded, and tidal and coastal processes begin to influence river mouths more strongly. Sandy sediment delivery to PT (MV33) ceases during MWP1b, then resumes during the Younger Dryas (ca. 12.5-11.5 ky BP) (Jorry et al., 2008)(Fig. 4.4), retaining generally felsic/sedimentary provenance (clusters 7 and 3, old to young) (Fig. 4.8d) consistent with modern Fly/Strickland sediment composition (Figs. 4.5 and 4.6) (Milliman, 1995; Brunskill, 2004). Elsewhere in the deep basins, sandy sediment delivery ceases (MV23 and 27) in some locations, while sediments of clusters 6, 12, and 1(uniquely at MV22) are reaching the deep MT, from sources that include fresh volcanics (cluster 1) as well as weathered and eroded mafic/ultramafic rocks (cluster 12). Because these deposits are largely localized on the eastern margin of MT, likely sources are proximal, upslope of MV22, from the Papuan Peninsula (Figs. 4.2 and 4.3b). Unlike other locations in this study, relatively rapid sediment accumulation continues at MV22 into the middle Holocene (Fig. 4.4, at least 24 cm/ky since 7.4 ky BP) (chapter-2 this thesis), containing abundant fresh pumice (Table 4.3, Figs. 4.9a and also 4.9d), which is consistent with proximal supply of fresh volcaniclastic sediments (Patterson, 2006).

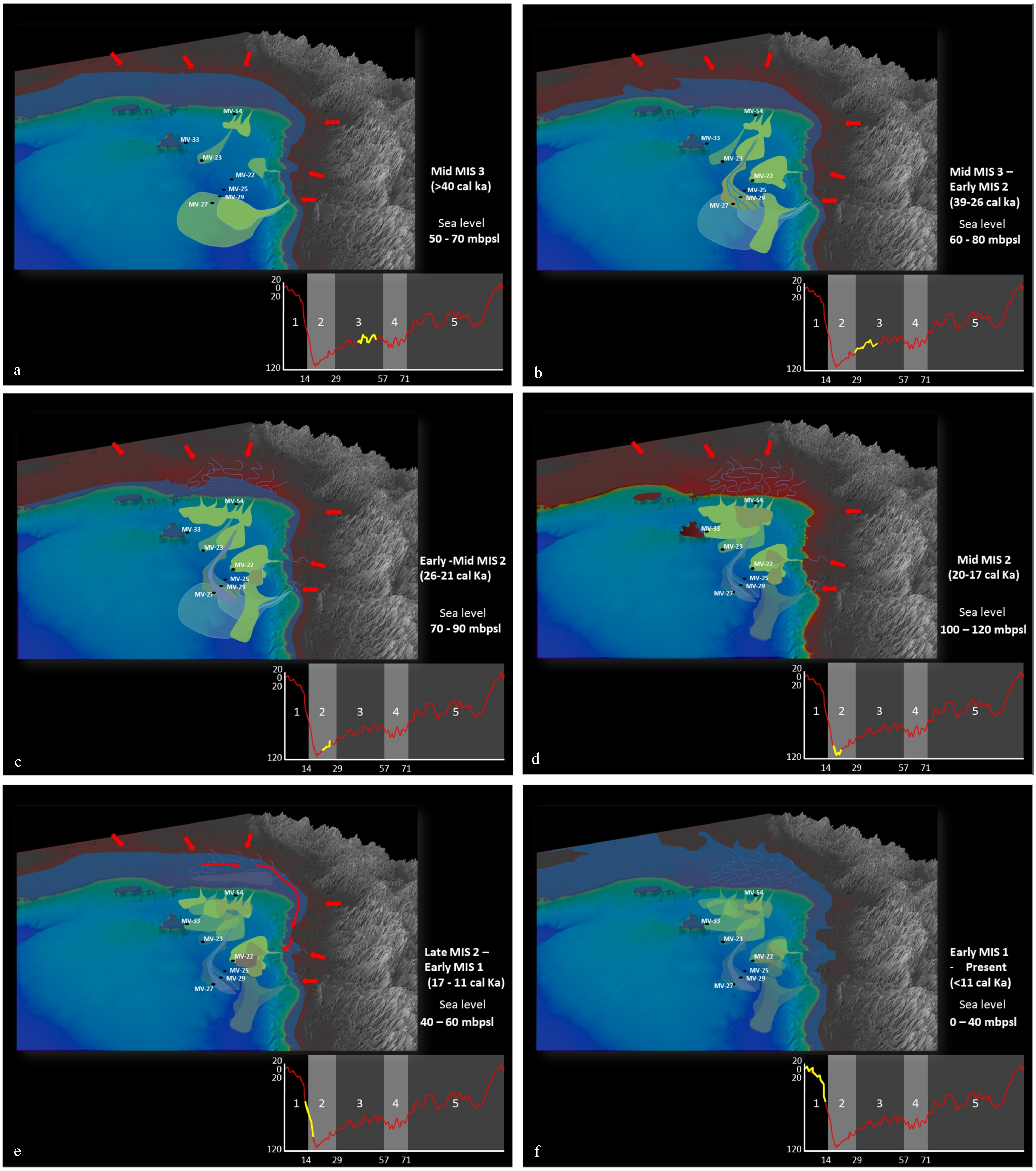


**Figure-4.11** (a-f) Late Quaternary source to sink reconstruction in GoP

### 4.6.Conclusion

This study of SEM-MLA provenance analysis has yields the following insights, regarding both applicability of this powerful analytical tool, and the geological evolution of deep GoP sedimentary basins since the late Pleistocene.

Methodology:

1. SEM-MLA can be used to replicate Gazzi-Dickinson provenance analysis. SEM-MLA results do not introduce artifacts due to methodology, and can yield a broader and more insightful classification of samples than manual point counts. For our samples, particle-based SEM-MLA counts yielded the broadest classification of samples, with no evidence of artifacts.
2. The combined use of SimPer and nMDS allows determination of sample clusters based on the information content of SEM-MLA analysis, rather than a prescribed three-dimensional space such as a ternary plot. This approach is much more effective at discriminating differences and similarities across large datasets with many parameters than is the case for more traditional QFL analysis.

Geology of Study Area:

3. The chemical index of alteration (CIA) shows that Pandora Trough in general is characterized by more highly weathered minerals compared to the Moresby Trough, and minimum values of CIA were evident for some locations near the time of the LGM, indicating some combination of low weathering rates, rapid erosion, and rapid transport from land to deep-sea basins.
4. Cluster analysis of sample mineralogy yields a story of sediment delivery along a ~500 km into basin margin that is much more complex than initially imagined. Results indicate

that sediment delivery to and conduit connectivity between deep-sea basins evolves over time due to the combined effects of eustasy and dynamic seabed morphology. Multiple terrestrial sediment sources along a ~500 km basin margin initially converge to form one continuous deep-sea system of channels and two major basins prior to 30 ky BP, that become bathymetrically separated by a large mass-transport deposit. Subsequent sea-level fall approaching the LGM initially drives re-partitioning of sediment sources to create multiple compositionally distinct depocentres, presumably due to migration and incision of individual rivers across the newly exposed coastal plain. Multiple separate deep-sea channels then regain compositional similarity near the end of the LGM, possibly due to regional erosion into compositionally similar catchment rocks. After this, sand transport to the deep basins shuts down, except for one depocentre (MV22). This is likely due to combined factor of (1) morphological setting where the shelf-slope distance is narrow thus ease the access from river mouth into shelf edge and reduce shelf trapping capacity (2) oceanographic processes namely long-shore drift current which actively entrain sediment during the flooding event in shelf corridor, and (3) based on mineralogical composition; probably contain an additional terrigenous influx from local volcanism that remain active into the Middle Holocene.

## 4.7.References

Anderson, M.J., Gorley, R.N., Clarke, R.K., 2008. PERMANOVA+ for PRIMER: Guide to software and statistical methods. PRIMER-E Ltd, Plymouth, UK

Bahlburg, H. and Dobrzinski, N. 2011: A review of the Chemical Index of Alteration (CIA) and its application to the study of Neoproterozoic glacial deposits and climate transitions; Chapter 6 in The Geological Record of Neoproterozoic Glaciations, E. Arnaud, G.P. Halverson and G. Shields-Zhou (ed.), The Geological Society, Memoir no. 36, p. 81–92.

Brunskill, G.J., 2004. New Guinea and Its Coastal Seas, a Testable Model of Wet Tropical Coastal Processes: an Introduction to Projects TROPICS. Cont. Shelf Res., v. 24, no. 19, p. 2273-2295.

Bloomer, 2005. "Using automated mineralogy to evaluate bioaccessibility of Pb-bearing mine waste." *Mineralogical Magazine* 76, no. 6: 1524. *GeoRef*, EBSCO*host* (accessed August 19, 2014).

Buckwalter-Davis, M., et al., 2012. "Using automated mineralogy to evaluate bioaccessibility of Pb-bearing mine waste." *Mineralogical Magazine* 76, no. 6: 1524. *GeoRef*, EBSCO*host* (accessed August 19, 2014).

Carson, B.E., Francis, J.M., Leckie, R.M., Droxler, A.W., Dickens, G.R., Jorry, S.J., Bentley, S.J., Peterson, L.C., Opdyke, B.N., 2008. Benthic foraminiferal response to sea level change in the mixed siliciclastic-carbonate system of Southern Ashmore Trough (Gulf of Papua), J. Geophys. Res., doi: 10.1029/2006JF000629

Chen, C.H., and Chen, J.A., 2000, Interactive diagnostic plots for multidimensional scaling with applications in psychosis disorder data analysis, Statistica Sinica, 10(2000), 665-691

Clarke, K.R., and Warwick, R.M., 2001. Change in Marine Communities: An Approach to Statistical Analysis and Interpretation (2nd ed.)PRIMER-E, Plymouth (2001)

Covault, J. A., Romans, B. W., Graham, S. A., Fildani, A., Hilley, G. E., (2011), Terrestrial source to deep-sea sink sediment budgets at high and low sea levels: Insights from tectonically active Southern California, Geology, 619-622, doi:10.1130/G31801.1

Covault, J.A., Normark, W.R., Romans, B.W., and Graham, S.A., (2007), Highstand fans of the California Borderland: The overlooked deep-water depositional system: Geology, v. 35, p. 783-786.

Daniell, J. J., 2008, Development of a bathymetric grid for the Gulf of Papua and adjacent areas: A note describing its development, J. Geophys. Res., 11 3, F01S15, doi:10.1029/2006JF000673.

Davies, H.L., 2012, The Geology of the New Guinea – the Cordilleran Margin of the Australian Continent, Episodes vol.35, no.1, p. 1-16.

Day, G., Dietrich, W.E., Rowland, J.C., Marshall, A., 2008, The depositional web on the floodplain of the Fly River, Papua New Guinea, J of Geophys. Res. : Earth Surface (2003-2012), vol.113, issue F1, doi: 10.1029/2006JF00062

Dickens, G. R., Droxler, A. W., Bentley, S. J., Peterson, L. C., Opdyke, B. N., Beaufort, L., & Zarikian, C. A. (2006). Sediment accumulation on the shelf edges, adjacent slopes, and basin floors of the Gulf of Papua. Margins Newsletter, 16, 1-5.

Dickinson, W.R. 1970. Interpreting detrital modes of greywacke and arkose. Journal of Sedimentary Petrology, 40, 695-707.

Dickinson, W.R., Suczek C.A., 1979. Plate Tectonics and Sandstone Compositions. AAPG Bulletin. 63, 2164-2182.

Dickinson, W.R., et al., 1983. "Provenance of North American Phanerozoic sandstones in relation to tectonic setting." Geological Society Of America Bulletin 94, no. 2: 222-235. GeoRef, EBSCOhost (accessed August 19, 2014).

Fandrich, R., et al., 2007. Modern SEM-based mineral liberation analysis. International Journal of Mineral Processing, 84(1), 310-320.

Febo, L. A., S. J. Bentley, J. H. Wrenn, A. W. Droxler, G. R. Dickens, L. C. Peterson, and B. N. Opdyke (2008), Late Pleistocene and Holocene sedimentation, organic carbon delivery, and paleoclimatic inferences on the continental slope of the northern Pandora Trough, Gulf of Papua, J. Geophys. Res., doi:10.1029/2006JF000677

Francis, J.M., Daniell, J.J., Droxler, A.W., Dickens, G.R., Bentley,S.J., Peterson, L.C., Opdyke, B.N., Beaufort, L., 2008. Deep-water Geomorphology of the mixed siliciclastic-carbonate system, Gulf of Papua. J. of Geophys Res., doi: 10.1029/2007JF000851

Garzanti, E.C., Ando, S., Scutella, M., 2000, Actualistic ophiolite provenance: the Cyprus case, J.Geol., 108: 199-218

Garzanti, E.C., Doglioni, G., Vezzoli and S Ando, 2007, Orogenic belts and orogenic sediment provenances, J.Geol., 115, 315-334, doi 10.1086/512755

Gonzales-Acebron, L., et al., 2010. Role of sandstone provenance in the diagenetic albitization of feldspars; a case study of the Jurassic Tera Group sandstones (Cameros Basin, NE Spain). *Sedimentary Geology*, *229*(1-2), 53-63. doi:10.1016/j.sedgeo.2010.06.005

Howell, AL., Bentley, S.J., Xu, K, Ferrell, R.E., Muhammad, Z, and Septama, E, 2014, A clay mineral provenance study of the Northern Pandora Trough Continental Margin, Papua New Guinea. Submitted July 2013, Marine Geology.

Ingersoll, R.V., et al., 1984. The effect of grain size on detrital modes; a test of the Gazzi-Dickinson point-counting method. Journal Of Sedimentary Petrology, 54(1), 103-116. doi:10.1306/212F83B9-2B24-11D7-8648000102C1865D

Jorry, S. J., A. W. Droxler, G. Mallarino, G. R. Dickens, S. J. Bentley, L. Beaufort, L. C. Peterson, and B. N. Opdyke (2008), Bundled turbidite deposition in the central Pandora Trough (Gulf of Papua) since Last Glacial Maximum: Linking sediment nature and accumulation to sea level fluctuations a millennial timescale, J. Geophys. Res., doi:10.1029/2006JF000649

Kiyokawa, S., & Yokoyama, K. (2009). Provenance of turbidite sands from IODP EXP 1301 in the northwestern Cascadia Basin, western North America. Marine Geology, 260(1), 19-29.

Kruskal, J. B. 1964. Multidimensional scaling by optimizing goodness of fit to a nonmetric hypothesis. *Psychometrika* 29, 1-27.

Kubo, Y., James Syvitski, Eric Hutton, Albert J. Kettner, 2006: Inverse modeling of post Last Glacial Maximum transgressive sedimentation using 2D-SedFlux: Application to the northern Adriatic Sea. Marine Geology, 234: 233 243.

Lisiecki, L. E., & Raymo, M. E. (2005). A Pliocene-Pleistocene stack of 57 globally distributed benthic δ18O records. *Paleoceanography*, *20*(1).

Liu, J.P., Milliman, J.D., Gao, S. and Cheng, P., 2004. Holocene development of Yellow River's subaqueous delta, North Yellow Sea, Marine Geology, 209(1-4):45-67, doi:10.1016/j.margeo.2004.06.009

Marsaglia, K.M., and Ingersoll, R.V., 1992. Compositional trends in arc related, deep-marine sand and sandstone: A reassessment of magmatic-arc provenance. Geologic Society of America Bulletin, 104, 1637-1649

Milliman, J.D., 1995. Sediment discharge to the ocean from small mountainous rivers: The New Guinea example. Geo-Marine Letters. 15. 127-133.

Morad, S., et al., 1990. Albitization of detrital plagioclase in Triassic reservoir sandstones from the Snorre Field, Norwegian North Sea. *Journal Of Sedimentary Petrology*, *60*(3), 411-425. doi:10.1306/212F91AB-2B24-11D7-8648000102C1865D

Muhammad, Z., et al., 2008. Excess 210Pb inventories and fluxes along the continental slope and basin of the Gulf of Papua, J. Geophys. Res., doi:10.1029/2006JF000676

Nesbitt, H.W., and Young, G. M., 1982. Early Proterozoic climates and plate motions inferred from major element chemistry of lutites. *Nature [London]*, *299*(5885), 715-717.

NSF-MARGINS, 2004, National Science Foundation MARGINS Program Science Plan 2004. http://www.nsfmargins.org/Publications/SciencePlans/MARGINS_SciencePlans2004.pdf, accessed 10/04,2014.

NSF Margins Office, 2009, S2S Nuggets and 2009 Review Documents. http://www.nsf-margins.org/S2S/S2S.html, accessed 11/18/2014.

Patterson, L. J. (2006), Petrological and geochemical investigations of deep sea turbidite sands in the Pandora and Moresby Troughs: Source to sink Papua New Guinea focus area, M. S. thesis, Louisiana State University.

Petzet, A., 2007. Exploration spreads into numerous remote and nonproducing basins. *Oil & Gas Journal*, *105*(12), 33. Exploration in Gulf of Papua.

Pigram C. J., and Davies, H. L., 1987, Terranes and the accretion history of the New Guinea Orogen: Bureau of Mineral Resources Journal of Australian Geology and Geophysics , v.10 p193-212

Pigram, C. J., P. J. Davies, D. A. Feary, and P. A. Symonds (1989), Tectonic controls on carbonate platform evolution in southern Papua New Guinea: Passive margin to foreland basin, Geology, 17, 199– 202.

Price, J. R., Velbel, M. A., 2003, Chemical weathering indices applied to weathering profiles developed on heterogenous felsic metamorphic parent rocks, Chemical Geology 202, 397-416

Ramseyer, K., Boles, J. R., and Lichtner, P.C., 1992, Mechanism of plagioclase albitization. Jour. Sed. Petrol., v. 62, p. 349-356

Shapiro, S. A., et al., 2007. The petrology and provenance of sand in the Bounty submarine fan, New Zealand. *Special Paper - Geological Society Of America*, *420*277-296. doi:10.1130/2006.2420(17) point counts to identify fluvial sources of sand in deep sea fan

Slingerland, R., Selover, R.W., Ogston, A.S., Keen, T.R., Driscoll, N.W., Milliman, J.D., 2008. Building the Holocene Clinothem in the Gulf of Papua: an Ocean Circulation Study. Jour. of Geophys. Res., v. 113, p. 1-17.

Steinshouer, D.W., et al., 1999. Maps showing geology, oil and gas fields, and geologic provinces of the Asia Pacific Region. U.S.G.S. Open File Report 97-470F.

Tcherepanov, E. N., A. W. Droxler, P. Lapointe, G. R. Dickens, S. J. Bentley, L. Beaufort, L. C. Peterson, J. Daniell, and B. N. Opdyke (2008), Neogene evolution of the mixed carbonate-siliciclastic system in the Gulf of Papua, Papua New Guinea, J. Geophys. Res., 113, F01S21, doi:10.1029/2006JF00068

Trevena, A. S., and Nash, W.P. 1979. Chemistry and provenance of detrital plagioclase. *Geology [Boulder]*, *7*(10), 475-478.

Trevena, A.S., and Nash, W.P., 1981. An electron microprobe study of detrital feldspar. Journal of Sedimentary Petrology, 51, 137-150.

Underwood, M. B., & Fergusson, C. L., 2005. Late Cenozoic evolution of the Nankai trench-slope system; evidence from sand petrography and clay mineralogy. *Geological Society Special Publications*, *244*113-129.

Weltje, G.J. and von Eynatten, H. (2004). Quantitative provenance analysis of sediments: review and outlook. Sedimentary Geology 171, 1-11.

Wright, L. D., Friedrichs, C. T., Kim, S. C., & Scully, M. E. (2001). Effects of ambient currents and waves on gravity-driven sediment transport on continental shelves. Marine Geology, 175(1), 25-45.

# CHAPTER 5

## The Late Quaternary deep-sea depositional system in the Gulf of Papua: linking source, dynamic sedimentation processes and depositional architecture, discussion and conclusion

### 5.1. Discussion and conclusion

This study has examined source to sink sediment delivery from river systems to the slope and deep-sea basins of the Gulf of Papua (GoP), over the last ~40 ky, at millennial temporal resolution and finer. The results have offered new insights into the the development of sedimentary successions in deep-sea basins, and also into approaches for provenance analysis. Chapter I is primarily introduction and context, with major products of research presented in chapters II-IV.

Chapter II is an integrated study of lithofacies, lithostratigraphy, and chronostratigraphy in the GoP. Six deep water lithofacies are identified based on core visual and textural observation. Chronological constraints permit an assessment of changes in sediment supply and depositional environments across time and space, from MIS 3 to MIS 1. The sediment delivery to the deep water GoP is dominated by two mechanisms, gravity-driven flows down slopes and into deep sea basins primarily during lowstands in western portions of the study area, and hemipelagic sediment accumulation during transgression and highstand. Although the sediment flux appears to be overall dominated by sediment gravity flows, hemipelagic sediment delivery is widespread during periods of sea level highstand. In eastern portions of the study area, off-shelf sediment delivery continued into the Holocene in sufficient local volumes to produce turbidity currents. This late, localized sediment delivery appears to have been facilitated by oceanographic processes that allowed seaward sediment transport after flooding of the shelf.

In summary, deep water sedimentation during the late Pleistocene and Holocene in the Gulf of Papua is characterized by mostly fine sediment delivery, controlled by local morphology and oceanographic processes. This modern analog differs in its complexity from traditional highstand-lowstand sediment-delivery paradigms.

Chapter III evaluated the morphology and seabed dynamics of the two major contrasting depocentres in the GoP (Pandora and Moresby Troughs), with their associated canyons, channels and slopes. The study incorporated multibeam bathymetric, geo-acoustic and core data to relate depositional processes, routing, timing and products over ~40 Ka time scales, during which the continental margin was exposed during sea level fall to the LGM, and was then drowned during the deglacial transgression. Our work has established 10 acoustic facies classes, based on the sound penetration, seismic internal characters and seafloor relief, facilitated by 3D seafloor visualization. Integration of acoustic facies with core physical properties, sedimentary fabric, and chronostratigraphy allowed placement of seafloor evolution into a well defined temporal framework.

This study revealed three possible pathways of sediment delivery to the deep sea. Pathway (1) is long distance transport of the sediment from Papuan Mainland via mature river across shelf and slope, to the Pandora basin floor and Moresby Channel to their final fate in the Coral Sea Basin. The channel developed into a major sediment transfer avenue, hosting large turbidity currents with the turbidite cloud reaching at least 30 Km laterally (evidence from core MV-23) and 200 m vertically (evidence from channel-levee flank deposits such as in MV-25, MV-27 and MV-29). Pathway (2) is the short distance sediment transport apparently from the collision margin of the Papuan Peninsula, delivered via small rivers across a narrow shelf into large deep-sea canyons. Major depositional units include a large sediment-wave like feature at the western toe of slope in Moresby Trough. There are two possibilities of such processes to create this element: a large wave with undulatory morphology created by flow interaction with the bed, or formation as a drape over pre-existing undulatory topography, possibly from the remnant of a past MTD.

Pathway (3) is the intermediate- to long-distance delivery from northern GoP rivers and Papuan Peninsula along coastal pathways to the Moresby Trough when the shelf edge is subaqueous, via oceanic and coastal hydrodynamic transport.

We propose two developments in the source-to-sink narrative for our study area during the past ~40 ky. (1) In the Pandora Trough, turbidite sedimentation is dominant from late MIS-3 to the end of MIS-2 (>40 Ka - 14 Ka), and ceased by early Holocene due to relief modification caused by MTD, rising sea level and associated shelf trapping of sediment. (2) Turbidite sedimentation continued in the Moresby Trough, although at a slower rate, into the Holocene transgression. Sediment sources to deep water included reworked shelf edge deposits, and more direct river-mouth supply entrained by coastal currents on the flooding continental shelf (<~15 Ka). This flooding and current system enabled coalescence of multiple river sources to supply fan aggradation in the Moresby Trough.

The understanding of this modern deepwater analog provides insights on the detailed control on the sub-reservoir scale of deep-sea sand delivery and accumulation, controlled by local morphology and relief modification, and oceanographic processes.

Chapter IV is a provenance analysis of deep-water turbidite sands in the Moresby and Pandora troughs, using SEM-MLA and multivariate statistical methods. This chapter provides the following insights, regarding both applicability of this powerful analytical tool, and the geological evolution of deep GoP sedimentary basins since the late Pleistocene.

Methodology:

1. SEM-MLA can be used to replicate Gazzi-Dickinson provenance analysis. SEM-MLA results do not introduce artifacts due to methodology, and can yield a broader and more ternary QFL insightful classification of samples than manual point counts. For our samples, particle-based SEM-MLA counts yielded the broadest classification of samples, with no evidence of artifacts.

2. The combined use of SimPer and nMDS allows determination of sample clusters based on the information content of SEM-MLA analysis, rather than a prescribed three-dimensional space such as a ternary plot. This approach is much more effective at discriminating differences and similarities across large datasets with many parameters than is the case for more traditional QFL analysis.

Geology of Study Area:

3. The chemical index of alteration (CIA) shows that Pandora Trough in general is characterized by more highly weathered minerals compared to the Moresby Trough, and minimum values of CIA were evident for some locations near the time of the LGM, indicating some combination of low weathering rates, rapid erosion, and rapid transport from land to deep-sea basins.

4. Cluster analysis of sample mineralogy yields a story of sediment delivery along a ~500 km basin margin that is much more complex than initially imagined. Results indicate that sediment delivery to and conduit connectivity between deep-sea basins evolves over time due to the combined effects of eustasy and dynamic seabed morphology. Multiple terrestrial sediment sources along a ~500 km basin margin initially converge to form one continuous deep-sea system of channels and two major basins prior to 30 ky BP, that become bathymetrically

separated by a large mass-transport deposit. Subsequent sea-level fall approaching the LGM initially drives re-partitioning of sediment sources to create multiple compositionally distinct depocenters, presumably due to migration and incision of individual rivers across the newly exposed coastal plain. Multiple separate deep-sea channels then regain compositional similarity near the end of the LGM, possibly due to regional erosion into compositionally similar catchment rocks. After this, sand transport to the deep basins shuts down, except for one depocenter (MV22), fed by local volcanic, that remains active at least into the Middle Holocene.

The understanding of this modern analog has an implication to the petroleum exploration conceptual model, especially for a better prediction of sub-reservoir scale geometry (millennial – centennial time scale, metre-tens metre sedimentary unit) whether in the Gulf of Papua which is known to host major oil and gas reserves or other deep sea systems.

**5.2 Potential for Improvement and Future Work.**

Most scientific investigations tend to be incomplete, and allow room for improvement. In the present study, there are many uncertainties associated with the interpretation due to the limitations of the data. These include: depth of core penetration, wide spacing of cores, wide spacing and shallow penetration of of the sub-bottom profiles, the possibility of interpretation pitfalls from seismic resolution, projection, and side-sweep effect from the neighbouring high relief features. This study would have certainly benefitted from a more dense seismic grid using sources with greater seabed penetration, coring tools with greater penetration, and cores at closer spacing. A more intensive seismic survey was originally proposed for the PANASH cruise (A. Droxler, personal communication), but was not conducted due to regulatory problems. Some deeper cores in the study area do exist, with much greater penetration (e.g., cores collected by the R/V Marion Dufresene in 2005, including MD40 of Jorry et al., 2008), but these were not available for the present study. Nevertheless, with the limits of the data available, this study did provide new knowledge and insights described above.

Two major recommendations for future work are proposed. First, study of Marion Dufresne cores from the deep basins should be conducted to develop a more complete picture of shelf to basin sediment delivery over more time than a partial glacial cycle. Ongoing studies of these cores are primarily biostratigraphic in nature, and would benefit from more physical sedimentological evaluation. Second, the analytical and statistical approaches used here for provenance analysis (SEM-MLA, SimPer, and nMDS) could be evaluated in more detail to produce a standard detrital provenance methodology, as a potential alternative or successor to the Gazzi-Dickinson approach. Such a development would standardize advanced analytical techniques that allow for much richer analysis, data extraction, and interpretation than is possible with more traditional approaches.

### 5.3 References

Martin, D.P., Nittrouer, C.A., Ogston, A.S., Crockett, J.S., 2008. Tidal and Seasonal Dynamics of a Muddy Inner Shelf Environment, Gulf of Papua. Jour. of Geophys. Res., v. 113, p. 1-18.

Slingerland, R., Driscoll, N.W., Milliman, J.D., Miller, S.R., Johnstone, E.A., 2008a. Anatomy and growth of a Holocene clinothem in the Gulf of Papua. Journal of Geophysical Re-se ar ch 11 3, 1–16.

Slingerland, R., Selover, R.W., Ogston, A.S., Keen, T.R., Driscoll, N.W., Milliman, J.D., 2008a. Building the Holocene Clinothem in the Gulf of Papua: an Ocean Circulation Study. Jour. of Geophys. Res., v. 113, p. 1-17.

Walsh, J.P., Nittrouer, C.A., Palinkas, C.M., Ogston, A.S., Sternberg, R.W., Brunskill, G.J., 2004. Clinoform Mechanics in the Gulf of Papua, New Guinea. Cont. Shelf Res., v. 24, p. 2487-2510.

# Appendices

| No | Section | Segment | Location | Start | | End | | Length | depth range | | intersection | core penetrated | Facies | Description | color code | line code |
|---|---|---|---|---|---|---|---|---|---|---|---|---|---|---|---|---|
| | | | | x | y | x | y | Km | min | max | | | | | | |
| 1 | 0001_2004_083 | 1 | moresby | 147.30595 | -10.16666 | 147.231281 | -10.216641 | 22.63 | 2260 | 2410 | n/a | | 2b | Strong continuous paralel sub bottom echo, with slightly overlaping broad hyperbolae (3.8 - 4.5 km), distinct layering with thickness of 2 - 8 m, sound penetration: 75-80 m | | |
| | | 2 | moresby | 147.231281 | -10.216641 | 146.846925 | -10.0333345 | 61 | 2320 | 2410 | 0001_2004_082 @ 147.1333;-10.1667 | | 1a | strong flat non prolonged to semi prolonged sub bottom reflector, with shallow to medium penetration 40 -80 m | | |
| | | 3 | moresby | 146.846925 | -10.033335 | 146.719957 | -10.033356 | 13.9 | 2280 | 2305 | n/a | | 1b | strong semi prolonged sub bottom reflector, with indistinct discontinous reflector, iregular surface, sound penetration: 70-80 m | | |
| | | 4 | moresby | 146.719957 | -10.033356 | 146.324825 | -9.961541 | 47.5 | 2210 | 2305 | n/a | MV-29 | 1a | strong semi prolonged sub bottom reflector, with indistinct discontinous reflector, iregular surface, sound penetration: 70-80 m. | | |
| 2 | 0001_2004_082 | 1 | moresby | 146.3789303 | -10.00882 | 146.205715 | -10.0810296 | 20.5 | 2160 | 2240 | 0001_2004_083 @ 146.3587; -10.0191 | | 1a | strong flat non prolonged to semi prolonged sub bottom reflector, with shallow to medium penetration, 100 at the lower point, decreasing to 60-80 m at the higher topography 50 m at the channel, u shape channel, 15-25 m depth, 880 m width. | | |
| | | 2 | moresby | 146.205715 | -10.08103 | 146.151749 | -10.10349 | 6.41 | 2150 | 2155 | n/a | | 3e | transparent lens, convex up, strong echo of type 1a in the base penetration: 50 m, probably slumping/ debris from upper slope | | |
| | | 3 | moresby | 146.151749 | -10.10349 | 146.0988 | -10.12555 | 6.291 | 2060 | 2150 | n/a | | 1b | strong semi prolonged sub bottom reflector, with very indistinct discontinous reflector, flat surface, sound penetration: 50-60 m. | | |
| | | 4 | moresby | 146.0988 | -10.12555 | 146.085139 | -10.166675 | 20.3 | 1850 | 2060 | | | 3c | strong seafloor echo, continous parallel sub-bottom reflector with narow and non overlapping hyperbolae (0.7-1 km) distinct layering with interval of 4-6 m, shallow penetration: 40 m, high relief. | | |
| | | 5 | moresby | 146.085139 | -10.166675 | 146.291554 | -10.166685 | 22.6 | 2025 | 2100 | | | 1b | strong semi prolonged sub bottom reflector, with very indistinct discontinous reflector, flat surface, sound penetration: 50-60 m | | |
| | | 6 | moresby | 146.291554 | -10.166685 | 146.422112 | -10.166663 | 14.3 | 2100 | 2170 | | | 2b | medium to strong seafloor echo, continous - semi continous parallel sub-bottom reflector, very narrow hyperbolae (0.5-1 km) with rugous surface. Semi distinct layering with interval of 5-10 m medium penetration (70m), layering diminish toward east | | |
| | | 7 | moresby | 146.422112 | -10.166663 | 146.539537 | -10.166626 | 12.9 | 2170 | 2180 | | | 1b | strong semi prolonged sub bottom reflector, with very indistinct discontinous reflector, flat surface, sound penetration: 50 m, filling the valley area, gradually changes to facies 3D toward east. | | |
| | | 8 | moresby | 146.539537 | -10.166626 | 146.9437 | -10.16666 | 58 | 2070 | 2375 | | MV-27 | 2b | medium to strong seafloor echo, continous - semi continous parallel sub-bottom reflector, narrow hyperbolae (1.2 km) locally rugous surface and flat surface. Semi distinct layering with interval of 2-10 m, medium penetration of 70 m, abruptly changes into facies 1a. | | |
| | | 9 | moresby | 146.9437 | -10.16666 | 147.18 | -10.166679 | 12.1 | 2375 | 2430 | 0001_2004_083 @ 147.1333;-10.1667 | | 1a | strong flat non prolonged to semi prolonged sub bottom reflector, with medium penetration of 80 m, in eastern part were overlied by debris flow. | | |
| | | 10 | moresby | 147.18 | -10.166679 | 147.244844 | -10.166659 | 7.097 | 2350 | 2410 | | | 3e | transparent lens, convex up, strong echo of type 1b in the base medium penetration of 80 m, interpreted as slumping or thin debris flow from upper slope | | |
| | | 11 | moresby | 147.244844 | -10.166659 | 147.306363 | -10.16667 | 6.55 | 2280 | 2400 | | | 2b | strong continuous paralel sub bottom echo, with overlaping broad hyperbolae (3.5 m), distinct to indistinct layering with thickness of 2 - 15 m, sound penetration: 100 m | | |
| 4 | 0007_2004_080 | 1 | moresby | 147.11188 | -9.551 | 146.937 | -9.61 | 20.26 | 570 | 2050 | | | 3e | transparent lens, semi continous seafloor echo with irregular undulating surface weak/transparent sub-bottom reflector, shallow penetration 40 m, some artifact | | |
| | | 2 | moresby | 146.937 | -9.61 | 146.7936 | -9.6608 | 16.7 | 2055 | 2130 | | | 2b | med-strong continuous paralel sub bottom echo, smooth surface low relief no hyperbolae, distinct layering with thickness of 1-5 m, gradually changes into facies 1c, sound penetration of 80 m | | |
| | | 3 | moresby | 146.7936 | -9.6608 | 146.6447 | -9.7126 | 17.31 | 2115 | 2130 | | | 1c | strong irregular highly prolonged seafloor echo, slightly or no overlapping hyperbolae (1-5 Km width) sound penetration: 60 m locally drapped by 2 m transparent layer | | |
| | | 4 | moresby | 146.6447 | -9.7126 | 146.325 | -9.824 | 37.2 | 2055 | 2090 | | MV-22 | 3d | strong seafloor echo, continous -semi continous parallel sub-bottom reflector, narrow to medium width hyperbolae (0.9-2.5 Km), layering with 0.5 - 2 m thickness gradation to facies 3C toward west (near the channel) sound penetration of 70 m | | |
| | | 5 | moresby | 146.325 | -9.824 | 146.27196 | -9.842685 | 6.1 | 2065 | 2085 | | | 3c | distinct layering with thickness of 5-10 m, upper 25 m dominated by weak echo, transparent layer, with strong base echo resemble facies 3d on the base, total sound penetration : 50 m. | | |
| | | 6 | pandora | 146.27196 | -9.842685 | 146.21 | -9.864 | 7.19 | 2085 | 2143 | | | 1a | strong flat non prolonged to semi prolonged sub bottom reflector, with shallow penetration of 20-40 m, mostly associated with chanell thalweg and wing. Channel a (east) is 63 m depth to the top of levee, 2.6 km width interpreted as the active channel, channel b (west) is 38 m depth, 1.2 km width, filled partially by mud interpreted as abandoned. | | |
| | | 7 | pandora | 146.21 | -9.864 | 146.129 | -9.892 | 8.8 | 2080 | 2090 | | | 1b | strong semi prolonged sub bottom reflector, with very indistinct discontinous reflector,rugous surface, with thin transparent layer (1m) sound penetration 40-50 m | | |
| | | 8 | pandora | 146.129 | -9.892 | 145.915652 | -9.96677 | 24.801 | 2075 | 2085 | | MV-23 proj 6.7 km | 2b | strong continous seafloor echo with continous to semi-continous parallel sub-bottom reflector, showing divergent trend toward east, distinct strong reflector showing thin layering (less than 1 m) thicker bottomward ( 1- 5 m) sound penetration 30-40 m | | |
| 5 | 0008_2004_082 | 1 | moresby | 146.56044 | -9.933313 | 146.399167 | -10.000398 | 19.17 | 2175 | 2210 | | MV-25 | 2b | medium-strong seafloor echo, continous -semi continous parallel sub-bottom reflector with indistinct layering, average thickness = 2 m, sound penetration of 50 m | | |

| | | | | | | | | | | | | | | |
|---|---|---|---|---|---|---|---|---|---|---|---|---|---|---|
| | | 2 | moresby | 146.399167 | -10.000398 | 146.37893 | -10.00882 | 2.469 | 2200 | 2230 | | | 1a | strong flat non prolonged to semi prolonged sub bottom, sound penetration of 60 m rough surface with wide hyperbolae (1-1.5 km), showing channel with width of 800m and 30 m depth, filled by mud |
| 6 | 0005_2004_079 | 1 | pandora | 145.014495 | -9.296638 | 145.05525 | -9.36 | 8.295 | 660 | 1000 | | | 3e | semi continous seafloor echo with irregular undulating surface weak/transparent sub-bottom reflector, deep penetration (100m)in shelf, medium penetration in slope (4-60 m), hard reflector 60 m from seafloor, layering ( 5-15 m). |
| | | 3 | pandora | 145.05525 | -9.36 | 145.05949 | -9.3623 | 0.53 | 1000 | 1000 | | | 1a | strong flat non prolonged to semi prolonged sub bottom reflector, with medium penetration of 80 m, possibility caused by orientation of the section (could interpreted as 3a) |
| | | 4 | pandora | 145.05949 | -9.3623 | 145.108 | -9.3716 | 5.422 | 1000 | 1130 | 0007_2004_091 @ 145.0979; -9.3704 | | 3a | prolonged echo, no sub-bottom reflector medium penetration of 40 m in rugous area, 60 m in flat area |
| | | 5 | pandora | 145.108 | -9.3716 | 145.142 | -9.376 | 3.762 | 1230 | 1345 | | | 1a | strong flat non prolonged to semi prolonged sub bottom reflector, steep gradient , with medium penetration of 50-60 m gradually changes to facies 3d eastward. |
| | | 6 | pandora | 145.142 | -9.376 | 145.238 | -9.389095 | 10.6 | 1345 | 1430 | | | 3d | medium-strong seafloor echo, continous -semi continous parallel sub-bottom reflector, layering with 2 - 10 m thickness, showing alternating between transparent layer and dark layer, locally folded rugous surface, interpreted as slide, penetration= 60 m upper part layering = 20 m below 40 m. |
| | | 7 | pandora | 145.238 | -9.389095 | 145.8382 | -9.4696 | 66.44 | 1430 | 1820 | 0007_2004_091 @ 145.6912; -9.45016 | | 3b | overlapping hyperbolae (50-200 m)locally shown a pounded soft sediment with transparent layer 20 m depth, 2-3 km width, penetration = 60-100 m. |
| | | 8 | pandora | 145.8382 | -9.4696 | 146.107 | -9.505 | 29.74 | 1830 | 1965 | | | 1c | strong irregular highly prolonged seafloor echo, slightly or no overlapping hyperbolae (0.5-1 Km width) sound penetration: 60 m filling the low area. |
| | | 10 | moresby | 146.107 | -9.505 | 146.767 | -9.59 | 72.3 | 1890 | 2080 | | | 3d | medium-strong seafloor echo, continous -semi continous parallel sub-bottom reflector, layering with 2 -5 m, showing alternating transparent and dark layer, depth of penetration= 40-60 m |
| | | 12 | moresby | 146.672 | -9.58 | 146.907012 | -9.61133 | 26 | 2080 | 2110 | | | 3a | medium seafloor echo, continous -semi continous parallel sub-bottom reflector, layering with alternated transparent and dark layer, depth of penetration= 60-80 m |
| 7 | 0004_2004_085 | 1 | pandora | 145.585 | -9.9043 | 145.665 | -9.9247 | 9.052 | 1790 | 1790 | | | 2b | strong continous seafloor echo with continous to semi-continous parallel sub-bottom reflector, divergent toward N-NW distinct strong reflector showing thin layering (less than 1 to 2 m) sound penetration 50 -60 m |
| | | 3 | pandora | 145.665 | -9.9247 | 145.73698 | -9.796 | 45.41 | 1860 | 2010 | | | 3c | medium continuous paralel sub bottom echo, broad overlapping hyperbolae 2-4 Km, distinct layering with thickness of 2-5 m, sound penetration of 40 m. |
| | | 4 | pandora | 145.73698 | -9.796 | 145.54977 | -9.7486 | 21.18 | 1770 | 1790 | 000_2004_085 @ 145.6417; -9.7719 | | 2b | strong continous seafloor echo with continous to semi-continous parallel sub-bottom reflector, divergent toward N-NW distinct strong reflector showing thin layering (less than 1 to 2 m) sound penetration 60 -80 m, event terminated at structural ridges |
| | | 5 | pandora | 145.54977 | -9.7486 | 145.5246 | -9.7422 | 2.85 | 1100 | 1720 | | | 3b | medium seafloor echo, highly prolonged, without sub-bottom reflector, broad overlapping hyperbolae (3.1 km), sound penetration = 60 m, very steep gradient data unreliable in some segment |
| | | 6 | pandora | 145.5246 | -9.7422 | 145.378 | -9.70499 | 16.6 | 1720 | 1740 | | | 3a | medium seafloor echo, continous -semi continous parallel sub-bottom reflector, layering with 2 -8 m, showing alternating transparent and dark layer, depth of penetration= 60-70 m |
| | | 7 | pandora | 145.378 | -9.70499 | 145.33335 | -9.6655 | 8.237 | 1720 | 1745 | | | 3e | transparent lens, convex up, strong echo of type 1a in the base penetration: 80 m, low gradient, lenses with thickness 15-30 m, 8.237 km length, deposited toward S-Sw |
| | | 8 | pandora | 145.33335 | -9.6655 | 145.5925 | -9.6685 | 33.63 | 1640 | 1760 | | | 3b | strong seafloor echo, highly prolonged, without sub-bottom reflector, close space intensely overlapping hyperbolae (50-200 m) penetration = 80 m, some showing intensively thrusting |
| | | 9 | pandora | 145.5925 | -9.6685 | 145.600034 | -9.86668 | 31.36 | 1770 | 1780 | 000_2004_085 @ 145.6417; -9.7719 | MV-33 | 2b | strong continous seafloor echo with continous to semi-continous parallel sub-bottom reflector, divergent toward S-SW distinct strong reflector showing distinct layering of average 5m sound penetration 50 -60 m in distal part |
| 8 | 0007_2004_091 | 1 | pandora | 145.08397 | -9.352 | 145.323127 | -9.5822 | 38.484 | 1030 | 1645 | 0005_2004_079 @ 145.0979; -9.3704 | | 3e | transparent lens, convex up, medium echo of type 3a in the base penetration: 80 m, low gradient, lenses with thickness 10-25 m, 7.884 Km length |
| | | 3 | pandora | 145.323127 | -9.5822 | 145.611177 | -9.6025 | 47.16 | 1660 | 1760 | | | 3b | strong seafloor echo, highly prolonged, without sub-bottom reflector, close space intensely overlapping hyperbolae (50-200 m) penetration = 50 m, some showing extensional gashes and pounded sediment. |
| | | 4 | pandora | 145.611177 | -9.6025 | 145.618342 | -9.6018 | 4.463 | 1760 | 1765 | | | 2b | strong continous seafloor echo with continous to semi-continous parallel sub-bottom reflector, pounded and thicker toward mid of the depocenter, distinct layering of less than 1 m to 5 m, sound penetration total= 40m, pounded sediment = 25 m |
| | | 5 | pandora | 145.618342 | -9.6018 | 145.757 | -9.326 | 34.26 | 1645 | 1760 | | | 3b | strong seafloor echo, highly prolonged, without sub-bottom reflector, close space intensely overlapping small hyperbolae less than 200m and wide hyperbolae 2-3.5 km resemble facies 3c penetration = 50 m, some showing extensional gashes and pounded sediment |
| | | 6 | pandora | 145.757 | -9.326 | 145.966685 | -9.00008 | 42.94 | 1610 | 1720 | | | 1c | strong irregular highly prolonged seafloor echo, slightly or no overlapping hyperbolae (1-5 Km width) sound penetration: 60 m sometimes showing layering |
| 9 | 0007_2004_092 | 1 | pandora | 145.966685 | -9.00008 | 145.9422 | -8.92497 | 8.774 | 1500 | 1610 | | | 1c | strong irregular highly prolonged seafloor echo, no overlapping hyperbolae, moderate gradient, sound penetration = 60 m |

| | | | | | | | | | | | | | | |
|---|---|---|---|---|---|---|---|---|---|---|---|---|---|---|
| | | 2 | pandora | 145.9422 | -8.92497 | 145.97044 | -8.69928 | 27.31 | 970 | 1500 | 0006_2004_089 @ 145.936; -8.7295 | | 3e | series of transparent lens, convex up, medium echo of type 1c in the base, steep gradient, penetration= 50 m, steep gradient lenses with thickness of 10-15 m, 6 -9 Km length |
| | | 3 | pandora | 145.97044 | -8.69928 | 146.043666 | -8.8153 | 30.88 | 760 | 980 | 0006_2004_088 @146.0580; -8.7998 | | 3c | medium continuous paralel sub bottom echo, no overlapping wide hyperbolae (3.5 km), distinct layering with thickness of 10 m sound penetration of 70 m, drapped by thin transparent layer 1 -2 m. |
| 10 | 0006_2004_088 | 1 | pandora | 145.7558 | -8.63 | 145.797 | -8.6038 | 5.445 | 770 | 880 | | | 3c | weak-medium continuous paralel sub bottom echo, no overlapping wide hyperbolae (2.5 km), distinct layering with thickness of 10 m sound penetration of 50-80 m, drapped by thin transparent layer 1 -2 m. |
| | | 2 | pandora | 145.797 | -8.6038 | 145.8367 | -8.582098 | 4.991 | 840 | 880 | | | 2a | semi continous seafloor echo with irregular undulating surface weak/transparent sub-bottom reflector, penetration = 70m transparent layer with 20 m thickness, overlayed with thin 1-2 m transparent layer. |
| | | 3 | pandora | 145.8367 | -8.582098 | 146.018341 | -8.7666 | 111.9 | 320 | 800 | loop @ 146.6457; -8.593<br>0007_2004_092 @ 146.0580; -8.7998 | MV-49,MV-51, Mc-50 | 3c | weak-medium continuous paralel sub bottom echo, no overlapping wide hyperbolae (4.5 km), distinct layering with thickness of 10 m sound penetration of 90 m, showing alternating between transparent and dark layer. |
| 11 | 0006_2004_089 | 1 | pandora | 146.0183 | -8.7666 | 145.94516 | -8.7387 | 11.9 | 890 | 1110 | | | 3c | v. weak-medium continuous paralel sub bottom echo, no overlapping wide hyperbolae (4.5 km), indistinct layering with thickness of 10 m disrupting in some place with facies 1c, with strong echo, rugous surface sound penetration of 70 m, drapped by 5 m transparent layer |
| | | 2 | pandora | 145.94516 | -8.7387 | 145.833 | -8.6679 | 23.02 | 1000 | 1110 | | | 2a | semi continous seafloor echo with irregular/ rough surface weak/transparent sub-bottom reflector, penetration = 70m transparent layer with10-15 20 thickness, overlayed with thin 1-2 m transparent layer. |
| | | 3 | pandora | 145.833 | -8.6679 | 145.766 | -8.78677 | 15.13 | 970 | 1055 | | | 3c | weak-medium continuous paralel sub bottom echo, no overlapping wide hyperbolae (4.5 km), semi distinct layering with thickness of 10 m overlayed with type 2a facies, sound penetration = 50-80 m |
| | | 4 | pandora | 145.766 | -8.78677 | 145.474 | -8.67364 | 36.6 | 550 | 1180 | | | 3e | series of transparent lens, convex up, medium echo of type 1c in the base, steep gradient, penetration= 50 m, lenses thickness of 5-10 m with 4-6 km length. |
| 12 | 0006_2004_090 | 1 | pandora | 145.474 | -8.67364 | 145.353 | -8.741 | 17.14 | 140 | 640 | | | 3e | transparent lenses, multi stage, convex up, with lenses thickness of 10 m in upper slope to 25 m in lower slope, no hyperbolae, rugged surface, high gradient, sound penetration = 70-80 m |
| | | 2 | pandora | 145.353 | -8.741 | 145.292833 | -8.77999 | 18.51 | 120 | 140 | | | 2a | strong semiprolonged seafloor echo with irregular/ rough surface weak/transparent sub-bottom reflector, penetration = 60 80m, low gradient or almost flat. |
| | | 3 | pandora | 145.292833 | -8.77999 | 145.352167 | -8.8579 | 10.84 | 140 | 860 | | | 3e | transparent lenses, multi stage, convex up, with lenses thickness of 5 m above and to 15-20 m underneath , no hyperbolae, rugged surface, high gradient, sound penetration = 45-70 m |
| | | 4 | pandora | 145.352167 | -8.8579 | 145.388672 | -8.936333 | 16.62 | 750 | 1025 | | MV-54 | 3a | weak to medium single seafloor echo with overlapping hyperbolae (narrow, 50-300m) prolonged - semi prolonged echo, no sub bottom reflector, sound penetration of 50-60 m |
| | | 5 | pandora | 145.388672 | -8.936333 | 145.37756 | -8.9337 | 1.315 | 880 | 920 | | | 2a | strong semiprolonged seafloor echo with irregular/ rough surface,mostly overlain by 5 m transparent layer in the surface, weak/transparent sub-bottom reflector, penetration = 60-80m, moderate gradient |
| | | 6 | pandora | 145.37756 | -8.9337 | 145.222625 | -8.897133 | 17.5 | 240 | 920 | | | 3e | thin transparent lenses (1-2 m), covering 3c type facies in some place, convex up strong non prolonged - semi prolonged echo, sound penetration of 50 m. |
| | | 7 | pandora | 145.222625 | -8.897133 | 145.236542 | -8.938995 | 20.3 | 120 | 180 | | MV-55 | 2a | strong semiprolonged seafloor echo with irregular/ rough surface, no sub-bottom reflector, showing small hyperbolae (20-50 m width) and isolated wide hyperbolae 4 km, 20 m depth, sound penetration = 80 - 100 m. |
| | | 8 | pandora | 145.236542 | -8.938995 | 145.28263 | -8.97146 | 6.219 | 140 | 720 | | | 3e | thin semi transparent lenses (1-5 m), convex up, strong reflector with semi prolonged echo, with sound penetration of 40 m. |
| 13 | 0005_2004_088 | 1 | pandora | 145.83555 | -8.4354 | 145.800735 | -8.43627 | 6.246 | 370 | 400 | 0005_2004_087 @ 145.83555; -8.4354 | | 3e | thick semi transparent lenses (40 m), convex up, medium to weak reflector underneath, with surface resembles facies 1c. |
| | | 2 | pandora | 145.800735 | -8.43627 | 145.6296 | -8.4499 | 18.41 | 140 | 280 | | | 2a | strong semiprolonged seafloor echo with irregular/ rough surface, no sub-bottom reflector, showing |
| | | 3 | pandora | 145.6296 | -8.4499 | 145.6493 | -8.72583 | 42.48 | 480 | 920 | | MC-19 projected | 3e | thick semi transparent lenses (40 m), convex up, medium to weak reflector underneath, with surface resembles facies 3a. |
| | | 4 | pandora | 145.6493 | -8.72583 | 145.7558 | -8.63 | 16.5 | 835 | 940 | | | 3a | weak to medium single seafloor echo with overlapping hyperbolae (narrow, 50-300m) prolonged - semi prolonged echo, no sub bottom reflector, sound penetration of 50-60 m |
| 14 | 0005_2004_087 | 1 | pandora | 146.19281 | -8.60794 | 146.158 | -8.61305 | 4.002 | 95 | 130 | | | 2a | strong reflector with high-prolonged seafloor echo, very irregular/ rough surface, sub-bottom reflector occur, layering with average thickness of 3-8 m, depth penetration, (>100 m). |
| | | 2 | pandora | 146.158 | -8.61305 | 146.121231 | -8.610325 | 4.054 | 120 | 460 | | | 3e | thick semi transparent lenses (40 m), convex up, medium to weak reflector underneath, steep gradient with surface resembles facies 1c, penetration: 80 m |
| | | 3 | pandora | 146.121231 | -8.610325 | 145.967117 | -8.461535 | 24.7 | 275 | 675 | | | 3c | weak-medium semicontinuous paralel sub bottom echo, layer showing intensely folded no hyperbolae, rugous surface, with layer thickness of 6-10m, stratigraphic terminated by topography high, facies 1d on the base, sound penetration of 80 m. |
| | | 4 | pandora | 145.967117 | -8.461535 | 145.7987 | -8.4671 | 29.6 | 350 | 440 | 0005_2004_088 @ 145.83555; -8.4354 | MV-46 | 3e | thick semi transparent lenses (40 m), convex up, medium to weak reflector underneath, steep gradient with surface resembles facies 1d, penetration: 80 m |
| | | 5 | pandora | 145.7987 | -8.4671 | 145.83439 | -8.454 | 12.36 | 420 | 690 | | | 3c | strong paralel sub bottom echo, no hyperbolae, smooth surface, layer thickness of 2-10 m, alternating between transparent and dark layer, sound penetration of 60-70m |
| | | 6 | pandora | 145.83439 | -8.454 | 145.8358 | -8.394 | 7.229 | 140 | 320 | 0005_2004_088 @ 145.83555; -8.4354 | | 3e | thick semi transparent lenses (20 m), convex up, divergent toward down slope/ south underneath, steep gradient with base resembles facies 1b, penetration: 50-60 m |
| | | 7 | pandora | 145.8358 | -8.394 | 145.793869 | -8.38648 | 24.9 | 70 | 140 | | MV-41 | 2a | strong reflector with high-prolonged seafloor echo, very irregular/ rough surface, no sub-bottom reflector, transparent layer with thickness of 10-30 m, base surfaces resemble facies 1b, moderate-gentle gradient, sound penetration of >130m |
| | | 8 | pandora | 145.793869 | -8.38648 | 145.83555 | -8.4354 | 24.9 | 140 | 400 | 0005_2004_088 @ 145.83555; -8.4354 | | 3e | thick semi transparent lenses (20 m), convex up, divergent toward down slope/ south underneath, steep gradient with base resembles facies 1b, penetration: 50-60 m |

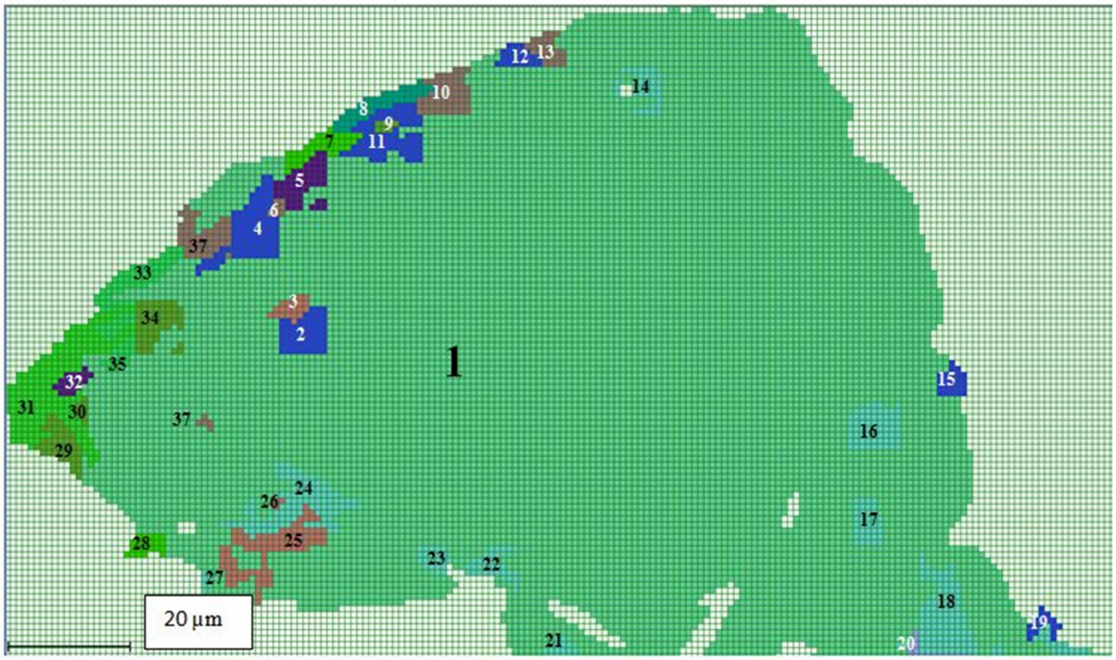


1. Grain Based point count: include all grains which are > 3.9 µm (e.g. = no.1, 2, 4,5 etc)
2. Particle based point count: include all grains which are > 62.5 µm (e.g = no.1)
3. Area based point count: include all total number of grids

| Physiographic Position | Density | Formula | Reference | Pandora Trough Slope | | | | Pandora Trough Basin Floor | | | | | | | | | | | | | | | | | | | |
|---|---|---|---|---|---|---|---|---|---|---|---|---|---|---|---|---|---|---|---|---|---|---|---|---|---|---|---|
| Sample | | | | MV54-49 | MV54-180 | MV54-320 | MV54-360 | MV23-113 | MV23-155 | MV23-239 | MV23-327 | MV23-416 | MV23-506 | MV23-698 | MV23-732 | MV23-779 | MV23-805 | MV23-940 | MV23-980 | MV33-314 | MV33-521 | MV33-628 | MV33-817 | MV33-916 | MV33-1036 | MV33-1115 | MV33-1173 |
| Altered minerals/clay | 2.6 | Al2Si2O5(OH)4 | | 16306 | 8586 | 14250 | 14424 | 18222 | 23309 | 15823 | 19474 | 17463 | 18534 | 19302 | 13867 | 14820 | 17163 | 19207 | 13920 | 14766 | 12681 | 14057 | 13931 | 12983 | 13693 | 13937 | 10343 |
| Amphibole | 3.23 | Ca2[Mg4(Al0.75Fe0.25)]Si7AlO22(OH)2 | | 3623 | 1067 | 1949 | 2234 | 3489 | 4198 | 3295 | 4384 | 2743 | 1163 | 1541 | 941 | 772 | 1104 | 1412 | 1354 | 1255 | 676 | 910 | 992 | 793 | 1121 | 1092 | 1000 |
| Biotite | 3 | K(Mg,Fe)3(AlSi3O10)(OH)2 | Klein | 173 | 55 | 68 | 111 | 289 | 219 | 89 | 191 | 79 | 20 | 80 | 20 | 27 | 34 | 45 | 66 | 37 | 24 | 25 | 28 | 21 | 54 | 42 | 29 |
| Quartz | 2.65 | SiO2 | Jones | 4358 | 3256 | 3780 | 3212 | 5205 | 6810 | 4257 | 5146 | 4152 | 7632 | 7412 | 5375 | 4695 | 5269 | 6249 | 4897 | 5000 | 3127 | 3329 | 2329 | 3063 | 3390 | 3496 | 2016 |
| Quartz_mixture | 2.65 | SiO2 | Jones | 7140 | 3276 | 6843 | 9306 | 5989 | 11487 | 5903 | 6999 | 10836 | 6568 | 13059 | 4288 | 4113 | 11501 | 10610 | 6530 | 7306 | 7529 | 7530 | 6267 | 6693 | 7688 | 8350 | 5532 |
| Chloritoid | 3.54 | (Fe1.2,Mg0.6Mn0.2)2Al4Si2O10(OH)4 | | 1086 | 612 | 712 | 523 | 1902 | 1804 | 1420 | 2088 | 466 | 498 | 426 | 358 | 330 | 272 | 401 | 265 | 398 | 211 | 276 | 255 | 197 | 344 | 269 | 77 |
| Epidote | 3.4 | Ca2(Al,Fe)3Si3O12OH | Jones | 522 | 221 | 294 | 508 | 2172 | 1434 | 1417 | 2370 | 1234 | 376 | 531 | 271 | 715 | 271 | 706 | 562 | 145 | 141 | 159 | 153 | 185 | 203 | 254 | 110 |
| Garnet | 3.74 | Mg3Al2(SiO4)3 | | 769 | 379 | 1036 | 429 | 1430 | 1263 | 761 | 1020 | 413 | 338 | 348 | 346 | 316 | 390 | 193 | 174 | 978 | 175 | 355 | 364 | 293 | 440 | 359 | 115 |
| Anorthite | 2.76 | CaAl2Si2O8 | Klein | 5227 | 2334 | 3895 | 5326 | 6697 | 7472 | 5578 | 7050 | 5840 | 4120 | 5508 | 3294 | 4728 | 4699 | 5113 | 4067 | 2142 | 4179 | 3877 | 3619 | 3841 | 3949 | 3813 | 2960 |
| Albite | 2.62 | NaAlSi3O8 | Klein | 2803 | 1199 | 1818 | 1975 | 4613 | 4025 | 2753 | 3984 | 2918 | 2532 | 3593 | 1987 | 2430 | 2693 | 3026 | 2590 | 1788 | 2234 | 2227 | 1753 | 1861 | 2320 | 2350 | 1483 |
| Diopside | 3.2 | CaMg0.9Fe0.1Al0.1Si1.9O6 | Klein | 68 | 61 | 26 | 64 | 409 | 369 | 230 | 473 | 348 | 96 | 144 | 38 | 125 | 53 | 267 | 160 | 34 | 41 | 17 | 40 | 26 | 17 | 53 | 27 |
| Augite | 3.4 | (Ca0.9Na0.1)(Mg0.9Fe0.2Al0.4Ti0.1)(Si1.9Al)2O6 | | 143 | 25 | 63 | 147 | 618 | 312 | 363 | 636 | 430 | 172 | 161 | 46 | 226 | 127 | 188 | 228 | 403 | 324 | 252 | 292 | 257 | 275 | 324 | 204 |
| Enstatite | 3.3 | Mg0.85Fe0.1Ca0.05Si0.95Al0.05O3 | Klein | 8 | 8 | 2 | 27 | 23 | 20 | 25 | 9 | 14 | 7 | 34 | 9 | 16 | 8 | 24 | 36 | 3 | 10 | 1 | 4 | 7 | 10 | 12 | 4 |
| Titanite | 3.5 | CaTiSiO5 | | 60 | 73 | 37 | 50 | 352 | 312 | 324 | 507 | 255 | 58 | 90 | 47 | 115 | 23 | 164 | 79 | 23 | 35 | 32 | 31 | 46 | 36 | 58 | 27 |
| Ilmenite | 4.8 | FeTiO3 | Klein | 596 | 172 | 381 | 284 | 439 | 657 | 436 | 467 | 367 | 164 | 337 | 156 | 170 | 248 | 258 | 221 | 306 | 255 | 205 | 257 | 253 | 218 | 232 | 173 |
| Magnetite | 5.2 | Fe3O4 | MP Jones | 184 | 96 | 55 | 60 | 241 | 380 | 272 | 411 | 123 | 44 | 133 | 75 | 124 | 66 | 108 | 122 | 97 | 40 | 50 | 62 | 50 | 55 | 58 | 33 |
| Muscovite | 2.8 | KAl2(AlSi3O10)(OH)2 | Klein | 5027 | 2681 | 4788 | 3017 | 7134 | 6857 | 4287 | 5754 | 4336 | 4744 | 4670 | 3650 | 4139 | 4816 | 3756 | 3063 | 6115 | 3390 | 4183 | 4358 | 3758 | 3979 | 3479 | 1963 |
| Fosterite | 3.32 | (Mg1.6Fe0.4)SiO4 | | 42 | 12 | 35 | 15 | 91 | 64 | 16 | 43 | 55 | 74 | 77 | 30 | 75 | 30 | 47 | 45 | 18 | 34 | 25 | 21 | 10 | 23 | 37 | 13 |
| Orthoclase | 2.57 | KAlSi3O8 | Jones | 2162 | 897 | 1246 | 1244 | 742 | 1907 | 1288 | 914 | 1173 | 1185 | 2042 | 926 | 1114 | 1304 | 1903 | 1317 | 977 | 1590 | 1339 | 1256 | 1399 | 1454 | 1380 | 1206 |
| Monazite | 5.1 | (La,Ce)PO4 | Jones | 2 | 1 | 7 | 0 | 1 | 3 | 3 | 7 | 1 | 2 | 5 | 3 | 1 | 3 | 3 | 1 | 1 | 1 | 2 | 0 | 0 | 2 | 0 | 0 |
| Pumic-glass | 0.82 | (SiO2)(K2O)(Na2O) | | 1716 | 408 | 1219 | 3154 | 1891 | 1593 | 1350 | 1835 | 3002 | 2806 | 2977 | 1720 | 1357 | 2795 | 2035 | 2991 | 1090 | 1388 | 1109 | 1267 | 1320 | 1559 | 1706 | 2892 |
| Rutile | 4.3 | TiO2 | Klein | 54 | 37 | 34 | 33 | 37 | 67 | 39 | 40 | 73 | 31 | 78 | 17 | 31 | 30 | 43 | 33 | 245 | 345 | 391 | 342 | 372 | 378 | 315 | 258 |
| Spinel | 4 | Mg0.8Fe0.2Al1.9Cr0.1O4 | Jones | 2 | 1 | 0 | 4 | 3 | 2 | 3 | 1 | 2 | 3 | 3 | 1 | 9 | 3 | 3 | 4 | 2 | 1 | 5 | 1 | 0 | 2 | 2 | 1 |
| Sphalerite | 4 | ZnS | Klein | 1 | 0 | 0 | 4 | 0 | 0 | 2 | 2 | 3 | 0 | 1 | 0 | 1 | 0 | 3 | 3 | 1 | 1 | 2 | 1 | 0 | 1 | 0 | 1 |
| Calcite | 2.71 | CaCO3 | Klein | 1 | 1 | 0 | 0 | 1 | 0 | 1 | 2 | 1 | 0 | 2 | 0 | 1 | 1 | 2 | 0 | 0 | 1 | 0 | 0 | 1 | 0 | 0 | 0 |
| Zircon | 4.7 | ZrSiO4 | | 13 | 13 | 7 | 8 | 13 | 16 | 13 | 7 | 19 | 18 | 24 | 5 | 13 | 13 | 16 | 20 | 9 | 7 | 5 | 7 | 10 | 5 | 8 | 6 |
| Dolomite | 2.85 | CaMg(CO3)2 | Klein | 1 | 0 | 0 | 0 | 0 | 0 | 0 | 0 | 1 | 0 | 1 | 1 | 1 | 0 | 0 | 0 | 0 | 0 | 0 | 0 | 0 | 0 | 0 | 0 |
| Iron_sulphide | 4.19 | CuFeS2 | | 85 | 28 | 30 | 27 | 210 | 142 | 150 | 241 | 63 | 26 | 60 | 41 | 37 | 31 | 45 | 41 | 54 | 20 | 34 | 36 | 12 | 49 | 39 | 29 |
| Staurolite | 3.64 | Fe1.4Li0.1Mg0.1Al8.6Si3.9Al0.1O21.7(OH)2.3 | | 32 | 13 | 16 | 7 | 25 | 13 | 16 | 14 | 1 | 13 | 4 | 2 | 109 | 9 | 9 | 1 | 0 | 1 | 4 | 2 | 1 | 0 | 10 | 4 |
| Al_Silicate | 2.9 | Al2SiO5 | | 743 | 157 | 557 | 349 | 336 | 265 | 277 | 212 | 151 | 455 | 172 | 270 | 2396 | 576 | 218 | 362 | 450 | 861 | 985 | 1230 | 1297 | 906 | 694 | 706 |
| Tourmaline | 3.27 | NaFe1.75Mg0.5Al6.75Si6O18(BO3)3(OH)4 | | 98 | 37 | 138 | 86 | 207 | 95 | 78 | 79 | 39 | 58 | 27 | 33 | 52 | 66 | 31 | 32 | 30 | 40 | 76 | 40 | 69 | 72 | 83 | 16 |
| Pyrrhotite | 4.6 | FeS | MP Jones | 3 | 0 | 1 | 2 | 4 | 3 | 2 | 2 | 1 | 1 | 3 | 0 | 3 | 1 | 3 | 1 | 0 | 0 | 0 | 2 | 1 | 1 | 4 | 0 |
| Perthite | 2.56 | KAlSi3O8NaAlSi3O8 | | 5539 | 1912 | 4378 | 7073 | 3346 | 5841 | 3352 | 3546 | 6893 | 4598 | 8342 | 3184 | 4069 | 8182 | 6824 | 4936 | 4755 | 7209 | 6107 | 8923 | 6220 | 5593 | 5393 | 6030 |
| Xenotime | 5 | YPO4 | | 1 | 1 | 1 | 0 | 0 | 2 | 1 | 0 | 0 | 0 | 1 | 0 | 3 | 1 | 1 | 0 | 0 | 0 | 0 | 0 | 0 | 1 | 0 | 0 |
| Pentlandite | 5 | (Fe,Ni)9S8 | Jones | 0 | 0 | 0 | 0 | 0 | 0 | 0 | 0 | 1 | 0 | 2 | 0 | 0 | 1 | 0 | 0 | 0 | 0 | 0 | 0 | 0 | 0 | 0 | 0 |
| corundum | 4.02 | Al2O3 | Klein | 25 | 0 | 8 | 2 | 2 | 1 | 15 | 9 | 0 | 17 | 4 | 6 | 70 | 21 | 6 | 1 | 4 | 2 | 8 | 2 | 7 | 1 | 10 | 9 |
| Apatite | 3.2 | Ca5(PO4)3F | Klein | 0 | 2 | 0 | 3 | 1 | 3 | 3 | 4 | 1 | 2 | 3 | 0 | 2 | 3 | 8 | 2 | 2 | 1 | 0 | 0 | 0 | 0 | 0 | 0 |
| Barite | 4.4 | BaSO4 | Jones | 0 | 0 | 0 | 0 | 0 | 0 | 0 | 0 | 0 | 0 | 3 | 0 | 0 | 0 | 0 | 3 | 0 | 0 | 0 | 0 | 0 | 0 | 0 | 0 |
| Cordierite | 2.6 | Mg1.5Fe0.5Al4Si5O18 | | 39 | 12 | 20 | 57 | 59 | 68 | 99 | 49 | 40 | 47 | 97 | 15 | 28 | 32 | 43 | 48 | 12 | 25 | 28 | 40 | 10 | 30 | 24 | 19 |
| Akermanite | 2.94 | Ca2Mg(Si2O7) | | 5 | 2 | 1 | 4 | 20 | 22 | 6 | 13 | 33 | 1 | 28 | 1 | 2 | 4 | 4 | 10 | 5 | 1 | 1 | 1 | 0 | 1 | 8 | 2 |
| Serpentine | 2.3 | Mg3Si2O5(OH)4 | Klein | 24 | 3 | 23 | 5 | 7 | 19 | 27 | 9 | 17 | 39 | 25 | 18 | 11 | 12 | 14 | 4 | 4 | 9 | 14 | 15 | 5 | 6 | 13 | 1 |
| Glass-slide | 2.4 | | | 20 | 0 | 3 | 5 | 7 | 1 | 42 | 10 | 12 | 17 | 7 | 4 | 31 | 3 | 4 | 9 | 0 | 1 | 1 | 0 | 0 | 2 | 3 | 0 |
| Unknown | 2 | | | 908 | 860 | 947 | 1251 | 1521 | 1654 | 676 | 826 | 1177 | 899 | 2779 | 344 | 822 | 1583 | 1322 | 933 | 538 | 248 | 352 | 379 | 415 | 488 | 1130 | 295 |
| Total Particle Count | | | | **59609** | **28498** | **48668** | **55030** | **67748** | **82709** | **54692** | **68828** | **64776** | **57358** | **74136** | **41389** | **48099** | **63441** | **64314** | **49131** | **48993** | **46858** | **47973** | **48300** | **45476** | **48366** | **49037** | **37584** |

| Physiographic Position / Sample | Density | Formula | Reference | Moresby Trough Fan MV22-165 | MV22-397 | MV22-502 | MV22-562 | MV22-674 | MV22-808 | MV22-936 | MV22-1113 |
|---|---|---|---|---|---|---|---|---|---|---|---|
| Altered minerals/clay | 2.6 | Al2Si2O5(OH)4 | | 19799 | 12690 | 12505 | 12991 | 18921 | 13379 | 8967 | 20327 |
| Amphibole | 3.23 | Ca2[Mg4(Al0.75Fe0.25)]Si7AlO22(OH)2 | | 5194 | 2299 | 2058 | 4332 | 2130 | 1438 | 680 | 3122 |
| Biotite | 3 | K(Mg,Fe)3(AlSi3O10)(OH)2 | Klein | 775 | 104 | 160 | 208 | 70 | 32 | 23 | 70 |
| Quartz | 2.65 | SiO2 | Jones | 520 | 3427 | 2899 | 650 | 3781 | 3859 | 2286 | 4838 |
| Quartz_mixture | 2.65 | SiO2 | Jones | 18991 | 4553 | 4617 | 11944 | 11914 | 4998 | 2157 | 11565 |
| Chloritoid | 3.54 | (Fe1.2,Mg0.6Mn0.2)2Al4Si2O10(OH)4 | | 218 | 939 | 757 | 77 | 705 | 344 | 266 | 921 |
| Epidote | 3.4 | Ca2(Al,Fe)3Si3O12OH | Jones | 279 | 1035 | 855 | 171 | 824 | 1068 | 399 | 2065 |
| Garnet | 3.74 | Mg3Al2(SiO4)3 | | 28 | 414 | 514 | 20 | 265 | 103 | 94 | 349 |
| Anorthite | 2.76 | CaAl2Si2O8 | Klein | 6321 | 4701 | 4916 | 4198 | 7491 | 5224 | 3400 | 8110 |
| Albite | 2.62 | NaAlSi3O8 | Klein | 28 | 2452 | 2387 | 95 | 3284 | 3079 | 1657 | 3707 |
| Diopside | 3.2 | CaMg0.9Fe0.1Al0.1Si1.9O6 | Klein | 11 | 227 | 180 | 26 | 77 | 386 | 189 | 530 |
| Augite | 3.4 | (Ca0.9Na0.1)(Mg0.9Fe0.2Al0.4Ti0.1)(Si1.9Al)2O6 | | 355 | 251 | 224 | 603 | 261 | 250 | 170 | 877 |
| Enstatite | 3.3 | Mg0.85Fe0.1Ca0.05Si0.95Al0.05O3 | Klein | 5 | 21 | 17 | 4 | 24 | 13 | 7 | 18 |
| Titanite | 3.5 | CaTiSiO5 | | 14 | 211 | 183 | 8 | 95 | 158 | 60 | 430 |
| Ilmenite | 4.8 | FeTiO3 | Klein | 192 | 342 | 364 | 256 | 556 | 219 | 159 | 594 |
| Magnetite | 5.2 | Fe3O4 | MP Jones | 299 | 190 | 142 | 226 | 103 | 93 | 41 | 151 |
| Muscovite | 2.8 | KAl2(AlSi3O10)(OH)2 | Klein | 89 | 3215 | 4298 | 126 | 4160 | 3300 | 2930 | 5383 |
| Fosterite | 3.32 | (Mg1.6Fe0.4)SiO4 | | 8 | 31 | 48 | 2 | 40 | 10 | 7 | 32 |
| Orthoclase | 2.57 | KAlSi3O8 | Jones | 426 | 857 | 932 | 268 | 2326 | 887 | 523 | 1250 |
| Monazite | 5.1 | (La,Ce)PO4 | Jones | 1 | 0 | 1 | 0 | 1 | 1 | 2 | 1 |
| Pumic-glass | 0.82 | (SiO2)(K2O)(Na2O) | | 19697 | 1527 | 1758 | 11936 | 4079 | 1734 | 906 | 2207 |
| Rutile | 4.3 | TiO2 | Klein | 5 | 39 | 72 | 3 | 59 | 49 | 58 | 106 |
| Spinel | 4 | Mg0.8Fe0.2Al1.9Cr0.1O4 | Jones | 1 | 2 | 3 | 1 | 1 | 2 | 3 | 7 |
| Sphalerite | 4 | ZnS | Klein | 0 | 1 | 0 | 0 | 0 | 1 | 0 | 1 |
| Calcite | 2.71 | CaCO3 | Klein | 2 | 2 | 1 | 1 | 1 | 6 | 0 | 0 |
| Zircon | 4.7 | ZrSiO4 | | 38 | 14 | 14 | 34 | 9 | 15 | 9 | 20 |
| Dolomite | 2.85 | CaMg(CO3)2 | Klein | 0 | 0 | 0 | 0 | 0 | 0 | 0 | 0 |
| Iron_sulphide | 4.19 | CuFeS2 | | 113 | 130 | 150 | 124 | 114 | 39 | 26 | 143 |
| Staurolite | 3.64 | Fe1.4Li0.1Mg0.1Al8.6Si3.9Al0.1O21.7(OH)2.3 | | 1 | 17 | 9 | 0 | 20 | 15 | 9 | 10 |
| Al_Silicate | 2.9 | Al2SiO5 | | 4 | 300 | 787 | 9 | 976 | 272 | 322 | 274 |
| Tourmaline | 3.27 | NaFe1.75Mg0.5Al6.75Si6O18(BO3)3(OH)4 | | 9 | 69 | 117 | 3 | 92 | 29 | 22 | 63 |
| Pyrrhotite | 4.6 | FeS | MP Jones | 19 | 13 | 12 | 17 | 5 | 3 | 1 | 14 |
| Perthite | 2.56 | KAlSi3O8NaAlSi3O8 | | 15646 | 2766 | 3522 | 13132 | 10302 | 3928 | 2390 | 8500 |
| Xenotime | 5 | YPO4 | | 0 | 0 | 1 | 0 | 0 | 0 | 1 | 1 |
| Pentlandite | 5 | (Fe,Ni)9S8 | Jones | 6 | 0 | 0 | 9 | 1 | 0 | 0 | 1 |
| corundum | 4.02 | Al2O3 | Klein | 0 | 3 | 9 | 0 | 12 | 1 | 8 | 9 |
| Apatite | 3.2 | Ca5(PO4)3F | Klein | 8 | 1 | 1 | 35 | 3 | 0 | 0 | 4 |
| Barite | 4.4 | BaSO4 | Jones | 0 | 0 | 0 | 0 | 1 | 0 | 0 | 0 |
| Cordierite | 2.6 | Mg1.5Fe0.5Al4Si5O18 | | 36 | 34 | 44 | 30 | 116 | 40 | 25 | 50 |
| Akermanite | 2.94 | Ca2Mg(Si2O7) | | 116 | 2 | 1 | 122 | 3 | 1 | 1 | 42 |
| Serpentine | 2.3 | Mg3Si2O5(OH)4 | Klein | 1 | 0 | 0 | 0 | 2 | 0 | 0 | 4 |
| Glass-slide | 2.4 | | | 1 | 10 | 4 | 1 | 2 | 8 | 2 | 7 |
| Unknown | 2 | | | 3807 | 362 | 510 | 1886 | 1954 | 342 | 186 | 1349 |
| Total Particle Count | | | | **93063** | **43251** | **45072** | **63548** | **74780** | **45326** | **27986** | **77152** |

| Physiographic Position / Sample | Moresby Trough Channel MV25-246 | MV25-340 | MV25-475 | MV25-554 | MV25-630 | MV25-954 | MV25-1073 | MV25-1104 | MV25-1210 | MV29-184 | MV29-259 | MV29-413 | MV29-510 | MV29-611 |
|---|---|---|---|---|---|---|---|---|---|---|---|---|---|---|
| Altered minerals/clay | 12321 | 16972 | 18924 | 6959 | 11170 | 11968 | 12659 | 15769 | 19768 | 10860 | 10199 | 12548 | 10478 | 10517 |
| Amphibole | 2163 | 3276 | 3563 | 671 | 1137 | 729 | 1764 | 2114 | 3070 | 1987 | 3451 | 3798 | 1796 | 3056 |
| Biotite | 252 | 221 | 174 | 3 | 13 | 1 | 19 | 56 | 102 | 80 | 299 | 258 | 63 | 59 |
| Quartz | 2291 | 4200 | 5005 | 2911 | 3126 | 3750 | 3575 | 4522 | 4371 | 3897 | 3466 | 4499 | 3868 | 3492 |
| Quartz_mixture | 7191 | 7200 | 7540 | 3650 | 5416 | 6018 | 8069 | 8024 | 10958 | 6253 | 7216 | 8394 | 7139 | 9546 |
| Chloritoid | 861 | 1394 | 1578 | 38 | 121 | 51 | 315 | 561 | 1028 | 720 | 1274 | 1721 | 620 | 643 |
| Epidote | 741 | 1437 | 1415 | 405 | 795 | 809 | 1128 | 668 | 1378 | 856 | 1224 | 1966 | 1111 | 1332 |
| Garnet | 851 | 706 | 549 | 2 | 15 | 7 | 63 | 133 | 544 | 391 | 1165 | 1237 | 278 | 285 |
| Anorthite | 4785 | 5609 | 6224 | 2794 | 3801 | 3799 | 4270 | 6041 | 7874 | 4262 | 4213 | 5375 | 4858 | 6108 |
| Albite | 1811 | 2981 | 3038 | 1371 | 1981 | 2349 | 2181 | 3663 | 3348 | 2341 | 2006 | 4422 | 2387 | 2699 |
| Diopside | 205 | 476 | 226 | 168 | 177 | 106 | 324 | 152 | 189 | 376 | 540 | 401 | 392 | 654 |
| Augite | 308 | 488 | 376 | 79 | 249 | 155 | 385 | 207 | 424 | 388 | 928 | 1085 | 1038 | 1148 |
| Enstatite | 15 | 21 | 21 | 13 | 16 | 2 | 14 | 42 | 17 | 36 | 69 | 5 | 24 | 62 |
| Titanite | 152 | 329 | 242 | 85 | 109 | 114 | 208 | 109 | 181 | 258 | 307 | 590 | 285 | 299 |
| Ilmenite | 543 | 686 | 515 | 80 | 96 | 82 | 262 | 279 | 473 | 445 | 544 | 448 | 308 | 390 |
| Magnetite | 199 | 358 | 190 | 56 | 12 | 6 | 61 | 121 | 98 | 462 | 383 | 337 | 113 | 218 |
| Muscovite | 3587 | 5408 | 5571 | 1018 | 2718 | 2843 | 3406 | 3206 | 5168 | 3174 | 4725 | 6146 | 4882 | 3750 |
| Fosterite | 39 | 36 | 48 | 2 | 14 | 4 | 16 | 15 | 19 | 65 | 24 | 41 | 11 | 17 |
| Orthoclase | 950 | 1170 | 1676 | 886 | 915 | 1261 | 1253 | 1967 | 1506 | 1086 | 1288 | 826 | 1460 | 1237 |
| Monazite | 4 | 1 | 2 | 0 | 1 | 0 | 2 | 1 | 5 | 3 | 6 | 1 | 1 | 4 |
| Pumic-glass | 1844 | 1964 | 2861 | 1153 | 3367 | 2982 | 2257 | 4005 | 2584 | 1358 | 2228 | 2280 | 1959 | 4617 |
| Rutile | 84 | 95 | 77 | 16 | 47 | 36 | 60 | 41 | 68 | 344 | 275 | 506 | 406 | 338 |
| Spinel | 5 | 2 | 5 | 2 | 7 | 3 | 14 | 6 | 3 | 8 | 4 | 2 | 11 | 6 |
| Sphalerite | 0 | 1 | 0 | 1 | 2 | 1 | 3 | 2 | 3 | 1 | 6 | 2 | 3 | 0 |
| Calcite | 1 | 2 | 4 | 0 | 0 | 1 | 2 | 0 | 5 | 0 | 2 | 1 | 0 | 0 |
| Zircon | 12 | 13 | 18 | 11 | 7 | 10 | 22 | 11 | 16 | 19 | 29 | 25 | 25 | 18 |
| Dolomite | 0 | 0 | 0 | 0 | 0 | 0 | 0 | 0 | 1 | 0 | 0 | 0 | 0 | 0 |
| Iron_sulphide | 154 | 121 | 104 | 7 | 8 | 12 | 49 | 50 | 65 | 128 | 341 | 152 | 35 | 71 |
| Staurolite | 40 | 9 | 21 | 0 | 11 | 3 | 5 | 10 | 10 | 2 | 1 | 0 | 15 | 5 |
| Al_Silicate | 599 | 649 | 589 | 44 | 280 | 158 | 161 | 256 | 532 | 220 | 385 | 392 | 578 | 236 |
| Tourmaline | 134 | 89 | 166 | 4 | 14 | 18 | 19 | 31 | 156 | 28 | 77 | 29 | 22 | 15 |
| Pyrrhotite | 2 | 1 | 3 | 1 | 0 | 0 | 3 | 1 | 1 | 4 | 46 | 13 | 8 | 6 |
| Perthite | 4275 | 4204 | 4714 | 2779 | 3986 | 4465 | 6087 | 5724 | 7482 | 3527 | 4247 | 3338 | 5366 | 7108 |
| Xenotime | 2 | 3 | 1 | 1 | 0 | 0 | 0 | 0 | 0 | 0 | 3 | 2 | 0 | 0 |
| Pentlandite | 0 | 0 | 0 | 0 | 0 | 0 | 0 | 0 | 0 | 0 | 0 | 0 | 0 | 0 |
| corundum | 7 | 4 | 21 | 0 | 10 | 16 | 5 | 22 | 3 | 2 | 0 | 3 | 4 | 3 |
| Apatite | 1 | 3 | 3 | 3 | 0 | 2 | 3 | 3 | 0 | 8 | 19 | 14 | 10 | 8 |
| Barite | 0 | 1 | 0 | 0 | 0 | 0 | 0 | 0 | 0 | 0 | 5 | 0 | 0 | 0 |
| Cordierite | 51 | 46 | 59 | 45 | 20 | 12 | 59 | 58 | 35 | 61 | 107 | 56 | 38 | 208 |
| Akermanite | 26 | 14 | 7 | 2 | 9 | 1 | 43 | 4 | 12 | 11 | 15 | 8 | 2 | 12 |
| Serpentine | 0 | 2 | 26 | 0 | 0 | 1 | 5 | 0 | 1 | 8 | 0 | 0 | 0 | 0 |
| Glass-slide | 2 | 103 | 27 | 0 | 133 | 117 | 22 | 7 | 12 | 1 | 0 | 2 | 4 | 3 |
| Unknown | 1111 | 783 | 490 | 632 | 478 | 334 | 2570 | 410 | 1456 | 287 | 525 | 584 | 620 | 596 |
| Total Particle Count | **47619** | **61078** | **66073** | **25892** | **40261** | **42226** | **51363** | **58291** | **72966** | **43957** | **51642** | **61507** | **50218** | **58766** |

| Physiographic Position / Sample | Eastern Field Platform MV27-248 | MV27-343 | MV27-462 | MV27-480 | MV27-547 | MV27-760 | MV27-1289 |
|---|---|---|---|---|---|---|---|
| Altered minerals/clay | 14477 | 11895 | 15292 | 17333 | 12040 | 15572 | 12035 |
| Amphibole | 886 | 1464 | 2467 | 1325 | 1556 | 2705 | 1847 |
| Biotite | 25 | 43 | 79 | 47 | 42 | 116 | 56 |
| Quartz | 5082 | 3558 | 3927 | 5649 | 3533 | 2862 | 2958 |
| Quartz_mixture | 5748 | 5949 | 7005 | 6604 | 5270 | 7637 | 4795 |
| Chloritoid | 269 | 380 | 726 | 460 | 572 | 828 | 642 |
| Epidote | 232 | 391 | 1142 | 383 | 582 | 1126 | 963 |
| Garnet | 122 | 234 | 304 | 165 | 197 | 758 | 221 |
| Anorthite | 3517 | 3498 | 6139 | 4988 | 4413 | 5278 | 4295 |
| Albite | 2462 | 1903 | 3135 | 3135 | 2267 | 2544 | 2529 |
| Diopside | 52 | 129 | 370 | 142 | 170 | 159 | 171 |
| Augite | 59 | 118 | 354 | 135 | 223 | 316 | 254 |
| Enstatite | 12 | 25 | 27 | 12 | 20 | 4 | 11 |
| Titanite | 65 | 123 | 239 | 95 | 103 | 80 | 153 |
| Ilmenite | 129 | 291 | 371 | 223 | 222 | 394 | 230 |
| Magnetite | 49 | 177 | 240 | 119 | 124 | 104 | 71 |
| Muscovite | 2737 | 2599 | 3566 | 3252 | 2889 | 4906 | 3458 |
| Fosterite | 28 | 37 | 51 | 16 | 65 | 22 | 46 |
| Orthoclase | 1084 | 1177 | 1604 | 1672 | 970 | 1073 | 1050 |
| Monazite | 0 | 1 | 0 | 2 | 0 | 0 | 0 |
| Pumic-glass | 3323 | 1427 | 3056 | 3107 | 2820 | 1836 | 1959 |
| Rutile | 28 | 48 | 34 | 31 | 32 | 33 | 29 |
| Spinel | 2 | 1 | 0 | 5 | 7 | 3 | 1 |
| Sphalerite | 1 | 0 | 3 | 1 | 3 | 0 | 0 |
| Calcite | 0 | 0 | 1 | 2 | 1 | 0 | 0 |
| Zircon | 4 | 8 | 21 | 15 | 9 | 12 | 15 |
| Dolomite | 1 | 0 | 1 | 1 | 1 | 0 | 0 |
| Iron_sulphide | 26 | 45 | 93 | 61 | 62 | 99 | 42 |
| Staurolite | 9 | 2 | 2 | 11 | 17 | 21 | 16 |
| Al_Silicate | 231 | 164 | 168 | 299 | 199 | 430 | 245 |
| Tourmaline | 41 | 36 | 51 | 35 | 40 | 77 | 56 |
| Pyrrhotite | 2 | 1 | 5 | 7 | 13 | 2 | 2 |
| Perthite | 3691 | 3879 | 5036 | 4810 | 3797 | 5584 | 3648 |
| Xenotime | 3 | 0 | 0 | 0 | 0 | 0 | 0 |
| Pentlandite | 0 | 0 | 0 | 0 | 1 | 0 | 0 |
| corundum | 2 | 2 | 13 | 8 | 8 | 23 | 1 |
| Apatite | 2 | 7 | 3 | 0 | 1 | 1 | 1 |
| Barite | 0 | 0 | 0 | 0 | 0 | 0 | 0 |
| Cordierite | 19 | 47 | 76 | 29 | 47 | 22 | 29 |
| Akermanite | 1 | 2 | 4 | 0 | 6 | 2 | 1 |
| Serpentine | 8 | 2 | 8 | 4 | 17 | 0 | 6 |
| Glass-slide | 10 | 3 | 74 | 156 | 117 | 1 | 4 |
| Unknown | 498 | 945 | 490 | 571 | 624 | 910 | 352 |
| Total Particle Count | **44937** | **40611** | **56177** | **54910** | **43080** | **55540** | **42192** |